
Searching for transits in the WTS with the difference imaging light curves



Jesús Zendejas Domínguez

München 2013

Searching for transits in the WTS with the difference imaging light curves

Dissertation an der Fakultät Physik
Dissertation of the Faculty of Physics

Ludwig-Maximilians-Universität München
at the Ludwig Maximilian University of Munich

für den Grad des
for the degree of

Doctor rerum naturalium

vorgelegt von
presented by **Jesús Zendejas Domínguez**

aus México, D.F.
from

München, den 6. Dezember 2013

Erstgutachter: Priv. Doz. Dr. Roberto Saglia
Zweitgutachterin: Prof. Dr. Barbara Ercolano
Tag der mündlichen Prüfung: 10. Februar 2014

*A los personajes de esta historia
a la vida...*

Zusammenfassung

Die Suche nach Exoplaneten ist heute eine der interessantesten und aktivsten Forschungsgebiete in der Astronomie. Vor allem erdähnliche Planeten sind das Ziel diverser Forschungsprojekte, da diese, sofern sie in einem bestimmten Abstand um ihrem Mutter-Stern kreisen, eine Oberflächentemperatur aufweisen, die ein Vorkommen von Wasser in flüssiger Form ermöglicht und somit "habitable" sind. Außerdem sorgt die Entdeckung von Gasriesen in kurzperiodischen Umlaufbahnen für wichtige Erkenntnisse zu Modellen, die die Planetenbildung und orbitale Migration beschreiben. Viele Projekte haben es sich zum Ziel gesetzt, Planeten außerhalb unseres Sonnensystems zu finden und zu charakterisieren. Eines dieser Projekte ist der WFCam Transit Survey (WTS), ein Pionierprogramm, das sich durch eine besondere Zielsetzung und Methodik auszeichnet. Die Beobachtungen für WTS haben im August 2007 am United Kingdom Infrared Telescope in Hawaii begonnen. Der Survey unternimmt die erste Suche nach Exoplaneten im nah-infraroten Wellenlängenbereich, welcher für die Suche nach Planeten um M-Zwerg optimal ist. Ursprünglich waren für das Projekt etwa 200 Nächte geplant - verteilt auf insgesamt vier Felder, welche über das Jahr verteilt beobachtet wurden. Die gewonnenen Daten werden in einer automatischen Pipeline prozessiert, um Lichtkurven mit Aperturphotometrie zu erstellen. Für das Feld mit den meisten Beobachtungen ("19h-Feld" mit 1145 Belichtungen) erzeugen wir ein alternatives Set an Lichtkurven mit "difference imaging", einer photometrischen Methode, die sich in der Vergangenheit für Felder mit hohen Sterndichten als überlegen herausgestellt hat. Ein quantitativer Vergleich zwischen der photometrischen Genauigkeit der beiden Methoden wurde in dieser Arbeit durchgeführt. Wir korrigieren außerdem systematische Effekte unter Verwendung des "system" Algorithmus, skalieren die unrealistischen Fehlerbalken in den Lichtkurven und vergleichen diese mit den ursprünglichen. Die Ergebnisse zeigen, dass die Lichtkurven der Aperturphotometrie geringfügig höhere Genauigkeit für Objekte mit $J < 16$ mag aufweisen. Difference imaging Lichtkurven zeigen dagegen eine deutliche Verbesserung für schwächere Sterne. Um Transits von Planeten zu detektieren, verwenden wir eine modifizierte Version des "box-fitting" Algorithmus. Unsere Implementierung erweitert den Algorithmus um einem Trapezoid-Fit des Transitbereichs in der gefalteten Lichtkurve. Wie wir zeigen, liefert dieser Fit bessere Resultate als der reine Box-Fit.

Wir beschreiben ein Set von Selektionskriterien, mit welchem wir nach Transit-Kandidaten in den Lichtkurven suchen. Diese Kriterien beinhalten einen Parameter, der von unserem Detektionsalgorithmus berechnet wird: der V -Form Parameter. Dieser hat sich als sehr nützlich herausgestellt, um automatisch bedeckungsveränderliche Doppelsterne zu identifizieren und diese von der Suche nach Planeten auszuschließen. Wir optimieren die Kriterien über Monte-Carlo Simulationen von künstlichen Transitsignalen, welche in die realen WTS Lichtkurven eingespeist und durch unseren Detektionsalgorithmus analysiert werden. Wir führen die Optimierung der Selektionskriterien separat für zwei getrennte Sets von Lichtkurven durch, jeweils eines für F-G-K Sterne und für M-Sterne. Um nach Transits von Planeten zu suchen, werden die optimierten Kriterien auf die Lichtkurven von

Aperturphotometrie und difference imaging Photometrie angewendet. Auf diese Weise werden die 200 besten Transitkandidaten aus $\sim 475\,000$ Quellen automatisch selektiert. Danach wird eine visuelle Untersuchung der gefalteten Lichtkurven vorgenommen, um klare Fehldetektionen zu entfernen. Anschließend werden weitere Analyseschritte für die vielversprechendsten 18 Kandidaten durchgeführt, was es uns ermöglicht, diese Objekte als Planeten-Kandidaten oder bedeckungsveränderliche Doppelsterne zu klassifizieren. Wir haben einen vielversprechenden Planetenkandidaten gefunden, der um einen späten G-Stern kreist, für welchen wir eine photometrische Nachbeobachtung vorschlagen. Die davon unabhängige Analyse der M-Stern Lichtkurven führte zu keiner Detektion. Damit können wir die Nullhypothese und die oberen Limits für die Häufigkeit von Gasriesen um M-Zwerg mit $J \leq 17$ mag aus einer früheren Studie bestätigen. In dieser Arbeit erweitern wir die Suche nach Planetentransits auf Sterne mit $J \leq 18$ mag, was es uns ermöglicht, ein Limit von 1.1 % für die Häufigkeit von kurzperiodischen Gasriesen um M-Zwerg zu setzen, was deutlich niedriger ist als die Limits anderer Publikationen.

Der Mangel an Hot Jupiters um M-Zwerg spielt eine wichtige Rolle für die Theorien von Planetenentstehung von Exoplaneten um Sterne mit niedriger Masse. Das Fehlen von Gasriesen in kurzperiodischen Orbits um M-Sterne zeigt, dass der Disk-Instabilitätsmechanismus in Kombination mit einer Migration des Orbits nicht benötigt wird, um die Planetenbildung zu beschreiben. Die deutlich geringere Effizienz des “Core Accretion” Modells, Jupiter um kühle Sterne zu erzeugen, wird durch die Nullhypothese bestätigt. Unser oberes Limit ist jedoch immer noch höher als die Detektionsraten von kurzperiodigen Gasriesen um heißere Sterne. Wir können also kein abschließendes Fazit über die Entstehungsmodelle von jupiterähnlichen Planeten um kühle, massearme Hauptreihensterne ziehen. Momentan gibt es noch nicht ausreichende Beobachtungen, um die Vorhersage, dass Hot Jupiters weniger häufig um M-Sterne als um sonnenähnliche Sterne sind, zu untermauern. Um dies zu erreichen, muss eine noch grössere Anzahl an M-Sternen beobachtet werden. Dies könnte durch eine umfassende Analyse aller vier WTS Felder erreicht werden oder aber durch andere momentan durchgeführte M-Zwerg Transit Surveys wie etwa Pan-Planets oder PTF/M-Dwarfs, welche nahezu 100 000 M-Sterne beobachten. Aktuelle und zukünftige Weltraummissionen wie *Kepler* und GAIA könnten ebenfalls weitere Erkenntnisse über die Häufigkeit von Hot Jupiters um massearme Sterne liefern.

Im letzten Teil dieser Arbeit präsentieren wir weitere Anwendungen der difference imaging Lichtkurven. Wir haben insgesamt fünf lichtschwache, bedeckungsveränderliche Doppelsternsysteme mit extrem kurzen Perioden unterhalb von 0.23 Tagen detektiert. Ausserdem konnten wir zwei weitere unbestätigte und ein bestätigtes bedeckungsveränderliches M-Zwerg/M-Zwerg Doppelstern-System finden. Alle in dieser Arbeit präsentierten Detektionen demonstrieren die Stärken der difference imaging Methode, welche vor allem bei lichtschwächeren Magnituden entscheidende Vorteile bringt.

Abstract

The search for exo-planets is currently one of the most exciting and active topics in astronomy. Small and rocky planets are particularly the subject of intense research, since if they are suitably located from their host star, they may be warm and potentially habitable worlds. On the other hand, the discovery of giant planets in short-period orbits provides important constraints on models that describe planet formation and orbital migration theories. Several projects are dedicated to discover and characterize planets outside of our solar system. Among them, the Wide-Field Camera Transit Survey (WTS) is a pioneer program aimed to search for extra-solar planets, that stands out for its particular aims and methodology. The WTS has been in operation since August 2007 with observations from the United Kingdom Infrared Telescope, and represents the first survey that searches for transiting planets in the near-infrared wavelengths; hence the WTS is designed to discover planets around M-dwarfs. The survey was originally assigned about 200 nights, observing four fields that were selected seasonally (RA = 03, 07, 17 and 19h) during a year. The images from the survey are processed by a data reduction pipeline, which uses aperture photometry to construct the light curves. For the most complete field (19h-1145 epochs) in the survey, we produce an alternative set of light curves by using the method of difference imaging, which is a photometric technique that has shown important advantages when used in crowded fields. A quantitative comparison between the photometric precision achieved with both methods is carried out in this work. We remove systematic effects using the *sysrem* algorithm, scale the error bars on the light curves, and perform a comparison of the corrected light curves. The results show that the aperture photometry light curves provide slightly better precision for objects with $J < 16$. However, difference photometry light curves present a significant improvement for fainter stars. In order to detect transits in the WTS light curves, we use a modified version of the box-fitting algorithm. The implementation on the detection algorithm performs a trapezoid-fit to the folded light curve. We show that the new fit is able to produce more accurate results than the box-fit model.

We describe a set of selection criteria to search for transit candidates that include a parameter calculated by our detection algorithm: the V -shape parameter, which has proven to be useful to automatically identify and remove eclipsing binaries from the survey. The criteria are optimized using Monte-Carlo simulations of artificial transit signals that are injected into the real WTS light curves and subsequently analyzed by our detection algorithm. We separately optimize the selection criteria for two different sets of light curves, one for F-G-K stars, and another for M-dwarfs. In order to search for transiting planet candidates, the optimized selection criteria are applied to the aperture photometry and difference imaging light curves. In this way, the best 200 transit candidates from a sample of $\sim 475\,000$ sources are automatically selected. A visual inspection of the folded light curves of these detections is carried out to eliminate clear false-positives or false-detections. Subsequently, several analysis steps are performed on the 18 best detections, which allow us to classify these objects as transiting planet and eclipsing binary candidates. We report one

planet candidate orbiting a late G-type star, which is proposed for photometric follow-up. The independent analysis on the M-dwarf sample provides no planet candidates around these stars. Therefore, the null detection hypothesis and upper limits on the occurrence rate of giant planets around M-dwarfs with $J \leq 17$ mag presented in a prior study are confirmed. In this work, we extended the search for transiting planets to stars with $J \leq 18$ mag, which enables us to impose a more strict upper limit of 1.1 % on the occurrence rate of short-period giant planets around M-dwarfs, which is significantly lower than other limit published so far.

The lack of Hot Jupiters around M-dwarfs play an important role in the existing theories of planet formation and orbital migration of exo-planets around low-mass stars. The dearth of gas-giant planets in short-period orbit detections around M stars indicates that it is not necessary to invoke the disk instability formation mechanism, coupled with an orbital migration process to explain the presence of such planets around low-mass stars. The much reduced efficiency of the core-accretion model to form Jupiters around cool stars seems to be in agreement with the current null result. However, our upper limit value, the lowest reported so far, is still higher than the detection rates of short-period gas-giant planets around hotter stars. Therefore, we cannot yet reach any firm conclusion about Jovian planet formation models around low-mass and cool main-sequence stars, since there are currently not sufficient observational evidences to support the argument that Hot Jupiters are less common around M-dwarfs than around Sun-like stars. The way to improve this situation is to monitor larger samples of M-stars. For example, an extended analysis of the remaining three WTS fields and currently running M-dwarf transit surveys (like Pan-Planets and PTF/M-dwarfs projects, which are monitoring up to 100 000 objects) may reduce this upper limit. Current and future space missions like *Kepler* and GAIA could also help to either set stricter upper limits or finally detect Hot Jupiters around low-mass stars.

In the last part of this thesis, we present other applications of the difference imaging light curves. We report the detection of five faint extremely-short-period eclipsing binary systems with periods shorter than 0.23 d, as well as two candidates and one confirmed M-dwarf/M-dwarf eclipsing binaries. The detections and results presented in this work demonstrate the benefits of using the difference imaging light curves, especially when going to fainter magnitudes.

Contents

Zusammenfassung	ix
Abstract	xi
Contents	xv
List of Figures	xviii
List of Tables	xix
List of Constants	xxii
List of Abbreviations	xxvi
1 Introduction	1
1.1 Historical Context	1
1.2 General outlook of this work	4
1.3 Planet formation theory	6
1.3.1 The core-accretion/gas-capture model	7
1.3.2 The disk instability model	9
1.4 Orbital migration of exo-planets	10
1.4.1 Type I migration	11
1.4.2 Type II migration	13
1.4.3 Type III migration	14
1.5 Planet detection techniques	15
1.5.1 Timing	15
1.5.2 Microlensing	17
1.5.3 Imaging	19
1.5.4 Astrometry	21
1.5.5 Radial velocity	23
1.5.6 Transit method	26
1.5.7 False-positives in transit surveys	32
1.5.8 Further implications of the transit method	32
1.6 Transit surveys	35

1.6.1	CoRoT	37
1.6.2	<i>Kepler</i>	39
1.6.3	SuperWASP	41
1.6.4	M-dwarf Transit surveys	42
1.6.5	MEarth	43
1.7	M-dwarfs	45
1.7.1	Planet formation around M-dwarfs	46
1.7.2	Habitability and development of life on planets around M-dwarfs	48
1.8	Structure of this Thesis	51
2	The Wide Field Camera Transit Survey	53
2.1	The Wide Field Camera	54
2.2	2D-image reduction pipeline	55
2.3	Astrometry and Photometry	57
2.4	Master catalogues	58
2.5	Aperture photometry light-curve construction	59
2.6	Bad epoch filtering	59
2.7	Transit detection	60
3	The WTS Difference Imaging light curves	61
3.1	Difference Imaging Analysis	62
3.2	DI light curve extraction	64
3.3	The <i>sysrem</i> algorithm	64
3.4	Quality of the DI light curves and comparison with the AP method	67
3.5	Correction of the point-by-point errors derived from the individual images	69
4	Transit detection algorithm	77
4.1	The box-fitting algorithm	77
4.2	Implementations to the Box-fitting algorithm: The <i>V</i> -shape parameter	81
5	Selection Criteria	85
5.1	Description of the Selection Criteria	85
5.2	Optimization of Selection Criteria	87
5.3	Simulations and optimization strategy	87
5.4	Candidates detected around F-G-K stars	89
5.4.1	Characterization of the host star	91
5.4.2	Secondary eclipse fit	102
5.4.3	Transit fit	104
5.4.4	Discussion of the candidates	107
6	M-dwarfs in the WTS	109
6.1	Selection criteria for M-dwarfs	109
6.2	Candidates detected around M-stars	112

6.3	WTS sensitivity analysis for M-dwarfs with $J \leq 17$ mag	119
6.4	Extended analysis for M-dwarfs with $J \leq 18$ mag	122
7	Other applications of WTS DI light curves	125
7.1	Extremely-short-period eclipsing binaries	125
7.2	M-dwarf/M-dwarf eclipsing binaries	130
8	Conclusions and outlook	133
A	Summary of co-author papers	137
	Bibliography	158
	Acknowledgments	159
	Curriculum Vitae	161

List of Figures

1.1	Geocentric and Heliocentric models	2
1.2	Historical philosopher and scientist	3
1.3	Protoplanetary disks	7
1.4	Surviving bodies as a function of time during planet formation process	9
1.5	Type I migration	12
1.6	Type II migration	14
1.7	Planet detections techniques	16
1.8	Periodic variations of PSR1257 + 12 detected by timing method	17
1.9	Microlensing event configuration	18
1.10	Paczynski curve of a microlensing event	19
1.11	First extra-solar planet detected with the imaging method	21
1.12	Astrometric variation of a star's trajectory	22
1.13	Radial velocity measurements of a star with a planetary system	24
1.14	Radial velocity measurements of Planetary system with high eccentricity	26
1.15	Diagram of a transit event	27
1.16	Geometry of a planet transiting its parent star	28
1.17	Transit probability for planets in the Solar System	30
1.18	Example of a false-positive	33
1.19	Histogram of detected periods in the WTS light curves	34
1.20	Thermal emission of the TrES-3b	36
1.21	planetary radius distribution of planets detected by <i>Kepler</i>	40
1.22	Hertzsprung-Russell diagram	46
1.23	Habitable Zone	51
2.1	Wide Field Camera (WFCam)	56
2.2	Configuration of 8 tailed pawprints (a-h) obtained with WFCam	57
2.3	Profile of the transmission curves of the <i>ZYJHK</i> broad-band filters	57
3.1	Difference Imaging process	65
3.2	RMS difference between the WTS light curves before and after <i>sysrem</i>	71
3.3	RMS of the WTS light curves as a function of the <i>J</i> -band mag	72
3.4	Difference between the RMS of DI and AP light curves	73
3.5	Histogram of periods before and after applying the <i>sysrem</i> algorithm	73

3.6	RMS of the WTS light curves as a function of the J -band mag	74
3.7	Corrected RMS/median(error) distribution of WTS light curves	75
3.8	Histogram of the RMS scatter divided by the median error	76
4.1	Folded light curve and SR-spectrum of WTS-2b	80
4.2	Geometry of the symmetrical trapezoid-fit.	82
4.3	Comparison between box and V -shape fits	82
4.4	χ^2_{dof} comparison between trapezoid-fit and box-fit	83
4.5	Trapezoid-fit of planet and binary cases	84
5.1	Optimization of selection criteria process	93
5.2	Comparison between the P_{sim} and P_{det}	94
5.3	Detection efficiency F-G-K stars	95
5.4	Detection efficiency as a function of S/N	96
5.5	Object rejected by visual inspection	97
5.6	Candidates around F-G-K stars found in the WTS 19h field	98
5.7	χ^2 as a function of the input visual extinction used in the SED fit	100
5.8	Best SED Kurucz ATLAS9 model derived with the VOSA for 19b1-02162	100
5.9	Best-fitting model of 19b-1-02162 (J -band)	105
5.10	Best-fitting model of 19b-1-02162 (i' -band)	105
5.11	Zoom-in image of 19b1-02162 and its neighborhood	107
6.1	Color cuts used to identify M-dwarfs in the WTS	110
6.2	Detection efficiency as a function of number of detections for M-dwarfs	111
6.3	Detection efficiency for M-dwarfs	113
6.4	Phase-folded light curves of eight candidates around M-dwarfs	114
6.5	Detection efficiency for the sensitivity analysis of the WTS ($J < 17$)	121
6.6	Upper limits on the fraction of planets around M-dwarfs in WTS	124
7.1	Extremely-short-period M-dwarf binary comparison	126
7.2	Phase-folded light curves of the five extremely-short-period M-dwarf binaries	129
7.3	Phase-folded light curves of the MEB candidate 19c4-06354	131

List of Tables

1.1	Space missions that search and characterize transiting planets	38
2.1	Characteristics of the fields observed in the WTS	54
2.2	<i>ZYJHK</i> NIR filters of the WFCam	55
5.1	Optimized selection criteria for DI light curves (F-G-K stars)	90
5.2	Optimized selection criteria for AP light curves (F-G-K stars)	90
5.3	Broadband photometric measurements and coordinates of F-G-K host stars	99
5.4	Characterization of host F-G-K stars	101
5.5	Comparison between planet and binary scenarios (F-G-K stars)	103
5.6	Characterization of candidates around F-G-K stars	106
6.1	Optimized selection criteria for the DI light curves (M-dwarfs)	112
6.2	Optimized selection criteria for the AP light curves (M-dwarfs)	112
6.3	Broadband photometric measurements and coordinates of host M-dwarfs	115
6.4	Characterization of host M-dwarfs	116
6.5	Planet and binary scenario comparison for candidates around M-dwarfs	117
6.6	Characterization of candidates around M-dwarfs	118
6.7	Sensitivity analysis for M-dwarfs with $J \leq 17$ mag	123
7.1	List of extremely-short-period M-dwarf binaries	128

List of Constants and Acronyms

- $G = 6.67384 \times 10^{-11} \text{m}^3 \text{kg}^{-1} \text{s}^{-2}$... Gravitational constant
- $c = 299792458 \text{ms}^{-1}$... speed of light in vacuum
- $M_{\odot} = 1.989 \times 10^{30} \text{kg}$... Mass of the Sun
- $R_{\odot} = 6.963 \times 10^8 \text{m}$... Radius of the Sun
- $L_{\odot} = 3.839 \times 10^{26} \text{W}$... Luminosity of the Sun
- $M_{\oplus} = 5.972 \times 10^{24} \text{kg}$... Mass of the Earth
- $R_{\oplus} = 6.378 \times 10^6 \text{m}$... Radius of the Earth
- $R_{\text{Jup}} = 7.149 \times 10^7 \text{m}$... Radius of the Earth
- $M_{\text{Jup}} = 1.899 \times 10^{27} \text{kg}$... Mass of the Earth
- $\text{pc} = 3.0856776 \times 10^{16} \text{m}$... parallax second
- $\text{AU} = 1.496 \times 10^{11} \text{m}$
- $\pi = 3.14159265359$

List of Abbreviations

- A_v ...Visual extinction
- AP...Aperture photometry
- APACHE...A PATHway toward the Characterization of Habitable Earths
- arcsec...arcsecond
- arcmin...arcminute
- BLS...Box-fitting least square
- CASU...Cambridge Astronomical Survey Unit
- CCD...Charge-Coupled Device
- CHZ...Continious habitable zone
- CoRoT...COnvection ROtation and Planetary Transits
- d...Days
- DEC...Declination
- deg...Degrees
- DI...Difference imaging photometry
- dM...M-dwarfs
- ESA...European Space Agency
- ESO...European Southern Observatory
- FCM...Flux conservation method
- HARPS...High Accuracy Radial velocity Planet Searcher
- HJ... Hot Jupiter
- HZ...Habitable zone
- IDs...Identification numbers
- INT...Isaac Newton Telescope
- JCMT...James Clerk Maxwell Telescope

- LSM...Least-square method
- mag...Magnitude
- mmag...Milli-magnitude
- M_p ...Planetary mass
- M_\star ...stellar mass
- MEB...M-dwarf/Mdwarf eclipsing binary
- Myr...Mega-year (10^6 years)
- Myr...Giga-year (10^9 years)
- NIR...NearInfraRed
- PSF...Point spread function
- P ...Period
- PTF/M-dwarfs...Palomar Transient Factory/M-dwarfs
- P_{sim} ...Simulated period
- P_{det} ...Detected period
- R_p ...Planetary radius
- R_\star ...Stellar radius
- RA...Right ascension
- RMS...Root main square
- SDSS...Sloan Digital Sky Survey
- SED...Spectral energy distribution
- S/N ...Signal-to-Noise ratio
- S/N_{rem} ...Signal-to-Noise Removed
- SDE...Signal detection efficiency
- S_{red} ...Signal-to-Red-Noise
- TRAPPIST...TRAnsiting Planets and Planetesimals Small Telescope
- T_{eff} ...Effective temperature

- UKIDSS...United Kingdom Deep Sky Survey
- UKIRT...United Kingdom Infrared Telescope
- VLT...Very Large Telescope
- VOSA...Virtual Observatory SED Analyzer
- WCS...World coordinates system
- WFAW...Wide Field Astronomy Unit
- WFCam...Wide Fiel Camera
- WFS...Wide Field Survey
- WTS...Wide Field Camera Transit Survey
- yr...Years
- 2MASS...2-Micron All-Sky Survey

Chapter 1

Introduction

1.1 Historical Context

I would like to start this work with a question that has been present during all human history: *Are we alone in the Universe?*

Over time, humans have tried to answer this controversial and exciting question. Basically, all great civilizations and cultures on the Earth have speculated on the idea of other worlds in the Universe or life outside the Earth. Back in ancient history, there were civilizations that conceived these ideas. For example, the Sumer, a culture that thrived in southern Mesopotamia more than 4000 years ago, had already a conception of life outside the Earth; they believed that all the human legacy had been brought to Earth by extraterrestrial beings (Steel & Hennessy, 2001). Centuries later, other important civilizations such as Greeks and Romans also contributed to support the notion of extraterrestrial life. Their ideas were based on the mythology of these cultures, which associated the Moon or other celestial bodies as the abode of gods. Alike, personalities from different epochs and cultures provided new thoughts, supporting the notion of other worlds and extraterrestrial life. For instance, the manuscripts of Anaxagoras (a Greek philosopher who lived in the 5th century BC) were the first writing records that mentioned the term Panspermia (Korpikiewicz, 1978), which is the hypothesis that life has been distributed around the Universe by celestial bodies as comets, asteroids, or meteoroids (Franck et al., 2007).

Nevertheless, the ideas of life outside the Earth was criticized and censured by the arrival of the Aristotelian philosophy (~322 BC) that dominated for a long period the world conception of the western cultures. His philosophy did not support the notion of plurality of worlds, since according to his perception of the Universe, all matter was contained on the Earth. The Aristotle current later influenced the Christian church, which also contributed to censor and suppress the notion of worlds and life outside of the Earth. The Church position was also supported by the geocentric model described in the *Almagest* (see Figure 1.1(a)), the most important astronomical treatise written by the Greek-Roman citizen Claudius Ptolemy (Pescic, 2001). From the 12th century, the ideas of inhabitants on new worlds claimed many lives; people that expressed openly these ideas were judged as heretic and killed by the Inquisition. Perhaps, the most known case was the appearance of *De l'Infinito Universo et Mondi* (On the Infinite Universe and Worlds), a text published

in 1584 by the Italian philosopher Giordano Bruno. The ideas presented in his manuscript were the most modern statement in that regard, which declared *"Innumerable suns exist; innumerable earths revolve about these suns in a manner similar to the way planets revolve around our Sun.....These worlds have no less virtue nor a nature different to that of our Earth and contain animals and inhabitants like Earth"* (Bruno, 1980). For this publication, Giordano Bruno was arrested and sentenced to death for heresy. He was burned in Rome in 1600.

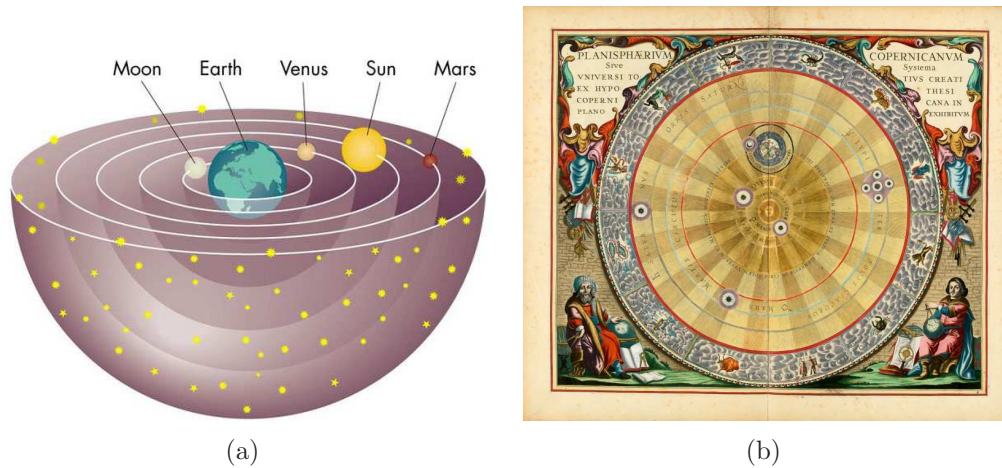


Figure 1.1: a) Artistic representation of the Claudius Ptolemy's geocentric model (The image was taken from redOrbit.com). b) Painting representation of the Heliocentric model proposed by Nicolaus Copernicus. The image is from the Dutch-German cartographer Andreas Cellarius published in *Planisphaerium Copernicum Universi Totius Creati Ex Hypothesi Copernicana in Plano* (1660)

At the same time, an important intellectual movement occurred in Western Europe. In science, and particularly in astronomy, outstanding advances in the knowledge, and a new picture of the Universe emerged with the invention of the telescope. The astronomical observations became more precise and the old geocentric model and Aristotelian physics did not agree with the new observational evidence any more. By that time, other theories also criticized the Ptolemy's geocentrism. In 1543, the Polish astronomer Nicolaus Copernicus published the *De Revolutionibus Orbium Caelestium* (On the Revolutions of the Celestial Spheres), in which he proposed the Heliocentric model (Gingerich 1999, Figure 1.1(b)). This period and particularly Copernicus's work are extensively accepted as the start of the scientific revolution, which became the basis of modern science. Years later, the contribution to astronomy and physics made by important scientist revolutionized further the perception of the Earth and Universe. For instance, the Italian scientist Galileo Galilei (1564-1642), considered as the father of modern science, carried out important improvements on the telescope, allowing him to perform new observations that provided valuable information of the Solar System; for example, the discovery of the four largest Jupiter's moons, and confirmation of the phases of Venus (Gingerich, 2011). The Danish astronomer Tycho Brahe (1546-1601) also objected Aristotelian physics and the geocentric model based

on accurate observations of planetary bodies. In those days, Tycho Brahe had an assistant, the German astronomer Johannes Kepler, who subsequently made major contributions to astronomy and the notion of the Solar System. He published several documents using observations and data from his teacher. The most famous of Kepler's works were *Astronomia nova* (New Astronomy) and *Harmonices Mundi* (The Harmony of the World), in which he described the laws of the planetary motion (Kepler's laws) and provided the basis of the Universal Gravitation theory (Rodgers et al., 1980).

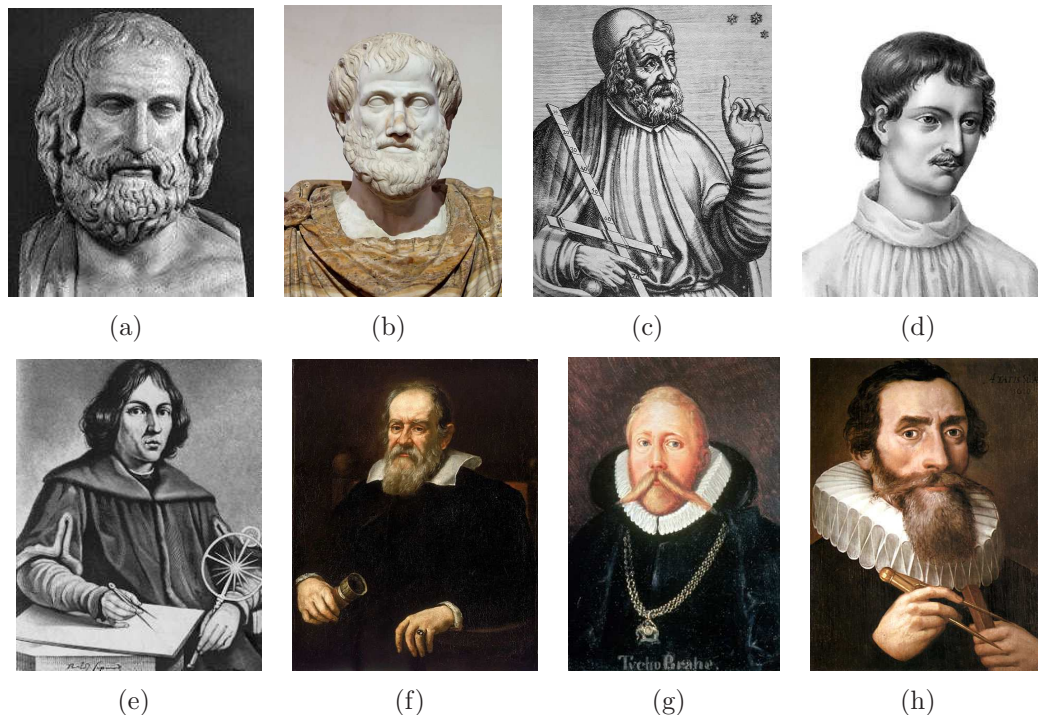


Figure 1.2: Historical philosopher and scientist that influenced the evolution of our understanding about the Universe through the human history. Their ideas have also provided a perspective of extraterrestrial life and worlds : a) Anaxagoras, b) Aristotle, c) Claudius Ptolemy, d) Giordano Bruno, e) Nicolaus Copernicus, f) Galileo Galilei, g) Tycho Brahe, and h) Johannes Kepler. (These figures are the Public domain taken from <http://commons.wikimedia.org/>)

With the new understanding of the Solar System and the Universe, it became clear that the Earth was only another planet orbiting around the Sun, and the new era of science started to take part in the extraterrestrial life ideas. However, although this scientific revolution certainly changed the perception of the Universe, and Church showed sign of more tolerance in view of the evident intellectual-social movement during the 17th, 18th, and 19th centuries, the conceptualization of life outside the Earth were mere speculations. Significant progress regarding the scientific treatment of these ideas started by the end of the 19th century. By that time, the telescope had gained important improvements, leading to better observations of celestial bodies. From the mid-twentieth century, the perspectives of life on the Moon and other bodies of the Solar System was decisively

dismissed based on the knowledge acquired during the previous years. Nevertheless, the presence of primitive life on some objects from the Solar System is still an open question and a topic of intense research. From the mid-20th century, several projects have been developed to search for signs of extraterrestrial life. Although many of these projects have been focused on searching for evidences of life in our own Solar System, the scientific community has started to see beyond the limits of our Solar System, attempting to find indirectly signs of any evolutionary state of life.

1.2 General outlook of this work

The historical background about extraterrestrial life discussed above explains why in recent years the search for exo-planets has become an interesting and exciting field in astronomy. Astronomers attempt to find potential habitable planets where there might be appropriate conditions for the origin and evolution of life. The first extra-solar planets were found in 1992 by Wolszczan & Frail (1992), reporting at least two planet-sized bodies orbiting the pulsar PSR1257 + 12. Three years later Mayor & Queloz (1995) announced the first extra-solar planet orbiting its host main-sequence star and since then, exo-planets are being discovered with an ever increasing rate, reaching about 1000 confirmed planets.

Nowadays, there are many techniques to detect directly or indirectly exo-planets. For example, direct imaging, microlensing, astrometry, radial velocity and the transit methods, which represent the most popular techniques to search for exo-planets. Measuring the host star's radial velocity variations represents one of the most successful techniques to detect exo-planets, nevertheless only few parameters of the planetary system can be determined with this method. This changes if we search for a planet transiting its host companion. A transit occurs when a planet blocks part of the surface from the star causing a slight and periodic variation in its brightness, which can be detected by a photometric analysis. This analysis provides information of the planet and its host star, and together with radial velocity measurements, important physical parameters of the transiting planet can be deduced, such as mass and radius. The first planetary transit signal was reported in 2000 (Charbonneau et al., 2000; Henry et al., 2000) and since this discovery, several (~450) exo-planets have been detected transiting their host star. In Section §1.5, we describe the most popular and successful methods to detect exo-planets, with special attention on the radial velocity and transit methods, since they are part of the core of this thesis.

Recently, several transit missions and surveys have been launched to find and characterize new exo-planets. The most exciting and successful projects designed to detect periodic transits are the space missions *Kepler* (Borucki et al., 2010) and CoRoT¹ (Aigrain et al., 2008; Barge et al., 2008a). *Kepler* was launched on March 6, 2009 to observe more than 150 000 stars and it was designed to find a large number of Earth-size planets and Super-Earths. The number of transiting planets has considerably increased with the start of the *Kepler* mission; until September 2013, there were nearly 3500 transit candidates² and

¹Convection, Rotation and Planetary Transits

²see <http://planetquest.jpl.nasa.gov/kepler/table>

many of them are expected to be confirmed as planets in the near future. On the other hand, CoRoT started to operate in December 2006, and was originally designed to find and characterize exo-planets with properties comparable to rocky planets in our Solar System. Nevertheless, in June 2013, it was announced the culmination of the CoRoT mission, after six years of successful operation. A brief discussion of these missions and other transit surveys are presented in Section §1.6.

Earth-like planets are particularly interesting because if they revolve in the habitable zone³ (HZ) of their host star (Kasting et al., 1993), the environment may be adequate to support liquid water on the surface of the planet, which is believed to be a key for the development of life. Cool and low-mass stars (in particular main-sequence M-dwarfs) are the most promising candidates to find Earth-like planets and Super-Earths. Due to their small stellar radii, the change in their brightness caused by a transiting planet around them is more evident. For instance, an Earth-size planet orbiting a $0.1 R_{\odot}$ ($\sim 0.08 M_{\odot}$) star produces a transit of 1 % depth (Kaltenegger & Traub, 2009), a similar effect occurs when a Jupiter radius planet blocks a Sun-like star.

Searching for transiting planets at near-infrared (NIR) wavelengths provides important advantages to detect transiting planets around M-dwarfs, since the peak of the Spectral Energy Distribution (SED) of these stars falls in this spectral range. Several projects are dedicated to study transiting planets around M-dwarfs; however, so far there are only two transit projects focused on finding exo-planets around cool and low-mass stars at NIR wavelengths: the MEarth (see Section §1.6.5) project and the Wide-Field Camera⁴ (WFCam) Transit Survey (WTS). The WTS is a pioneer project operated since 2007 with observations from the United Kingdom InfraRed Telescope (UKIRT) that stands out for its particular aims and methodology. The WTS was originally focused on the discovery of rocky planets and potentially habitable planets using the transit method for the first time at the NIR wavelength regime. In Chapter §2, we describe in detail the main characteristics of the WTS.

In the remaining part of this chapter, we give a brief description of planet formation and orbital migration theories to put in context the search of exo-planets around M-dwarfs (§1.3 and §1.4). We also describe the most common methods to detect extra-solar planets, explaining in detail the radial velocity and transit methods (§1.5). Since this work is focused on searching for exo-planets with the transit method, in §1.6, we describe some outstanding transit surveys, such as *Kepler*, CoRoT and the MEarth project. A general discussion about M stars, including the theory of planet formation and habitability around these stars is presented in Section §1.7. Finally, we show the structure of this thesis in Section §1.8.

³See §1.7.2

⁴Wide-Field Camera, see <http://www.jach.hawaii.edu/UKIRT/instruments/wfcam/>

1.3 Planet formation theory

The planet formation process has been extensively discussed during many years. Despite this, the topic is still heavily debated in the literature. The first plausible hypothesis arose in the 18th century, when scientists and philosophers attempted to explain the formation of our own Solar System. For example, Georges Louis Leclerc de Buffon proposed that planets had been formed by the collision of a massive comet with the Sun, causing ejection of material that subsequently condensed and formed planets (Karttunen et al., 1987). Also, in the 18th century, the French mathematician and astronomer Pierre-Simon Laplace (1749-1827) proposed a theory, in which argued that planets were formed from gas rings ejected from the collapsing Sun; this hypothesis is analogous to the accepted theories of regular satellites formation in the Solar System (Crida & Charnoz, 2012). At the same time, the well-known philosopher Immanuel Kant (1724-1804) proposed that Sun and planets were simultaneously formed from the same large rotating nebula, the so-called *nebular hypothesis*. Although this was originally proposed to explain the origin of the Solar System, scientists eventually adopted it as a general theory for planet formation. Nevertheless, the *nebular hypothesis* initially showed some difficulties to account for important physical aspects, like the distribution of the angular momentum in the Solar System. This led to the development of new theories during the 19th and 20th centuries, attempting to solve the controversy.

In mid-20th century, scientists returned to the *nebular hypothesis*, suggesting that magnetic forces might transfer angular momentum from the Sun to the planetary nebula (Karttunen et al., 1987). The new and modified version of the *nebular hypothesis* affirmed that planet formation was strongly correlated with the stellar formation process. This theory was well received by the astronomy community and nowadays represents the basis of the existing theories that explain the planet formation process. This theory starts with the collapse of a massive cloud of gas and dust due to gravitational instability (Pudritz, 2002). This process results in the appearance of an accretion disk around the young stellar object (Andre & Montmerle, 1994), which under certain circumstances (see below) turns into a protoplanetary disk that eventually gives birth to a planet system. The protoplanetary disks have been often observed in regions of stellar formation (see Figure 1.3). However, planet formation theory still has many open problems to solve, for instance it can not explain accurately how the angular momentum is lost from the original rotating nebula during the planet formation. Also, it is not clear how the planets are formed from the protoplanetary disk. With the improvements in observations and the discoveries of exo-planets during the last years, new models have emerged trying to explain this process and some of these questions have been partially solved. Perhaps the most accepted models to explain planet formation are the core-accretion/gas-capture (CAGC) model (Ruden, 1999), which gives an appropriate explanation for the inner and rocky planet formation, and the disk instability model (Boss, 1997a) that describes the formation of the gas-giant planets.

Constraining planet formation and orbital migration of exo-planets theories is one of the main physical motivation of this work. In particular, planet formation around low-mass stars represents an important role in this thesis, since the WTS is designed to detect planets around M-dwarfs. Although the CAGC and disk instability models can explain

the formation of rocky and giant planets with long-period orbits ($P > 10$ d), and the presence of Jovian planets with close-in orbits can be addressed by orbital migration models (see details below), the lack of discovery of Hot Jupiters around M-dwarfs suggests that formation of such planets is not as common as it is around Sun-like stars. In the next two sections, we describe the CAGC and disk instability models. A description of the orbital migration of exo-planets theory is summarized in Section §1.4. We separately present the particular case of planet formation around M-dwarfs in Section §1.7.1.

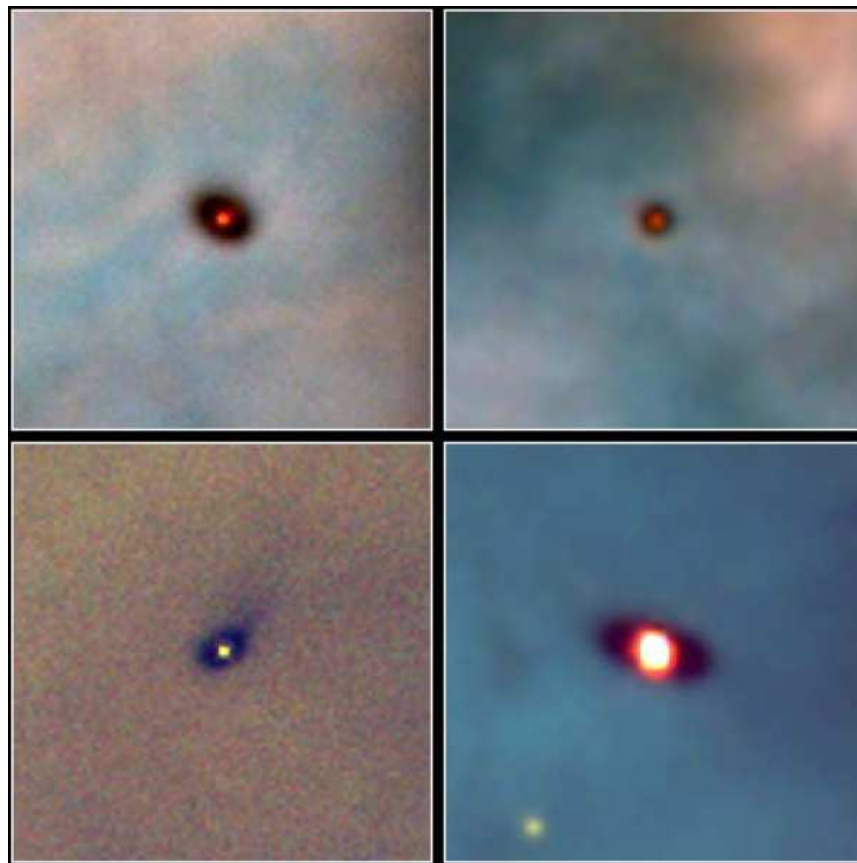


Figure 1.3: Hubble Space Telescope images of four protoplanetary disks around young stars in the Orion nebula captured by the Hubble Space Telescope. The bright center of each image is a young star surrounded by the protoplanetary disk. These disks might evolve into planetary systems. (Credit of the image: M. McCaughrean (Max Planck Institute for Astronomy), C.R. O'Dell (Rice University), and NASA)

1.3.1 The core-accretion/gas-capture model

In the previous section, we briefly mentioned that after the molecular cloud collapse during the early stage of the stellar formation process, an accretion disk is formed around the protostar due to conservation of angular momentum. If this accretion disk is massive enough, it will continue feeding the protostar, a period in which the accretion disk can

be called a protoplanetary disk, since a planetary system can be formed under these conditions (Montmerle et al., 2006). The central young protostar will accrete material from the protoplanetary disk becoming more massive. On average, the lifetime of an accretion disk of a solar-type mass star is about ~ 6 Myr (Haisch et al., 2001), during this time the temperature of the disk increases, reaching the inner region of the disk the highest temperatures (400-1000 K) due to the viscous dissipation of turbulence and the infall of the gas from the nebula (Chick & Cassen, 1997). During the first stage, the protoplanetary disk contains small dust grains which are subjected to the gravitational force of the central star and drag force exerted by the gas. Once the young protostar reaches the T-Tauri⁵ stage, the accumulation of these grains in the inner region leads to the formation of centimetre per metre sized particles (Kessler-Silacci et al., 2006). In the densest disk regions, these particles will further grow by collisions and accumulation, which become bodies that reach sizes up to 1 km. Such km-sized bodies are typically referred as planetesimals. At this stage, the gravitational force among such planetesimals becomes strong enough to attract smaller bodies around them, inducing further collisions until the planetesimals grow up to ~ 1000 km in diameter (commonly named planetary embryos, Kokubo & Ida 2002). This process is called run-away accretion and was proposed by the Russian Astronomer Viktor Sergeevich Safronov (Safronov, 1972). The typical time-scale of this process is of the order of 0.1 to 1.0 Myr, and by the end of the run-away accretion only a few hundred large-planetesimals have survived. However, these planetesimals still accrete smaller bodies until the disk keeps only about hundred Mars-Moon sized bodies, which will merge on time-scale ~ 10 Myr. High-resolution dynamical simulations have shown that the number of remaining objects are between 2-4 objects with masses between 0.4 and $2.6 M_{\oplus}$ (Raymond et al., 2006). Figure 1.4 shows the surviving bodies as a function of time of a typical protoplanetary disk of a Sun-like star.

The CAGC model further explains the formation of the gaseous planets during the gas-capture phase. This occurs when the rocky planetary core reaches $\sim 10 M_{\oplus}$, so that the gravitational forces is strong enough to capture gas from the surrounding disk. Nevertheless, the CAGC model has problems with the gas accretion time-scale. We mentioned above that the life-time of a protoplanetary disk is about 6 Myr, i.e., after this time no gas is left to be captured by the rocky planetary core. Numerical simulation have shown that the time-scale for the formation of a planet with similar orbital and mass conditions as Jupiter is of order of 10 Myr or longer (Pollack et al., 1996). This feature suggests that the CAGC might be effective in forming gas-giant planets only in relatively long-lived disks, which might reside in regions devoid of high-mass star formation, where the amount of gas is considerably higher (Boss, 2002). Another plausible theory to explain the gaseous planets is the disk instability model that will be explain in the next section.

⁵The T-Tauri stage is a phase of the stellar formation process where the temperature in the core of the protostar is not high enough to start the Hydrogen fusion. The T-Tauri objects are named as pre-main-sequence stars.

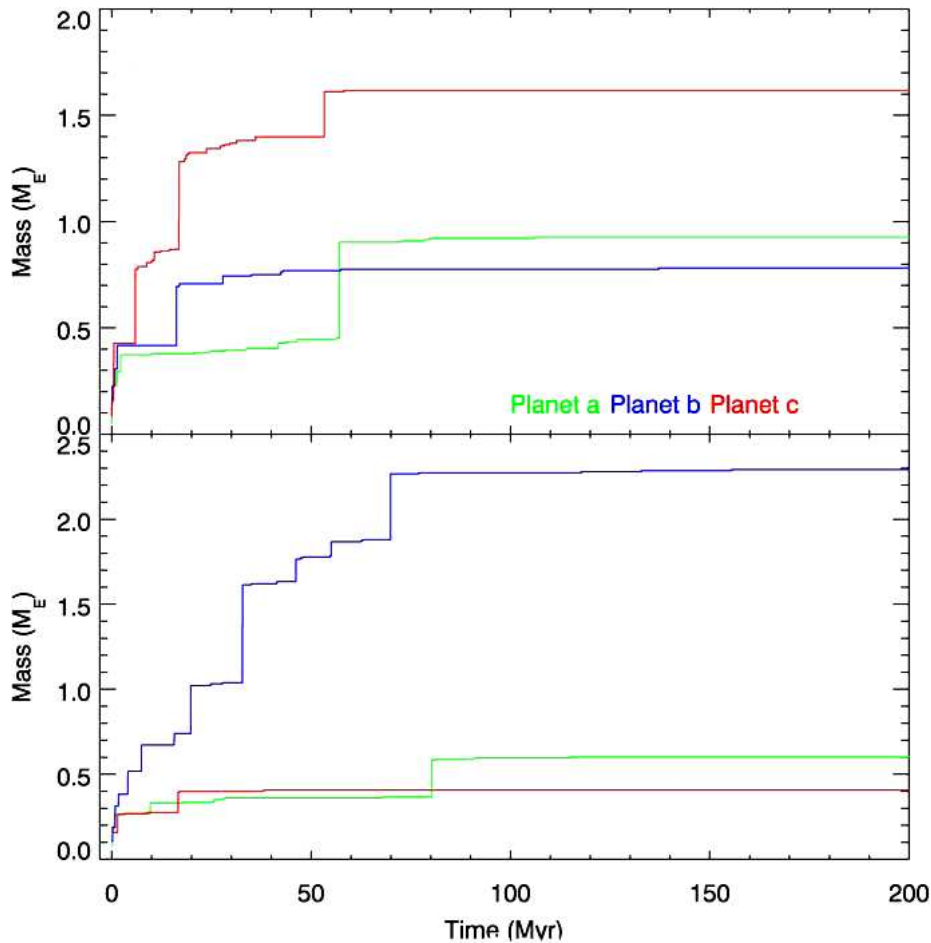


Figure 1.4: Masses of surviving bodies as a function of time. The plot corresponds to the simulations from Raymond et al. (2006). The two different frames represent different initial conditions. In the upper panel all bodies involved in the simulations interact gravitationally, while in the lower panel planetesimal interact with larger bodies (e.g. planetary embryos) but not with each other. Solid-color-lines represent three objects at different orbital distance: a) 0.55 AU, b) 0.98 AU, and c) 1.93 AU.

1.3.2 The disk instability model

The disk instability model was proposed by Boss (1997b) and subsequently reviewed by Durisen et al. (2007). The CAGC model presents a controversy with the time-scale during the gas-capture phase. The majority of protostars lose their gas disks in a few Myr, while the gas-capture process of a standard $10 M_{\oplus}$ solid planet core requires several mega-years to be completed. So that, the disk instability model arose to alternatively explain the gaseous planet formation in a relatively short time ($\sim 1\,000$ yr). The disk instability model suggests that a gas protoplanetary disk can suffer gravitational instabilities when it is cool and has a high surface density. Under these circumstances, the gravitational disk instability produces a disk fragmentation into dense clumps and substructures that may represent the precursors of the giant planets (Boss, 1997b). The physics of the gravitational instabilities

is quantified by the Toomre instability criterion (Toomre, 1964):

$$Q = \frac{c_s \kappa}{G \pi \Sigma}, \quad (1.1)$$

where c_s is the environment speed of sound, κ is the oscillation epicyclic frequency of a fluid element perturbed by a circular motion, G is the universal gravitational constant, and Σ is the surface density. The physics involved in this criterion suggests that a gas accretion disk becomes unstable when $Q < 1$; however further simulations have shown that non axisymmetric disturbance (which produce multi-armed spirals) can be unstable for $Q \lesssim 1.5$ (Papaloizou & Savonije, 1991). The disk instability model predicts the formation of gas-giant planets in a relatively short time and the model also describes the presence of gas-giants around very young stars (Boss, 1998), which the CAGC is not able to reproduce. There seems to be observational evidence of planet-sized bodies around these young stars (Forrest et al., 2004; Neuhäuser et al., 2005), which provide important support for the gas-giant planets formation due to a disk instability.

1.4 Orbital migration of exo-planets

According to the CAGC and disk instability models, rocky planets are born in the inner part of a protoplanetary disk and gas-giant planets in the outer parts. These models suggest that giant planets are formed in the outer regions, since the temperature close to star is too high, all volatile materials are evaporated and the remaining material is not sufficient to form a $\sim 10 M_{\oplus}$ solid-core, being the characteristic size of a gas-giant core (Wetherill, 1980). Despite this theoretical expectations, in 1995 Mayor & Queloz (1995) announced the discovery of the first extra-solar planet, orbiting a main-sequence star with a nearly circular orbit of ~ 0.052 AU. And since this discovery, many more Jupiter-size planets have been found with very short orbital distances; such planets are commonly called Hot Jupiters⁶. The discoveries of Hot Jupiter planets have led to new discussions regarding planet formation and evolution theories. Although the formation of gas-giant planets in the proximity of their parent star is theoretically feasible under certain circumstances (Wuchterl, 1996), several authors (e.g., Ward & Hourigan 1989 & Lin et al. 1996) have proposed that it is unlikely that such planets have been formed in their current location. Instead, they suggest that Jupiter-like planets may have formed by gradual solid-planetesimal accretion and capture of gas or a disk instability process in larger orbits (> 5 AU), and eventually migrated inward from the formation location.

The process of planet orbital migration has been extensively discussed in the literature. There are three mechanisms that may explain the migration of planets at closer orbits, which include planet-planet, planet-planetesimals, and planet-disk interactions:

- i) The first mechanism is caused by the interaction between three or more giant planets (Weidenschilling & Marzari, 1996), leading to gravitational encounters and ejections

⁶Hot Jupiters are exo-planets with physical characteristics similar to Jupiter (e.g. mass and radius) but higher surface temperatures, since they orbit very close to their host star

of one planet while the remaining planets are thrown both closer and farther from the star. Although this mechanism explains the high orbital eccentricity of some exo-planets, the probability of such collisions is very low and the current number of detected Hot Jupiters cannot be suitably explained by this mechanism.

- ii) Another possible orbital migration process was proposed by Malhotra (1993), which suggests the interaction between a planet and planetesimals that orbit around it. This interaction again produces the expulsion of several planetesimals while the planet suffers a migration orbit. Nevertheless, a planet will suffer a substantial change in its orbit if the total mass of the planetesimal around it is comparable to its own mass. Although this type of orbital evolution may explain the migration of Neptune-like planets, some authors claim that the planet-planetesimals interaction is a nonviable process to explain the current orbital parameter distribution of Hot Jupiters.
- iii) The third mechanism that explains the orbital planet migration is associated to the tidal interaction between a protoplanet and the surrounding gas from the protoplanetary disk (Goldreich & Tremaine, 1979; Lin & Papaloizou, 1979). This mechanism has been more accepted in the community, since it is more appropriated to explain the current number of Hot Jupiters and their orbital distribution. The planet-disk mechanism uses the angular momentum exchange between planet and disk material to address the orbital migration. This mechanism leads to three different migration types, which are discussed in more detail below.

1.4.1 Type I migration

The Type I migration involves a low-mass protoplanet ($M_p \lesssim 0.1 M_{\text{Jup}}$) that interacts with the gas in the disk (Goldreich & Tremaine, 1980; Ward, 1997), creating perturbations that are propagated as density waves in the disk outside and inside of the Lindblad and corotation resonances⁷. In this case, the waves created by the low-mass planet are not strong enough to significantly perturb the surface density profile of the disk (Type II migration, see below). The protoplanet acts on the density waves by exerting torques nearby these resonances, causing angular momentum exchange. This occurs while the planet stays embedded in the disk and the migration will be controlled by the total torque produced in the inner and outer parts of both resonances. This can be estimated considering the contribution of individual torques exerted at Lindblad and corotation resonances, where resonance at inner regions will add angular momentum to the planet, whereas at outer parts will remove it. The angular momentum exchange is only significant close to these resonances, since the waves away from them have small wavelength, so that the contribution to the net torque in these regions is very small. Several authors (Tanaka et al., 2002;

⁷Lindblad resonances are the cause of spiral density waves in a disk. In a planet-orbital evolution context, Lindblad resonances are found at the location where the epicyclic frequency of the protoplanetary disk is a multiple of the planet's orbital period. On the other hand, corotation resonances occur in regions where the planet orbits with the same angular velocity as the surrounding disk material, producing mutually a gravitational effect (Tanaka et al., 2002).

Artymowicz, 1993) have carried out two and three-dimensional simulations to perform an analysis of the density waves and thus estimate the contribution of the torques exerted in the vicinity of Lindblad and corotation resonances. These simulations show that a laminar and circular disk without presence of a magnetic field produces a negative torque in outer Lindblad resonances, which removes angular momentum, and positive torque in the inner parts, adding angular momentum to the planet. If the negative torque dominates the total contribution, it results in an inward radial migration of the planet.

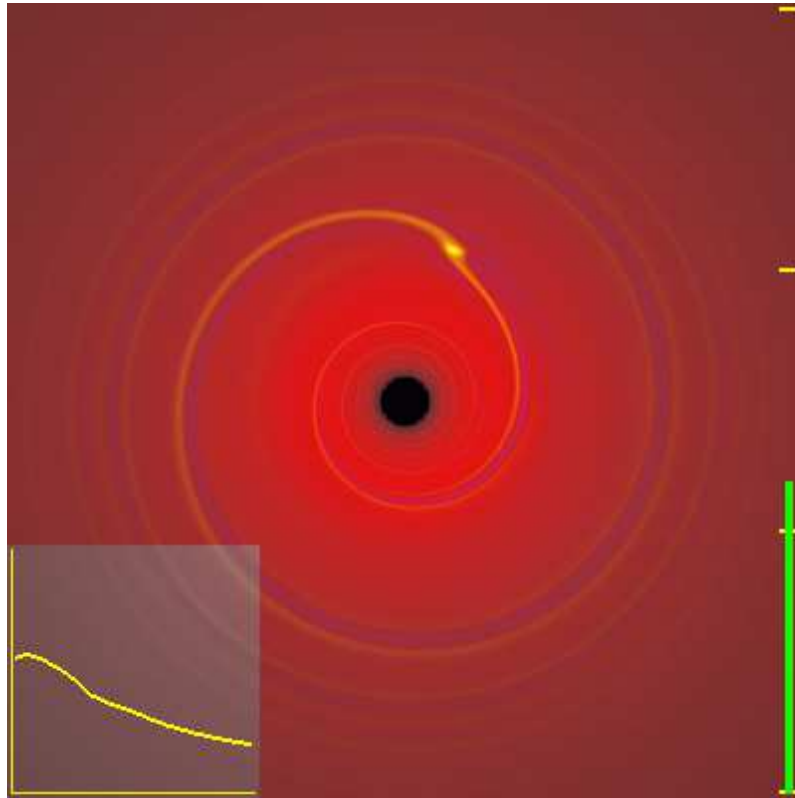


Figure 1.5: Interpretation of the interaction between a planet with a protoplanetary disk. The image corresponds to two-dimensional hydrodynamic simulation with a locally isothermal equation of state and a constant kinematic viscosity. The figure shows a low-mass planet creating a slight wave in the disk, however the averaged surface density profile (yellow curve) is not perturbed significantly. For details and credits of the figure, we refer to Armitage & Rice (2005).

The time-scale of this process is about $\sim 10^5$ yr. This represents a problem for the survival of planets, since the typical life-time of a protoplanetary disk is $\sim 10^6$ yr. During this time the protoplanet may migrate into the central protostar before becoming a giant planet (Korycansky & Pollack, 1993). Several solutions have been proposed to solve this problem. For example, Terquem (2003) proposes a toroidal magnetic field, which produces magnetic resonances, generating (as the Lindblad resonances) negative/positive torques. If the magnetic field is large enough and the positive magnetic torque dominates the negative torque, the Lindblad contribution becomes less important, producing a deceleration of Type I migration. Another possible solution was proposed by Adams & Bloch (2009),

suggesting that the interaction of protoplanets with a turbulent and magnetized disk may cause a stochastic perturbation, and that the corresponding turbulent fluctuations produce additional stochastic torques that interact with the Lindblad torques and subsequently induce the stoppage of Type I migration. Figure 1.5 shows a graphic representation of Type I migration.

1.4.2 Type II migration

Type II migration occurs when the mass of the protoplanet is big enough ($\sim 1 M_{\text{Jup}}$) to induce a gap in the disk, due to the interaction and subsequent angular momentum exchange between disk and protoplanet (Lin & Papaloizou, 1986). The transfer of angular momentum occurs in both the inner and outer parts of the protoplanet orbit, being positive for the faster matter moving in the inside part of the protoplanet orbit and negative in the exterior region. The angular momentum exchange is produced locally, so the disk material nearby the protoplanet is thrown away, i.e., the gap around is formed. At this point, the orbital evolution is closely related to the viscous conditions of the disk, since the gap will maintain if the angular momentum exchange equals the angular momentum flow produced by the viscosity of the disk. If the conditions for the formation and conservation of a gap are satisfied, the outward angular momentum flux from the inner part of the disk is absorbed by the planet while injecting angular momentum to the outer part of the disk. When this contribution is not balanced, the planetary orbit changes its angular momentum and migrates. Two and three-dimensional hydrodynamic simulations have shown that the outer contribution dominates during this process, therefore the planet spirals inward (Nelson et al., 2000; D'Angelo et al., 2003).

The time-scale for Type II migration is about 10^5 yr (D'Angelo et al., 2003), from an original position of 5 AU, and even shorter ($\sim 10^4$ yr) if the protoplanet mass exceeds the local mass of the disk (Papaloizou & Terquem, 2006). This represents the same time-scale problem as in Type I migration, i.e., the typical migration-time is shorter than the dissipation of the disk, so that the protoplanet should fall into the central star. Several scenarios have been proposed to solve this problem. For example, Lin et al. (1996) proposed that a tidal interaction with a fast rotating star may stop the orbital migration at a few AU from the star. Another possibility is mass transfer from the planet to the star in case the planet exceeds the Roche lobe⁸, resulting in an outwards migration due to the conservation of the angular momentum (Trilling et al., 1998). According to Trilling et al. (1998), a giant planet may also survive if a series of giant planets are formed and migrate into the star, and a remaining planet stops its migration once the disk finally dissipates. Recently, a new explanation to stop a Type II migration has emerged. This model suggests that if two or more planets are formed at similar time in relative close orbital distances, they may migrate into a resonant relationship and their gaps can overlap, causing them to stop the migration (Morbidelli et al., 2007).

⁸The Roche lobe is the region around a star in which orbiting material is gravitationally bound to the star. Frequently, the Roche lobe is referred to the gravitational interaction between stars in binary systems, however can also be associated to the interaction star-protoplanet during the formation phase.

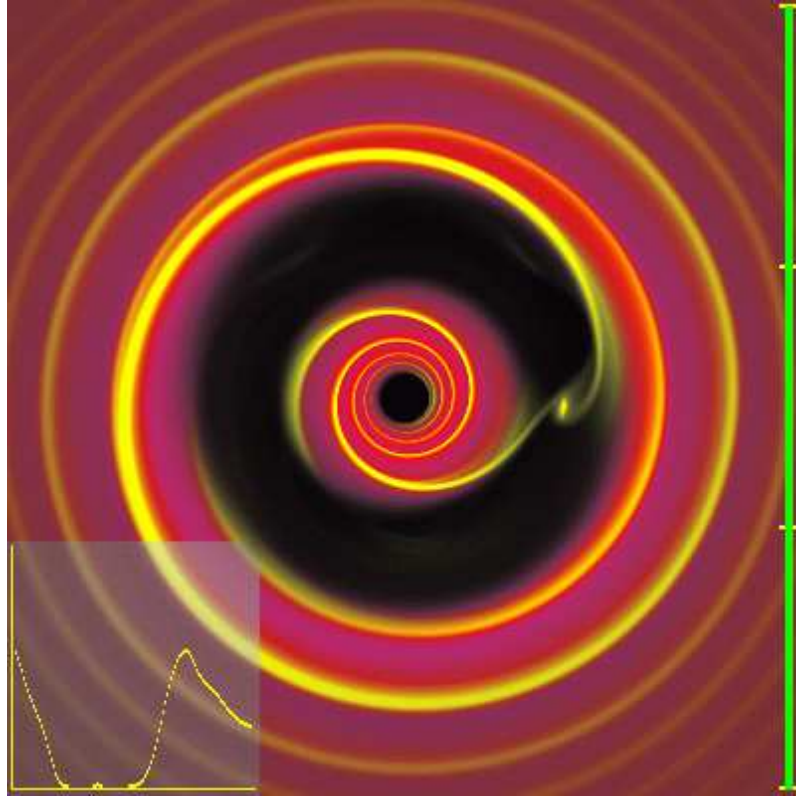


Figure 1.6: Unlike Type I migration, this plot shows a massive object ($\sim 10 M_{\text{Jup}}$) creating gap in the disk, which is reflected in the density profile of the disk (yellow-solid curve). (credits of the figure Armitage & Rice (2005)).

1.4.3 Type III migration

The Type III migration or runaway model was proposed by Masset & Papaloizou (2003) and subsequently reviewed and discussed by Artymowicz (2004). This model explains the planet orbital migration in a short time-scale for massive disks by assuming coorbital torques. Coorbital here refers to a torque exerted on a protoplanet by the disk material flowing through the orbit. This occurs when a gap is partially formed due to a low-mass protoplanet in a massive disk. The coorbital torque has both positive and negative feedback, the two contributions do not cancel if the coorbital region is almost consumed. In this case, a net corotation torque is produced, which scales with the drift rate and the mass deficit⁹ in the coorbital region, which has the same sign as the drift rate. The above leads to a positive contribution on the migrating planet. The runaway migration is normally used to explain the orbital characteristics of close orbiting sub-Jovian planets (Masset, 2008), i.e. a planet with mass between 0.1-0.3 M_{Jup} . More recent works about

⁹The term drift rate refers to the orbital migration rate, either inward or outward, due to corotation torques produced in a disk. On the other hand, the mass deficit is closely related to the migration rate. In a low mass disk, where this value is negligible, the torques are almost independent of the migration rate (Ebel, 2007)

Type migration III can be found in Pepliński et al. (2008a) and Pepliński et al. (2008b).

So far, we have described the different mechanisms of planet formation and orbital migration of extra-solar planets. The GAGC model is able to explain the formation of rocky and low-mass planets. Nevertheless, the GAGC model presents problems to account the formation of giant planets due to time-scale differences. The disk instability model appears to be appropriate to account for the time-scales differences and predicts the formation of giant planets at large orbital distance. Moreover, the detection of Hot Jupiters can be explained by an orbital migration process. However, formation of giant planets around low-mass stars presents a difficulty. Although the disk instability model and an orbital migration process can explain the presence of Hot Jupiter around M-dwarfs, the lack of discoveries of such planets supports the idea that formation of giant planets around low-mass stars is not as common as it is around Sun-like stars. Therefore, Section §1.7.1 is dedicated to particularly present the different models that describe planet formation around M-dwarfs. Furthermore, we present in Section §6.3 and §6.4 a sensitivity analysis of the WTS that places upper limits on the frequency of short-period giant planets around M-dwarfs.

1.5 Planet detection techniques

The Extra-solar Planets Encyclopaedia¹⁰ (EPE) is a webpage operated by the Paris Observatory that is dedicated to update continuously the status of exo-planet discoveries. Until September 2013, the EPE had reported 974 exo-planets. So far, the detection techniques used in the discovery of such planets are radial velocity, astrometry, transit, microlensing, direct imaging and timing. Although there are more direct or indirect methods to detect extra-solar planets (see Figure 1.7), we briefly describe in the next sections the techniques mentioned above. Moreover, the radial velocity and transit methods are discussed in detail, since they currently represent the most successful techniques to detect exo-planets and are involved directly in the development of this thesis.

1.5.1 Timing

The timing method provided the first discovery of extra-solar planets, when two planetary companions were detected orbiting the pulsar PSR1257+12 (Wolszczan & Frail, 1992). This technique can be used when a star or stellar remnant shows a periodic and regular variability, as is shown in Figure 1.8. Eclipsing binaries and pulsars are examples of objects that can exhibit this kind of photometric variability and can show evidence of a planetary companion by measuring the timing variations of those periodic phenomena. The timing effects are caused by three different mechanism: i) gravitational perturbations, ii) Doppler effect, and iii) light travel time.

i) The gravitational perturbations are usually related to an eclipsing system (planets

¹⁰<http://exoplanet.eu/>

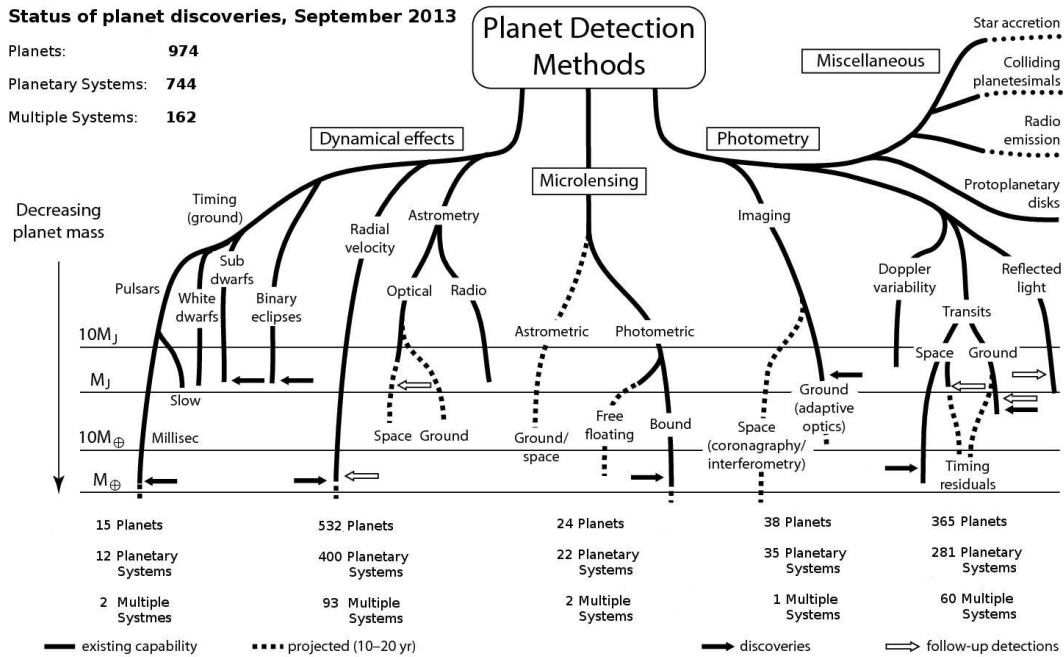


Figure 1.7: Diagram of the different planet detections techniques and current status of planet discoveries. (Source Perryman 2000. Numbers of discovery adapted to this work.)

or binary systems) where additional bodies in the system will perturb the orbit of the known eclipsing object. These perturbations produce variation in the light travel time, which can be measured and therefore used to infer the presence of the additional body. These variations are easier to detect if the perturbing body is near to the motion resonance¹¹ of other bodies in the system, since the gravitational effects are more significant. For transit systems this method is commonly called the transit timing variations and in systems where two planets have been detected transiting their host star, the density of both planets can be determined without other measurements (Holman & Murray, 2005).

- ii) The timing variability produced by the Doppler effect is usually employed with pulsars, through the pulse arrival times, and with eclipsing binary systems through the timing of eclipse ingress and egress. If the period of the pulsations or eclipses can be measured accurately, the interpretation of those measurements is identical to the variations in the radial velocity method.
- iii) The light travel time effect occurs when the reflex orbit of a star around the center of mass of a planetary system is sufficiently large that it allows the additional light

¹¹The motion resonance or orbital resonance occurs when two or more bodies mutually produce a periodic gravitational effects due to the correlation between their orbital period. This effect is cumulative and modifies the orbits of the involved bodies, resulting in a unstable interaction and exchange of angular momentum.

travel time across the orbit to be determined as a timing variation. This technique is also related to the Doppler shift timing method, since it represents the accumulated effects of the Doppler-shifted period that produces the timing anomaly. The timing method is extremely sensitive to small stellar orbit variations, hence this technique so far represents the method that is able to detect the smallest and lowest mass planets, even comparable or less than Earth's mass (Steffen & Agol, 2005).

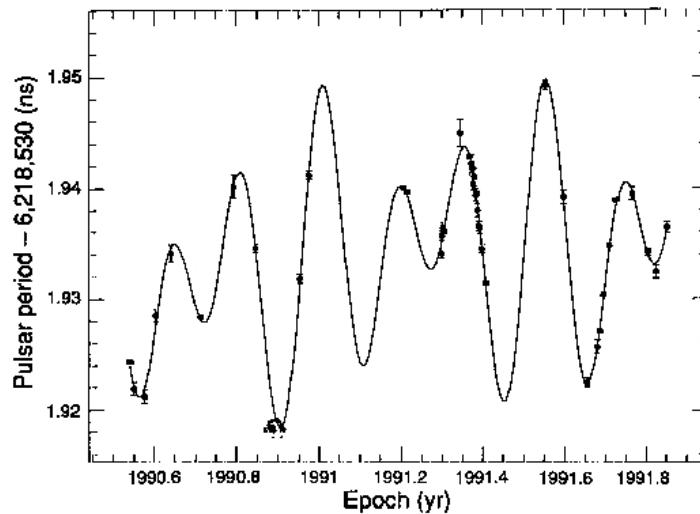


Figure 1.8: Periodic variations of PSR1257 + 12 and the corresponding model (solid lines) that describes the presence of two planetary companions. Plot taken from Wolszczan & Frail (1992).

1.5.2 Microlensing

A microlensing event is a particular case of the gravitational lens phenomenon, which occurs when a foreground massive object bends the light from a background source due to the curvature of the spacetime around this massive object. Unlike strong gravitational lenses¹², the background source in a microlensing event is usually a bright star from the Milky Way and the deflection of its light is produced by a second star or stellar remnant. The microlensing phenomenon occurs when the background source and the foreground object are aligned with the observer's line-of-sight; then, the gravitational potential of the closer star will bend the light, producing two images of the distant source that cannot be resolved individually due to the distance between lens and source (Figure 1.9 shows the configuration of a microlensing event). However, a brightening of the background star can be detected as a function of the projected angular separation between both objects, and also as a function of the shift in the apparent position of the combined image. The progression

¹²Strong gravitational lensing is typically associated with large-scale distances. The background sources and the deflecting objects are galaxies or even cluster of galaxies, resulting in multiple distorted images from the source (Carroll & Ostlie, 2006).

of this brightening is described by the so-called Paczynski curve (see Figure 1.10, Paczynski 2003), which shows the magnification of the background objects as a function of time. The detection of an exo-planet is possible if a planetary companion around the foreground object is located near to the path of the bended rays. The mass of the planet will also affect gravitationally the light from the source, producing a small perturbation in the Paczynski curve (see Figure 1.10), from which the planetary companion can be inferred (Mao & Paczynski, 1991).

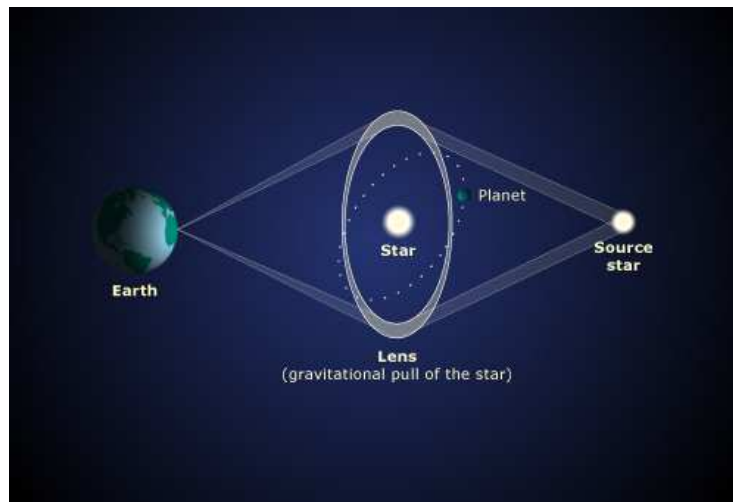


Figure 1.9: Configuration of a microlensing event produced, where the light from a background source is bended by a star that may be accompanied by a planet. (Credit of the figure: Maggy Wassilieff.'Astronomy-overview-Mt John Observatory', Te Ara - the Encyclopedia of New Zealand. URL:<http://www.TeAra.govt.nz/en/diagram/8008/gravitational-microlensing>)

Although the probability to observe a microlensing event is very low, observing in direction of the galactic center (high density of stars) reveals more than thousand magnifications of background stars per year (Udalski et al., 1992). There are teams around the world that constantly search for such magnifications (e.g. The Microlensing Observations in Astrophysics-MOA¹³ and The Optical Gravitational Lensing Experiment-OGLE¹⁴). Once a microlensing event is detected, this is notified to follow-up groups (e.g. μ FUN-PLANET collaboration¹⁵) to start intensive monitoring of such events. The magnification of the source lasts from some days to several weeks. If during this time the microlensing event shows anomalies, a quick high temporal resolution follow-up is performed in attempt to infer the presence of a planetary companion. From this analysis, important characteristics of the planetary system can be determined, such as the orbital distance and the mass of the planet.

The microlensing technique presents some clear advantages. For example, this method is extremely sensitive to detect Earth-mass planets, since it does not depend strongly

¹³<http://www.phys.canterbury.ac.nz/moa/>

¹⁴<http://ogle.astrouw.edu.pl>

¹⁵<http://planet.iap.fr/>

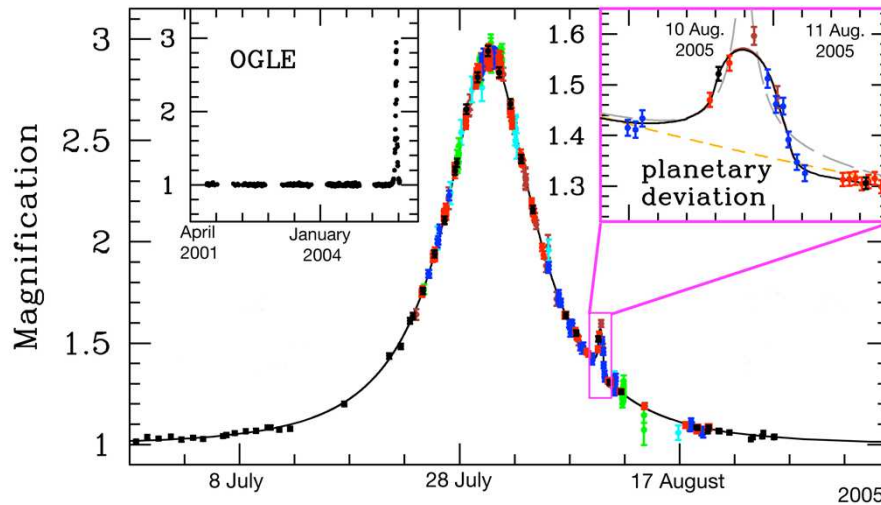


Figure 1.10: Light curve of a microlensing event occurred in the main-sequence M-dwarf OGLE-2005-BLG-390. The Paczyński curve shows clearly an anomaly, which is interpreted as a planet. (Credits: European Southern Observatory-ESO)

on the planet mass. This method also allows planets with large orbital distance to be discovered, and represents the only method capable to detect the most distant exo-planets in the Milky Way and potentially in other near galaxies, such as M31. On the other hand, the method also presents a clear disadvantage, namely that the microlensing events are unique (i.e they never happen again). Thus, further follow-up and measurements of the brightening are impossible. Moreover, if the planetary companion is too far, a follow-up and a subsequent confirmation of the planet is very difficult. Nevertheless, the microlensing technique presently represents the only method able to statistically reveal the galactic population of exo-planets.

1.5.3 Imaging

The imaging method is based on the direct detection of the exo-planet's photon-emission. In 2004, Chauvin et al. (2004) used an image from the Very Large Telescope¹⁶ (VLT) to report the object 2M1207-b as a planet candidate detected by direct imaging. One year later, 2M1207-b was confirmed as a planet, being the first exo-planet discovered by this technique (see Figure 1.11). Since then, thirty exo-planets have been discovered by capturing a direct image of them. The lack of detected planets by this method is due to the difficulties to separate the faint emission of the exo-planet from the much brighter contribution of the host star. The angular separation between the star and the planet, as well as, the flux ratio between both objects are decisive to achieve a direct detection of the

¹⁶The Very Large Telescope is a telescope that operates at the infrared and visible wavelengths. The VLT is located in the Atacama desert in Chile and is operated by the European South Observatory (ESO). According to scientific papers, the VLT represents the most productive ground-based telescope.

planetary companion. The brighter the parent star and smaller the angular separation, the more difficult it is to differentiate the light of the objects, so that exo-planets detected with the imaging method usually have large orbital distances. The angular distances between exo-planets and host companions are typically in the range of several decimals to few arcsecs. The light emitted by a planetary companion is produced by two different process:

- i) The first process occurs when the surface or atmosphere of the exo-planet reflects the stellar emission. The spectrum of the reflected emission will have a similar appearance to the one that belongs to the star. However, additional components can be detected in this spectrum according to the chemical composition of the surface and/or atmosphere of the exo-planet.
- ii) The second process is due to the own thermal emission generated by the exo-planet, which can be produced, either by intrinsic sources (e.g. the remaining heat of the planet formation), or heating of the exo-planet due to the radiation of the stellar companion.

The features mentioned above represent the main capability of the imaging method, since detecting direct photo-emission from exo-planets enables us to know the chemical composition of the planetary atmosphere, which can provide important information on the planet evolution, as well as, the detection of organic molecules or chemical compounds that can be used to infer the presence of life in such planets.

Once possible false scenarios have been rejected (e.g. detecting a background star instead of a planet) and the presence of an exo-planet is confirmed, the characterization of the system can be determined by measuring the common proper motion. Furthermore, if enough information exists about the relative position between planet and host companion, and the distance to the system is known, then the orbital characteristics of the exo-planet can be deduced. Using evolutionary stellar models to externally obtain physical parameters of the host star (e.g. stellar mass and radius) together with other detection techniques (e.g. radial velocity and transit methods) represents another possibility to obtain physical parameters of the system, such as the mass and radius of the planetary companion. Nevertheless, an indirect estimation of the mass might result in a large uncertainty in the measurements. Alternately, gravitational perturbation produced by a multi-planetary system can be used to estimate directly the mass of the planet in question.

Unlike other detection techniques, the imaging method has provided so far a small number of discoveries. Nevertheless, an important progress in the development of new instruments and techniques of observation is currently taking place. For example, the adaptive optics¹⁷ is being integrated to new generation of ground-based telescopes, and together with new space projects, the number of exo-planets detected by direct imaging will considerably increase. This will provide an unique opportunity to investigate directly the atmosphere and surface conditions of the exo-planets, opening a new windows in the search of extraterrestrial life.

¹⁷In astronomy, the adaptive optics is a technique used to improve the performance of optical systems by correcting the atmospheric effects in real-time

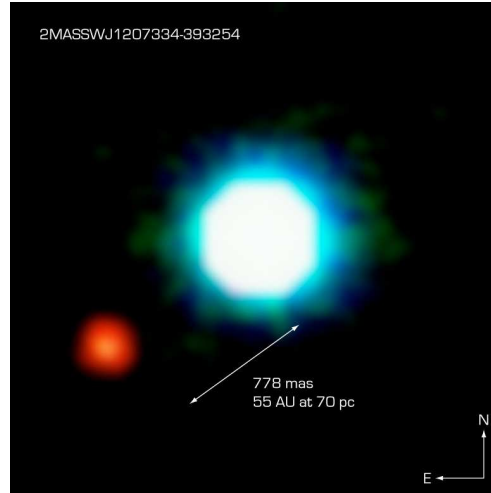


Figure 1.11: Image of 2M1207-b, the first extra-solar planet detected with a direct image. (Credits: ESO)

1.5.4 Astrometry

Historically, the astrometric method was the first technique employed to search for extra-solar planets, based on the success of finding binary systems by inferring the secondary companion from changes in the relative position in the sky of the dominant star. Unlike the radial velocity technique (see §1.5.5), the astrometric method involves accurate measurements of the two-dimensional tangential variations in the host star’s position on the sky. Due to mutual gravitation interactions, host star and planet orbit around a common barycenter. The amplitude of the astrometric signature produced by a planet with mass M_p , which orbits a star with a mass M_* and semi-major axes a_p is described by:

$$\theta = \frac{a_p}{d} \frac{M_p}{M_*} = \left(\frac{G}{4\pi^2} \right)^{1/3} \frac{M_p}{M_*^{2/3}} \frac{P^{2/3}}{d}, \quad (1.2)$$

where G is the gravitational constant, and d is the distance to the system. Eq.1.2 can also be expressed as

$$\theta = \left(\frac{M_p}{M_*} \right) \left(\frac{a_p}{1 \text{ AU}} \right) \left(\frac{d}{1 \text{ pc}} \right)^{-1} \text{ arcsec}. \quad (1.3)$$

From the above equations, we can deduce that the periodic astrometric displacements are very small, so measuring changes in the position of the star is extremely difficult. For instance, Jupiter produces a signature on the Sun of about 0.25 milliarcsec, as seen from a distance of 20 pc, while the astrometric signature caused by Earth as observed at the same distance is about ~ 1.5 microarcsec (Wright & Gaudi, 2013). Nevertheless, accurate measurements of these movements can reveal the presence of planet companions. Figure 1.12 shows an example of the displacement of a stars on the sky, which shows an astrometric offset due to a planetary companion.

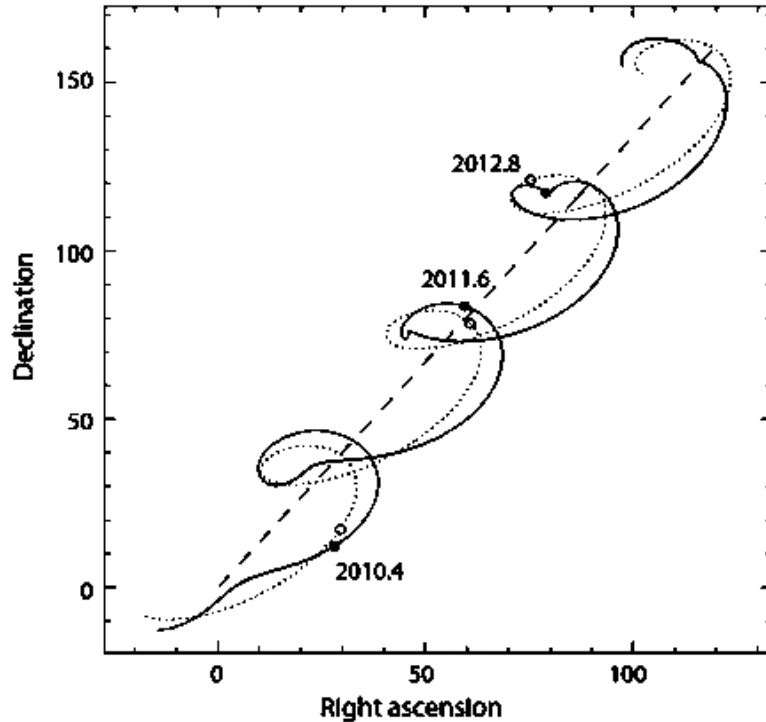


Figure 1.12: Displacement of the angular position of a Sun-like star with a proper motion of 50 milliarcsec, as seen from a distance of 50 pc. A $15 M_{\text{Jup}}$ planet orbits the star with a semi-major axes of 0.6 AU. The presence of the planet produces a mutual gravitational effect, resulting in astrometric variation of the star's trajectory (The scale of the axes is given in milliarcsec). Currently the precision to measure such tiny displacement is only reached from space. (Source:<http://www.markelowitz.com/Exoplanets.html>)

The astrometric method is able to provide information about the orbital characteristics of the system, such as the inclination and orientation of the planetary orbit. The technique is also sensitive to planets in all orbital inclinations. This represents an important advantage, since the true mass of a planet in any orbital configuration can be estimated. Another advantage of the astrometric technique is that it has more sensitivity to large orbital distances, so that planets with long periods can be discovered. However, this also can be a disadvantage, since a very long orbital period will require many years of observations to detect a complete orbit.

So far, no planet has been discovered by astrometric measurements; however, in 2002 Benedict et al. (2002) determined and confirmed for the first time using astrometric measurements (from the Hubble Space Telescope), the mass of the extra-solar planet Gliese 876b, which had been previously detected by Doppler spectroscopy. The astrometric method, so far has succeeded when is complementary used with other detections techniques, such as the radial velocity. Nevertheless, this might change in the near future. The European Space Agency (ESA) is expecting to launch the Gaia¹⁸ space-space mission in

¹⁸<http://sci.esa.int/science-e/www/area/index.cfm?fareaid=26>

December 2013 or January 2014. Gaia is planned to create a three-dimensional map of the Milky Way performing accurate positional measurements of about one billion stars during a period of five years. Such information may then lead to the first planet detections with the astrometric method.

1.5.5 Radial velocity

The radial velocity was originally used to detect eclipsing binary systems. Despite this, the gradual improvements on instruments and telescopes also enabled the dynamical effects produced by a planet on the host companion to be measured. The radial velocity method was responsible of the detection of the first exo-planet orbiting its host main-sequence star (Mayor & Queloz, 1995). After this discovery, the technique became the most productive method to find exo-planets: out of 974 extra-solar planets detected so far, 532 have been discovered with this method. Nevertheless, this will change in the near future when many of the transit-candidates found by the *Kepler* mission will be confirmed as planets.

In a planetary system, planet and host star move around a common center of mass (barycenter) due to the mutual gravitational interaction. The radial velocity method, as its name suggests, consists in measuring the radial component of the orbital movement of the stellar companion, where the magnitude of such movement directly depends on the mass of the planet (see below). This displacement can be estimated through the Doppler shift of the detected light, i.e, by measuring the displacement of the spectral lines of the stellar companion. Modern spectrometers currently allow us to measure the radial component of this movements down to 1 m/s or smaller for bright stars. Such measurements permit the detection of Super-Earths¹⁹ or even Earth-like planets around Sun-like and earlier-spectral type stars. Although the radial velocity signal does not depend on the distance of the planetary system, the technique is more sensitive to brighter stars, therefore this method is generally employed in the Solar System vicinity.

A major disadvantage of the radial velocity method is that, as long as the system's inclination angle is unknown, only the minimum mass of the planet can be estimated. That is, to obtain the real mass of the planet, the inclination orbit must be measured, for example using the transit method (see below). In addition to the mass, the radial velocity method provides information about the period, shape of the orbit and separation between exo-planet and parent star.

We describe below the main equations governing the radial velocity method and present explicitly the physical parameters of the system that can be inferred by this method:

Since the parent star and planet orbit around their common center of mass, we start by defining the *barycenter*:

$$a_{\star}M_{\star} = a_{\text{p}}M_{\text{p}}, \quad (1.4)$$

¹⁹The definition of Super-Earth refers to a exo-planet with a mass higher than the Earth's up to $10M_{\oplus}$, which is the limit for the gas-giant planets in the Solar System.

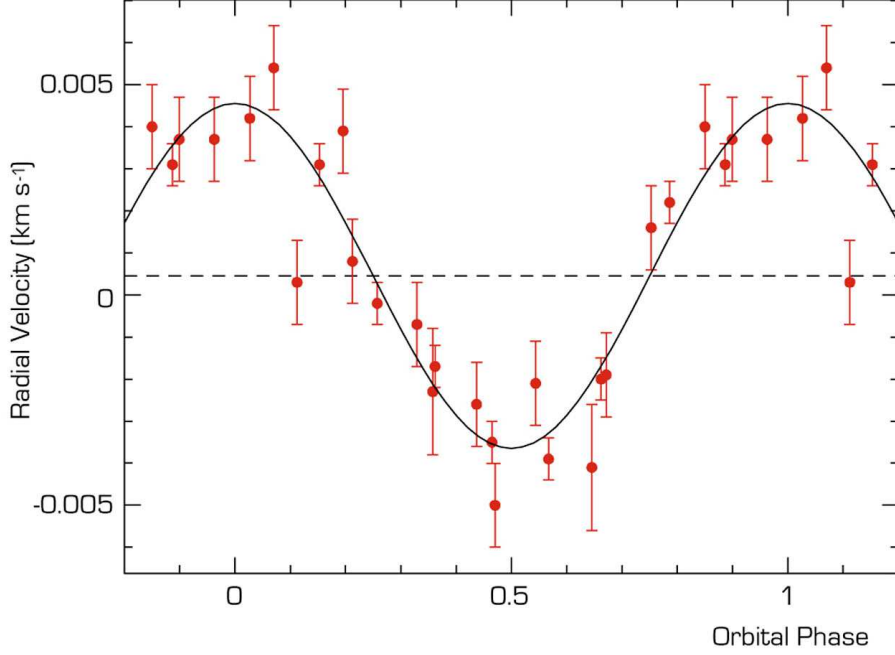


Figure 1.13: A typical radial velocity measurements phase-folded with an orbiting planet. The measurements correspond to a planet with $14 M_{\oplus}$ (minimum mass) orbiting the star μ -Arae in 9.5 d. (Credits: ESO)

where a_{\star} and a_p are the semi-major axes of the star and planet around their common center of mass and M_{\star} and M_p are the stellar and planetary masses respectively.

Assuming a circular stellar orbit with period P around this barycenter, the stellar orbital velocity is:

$$v_{\star} = 2\pi \frac{a_{\star}}{P} = 2\pi \frac{a_p}{P} \frac{M_p}{M_{\star}}, \quad (1.5)$$

where P and a_p are given by Kepler's 3rd Law:

$$(a_{\star} + a_p)^3 = \frac{G}{4\pi^2} P^2 (M_{\star} + M_p). \quad (1.6)$$

In a planetary system the host star's mass is typically much larger than the mass of the planet (i.e. $M_p \ll M_{\star}$), therefore the semi-major axis of the host companion is much smaller than the planet's semi-major axis. With this assumption, the Eq.1.6 reduces to:

$$a_p^3 = \frac{G}{4\pi^2} P^2 M_{\star}. \quad (1.7)$$

From this equation we can now express the orbital period P in Solar System units:

$$P = \left(\frac{a_p}{1 \text{ AU}} \right)^{3/2} \left(\frac{M_{\star}}{M_{\odot}} \right)^{-1/2}. \quad (1.8)$$

We can combine the last result with Eq.1.5 to obtain the stellar orbital velocity as a function of the orbital period P , stellar mass M_\star and planetary mass M_p :

$$v_\star = \left(\frac{2\pi G}{P}\right)^{1/3} \frac{M_p}{M_\star^{2/3}}. \quad (1.9)$$

However, we are not able to determine the real orbital velocity of the star, as long as we only have access to the radial component of the velocity ($v_\star \sin i$) and the inclination of the orbit is unknown. Therefore, the equation above is transformed into:

$$K = v_\star \sin i = \left(\frac{2\pi G}{P}\right)^{1/3} \frac{M_p \sin i}{M_\star^{2/3}}. \quad (1.10)$$

where K represents the velocity of the star projected along the line of sight, which can be also expressed in Solar System units in terms of the period P :

$$K = 28.4 \left(\frac{P}{1 \text{ yr}}\right)^{-1/3} \left(\frac{M_p \sin i}{M_{\text{Jup}}}\right) \left(\frac{M_\star}{M_\odot}\right)^{-2/3} [\text{m/s}] \quad (1.11)$$

or alternatively via semi-major axis a_p by using Eq.1.8:

$$K = 28.4 \left(\frac{a_p}{1 \text{ AU}}\right)^{-1/2} \left(\frac{M_p \sin i}{M_{\text{Jup}}}\right) \left(\frac{M_\star}{M_\odot}\right)^{-5/6} [\text{m/s}]. \quad (1.12)$$

So far, these equations only correspond to circular orbits. Such orbits provide a sinusoidal variation of the radial velocity measurements, from which the period P can be deduced directly. For planets in elliptical orbits, the radial component of the velocity is affected by the eccentricity e , whereby Eq.1.12 is transformed into (Papaloizou & Terquem, 2006):

$$K = v_\star \sin i = \left(\frac{2\pi G}{P}\right)^{1/3} \frac{M_p \sin i}{M_\star^{2/3}} \frac{1}{\sqrt{1-e^2}}. \quad (1.13)$$

Although the radial velocity variations of a non-circular orbit do not give a sinusoidal shape (see Figure 1.14), the eccentricity can be also determined by fitting such periodic variations. Therefore, the period P , eccentricity e , semi-major axis a_p and projected mass $M_p \sin i$ can all be derived by measuring and fitting K , if M_\star is known. As mentioned above, to determine the real mass of the exo-planet, we also need to estimate the inclination of the orbit i by an alternative technique, such as the transit method.

From Eq.1.13, it is clear that the radial velocity method is more sensitive to massive planets with shorter periods. Taking into account the current detection limit (1 m/s) provided by the new generation of telescopes and spectrometers, Jupiter-mass planets might be found orbiting around Sun-like stars by this technique, even for orbits with a semi-major axis up to several hundred AU. However, it is important to find a compromise with the orbital distance, since the detection of a planet can be only confirmed when an orbital period is completed. For such large semi-major axis, many years of observation would be required to reach a full orbit.

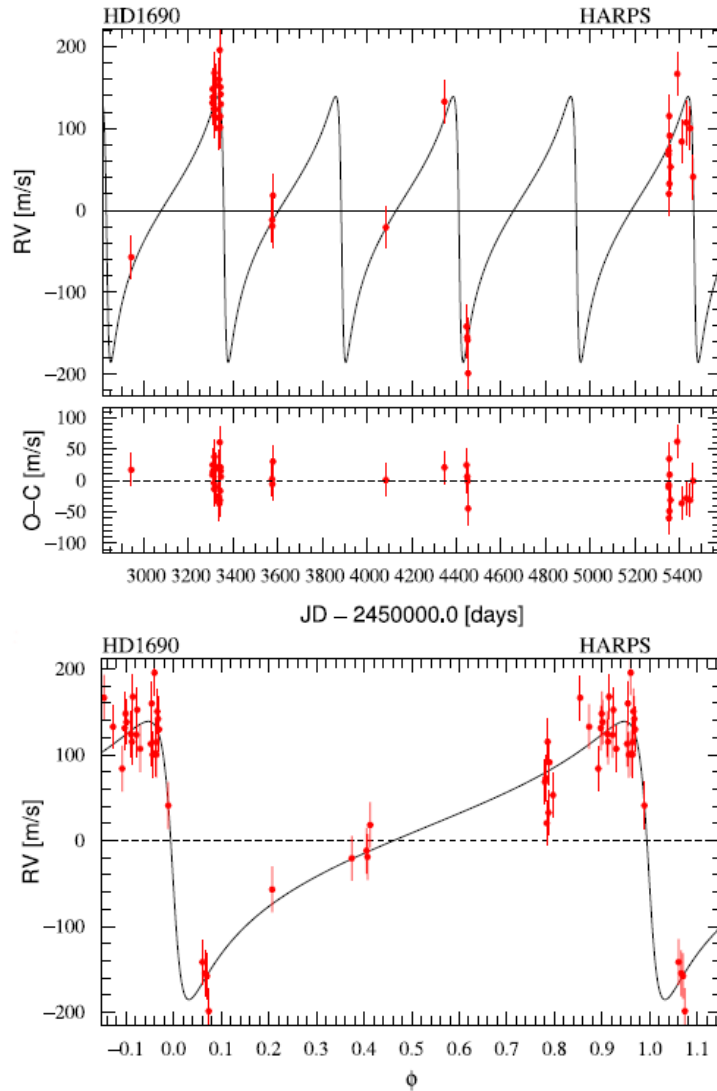


Figure 1.14: Planetary system with high eccentricity. The plot correspond to the radial velocity measurements and phase-folded radial velocity curve of the HD 1690, which hosts a planet (HD 1690 b) in an orbit with a $e = 0.64$, resulting in non-sinusoidal radial velocity variations. (source: Moutou et al. 2011)

1.5.6 Transit method

In recent years, after the initiation of the *Kepler* mission era (see below for more details) in the search for extra-solar planets, the transit method has become one of the most successful and popular techniques in the hunt for exo-planets. Although transit events had been observed for many years in binary systems, the first discussion of the effect produced by a planet on the brightness of its parent stars was presented by Struve (1952). Years later, a more solid treatment of the problem was discussed by Rosenblatt (1971). Subsequently, Borucki & Summers (1984) presented corrections of the previous predictions, providing a new perspective on the detection of transiting planets. Several years passed until the

first sign of a transit was detected. This discovery was published by Charbonneau et al. (2000), who reported a planet transiting the Sun-like star HD-209458. However, the companion of HD-209458 had previously been discovered with the radial velocity technique (Mazeh et al., 2000), so the first planet found with the transit method was instead OGLE-TR-56-b (Udalski et al., 2002b), which is a Jupiter-sized planet orbiting a Sun-like star with an orbital period of ~ 1.2 d.

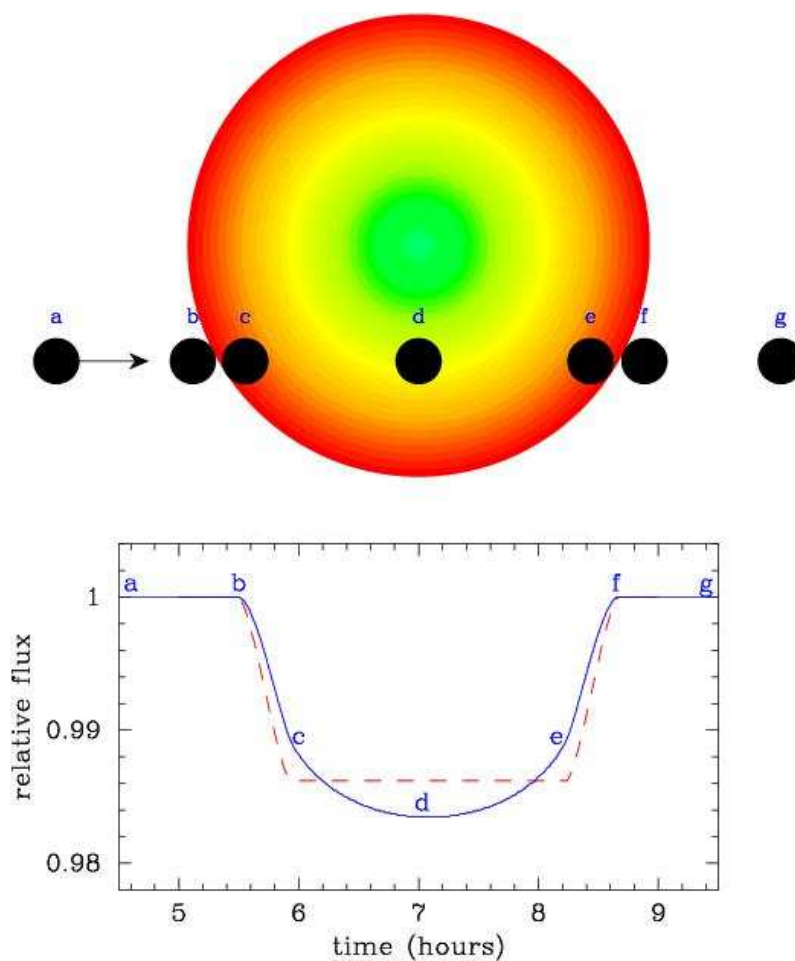


Figure 1.15: A transit event occurs when a planet passes in front of its parent star blocking partially the flux of the star. Such phenomena can be detected in the light curve of the star as a drop of the detected flux. The figure shows a diagram of a planet transiting the host star (top panel), which produces a drop in the luminosity of the star (bottom panel). (source: <http://www.fromquarkstoquasars.com/how-we-find-other-worlds/>)

A transit event occurs when the orbit of an exo-planet is closely aligned ($i \sim 90^\circ$) to the line-of-sight of an observer. In such cases, a drop in the stellar companion's brightness due to the fractional part of the stellar surface that is blocked by the planet may be detected (Figure 1.15). The detection of a planetary system with the transit method depends on several factors. For instance, the geometric probability that the transit event actually occurs, the sensitivity of the photometric measurement to detect the attenuation

of brightness of the host star produced by the transiting planet, as well as the observational time compared to the duration and frequency of the transit. If all the above conditions are satisfied, then a transit event can be detected.

We now introduce the main equations that relate the physical parameters of the stellar companion and planet involved in a transit. In the following, we assume circular orbits for simplicity in our discussion and also that the physical parameters of the star are significantly larger than the planetary ones, such as radii and masses ($R_p \ll R_*$ and $M_p \ll M_*$). We also assume that the distance of the planet to the parent star a_p is much larger than the physical radius of the star ($R_* \ll a_p$). For the more general case of an arbitrary scale of R_p , R_* , and a_p and eccentric orbits ($e > 0$), the below equations are considerably more complicated, however the essence of the problem can still be appreciated under our approximations. A full description of transit and occultation theory can be found in Winn (2010).

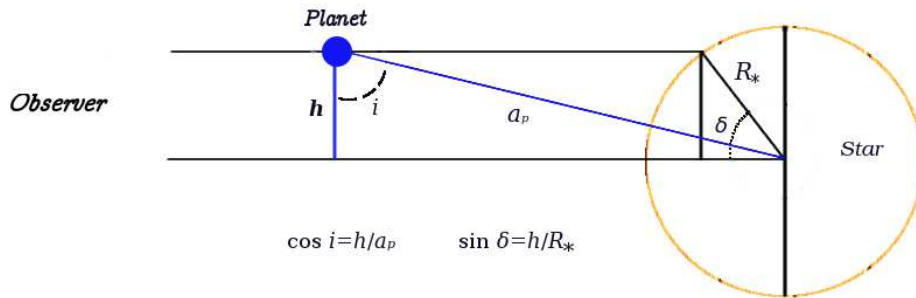


Figure 1.16: Geometry of a planet transiting its parent star.

First of all, we describe the geometric probability that a transit occurs. We mentioned above that a transit will be detected only if the inclination of the orbit is sufficiently inclined to the observer's line-of-sight. This scenario occurs when the impact parameter b of the planet's orbit in the stellar disk, is less or equal than the sum of the normalized radii. In a circular orbit we express this condition as:

$$b \equiv \frac{a_p \cos i}{R_*} \leq 1 + \frac{R_p}{R_*}. \quad (1.14)$$

Figure 1.16 shows the geometry of a transit event, where $\cos i$ represents the projection of the normal vector of the orbital plane with respect to the observer. From the above expression we can obtain the geometric transit probability by considering isotropic orbits

and uniform distribution of $\cos i$ by integrating over i :

$$P_{\text{tr}} = \frac{R_{\star} + R_{\text{p}}}{a_{\text{p}}}. \quad (1.15)$$

Under the assumption that $R_{\text{p}} \ll R_{\star}$, this equation transforms into:

$$P_{\text{tr}} = \frac{R_{\star}}{a_{\text{p}}}. \quad (1.16)$$

This expression suggests that a transit would be observed only if the inclination of the orbit exceeds certain minimum inclination i_{min} expressed as:

$$i_{\text{min}} = \cos^{-1} \frac{R_{\star}}{a_{\text{p}}}. \quad (1.17)$$

From Figure 1.16, we deduce that i_{min} corresponds to $h = R_{\star}$, where h is the stellar latitude. Another quantity that arises from the geometry of the transit probability is the relation between $\cos i$ and the stellar latitude δ :

$$\cos i = \frac{h}{a_{\text{p}}} = \frac{R_{\star} \sin \delta}{a_{\text{p}}}. \quad (1.18)$$

We deduce from this expression that a central transit corresponds to stellar latitude $\delta = 0^{\circ}$ with orbital inclination $i = 90^{\circ}$. On the other hand, i_{min} is reached when $\delta = 90^{\circ}$, which is representative of grazing eclipses²⁰. The geometric probability of a transit event favors planets that orbit large parent stars with smaller orbital distances. Figure 1.17 shows the transit event probability of planets in our Solar System. We observe that for inner rocky planets the probability is between 1.2 % and 0.30 % and decreases by a factor of ten for the giant-gaseous planets. If other planetary systems have similar orbital distributions as our Solar System, the probability to detect a single transit is very low, therefore several thousands of stars must be monitored in transit surveys to increase the statistic probability of finding a transiting planet. Transit surveys usually are designed to observe large number of stars, which can be achieved by observing either crowded fields (e.g. the Galactic plane) or using detectors that cover wide fields on the sky.

A periodic transit includes several phases, such as ingress, full transit, egress and occultation (i.e., the planet is behind the star). During ingress, the planet progressively start to block the disk of the star, which produces a smooth dimming of the light. The full transit occurs when the planet is completely in front of the stellar disk. The light curve is determined by limb-darkening, reaching the bottom of the curve when the planet passes in front of the brightest part of the star. The egress phase is symmetric to the ingress, in this

²⁰A grazing eclipse occurs when the inclination of the orbit only allows the transiting object to graze the limb of the parent companion, therefore the dimming depends of the fractional part of the disk that is eclipsed, which is usually less than the area of the transiting companion. In a non-grazing eclipse the entire disk of the transit objects falls inside of the host star and the drop of the brightness can be estimated as a function of R_{p} and R_{\star} (see main text). Grazing eclipses produced by Brown dwarfs or low-mass stars are a very common type of false-positives.

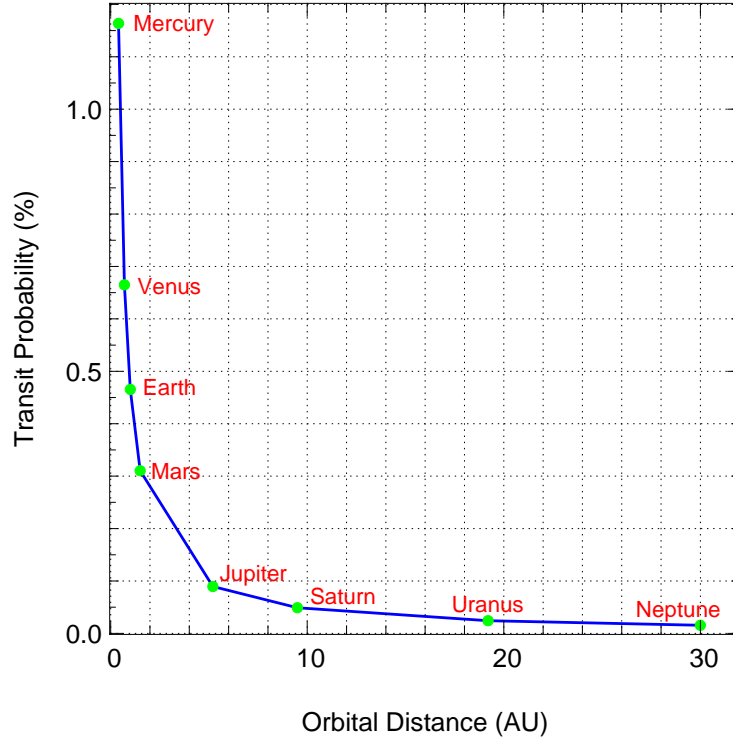


Figure 1.17: Transit probability as a function of the orbital distance a_p for planets in the Solar System.

case the star gradually recovers its full brightness. The transit light curves can be analyzed by analytic models. A description of such models can be found in Mandel & Agol (2002).

According to the description of a transit described above, a light curve of a star with a transiting planet can be approximated by a trapezoidal shape characterized by certain parameters of the transit, such as the fractional flux depth, the transit duration T_{tr} and the orbital period P . Assuming a non-grazing eclipse and constant surface brightness, the variation of the flux or depth of the transit is given by the ratio of the host star and transit companion:

$$\frac{\Delta F}{F} = \left(\frac{R_p}{R_\star}\right)^2. \quad (1.19)$$

For the case of a Jupiter-size planet orbiting a Sun-like star, this ratio is about $\sim 1\%$, whereas for an Earth-size planet, the quantity drops to 0.01% . The accuracy of ground-based telescopes (even for relative small ~ 20 cm apertures) is about 0.1% for bright stars, so Jovian-planets can be detected by such telescopes. The precision required to observe the transits of terrestrial planets around Sun-like stars is at present day only reached from space, and is limited by the variable extinction of the atmosphere. Nevertheless, Earth-like planets can also be found by ground-based telescopes if one targets cool and low-mass M-dwarf stars, since their brightness and physical size are small enough to detect the eclipse produced by such planets. M-dwarf transit surveys are currently in operation and

some of them have already provided positives results, such as finding super-Earths (see Section §1.6).

The transit duration T_{tr} can be expressed as a function of the orbital period, orbital distance, stellar radius, and orbital inclination (Winn, 2010):

$$T_{\text{tr}} = \frac{P}{\pi} \sqrt{\left(\frac{R_{\star}}{a_{\text{p}}}\right)^2 - \cos^2 i}. \quad (1.20)$$

This equation is only valid under the assumption that $a_{\text{p}} \gg R_{\star} \gg R_{\text{p}}$. The period and orbital distance of the planet can be then determined by Eq.1.7 if we are able to detect two or more transits and the stellar mass is known.

We can alternatively express the duration of the transit in terms of the stellar latitude, planetary and solar radii, period, and distance between, star and planet companion (Deeg, 1998):

$$T_{\text{tr}} = \frac{P}{\pi} \left(\frac{R_{\star} \cos \delta + R_{\text{p}}}{a_{\text{p}}} \right), \quad (1.21)$$

using again the Eq.1.7, we can rewrite the above equation as:

$$T_{\text{tr}} = \sqrt{\frac{4a_{\text{p}}}{\pi GM_{\star}}} (R_{\star} \cos \delta + R_{\text{p}}). \quad (1.22)$$

If the stellar mass and radius are known, the inclination of the orbital plane can be estimated by using the previous equations and combining the result with radial velocities measurements the real mass of the planet can be determined. Finally, the fractional transit duration τ can be expressed as the ratio of the transit duration and total orbital period, i.e,

$$\tau = \frac{T_{\text{tr}}}{P}. \quad (1.23)$$

Although measuring transit signals in light curves represents one of the most successful methods to detect and characterize exo-planets, this technique also presents important disadvantages. For example, the large number of false-positives and false-detection (see §1.5.7) found in transit surveys are a common problem that makes the search for exo-planets difficult. This is the major disadvantage of this method. Since an exo-planet cannot be found only by detecting a transit in front of the host companion, all transit detections require an additional confirmation, which is typically performed by radial velocity follow-up measurements. Any transit candidate must be monitored by low, mid, and high-resolution spectroscopy to confirm the planetary nature of the candidate. The follow-up programs are time-consuming and require a high cost, so that the follow-up of candidates can be challenging, specially for faint stellar companions (Koppenhoefer et al., 2013).

In conclusion, the detections of periodic transits represents one of the most successful techniques to detect exo-planets. Unlike other techniques (such as the radial velocity or microlensing), this method provides a variety of important parameter of the planetary system, for instance the radius of the planetary companion and the inclination of the

orbit, which can be used in combination with radial velocity measurements to estimate the real mass of the transiting planet, as well as its density. Moreover, once a candidate is confirmed as a planet, the transit method can be used to determine the surface temperature of the planet by analyzing the light curve of the parent star during the occultation phase (see Sec §1.5.8). Nowadays, several transit surveys are monitoring regions on the sky to search for transiting exo-planets. There are a wide diversity in the characteristics of these surveys. In Section §1.6, we present a review of transit surveys, describing in detail the most remarkable missions.

1.5.7 False-positives in transit surveys

In Section §1.5.6, we mentioned that transit surveys require to observe regions on the sky that allow us to monitor thousand or even several hundred thousand stars, compensating the low probability of finding a system with an orbital plane aligned to the line-of-sight of the observer ($i \sim 90^\circ$). Observing a large number of stars increases the rate of false-positives and false-detections. Both elements have conceptually different origins. A false-detection is produced if a light curve holds a significant number of systematic outliers, which can result in a fake signal. On the other hand, a false-positive is associated with real physical variability of the stellar flux, such as eclipsing binary systems or intrinsic variable stars. An example of a false-positive is shown in Figure 1.18. In the following, both scenarios are referred as false-positives for practical reasons.

Recently, Santerne et al. (2012) presented an analysis carried out on a sample of candidates from the *Kepler* mission, which showed that the false-positives rate might reach $\sim 35\%$. For ground-based transit surveys, this number could be considerably higher due to atmospheric effects, which cause photometric variability, producing a large amount of false-positives. Another important source of false-positives in ground-based surveys is the window-function introduced by the day/night cycle. This effect produces a high number of detections with periods close to half-day or an integer number of days, as shown in Figure 1.19. Other causes of false-positives are produced by real variability of the stellar flux. Such brightness variation of host stars can be produced by intrinsic variation of the host star (e.g. RR-Lyrae²¹), grazing eclipsing binaries or stellar spots. The large number of false-positives in transit surveys represents a major disadvantage to find planets by this method, so that transit surveys require strategies to eliminate as many false-positives as possible while keeping valuable candidates. In this work, we present a set of selection criteria used to reduce the number of false-positives from the WTS light curves (see §5.1).

1.5.8 Further implications of the transit method

In addition to the parameters of the planetary system that can be determined with the transit method (e.g. period, orbital inclination and planetary radius), this technique offers

²¹RR-Lyrae's are variable periodic stars that are commonly found in globular clusters (spherical associations of stars orbiting galactic cores). Due to their pulsation period-luminosity relation, RR-Lyrae stars are normally used to measure galactic distances.

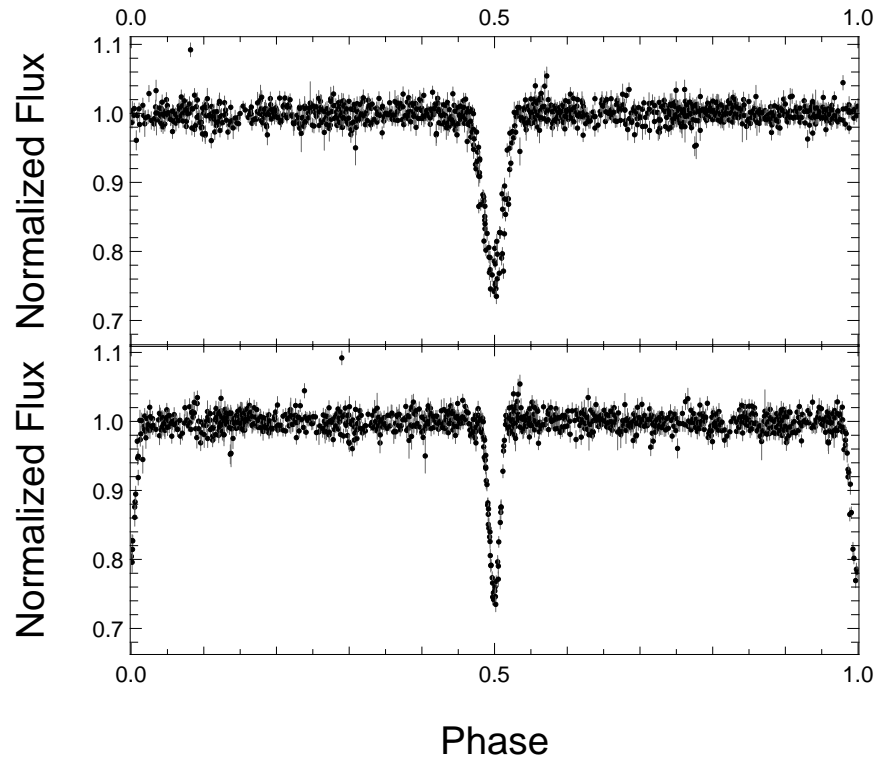


Figure 1.18: Example of a false-positive detected in transit surveys. The upper panel shows the folded light curve of a planet candidate, which results to be an eclipsing binary once the light curve is folded with double the period, where a secondary eclipse with different depth is observed (lower panel). The folded light curves correspond to an object detected in the WTS.

a wide variety of analyses that can be performed once a candidate has been confirmed as a planet and used to characterize the transiting companion or the planetary system.

Several authors (Holman & Murray, 2005; Agol et al., 2005) have proposed the possibility of detecting additional planets by measuring accurately transit timing variations (TTVs). TTVs are small differences in the transit mid-points produced by gravitational perturbations due to additional planets in the system. TTVs depend on the masses of planets and configuration of the orbits. For example, if a transiting hot Jupiter is perturbed by a second body with a mass of an Earth-like planet, the effect caused by the gravitational interaction can produce TTVs of about 0.1-1 minutes, which can currently be measured with high-precision photometry from ground-based telescopes. In 2011, the first extra-solar planet detected by TTVs was announced. The discovery was presented by Ballard et al. (2011), reporting the planet *Kepler-19c* with a orbital period of ~ 160 d and mass $\lesssim 6 M_{\text{Jup}}$. The planet *Kepler-19c* was inferred by TTVs of the transiting planet *Kepler-19b*.

Moons of extra-solar planets (exo-moons) might also be detected with the transit method. For example, Sartoretti & Schneider (1999) computed the probability to detect satellites of exo-planets, assuming that observations would be as long as the orbital period. Their results show a high probability (~ 1) if the exo-moon is large enough to produce a

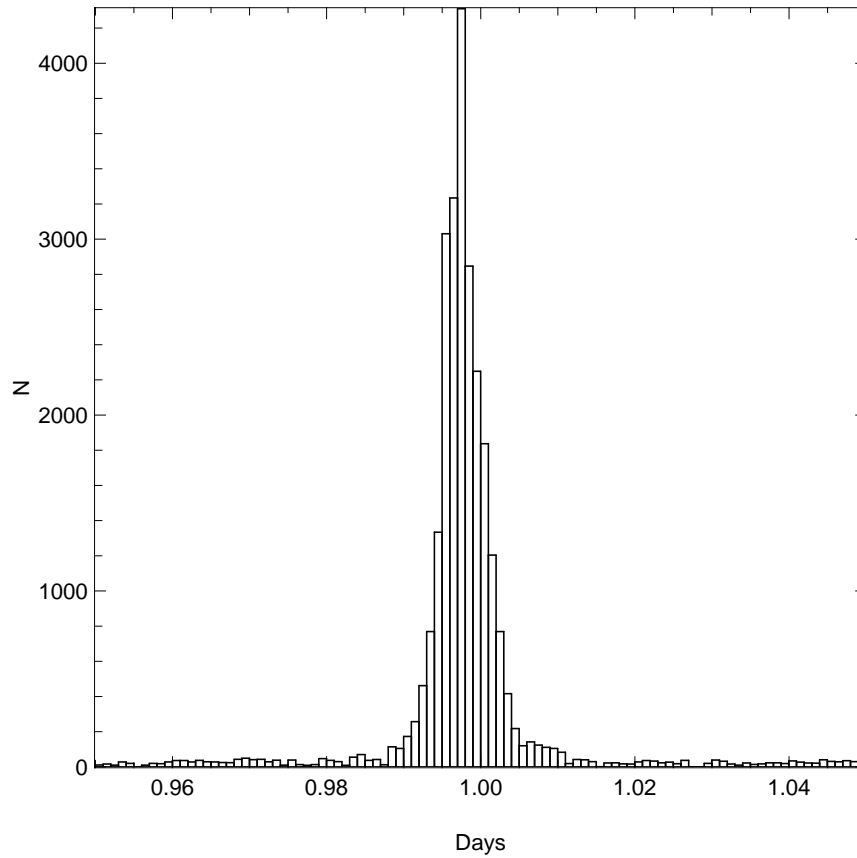


Figure 1.19: Histogram of detected periods in the WTS light curves. A large number of detections are around the one-day alias period.

detectable drop in the light curve of the host star. They also suggested that even if the satellite is not extended enough to cause a dimming, it might still be detected by TTVs. However, many authors have argued that determining the mass of the satellite only from TTV measurements would be impossible, since the period and orbital distance of the exo-moon cannot be estimated from TTV measurements. Nevertheless, Kipping (2009) pointed out that an exo-moon produces also transit duration variations (TDVs) and suggested that using these variations together with TTV measurements, the mass of the satellite can be determined. Recently, Kipping et al. (2009) investigated the detectability of HZ exo-moons by using *Kepler*-class photometry. They found that HZ exo-moons with masses down to $0.2 M_{\oplus}$ might be detected, and about $\sim 25\,000$ stars from the *Kepler*'s field of view may be surveyed for this propose.

Characterization of exo-planets is another task that can be performed with the transit method. During the different phases of a transit event, valuable information can be obtained by analyzing the light detected from the host star. A detailed analysis of this signal allows the observer to characterize the atmosphere composition and the surface temperature of the exo-planet.

The composition of the atmosphere can be determined by a precise spectroscopic anal-

ysis during the ingress/egress and full transit phases. When a planet eclipses its host companion, the light of the star passes through the planet's upper atmosphere, therefore additional absorption lines produced by atoms and molecules from the atmosphere can be detected by comparing the spectra of the star before and during the transit. Due to the low signal-to-noise ratio (S/N) of these spectral features, these measurements can currently be achieved only from space and for very bright stars. Several authors have reported chemical components in the atmospheres of some exo-planets. In 2002, a team led by Charbonneau (Charbonneau et al., 2002) used observations from the Hubble-Space-Telescope and high-precision spectrometry to report sodium in the atmosphere of the companion of HD209458. Further analyses in the transit of HD209458b revealed more components of its atmosphere, such as Oxygen, Carbon and atomic Hydrogen (Vidal-Madjar et al., 2003, 2004). Later, Tinetti et al. (2007) presented a spectroscopic analysis of the transit observations of the Hot Jupiter HD189733b. The analysis showed the presence of water vapor in the atmosphere, which is believed to be among the most abundant molecules in the atmosphere of Hot Jupiters.

In addition to the characterization of exo-planet atmospheres, the transit method can be also used to estimate the surface temperature of the exo-planets. During the occultation (the planet is completely behind its host star), a secondary drop is produced in the light curve of the parent companion because the thermal emission of the exo-planet is missing. This small dimming enables direct measurement of the planet's radiation by subtracting the stellar intensity before and during the occultation, then the surface temperature can be determined. The first thermal analyses of an extra-solar planet were carried out in parallel by two different teams (Deming et al., 2005; Charbonneau et al., 2005) using observations of the infrared Spitzer Space Telescope (Werner et al., 2004). Deming et al. (2005) reported the infrared thermal emission of HD209458b obtained from the secondary eclipse, which suggests a surface temperature of ~ 1130 K. On the other hand, Vidal-Madjar et al. (2004) presented the infrared photometric time series of the exoplanet TrES-1b, where the secondary depth corresponds (assuming black body emission) to an effective temperature of ~ 1060 K. Subsequently, several authors have reported observations of thermal emission of extra-solar planets (Demory et al., 2007; Harrington et al., 2007), and in some cases the thermal signal was even detected by ground-telescopes (de Mooij & Snellen, 2009; Sing & López-Morales, 2009). TrES-4b is a particular and interesting case of secondary eclipse analysis. Knutson et al. (2007) captured in the same observations the primary and secondary eclipses of this planet, being able to estimate the temperature of the night-side of the planet (~ 973 K).

1.6 Transit surveys

A new era in the search for exo-planets started when Charbonneau et al. (2000) announced the detection of the first transit signal of an extra-solar planet. Thus, the transit method became one of the most successful techniques to search for planets outside of the Solar System. Shortly after this discovery, the first project dedicated to detect transiting plan-

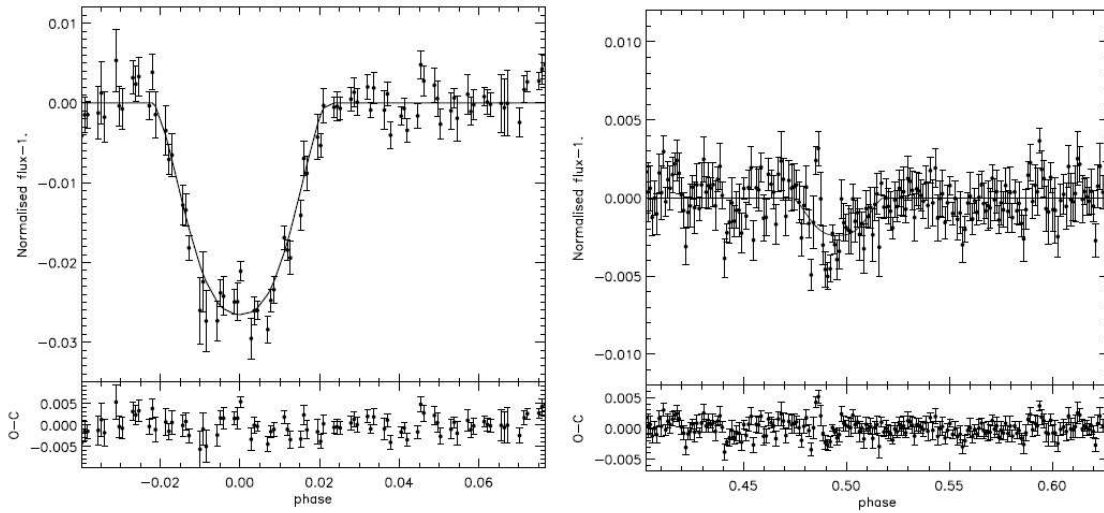


Figure 1.20: Thermal emission of the TrES-3b. The left panel shows the folded light curve of the primary eclipse, while the secondary eclipse is shown in the right panel. The best fitting model suggests that the temperature of the planet is about 2045K. The light curves correspond to photometric measurements in the K-band from the William Herschel Telescope (WHT) and the UKIRT. Source:de Mooij & Snellen (2009)

ets and low-luminosity objects arose, when the third phase of the Optical Gravitational Lensing Experiment-OGLE-III (Udalski et al., 2002a) started an extensive photometric observations of about 5×10^6 stars. Since then, more than 50 transit surveys and projects have been designed to monitor regions in the sky to search for periodic variability in the stellar flux caused by transiting planets, which have resulted in more than 300 exo-planets detected transiting their host star. Currently, transit surveys can be divided in two groups:

i) Ground-based telescopes transit surveys (GTTS). As the name suggests, these surveys are based on observations from ground-based telescopes with a wide variety in their operating characteristics. Nevertheless, they can globally be classified in wide-field and deep-field transit surveys. The wide-field surveys use arrays of several telescopes with small apertures down ~ 0.10 m. For example, the Hungarian-made Automated Telescopes-HATNet (Bakos et al., 2002, 2004) is a network that attempts to detect and characterize extra-solar planets, using six fully-automated small telescopes with a diameter of 0.11 m that cover an area in the sky of 8 square degrees. In general, the main advantages of the wide-field transit surveys are the large fields that can be observed, however due to the optical characteristics of the telescopes, their targets are limited to bright stars ($V \leq 13$ magnitude).

On the other hand, the deep-field transit surveys use observations from telescopes with larger optical diameters, so that these surveys are able to monitor stars with fainter magnitudes. An example of a deep-transit survey is the Pan-Planets project (Koppenhoefer et al., 2009). This survey uses observations from the 1.8m telescope at the Haleakala Observatories (Maui, Hawaii). The Pan-Planets survey has one of the largest Charge-Coupled

Device²² (CCD) camera in the world, which covers a field of 7 square degrees. Deep-transit surveys allow fainter objects to be monitored. Particularly, Pan-Planets is able to detect planets around star as faint as $i' = 18$ mag.

ii) Space-mission transit surveys (SMTS). SMTS are satellites or spacecrafts that orbit in different low Earth-orbits or Earth-trailing heliocentric orbits, which monitor stars from space to detect planetary transits. As for GTTS, there are a wide diversity of SMTS, from low-cost launch nanosatellites (Smith et al., 2010) to large and ambitious transit projects, as the *Kepler* mission (see below). SMTS offer an unique opportunity to study the stellar-flux variability without being effected by the Earth's atmosphere. Thereby, the light detected by SMTS provides valuable information that helps us to understand better the fields involved in the science of exo-planets, such as planet formation, orbital migration, and galactic distribution of extra-solar planets. So far, two SMTS have been launched and provided important discoveries (see below) . Moreover, the next generation space mission to detect transiting planets are being designed and are expected to be launched in the near future. For example, the PLATO project (Rauer & Catala, 2011), a candidate space mission of the European Space Agency (ESA), which aims to detect and characterize transiting extra-solar planets, including Earth-like planets in the HZ of bright stars. Plato may reveal information about the radii and masses of the planets from highly accurate photometric, as well as, atmospheric spectral characterization by combining observations with precise measurements of future spectroscopic telescopes. Table 1.1 shows a general view of most important transit-space projects designed so far. In addition, the next section describes in detail some of the most remarkable and successful transit surveys: the CoRoT, *Kepler* and SuperWASP projects.

1.6.1 CoRoT

The CONvection ROTation and planetary Transits (CoRoT) was the first space mission and spacecraft dedicated to detect transiting extra-solar planets (Aigrain et al., 2008; Barge et al., 2008a). In early stages, the project was proposed and funded by the French Space Agency CNES, and subsequently received additional financial support from ESA, Belgium, Austria, Germany, Spain and Brasil. CoRoT was originally designed as an asteroseismology²³ mission, however an exo-planet proposal was included to the original project after the announcement of the first extra-solar planet detected around a main-sequence star. CoRoT was launched on 27th of December 2006 and provided the first signal 20 days later. The first transiting planet was discovered in May 2007, when the CoRoT team reported the discovery of CoRoT-1b (Barge et al., 2008b); since then, more than 20 exoplanets were detected transiting their host stars. In addition to the contributions made to the asteroseismology and exo-planet fields, CoRoT has also provided new results to

²²A Charge-Coupled Device is a dispositive able to convert optical images into electrical signals which can be transformed in a digital signal. This dispositive are capacitors made of a photosensitive material that accumulate charge equivalent to the intensity of the incident light.

²³The asteroseismology studies the internal structure of stars by the interpretation of their frequency spectra as seismic waves.

Survey	Notes	reference
CHaracterizing ExOPlanet Satellite (CHEOPS)	(ESA)- launch 2017	Broeg et al. (2013)
CONvection, ROTation & planetary Transits (CoRoT)	France-Europe-Brazil-2013 Mission accomplished	Aigrain et al. (2008)
ExoplanetSat	USA	Smith et al. (2010)
ExtraSolar Planet Observations and Characterization (EPOCh)	NASA	Ballard et al. (2010)
Galactic Exoplanet Survey Telescope (GEST)	USA	Bennett & Rhie (2002)
<i>Kepler</i>	NASA On-going	Borucki et al. (2010)
Plato	ESA	Rauer & Catala (2011)
Transit Exoplanet Survey Satellite (TESS)	NASA in collaboration with several institutions-launch 2017	Ricker et al. (2010)
Gaia	ESA- Launch 2013/2014	de Bruijne (2012)
James Webb Space Telescope (JWST)	NASA, ESA & Canadian Space Agency (CSA)- Launch 2018	Clampin (2011)

Table 1.1: Upper rows show accomplished, on-going and future space missions aimed to search and characterize transiting planets. The two space mission presented in the lower rows will be partially dedicated to search and characterize exo-planets, since investigations on several fields in astronomy will be carried out by these missions.

different topics in astronomy, such as rotation, granulation and stellar activity, eclipsing binary systems, and stellar clusters.

The CoRoT mission is equipped with a telescope of 27 cm (2 mirrors off axis), and a wide-field camera that operates in the visible. The telescope has an extremely high performance baffle to minimize straylight on the detector. The light captured by the telescope is directed to the focal plane, which consists of four CCDs with 2048x4096 pixels arranged in a square pattern with a scale of 2.32 arcsec/pixels. Two of the CCDs are dedicated to asteroseismology, while the remaining two to the exo-planet program. The light curves of the targets are produced by on-board software using aperture photometry and subsequently down-linked to Earth every 512 s. All equipment is mounted in a spacecraft classified as mini-class satellite (630 kg), which was positioned into a polar orbit with an altitude of 896 km and a period of 6 714 s.

Initially, the mission was scheduled to operate only for 2.5 years, but the observation program was extended until 2015 after the first years of successful results. Unfortunately, in November 2012 CoRoT suffered a failure in the computer system, and no more data were transmitted from the spacecraft to Earth. On 24 June 2013, after several months of efforts to recover signal from the telescope, the retirement of the CoRoT mission was finally announced. Although the CoRoT mission has concluded, we have devoted this section to enhance the first space mission dedicated to detect transiting planets and its remarkable contributions to the exo-planets fields.

1.6.2 *Kepler*

The *Kepler* mission is so far the most exiting and successful space-mission dedicated to detect transiting exo-planets (Borucki et al., 2010). The *Kepler* mission was designed to determine the frequency of Earth-sized planets in and near the HZ of Sun-like stars by detecting periodic transits in these stars. The mission was launched on 6th March of 2009; since then, more than 150 extra-solar planets have been confirmed in 84 systems, from which 47 are multiple planet systems. Additionally, $\sim 3\,500$ transiting planets candidates have been detected, and it is expected that many of these objects will be confirmed as planets in the future by performing follow-up observations. The *Kepler* mission was also responsible for the discovery of the first Super-Earth orbiting in the HZ of a main-sequence star; this is the planet *Kepler-22b* (Borucki et al., 2012). These discoveries have shown that the presence of planets and multi planets system seems to be very common objects in the Galaxy. Moreover, the frequency of Earth-like planets in the HZ also appears to be higher than it was expected in the past. After the discovery of *Kepler-22b*, several planets have been detected orbiting in the HZ of their parent stars. Recently, Dressing & Charbonneau (2013) used data from *Kepler* to estimate the mean number of Earth-size planets in the HZ of cool stars ($T_{\text{eff}} < 4\,000$ K) to 0.15 and 0.04 planets per star for an optimistic and conservative scenarios respectively. *Kepler* has also discovered very unusual systems, such as planets orbiting a post-main-sequence red-giant star (Charpinet et al., 2011). Although *Kepler* mission is not designed to detect transiting planets around cool and low-mass stars, about 10 planets have been found orbiting M-dwarfs. Nevertheless, only one Hot Jupiter has been detected around such stars (*Kepler* – 45 b; Johnson et al. 2012), which represents the sole Jupiter-size planet with a period shorter than 10 d ($P \sim 2.4$ d) that orbits an M-dwarf. *Kepler* – 45 b has a mass of $M \approx 0.505 M_{\text{Jup}}$, a radius of $R \approx 0.96 R_{\text{Jup}}$, and is located at ~ 0.030 AU from its cool-host star ($T_{\text{eff}} \approx 3\,820$ K). Figure 1.21 shows the distribution of radii as a function of the host companion's T_{eff} of planets detected by the *Kepler* mission. In addition, the *Kepler* mission has also contributed in other fields. For example, more than 2 100 eclipsing binary systems have been detected, providing important information to put constraints on models of stellar evolution. The above represents unprecedented discoveries within the context of exo-planets, which have revolutionized our vision about this field in astronomy.

The mission is designed to constantly observe about 150 000 main-sequence stars with magnitudes brighter than $V = 14$ mag at the same region in the sky, in the direction of the constellations of Cygnus, Lyra and Draco. The *Kepler*'s spacecraft is equipped with a Schmidt telescope²⁴ of 0.95 m aperture and primary mirror of 1.4 meter diameter. The photometer consists in an array of 42 CCDs which are read every 6 seconds to avoid saturation. Each CCD has a size of 50×25 mm with 2200×1024 pixels, covering an area in the sky of 105 square degrees. The instrument offers a sensitivity capable of detecting a transit of an Earth-size around a Sun-like star with $V = 12$ magnitude

²⁴A Schmidt telescope or Schmidt camera is an optical telescope able to cover wide fields area in the sky. The design consists in a spherical primary mirror that collects the light that has previously passed through an aspherical correcting lens, which reduces the aberration effects in the images.

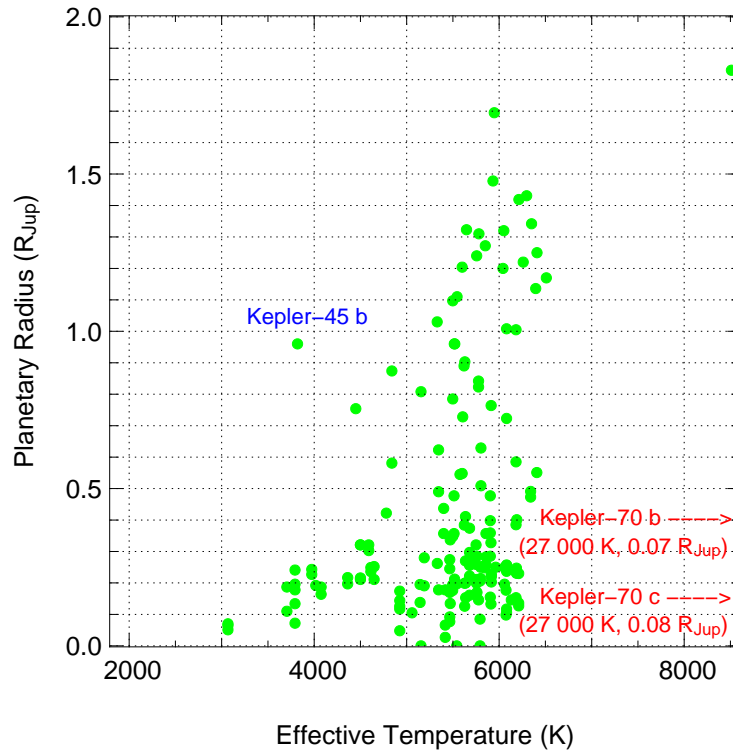


Figure 1.21: Planetary radius distribution as a function of host companion's T_{eff} of planets discovered by *Kepler*. Several planets have been detected orbiting M-dwarfs, but only one is a Hot Jupiter (*Kepler-45 b*). Other rare cases found by *Kepler* are the planets *Kepler-70 b,c*, which orbit a post-main-sequence red-giant star with a T_{eff} of 27 000 K.

in only 6.5 hours of integration. The data obtained by the instrument are stored in the spacecraft and sent to the ground every month. The data are collected in the Kepler Mission Science Operations Center and processed by the Science Processing Pipeline (Jenkins et al., 2010a,b), which includes several steps: level calibration, a photometric analysis, extraction and correction of light curves, transit detection algorithm, selection the candidates, and validation of candidates. The light curves are extracted using aperture photometry and subsequently corrected by removing signatures correlated with instrumental variables, such as pointing offsets and focus changes. Additionally outliers and discontinuities caused by pixel sensitivity changes are removed. The detection of periodic transits is carried out by the Transiting Planet Search (TPS), an algorithm that makes a time-adaptive approach that estimates the power spectrum of the observational noise as a function of time. Since *Kepler* mission is aimed to discovery Earth analogs around solar-like stars, the TPS is specifically designed to optimize the detection statistics for Earth-size planets around these stars, according to the noise properties of *Kepler*. The TPS is able to achieve super-resolution detection statistics, i.e., the TPS keeps up sensitivity to short orbital periods and transit durations. The selection of candidates is based on the detection statistic of the TPS; light curves that have maximum folded detection statistic exceeding 7.1σ are considered candidates. Then, they are subjected to further filters, such as rejections of false

positives due to obvious eclipsing binaries or any kind of correlated-noise (e.g. detector effects). Candidates that pass all the filters are sent to the follow-up teams to confirm or reject them as planets.

The orbit of *Kepler*'s spacecraft was planned to maximize the detection efficiency of periodic transits. This was accomplished by placing the spacecraft in an Earth-trailing heliocentric orbit that permits the field of view of the detector to be out of the ecliptic²⁵ plane, avoiding to be blocked periodically by the Sun or the Moon. The orbit with a period of 372.5 d allows the detector to observe continuously the same region in the sky, which is essential to obtain a high detection efficiency. An important advantage of this orbit is that the spacecraft is less affected by the torques exerted by the Earth (gravity gradients or magnetic moments), which provides a stable pointing position.

The *Kepler* mission was originally scheduled with a lifetime of 3.5 years. Due to problems to achieve the main goals of the project, in 2012 the mission was extended until 2016. However, during the last months the *Kepler* spacecraft has suffered breakdowns in two of the four reaction wheels, threatening the continuity of the mission. After several unsuccessful attempts to recover the reaction wheels, in August 2013, it was announced that *Kepler* ends its mission of hunting extra-solar planets by transit method, since the pointing precision required to detect Earth-size planets cannot longer be reached with the two remaining reaction wheels of the spacecraft. Nevertheless, NASA has proposed to readjust the mission to the current capabilities of the spacecraft, including alternative projects, which may include search of asteroids, comets and evidence of supernovas, detection of exo-planets by gravitational microlensing, or even search for habitable planets around white dwarfs²⁶(Kilic et al., 2013).

1.6.3 SuperWASP

The Wide Angle Search for Planets (SuperWASP) is an international academic network dedicated to search for extra-solar planets, which currently represents one the world leading projects in the discovery of transiting planets using ground-based telescopes (Pollacco et al., 2006). The SuperWASP consortium is formed by eight academic institutions: Cambridge University, the Instituto de Astrofisica de Canarias, the Isaac Newton Group of telescopes, Keele University, Leicester University, the Open University, Queen's University Belfast and St. Andrew's University. The project uses two robotics observatories located at the Observatorio del Roque de los Muchachos on the island of La Palma in the Canary Islands (SuperWASP-North) and at the South African Astronomical Observatory (SuperWASP-South), allowing observations in both hemispheres. The SuperWASP-North and SuperWASP-South provided the first observation in 2003 and 2005 respectively. Short after, the first discoveries were announced by Collier Cameron et al. (2007), who reported

²⁵The ecliptic is the apparent path of the Sun on the celestial sphere.

²⁶A white dwarf is a compact object with a very high density (a solar mass contained in a Earth-size object) and is composed of electron-degenerate gas, where the gravitational force is balanced by the pressure produced by this degenerate gas, avoiding a gravitational collapse. White dwarfs are one of different remnants of the final evolutionary state of the stars.

the detection of two planets with inflated radii of 1.33 and 1.26 R_{Jup} . These discoveries represented the start of a successful transit survey, which so far has confirmed more than 80 transiting planets. Most of these discoveries are Jupiter-size planets with short orbital periods ($\lesssim 10$ d), but none of them orbits an M-dwarf. Although the SuperWASP is not designed to discover planets around M-dwarfs, the null detections of Hot Jupiters corroborates the limited presence of such planets around the coolest main-sequence stars.

Both the SuperWASP-North and SuperWASP-South are an equatorial mount with 8 wide-field cameras. Each camera is equipped with a CCD that consists of 2048×2048 pixels with a size of $13.5 \mu\text{m}$. The field of view of each camera covers an area of ~ 64 square degrees with an angular scale of $13.7''/\text{pixel}$. The cameras observe extremely-wide fields, and the full 8-camera array is able to monitor up to 480 square degrees in the sky, being considerably larger than other conventional telescopes. During the first 6 months of observations, the SuperWASP-North provided more than ~ 6.7 million light curves of sources with $V \sim 7.5\text{-}15$ mag. The data collected by the cameras are automatically processed by a pipeline, which includes several steps. In a first interaction, the pipeline corrects the images removing errors caused by the detector or optical defects. Subsequently, the images are reduced by constructing and applying master bias, dark, and flat-field frames for each night of observation. The pipeline uses a variation of SExtractor algorithm (Bertin & Arnouts, 1996) to identify the positions of the objects in the field of view of the cameras. An external astronomical catalogue is used to match and identify the sources previously found by SExtractor. Aperture photometry is used to measure the stellar flux and construct the light curves of each single source that were identified in the previous steps. Finally, the detection of periodic transits is done by applying the box-fitting algorithm (see Section §4.1) to the light curves. The selection of potential candidates is divided into different steps. First, a χ^2 criterion is used to remove bad-fitting solutions, as well as, rejection of detections which show less than 2 transit points. The final stage to detect candidates is carried out by making cuts on two light curve statistics, the signal-to-red-noise ratio (S_{red} ; see §2.7) and the statistics called the antitransit -“ratio”, which is the ratio of the strongest peak in the detection and the strongest peak corresponding to a brightening. For more details about the selection of candidates see Collier Cameron et al. (2006). Candidates that pass these criteria are sent to the Geneva Planet Search group, who are in charge of carrying out spectroscopy follow-up of the best candidates.

1.6.4 M-dwarf Transit surveys

Studying and analyzing M-dwarfs provide us with important information that improves our understanding in several fields in astronomy. For example, since M-dwarfs represent the most abundant stars in the Galaxy, a suitable knowledge about their physical properties can provide strong constraints on the galactic stellar mass distribution theories. Moreover, inferring and analyzing their physical parameters is crucial to develop more accurate theoretical models that describe the formation and evolution of low-mass main-sequence stars (Birkby et al., 2012). Finally, searching for exo-planets around M-dwarfs has also gained especial attention in recent years, specially after the discovery of GJ 876d, the first Super-

Earth found around a red dwarf (Rivera et al., 2005). Nowadays, M-dwarfs are considered as one of the best targets to search for potentially habitable planets, as described below (§1.7.2).

Several projects are dedicated to study transiting planets around M-dwarfs, for example APACHE (Giacobbe et al., 2012; Sozzetti et al., 2013), Pan-Planets (Koppenhoefer et al., 2009), PTF/M-dwarfs (Law et al., 2012) and TRAPPIST²⁷ (Jehin et al., 2011). However, so far there are only two transit projects focused on finding exo-planets around cool and low-mass stars at NIR wavelengths, namely the MEarth project and the WTS. Searching for transiting planets at NIR wavelengths provides important advantages while detecting transits around M-dwarfs, since the peak of the SED of these stars falls in this spectral range.

Since the major focus of this thesis regards data obtained in the WTS, a full description of the survey is presented in Chapter §2. In addition, as the MEarth project is so far the only NIR transit survey aside from the WTS, next section (§1.6.5) is dedicated to show a general picture of the main characteristics of the MEarth survey.

1.6.5 MEarth

The MEarth project (Irwin et al., 2009; Berta et al., 2012) is a NIR transit survey that started observations in 2008 with 8 independent and identical robotic telescopes located at the Fred Lawrence Whipple Observatory on Mount Hopkins, Arizona. The project is remotely operated by a small team of scientists at the Harvard-Smithsonian Center for Astrophysics in Cambridge-Massachusetts, USA. The survey monitors individually $\sim 2\,000$ nearby (< 33 pc) M-dwarfs in the NIR and is designed to detect exo-planets that orbit in their HZ with planetary radius down to $2 R_{\oplus}$. The project attempts to provide critical information about masses, radii, and atmospheres of such planets, in an effort to characterize potentially habitable exo-planets. Each automated telescope is mounted on a German Equatorial mount²⁸ and has a primary mirror of ~ 0.4 m aperture. Each telescope has a 2048×2048 CCD with a pixel scale of 0.76 arcsec/pixel for a field of view of 26 arcmin. The telescopes observe constantly during clear nights $\sim 2\,000$ M-dwarfs from the Northern hemisphere. The telescopes are also equipped with 715-1000 nm filters, which optimize the photon-flux from M-dwarfs.

The data reduction and extraction of light curves consist of two different phases. In a first step, the images are corrected by accounting for nonlinearity in CCDs, applying a flat-field sensitivity map, and scaling dark exposures to remove part of the CCD dark current. The light curves are then constructed by performing aperture photometry on all detected sources, and subsequently a differential photometric correction for point sources is applied using an iterative, weighted, clipped fit that excludes variable stars from an

²⁷See abbreviation list to see complete names of M-dwarf transit surveys.

²⁸The German Equatorial mount is a mount for telescopes with a T-shape as its primary structure. The main advantage of such mount is the ability to follow the rotation of the sky, since one of its rotational axes is parallel to the Earth's rotation axis, allowing the telescope to follow and continuously observe objects on the celestial sphere.

external catalogue that is used as a comparison sample. A typical MEarth light curve has about 1 000 epochs with 20 minutes cadence, corresponding to one observational season. A full description of the data reduction process can be found in Irwin et al. (2007) and Berta et al. (2012).

The data from the MEarth survey are affected by several systematics produced by the weather and atmospheric conditions, instruments noise, and effects generated during the image reduction process. These issues led to develop the Method to Include Starspots and Systematics in the Marginalized Probability of a Lone Eclipse (MISS MarPLE), an algorithm for detecting periodic transits. MISS MarPLE differs considerably from the traditional transit detection algorithms (e.g. the BLS), which commonly fold a light curve in presence of any stellar flux variation that can be produced by instrumental effects or intrinsic stellar variability. Usually, transit surveys that employ algorithms based on BLS, additionally need to use algorithms that correct for both systematics and stellar variability. In contrast, MISS MarPLE can find transiting planets in irregularly spaced light curves, and simultaneously models systematics, variability and the photometry for each observational night. The transit statistic provided by MISS MarPLE, used to identify transiting planet candidates, is given by $D/\sigma > n$, where D is the maximum probability of a random single eclipse transit depth and σ is the width of the Gaussian probability distribution. The threshold fixed to consider a detection as a transit candidate is of $D > 7 - 8\sigma$. Note that MISS MarPLE was designed and optimized based on the observing campaign and instrumental characteristics, which present large gaps and inconstant systematics. For well-sampled and well-behaved light curves, the MISS MarPLE should provide same results as other transit detection algorithms; however for the particular characteristics of MEarth survey, the MISS MarPLE performs better results than BLS (Berta et al., 2012). For more details about the statistic transit detection and MISS MarPLE of the MEarth project, we also refer to Berta et al. (2012).

In 2009, the MEarth team announced the discovery of GJ1214 b (Charbonneau et al., 2009), the first Super-Earth that orbits an M-dwarf and detected using data from the survey. GJ1214 b has a mass of $6.55 M_{\oplus}$, a radius of $2.68 R_{\oplus}$, and an orbital period of 1.58 d. On the other hand, Irwin et al. (2010) also used data from the MEarth survey to detect an M-dwarf/brown-dwarf system, where the transiting companion has a mass of $33.7 M_{\text{Jup}}$ and orbital period of 2.89 d. So far, no Jupiter-size planets have been discovered by the MEarth project. In addition to the contribution to the exo-planets field, the project has also provided relevant information related to physical parameters of low-mass stars by studying rare M-dwarf eclipsing binary systems, such as very short and long-period eclipsing binaries, and brown dwarfs in multiple systems (Irwin et al., 2011b, 2010). Other studies that have been carried out with the survey is the analysis of starspots to measure the rotational velocity of M-dwarfs, which can provide relevant information about how angular momentum in low-mass stars evolves with age (Irwin et al., 2011a). Because of the successful first years of observations, the MEarth survey is planning to incorporate on the near future eight additional telescopes in the Southern hemisphere.

1.7 M-dwarfs

Low-mass main-sequence stars of spectral type M, also known as M-dwarfs or red-dwarfs, are the most abundant stars in the Galaxy, representing about 75 % of the total stellar population and half of the total stellar mass of the Galaxy (Scalo et al., 2007). M-dwarfs are commonly referred in the literature as dM or MV (where V represents the luminosity class corresponding to main-sequence stars), to differentiate them from red giant and supergiant stars²⁹. M-dwarfs have the lowest masses among main-sequence stars ranging roughly $0.075\text{-}0.6 M_{\odot}$ (Baraffe & Chabrier, 1996), implying also very low luminosities $\sim 10^{-4}\text{-}10^{-1} L_{\odot}$. These low luminosities are also translated into low T_{eff} that characterizes these objects, $\sim 1\ 850\text{-}3\ 800$ K (see Figure 1.22). The low temperatures of these faint stars means that the stellar emission peaks at infrared wavelengths, and also the stellar atmospheres can support neutral atoms and molecules. Thus a typical M-dwarf spectrum is dominated by molecular bands, for example heavy metal oxides like TiO and VO in the optical, and steam and carbon monoxide in the infrared (Tarter et al., 2007). These large range of masses, luminosities and T_{eff} result in a wide spectral-type classification, ranging from M0 for the most massive stars to M9 for the least massive. Note that the values provided above are only approximate ranges, since precise values of physical parameter of M-dwarfs are still under discussion. The general lack of observations of M-dwarfs makes it difficult to calibrate existing theoretical models that describe their physical properties and evolution. Nevertheless, this scenario is changing, since there are currently several projects dedicated to particularly study low-mass main-sequence stars. For instance, ongoing M-dwarf transit surveys (see §1.6.4) are providing information about the frequency of planets around these stars. These surveys also permit the analysis of peculiar stellar systems, such as M-dwarf-M-dwarf eclipsing binary systems, from which relevant information about the physical properties of the stellar companions can be determined (see Chapter §6).

Another particular characteristic of M-dwarfs is their long lifetime as main-sequence stars. Unlike massive stars that rapidly transform the Hydrogen in their nuclei into helium, M-dwarfs remain stable for longer periods due to their low masses and nuclear temperatures, which slow down the rate of hydrogen fusion. The main-sequence lifetime of M-dwarfs can last from 50 Gyr for the most massive stars to several trillion years for the ones with latest spectral-type (M9) (Scalo et al., 2007), i.e, no M-dwarf in the Milky Way is predicted to have evolved away from the main-sequence. As a consequence, M-dwarfs exhibit nearly constant luminosities during very long periods, which is a crucial factor for the habitability of exo-planets around these stars (see Section §1.7.2).

²⁹Red giants are low or intermediate mass stars ($\sim 0.3\text{-}8 M_{\odot}$) in a late phase of stellar evolution. These objects are post main-sequence stars that have exhausted the Hydrogen fusion fuel in their cores. They are characterized by either burning Hydrogen in their outer layers, surrounding a degenerate Helium core, or fusing Helium into carbon in their cores. The luminosity of red giants can be more than $\sim 10\ 000$ times the luminosity on the main-sequence. On the other hand, red supergiants are among the most massive ($8\text{-}12 M_{\odot}$) and luminous ($10^4\text{-}10^6 L_{\odot}$) stars. Such supergiants are massive enough to experience core burning of Helium and other heavier elements in a relative short time, so the expected life-time of these stars is only between $10^5\text{-}10^7$ yr before becoming supernova.

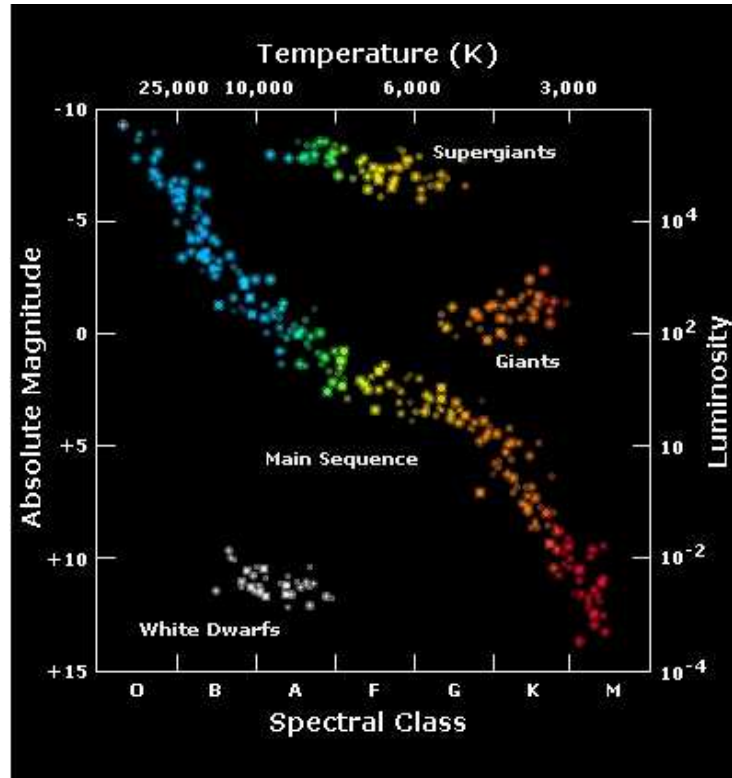


Figure 1.22: Hertzsprung-Russell diagram. M-dwarfs are located at the bottom-right corner of the diagram, being the main-sequence stars with lower masses and luminosities. (Credits of the image: ESA)

Most M-dwarfs transport energy from their core to the surface by convection, as energy transfer by radiation is less significant. According to the solar dynamo theory, this vigorous convective activity in the interior of M-dwarfs generates strong magnetic fields, resulting in strong surface stellar activity characterized by energetic flares, coronal mass ejections, strong coronal X-rays, and enhanced chromospheric UV emission (Osten et al., 2005). The magnetic fields in M-dwarfs can also be generated by stellar rotation. It has thus been argued that stellar activity is related to age by rotational braking (Skumanich, 1972), being stronger in younger stars, particularly thus with ages less than 1 Gyr. The high stellar activity of M-dwarfs is one of the most important constraints on the habitability of planets orbiting around them (see §1.7.2).

1.7.1 Planet formation around M-dwarfs

Planet formation around low-mass stars has been largely discussed for several years. Particularly, planet formation around M-dwarfs has caused a controversy due to the lack of observations of such stars. The recent discoveries of exo-planets around these stars have led to reconsider theoretical models of planet formation around M-dwarfs. Moreover, recent observations of young low-mass stars (1-2 Myr) from ground-based and space-based IR surveys have shown that protoplanetary disks surrounding such stars are as common

as they are around earlier spectral-type stars; therefore, planetesimal formation may thus occur as often as around Sun-like stars (Pascucci et al., 2011). This suggests that M-dwarfs are also suitable to host planets (Lada et al., 2006).

As a first requirement, the planetary disks around low-mass stars must be massive enough to eventually lead to the formation of a planet. Andrews & Williams (2005) reported observations of disks around young M-dwarfs, revealing significant massive disks of about a few percent of the stellar mass, being sufficient material to form planets. If the first condition is satisfied, planet formation theory says that rocky planets and gas-giant planets must be formed in different regions of the protoplanetary disk, so that the formation must follow different process. Different models have been proposed to explain the formation of both rocky and giant planets around M-dwarfs. For example, the formation of gas-giant planets have been addressed via the CAGC model and a correlation between the metallicity of M-dwarfs and the number of giant planets detected around these stars (Laughlin et al., 2004). These models predict that stars with higher metallicity should host more planets than those with lower metallicity, and similarly that the planet formation rate should be higher in more massive stars. This implies that M-dwarfs should therefore have less Jupiter-mass planets around them than Sun-like stars. Nevertheless, these models have been challenged because of the long time-scale required to form a Jupiter-mass planet (~ 10 Myr), which is longer than the disk lifetime. This issue has led to the development of alternative models that explain the formation of giant planets in a shorter time-scales. For example, Boss (2006a) have developed three-dimensional, radiative, gravitational hydrodynamical models that describe the giant planet formation around M-dwarfs in outer regions of the disk in a relative short time by means the disk instability model.

Due to the dearth of planets detected around these stars, the formation of Earth-like planets or Super-Earths around M-dwarfs has not been investigated in detail. However, several models have been proposed to explain the formation of these planets around low-mass stars. For example, Boss (2006b) presented a model that predicts the formation of Super-Earths via a disk instability mechanism. In this model, a Super-Earth is formed from the photo-evaporation of the gaseous envelopes of an earlier gas-giant planet affected by an energetic external source (e.g. a nearby massive star). Thus, the model predicts that M-dwarfs formed in regions of massive-star formation should hold Super-Earths, while giant planets must be formed around M-dwarfs that are born in regions of low-mass star formation. Other models scale the protoplanetary disk of an M-dwarf with the one of a Sun-like star, resulting in the formation of small and dry planets (Raymond et al., 2007). Other models predict that protoplanetary disks of M-dwarfs may be independent of host star mass and a Super-Earth could be formed in a low-mass star of $\sim 0.1 M_{\odot}$ (Montgomery & Laughlin, 2009).

1.7.2 Habitability and development of life on planets around M-dwarfs

The detection of the first extra-solar planets (Wolszczan & Frail, 1992) around the pulsar PSR1257+12 and the subsequent discoveries of the first Hot Jupiter and Earth-like exoplanets orbiting their host main-sequence star (Mayor & Queloz, 1995; Rivera et al., 2005) led to new perspectives in the search of extra-terrestrial life. Some first attempts have been made to understand the origin and evolution of life on Earth and how common and frequent life is in our Solar System, or even in the Galaxy.

As a first step to answer these questions, a general concept of life has to be provided. But, defining life has been theme of discussion in the human history, and providing a definition of life in a galactic scale may lead to endless philosophic and scientific discussions. Certainly, we cannot expect that other forms of life in the Universe are also ruled by the same characteristics as those on Earth. Based on this assumption, some theories have been proposed to describe other forms of life beyond Earth. For example, the theory presented by Feinberg et al. (1980), in which is proposed a form of life based on silicon chemistry. However, so far we have not detected life outside Earth, so presenting any different scheme of life is pure speculation. Hence we start from the notion of life that we know (i.e. life on Earth), extrapolating this knowledge to other regions in the Milky Way. We know that all forms of life on Earth are based on a group of 6 chemical elements: carbon, hydrogen, nitrogen, oxygen, phosphorus, and sulfur (commonly named with the acronym CHONPS), which are required for biochemical functionalities (Gargaud et al., 2011). These elements are the bases of any organic molecule present in all forms of life on Earth, such as nucleic acids, proteins and lipids. Moreover, the chemical compositions of the DNA³⁰ consists of chains of these elements (Chakrabarti et al., 2012). Carbon represents the most abundant element in biological molecules. This is mostly because it has the property of forming stable covalent bonds, resulting in an enormous variety of carbon-based molecules (usually called organic molecules).

Assuming that life in other regions of the Galaxy is also based on the same elements and bio-molecules, we know from Earth that liquid water plays an important role in most chemical reactions of such molecules³¹. For instance, liquid water has an active role in bio-molecular recognitions, such as the protein recognition of specific DNA sequences. Because of this, we may argue that liquid water is a basic requirement for life, at least from a biochemical point of view, therefore we typically assume that liquid water is an essential condition for the presence of life. More detailed information about the importance of liquid water for life can be found in Scalo et al. (2007).

So far, we have mentioned the biochemical characteristics of life on Earth, which are used as a reference to search for life in other regions of the Galaxy. Liquid water was also designed as an essential requirement for the presence of life. The next step in the search for life is to designate a place that may provide the minimum conditions to host life.

³⁰The Deoxyribonucleic acid or DNA is a molecule that encodes genetic information used in the development and functioning of all known living organisms.

³¹The water molecule dipole usually acts as solvent and facilitates the chemical reactions of molecules

Although several authors have suggested small bodies in the Solar System (e.g. asteroids or comets) as possible environments to host life (Gibson et al., 2010), we only consider planets and their moons (either from our Solar System or external planetary systems) as bodies that can potentially provide such conditions. This leads to the concept of habitability³². Several definitions and generalizations of habitability have been suggested over the years, including various thermal, geophysical, geochemical, and astrophysical conditions that a planet must have to support life (Dole, 1964; Stamenkovic & Breuer, 2012). Nevertheless, since liquid water is indispensable for any chemical interaction of bio-molecules, we typically consider a concept of habitability that includes the existence of liquid water on planets. From this condition, we introduce the concept of HZ of a planet or exo-planet. Like habitability, the concept of the HZ has been extensively discussed for many years, leading to several definitions of the HZ (Dole, 1964; Heath et al., 1999). Nevertheless, we review only situations in which the temperature of the object is primarily controlled by the stellar insolation. This definition was proposed by Kasting et al. (1993), which describes the HZ around main-sequence stars as the region around them, where the stellar radiation is sufficient to provide the energy needed for a rocky planet with atmosphere to have liquid water on its surface. The equation that describes the limits of the HZ is:

$$0.95 \text{ AU} \leq \frac{D}{\sqrt{L_*/L_\odot}} \leq 1.37 \text{ AU}, \quad (1.24)$$

where D is the orbital distance of the planet and L_* is the luminosity of the host star. Using this equation we can set the limits of the HZ of a Sun-like star from 0.95 to 1.37 AU, which varies in size for other stellar spectral type according to their luminosity. Figure 1.23 shows a representation of the HZ as derived from Eq.1.24, in which the HZs of the M-dwarf Gliese 581³³ and Sun are compared. The limits of the HZ are estimated by two different criteria. The inner edge was determined by the production of hydrogen in the middle atmosphere due to H_2O photolysis, resulting in the ejection of H to the space, so that the planet's surface eventually dries. The outer edge is estimated by the amount of CO_2 in the atmosphere of the planet. CO_2 can be produced by processes like weathering³⁴, which can control the surface temperature of the planets by producing a green house effect. Thus, the outer edge occurs at the stellar luminosity in which CO_2 condenses in the atmosphere, making the weathering feedback insignificant.

Although, we have described the basis for the habitability on planets around main-sequence stars, there is another factor that has to be taken into account. Due to stel-

³²The habitability of moons or exo-moons are beyond of the scope of this thesis, so from now the concept of habitability will be referred only to planets in our Solar System or exo-planets. However, a substantial information about habitability of exo-moon can be found in Kaltenecker (2010).

³³The M-dwarf Gliese 581 has a multiple planetary system that has been extensively discussed, since the number of planets around this star is still a polemic topic. So far, four planets have been confirmed; however there two more candidates that are questionable, from which one orbits within the HZ of the star. Nevertheless, Gliese 581 hosts the first detected potential habitable planet Gliese 581c (Udry et al., 2007; Selsis et al., 2007).

³⁴Weathering is the dissociation of minerals by chemical reactions through direct contact with the atmosphere.

lar evolution, the luminosity of stars vary as a function of time, i.e., the stellar luminosity increases as stars evolve, so the position of the HZ suffers an outward migration. Kasting et al. (1993) defined the concept of continuous habitable zone (CHZ) as the region around main-sequence stars, in which a planet can support liquid water on its surface before the star becomes a red giant. For a Sun-like star the width of the CHZ in a time-scale of 4.6 Gyr extends from at least 0.95 to 1.15 AU. The CHZ around earlier and more massive stars evolves faster and last less than 3 Gyr, which is the earliest record of life on Earth. On the other hand, less massive stars (later than mid-K) evolve more slowly, so that the HZs around them are wider, i.e., last longer than in other earlier main-sequence stars, therefore emergence and evolution of life is more likely in planets that orbit in the HZ of these stars.

The last statement makes red and cool main-sequence stars attractive hosts to search for habitable extra-solar planets. Particularly, M-dwarfs are currently considered promising candidates to host habitable worlds. Moreover, in Section §1.7.1 we mentioned that protoplanetary disks around these stars are as common as around Sun-like stars. This fact might lead to the formation of Earth-like planets around M-dwarfs. However, due to the peculiar physical characteristics of M-dwarfs, the habitability of planets around such stars have been harshly questioned (Dole, 1964). For example, although the CHZs of a typical M-dwarfs may last up to 100 Gyr, the edges of the HZ vary from 0.02 to 0.2 AU, so any planet orbiting in this region would become tidally locked (i.e, it would continuously keep the same side to the star), which may lead to the evaporation of the planet atmosphere on the illuminated side and to a freeze-out on the dark side. The high stellar activity of M-dwarfs is another argument against the habitability, since powerful flares or a high amount of X-ray or UV radiation could kill organisms on the surface of these planets. Also stellar winds from M-dwarfs could lead to a partial or full erosion of the planetary atmosphere, which is crucial for the planet habitability.

Despite the peculiar physical properties of M-dwarfs that make controversial the habitability of planets around these stars, several schemes have been proposed to solve the main problems of habitability around M-dwarfs. For instance, Haberle et al. (1996) propose a simple energy-balance model, which predicts atmospheric heat transport may prevent freeze-out on the dark side, which can also help to avoid the interaction of high energy radiation with living organisms. Other authors have suggested that a thick enough atmosphere or the presence of a magnetic field can prevent the atmospheric mass loss of planets by the interaction with stellar winds (Zendejas et al., 2010). Moreover, the fact that M-dwarfs represent the largest population of stars in the Galaxy provides statistically better perspectives to also find planetary systems. In addition, due to their low mass, the CHZs of M-dwarfs can last up to 100 Gyr, which may allow life to emerge and evolve even to complex organism. Furthermore, planets in the HZ of these stars orbit very close to them, and the most successful techniques to detect exo-planets are more sensitive to rocky planets with shorter periods (i.e., those that orbit close to their parent star). At the present time, several projects are dedicated to search for planets around M-dwarfs (see §1.6.4). So far, several planets have been detected orbiting such stars, but only few of them are Earth-like planets or Super-Earths. Nevertheless, recent discoveries of the *Kepler*

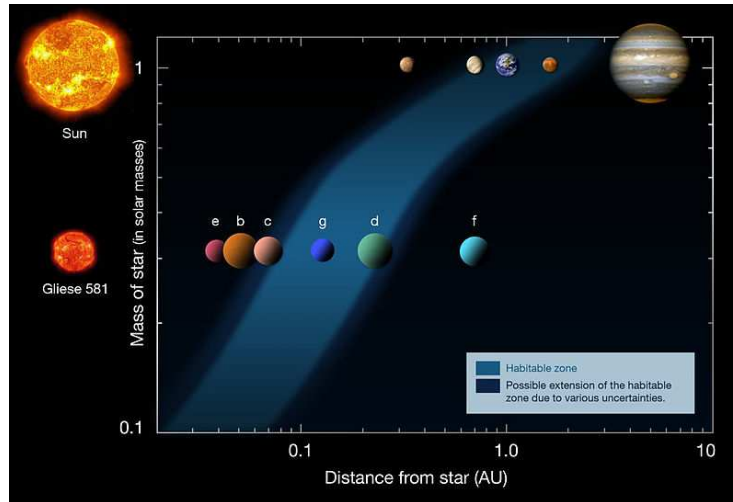


Figure 1.23: Representation of the HZ of the M-dwarf Gliese 581 and Sun as proposed by Kasting et al. (1993). In contrast with more massive stars, the HZ of M-dwarfs are much closer to them due to the low luminosity, which can vary from 0.02 to 0.2 AU. The image also shows the controversial (see main text) multiple planetary system of Gliese 581, hosting the first detected potential habitable planet (Udry et al., 2007; Selsis et al., 2007). Credits: ESO

mission and other ongoing projects dedicated to search for planets around M-dwarfs are revealing the presence of rocky planets around them. For example, Bonfils et al. (2013b) recently announced the first Super-Earth (GJ 163c) orbiting in the HZ of the M-dwarf GJ 163. In June 2013, another team (Anglada-Escudé et al., 2013) published the detection of a dynamically-packed planetary system around the M-dwarf GJ 667C, from which at least 3 planets are Super-Earths located in the HZ of the host star.

1.8 Structure of this Thesis

The detections of transiting planets using data from the WTS represents the core of this work. In the following, we explore the potential of the survey through a photometric technique that has shown special advantages when applied to crowded fields³⁵, the so-called difference imaging (DI) technique (see Chapter §3). We construct light curves using this technique and analyze the capabilities of the DI-light curves by comparing the photometric precision of light curves obtained with the aperture photometry technique (AP), which is included in the standard data reduction pipeline of the WTS (see Section §2.2). We search for transiting planets around stars with $J \leq 18$ magnitude using an algorithm based on the box-fitting least square algorithm (BLS), which includes an implementation that fits a trapezoid to the folded light curve (see Section §4.1). Furthermore, we consider and optimize a set of selection criteria to identify transiting planets candidates. The selection criteria include a new parameter provided by the detection algorithm that has the ability

³⁵Regions in the galaxies with high density stellar population

of automatically exclude potential eclipsing binary systems, the V -shape parameter (see Section §4.2). We visually inspect objects that pass the optimized selection criteria and reject detections that are clearly false-positives³⁶. In addition, a detailed analysis is carried out on objects that pass the visual inspection, which provides physical parameters of planetary and stellar companions. This analysis allows us to classify the best detections as planets or eclipsing binary candidates. The optimization of selection criteria and selection of candidates are independently carried out in two different sets, one for F-G-K stars, and another for M-dwarfs. This study allow us to set an upper limit on the occurrence rate of short-period giant planets around M-dwarfs from the WTS with $J \leq 18$. In addition, we investigate other advantages of the WTS DI-light curves, such as the search of M-dwarfs/M-dwarfs and extremely-short-period eclipsing binary systems.

The structure of this thesis follows the next outline:

In the following chapter, we describe the WTS and summarize the image reduction pipeline and the description of the AP technique. Chapter §3 gives a review of the WTS DI light curves, including a description of the DI method and the procedure of the light curve extraction. A quantitative comparison between the photometric precision of light curves obtained by the AP and DI techniques is also presented in this chapter. Chapter §4 presents our transit detection algorithm and its implementations (e.g., the V -shape parameter). In Chapter §5, we present our selection criteria used to detect planet candidates with the WTS light curves and the process to optimize the selection criteria. In Chapter §5 we also present the candidates that pass our optimized selection criteria for F-G-K stars and provide a detailed physical characterization of the best objects and their host stars. Chapter §6 presents the M-dwarf sample of the WTS. In Chapter §6, we also show the candidates around M-dwarfs that pass the optimize selection criteria. In addition, we carry out a sensitivity analysis of the WTS for short-period giant planets around M-dwarfs. Other applications of the WTS DI light curves, such as the detection of ultra-short-period and detached M-dwarf eclipsing binaries are shown in Chapter §7. We summarize our results in Chapter §8.

³⁶See §1.5.7

Chapter 2

The Wide Field Camera Transit Survey

The Wide Field Camera Transit Survey (WTS) is a pioneer program aimed to search for extra-solar planets in the near-infrared (NIR), and particularly designed to discover planets around M-dwarfs. The survey operates since August 2007 with observations from the United Kingdom Infrared Telescope (UKIRT). The UKIRT is equipped with the Wide Field Camera (WFCam; see below) and has a primary mirror of 3.8 m in diameter, being one of the largest ground-based telescope dedicated to exclusively observe in the NIR with a large field of view ~ 1.6 square degrees. The UKIRT is located on the top of the volcano Mauna Kea in Hawaii, and together with the James Clerk Maxwell Telescope (JCMT), is operated by the Joint Astronomy Center. Mauna Kea stands 4 207 m above sea level and the telescope is placed just few meters below this altitude, so observations are less affected by the water vapor of the atmosphere. Furthermore, darkness and weather contribute to provide one of the most suitable observing conditions in the northern hemisphere. Nevertheless, since the transit method is based on relative photometry, the survey can be performed in poor weather conditions, hence WTS is conducted as a back-up project, operating when the observing conditions are not suitable (seeing > 1 arcsec) for the main program of the UKIRT Infrared Deep Sky Survey (UKIDSS). The survey was originally assigned about 200 nights, observing four fields that were selected seasonally (RA = 03, 07, 17 and 19h) during a year, thereby the WTS provides a continuous observations campaign. The fields were chosen to be close to the Galactic plane to guarantee a suitable compromise between high stellar density and giant contamination. The selected fields also maintain the reddening on acceptable levels, which have in average a color-excess of $E(B-V) < 0.13$. In addition, the four fields were selected to contain a high number of M-dwarfs. In Table 2.1 we summarize the characteristics of the four fields. However, this work is only dedicated to study the RA = 19h field, which has been observed until May 2011 with about 1145 epochs and contains $\sim 475\,000$ sources of which $\sim 113\,000$ have magnitudes of $J \leq 18$. Although the WFCam provides data in 5 different passband (see below), all observations for the WTS are done in the J -band ($\lambda_{\text{eff}} \approx 1250$ nm), since the survey was originally designed to find planets around M-dwarfs and this passband covers the SED of such stars in a reasonable way. Observing in this wavelength provides further advantages, for example minimizing

the effects caused by starspots, which can induce variability (Goulding et al., 2013).

Field	RA (h m s)	Dec ($^{\circ}$ min sec)	Galactic l (deg)	Galactic b (deg)	No. of Epochs	Objects ($J < 18$)
19	19 34 48	+36 01 45.6	70.03	+07.83	1145	102428
17	17 15 00	+03 02 57.6	24.94	+23.11	709	39879
07	07 05 24	+12 03 45.6	202.89	+08.91	626	56070
03	03 39 00	+39 00 55.2	154.99	-12.99	392	36306

Table 2.1: Main characteristics of the fields observed in the WTS. Columns 2 and 3 show the coordinates of the center of the fields.

The WTS has provided relevant results, for instance the discovery of two uncommon Hot Jupiters, WTS1-b (Cappetta et al., 2012) and WTS2-b (Birkby et al., 2013b). WTS1-b is the first planet detected in the WTS, which orbits an early-F star with an orbital period of 3.35 d and has a planetary mass of $4.01 M_{\text{Jup}}$. The planetary radius is about $1.49 R_{\text{Jup}}$, which is one of the largest radii among Hot-Jupiters with masses between 3 and $5 M_{\text{Jup}}$. On the other hand, WTS2-b has the peculiarity of orbiting very close to its tidal destruction radius at a distance of ~ 0.02 AU, with a period of 1.02 d. The host companion is a K2V star, which is located about 1 kpc away. The mass and radius of WTS2-b are $1.12 M_{\text{Jup}}$ and $1.30 R_{\text{Jup}}$, respectively.

The WTS has also provided discoveries within the context of eclipsing binaries. For example, Nefs et al. (2012) announced the discovery of four ultra-short-period M-dwarf eclipsing binary systems, with periods shorter than 0.18 d, being the main-sequence binaries with shortest period reported so far. On the other hand, Birkby et al. (2012) reported a sample of 16 detached M-dwarf/M-dwarf eclipsing binaries, which nowadays provide the most accurate and model-independent method to measure fundamental physical parameters of these stars. The WTS has also provided studies in the stellar framework; for example, the analysis of variability on M-dwarfs due to spots (Goulding et al., 2012), and the study of white dwarfs (Steele et al., 2013). In the next section we will describe the characteristics of the WFCam.

2.1 The Wide Field Camera

The WFCam is a NIR camera mounted at the UKIRT (Casali et al., 2007), which has been designed to cover large fields in the sky and carry out large-scale surveys. In a clear night, the WFCam can collect upto 160GB in data, which are subjected to an on-line processing at the telescope, providing near real time data quality assessment and initial science results. Subsequently, the data are transferred to the Cambridge Astronomical Survey Unit (CASU) at Cambridge UK for a full reduction process (see below). All processed data are sent to the WFCam Science Archive at the The Wide Field Astronomy Unit (WFAU) in Edinburgh.

The WFCam consists of 4 Rockwell Hawaii-II arrays with 2048×2048 pixels in each panel that cover a field of view of ~ 0.19 square degrees with a resolution of 0.4 arcsec/pixels. The 4 detectors are distributed geometrically at the corners of a square with an autoguider

(see description below) located at the center of the frame (see Figures 2.1(a) and 2.1(b)). The separation between the detectors is of 12.83 arcmin, which corresponds to 94 % of the detector width. This array is usually called *pawprint*. Since the dimension and separation of the detectors have approximately the same size (~ 13 arcmin), a uniform target field can be achieved by tiling together independent pointed observations. A complete observation pattern of the WTS consists of 8 tailed *pawprints* (a-h), covering an area in the sky of ~ 1.6 square degrees (see Figure 2.2). Each *pawprint* is built up from a nine-point jitter pattern of 10s. An entire field is completed in about 15 min (8 *pawprints* \times 9-point jitter pattern \times 10sec + overheads); therefore, the WTS light curves have an average cadence of four data points per hour. The WFCam is also equipped with an autoguider, which consists in an optical CCD with pixel scale of 0.251 arcsec/pixel. The autoguider is located in the center of the focal plane and works by keeping fixed the center of a guide-star image in the intersection of four pixels from a configuration of 12×12 pixel in the CCD. (see Figure 2.1(b)). The autoguider's filter bandwidth is in the range of 600 to 1000nm, which permits the tracking of guide-stars with visual magnitudes between $V = 7-18$ mag.

The WFCam operates in the NIR wavelength range 830-2370nm, providing images in 5 different bands *ZYJHK*. The filters *JHK* were specifically developed to Mauna Kea Observatories specifications and are characterized in Hewett et al. (2006). The remaining two filters *ZY* were introduced by Warren & Hewett (2002) and subsequently characterized in (Hewett et al., 2006). Particularly, the *Z* filter has a similar effective wavelength to the Sloan Digital Sky Survey (SDSS) *z* filter. Table 2.2 summarize the main characteristics of the five passbands and Figure 2.3 shows the profile of broad-band filters.

Filter	λ_{eff} (nm)	Band width (nm)
<i>Z</i>	881.7	95
<i>Y</i>	1030.5	100
<i>J</i>	1248.3	160
<i>H</i>	1631.3	290
<i>K</i>	2201.0	340

Table 2.2: *ZYJHK* NIR filters of the WFCam.

2.2 2D-image reduction pipeline

Due to the large amount of data collected by the WTS, a pipeline to process the images automatically is required. The raw *J*-band images from the WTS are reduced by the image reduction pipeline of the Cambridge Astronomical Survey Unit¹ (CASU), which is used to process all images from the WFCam. The image reduction pipeline is based on the work

¹<http://casu.ast.cam.ac.uk/surveys-projets/wfcam>

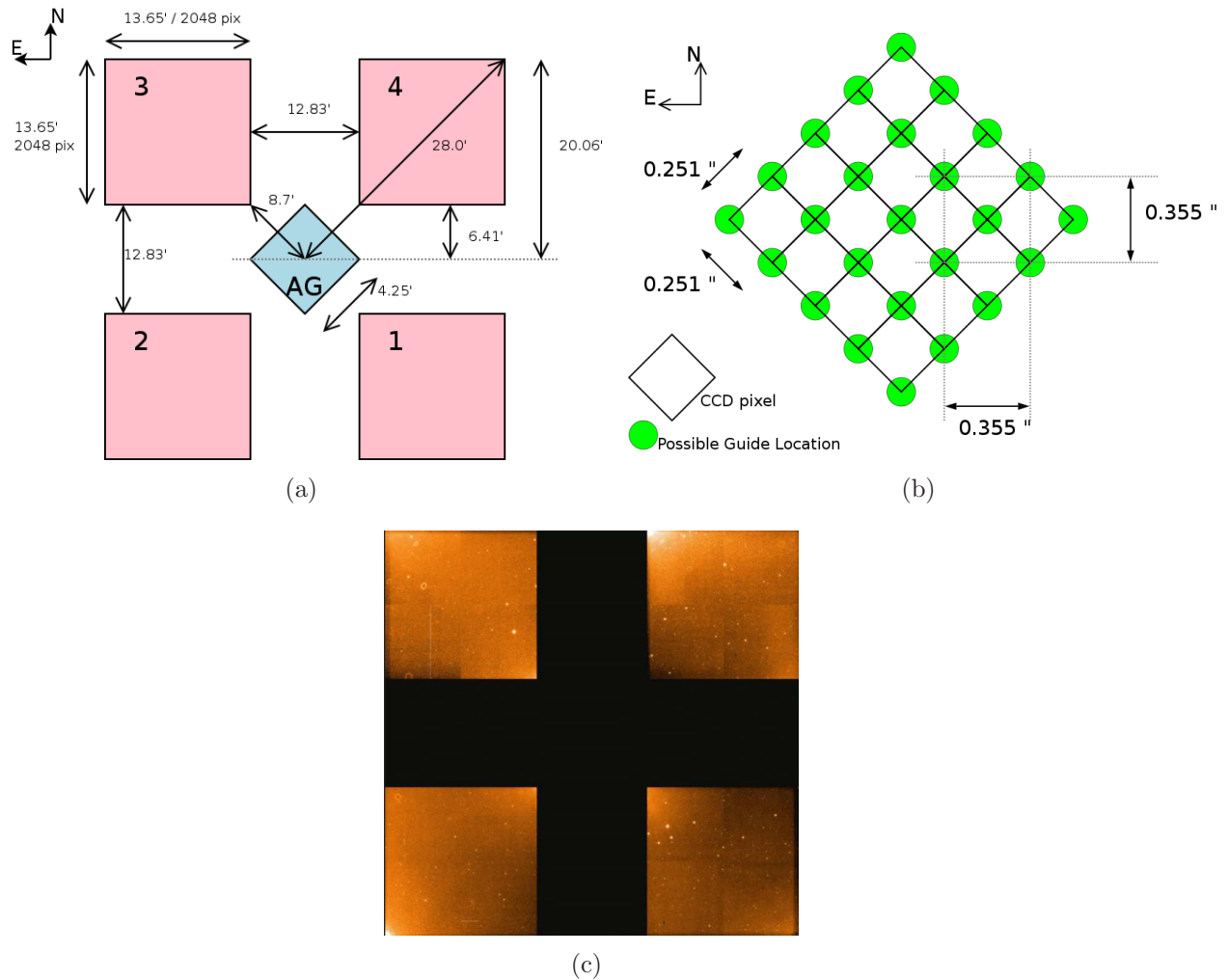


Figure 2.1: a) Focal plane layout of the WFCam. b) Configuration of the autoguider of the WFCam. c) Typical image from WFCam. Four panels are located geometrically at the corners of a square covering together a field of view of ~ 0.19 squares degrees. Source.- http://www.jach.hawaii.edu/UKIRT/instruments/wfcam/user_guide/description.html

developed by Irwin (1985) and later modified and adapted to the Isaac Newton Telescope (INT) Wide Field Survey (WFS) (Irwin & Lewis, 2001), and subsequently to the Monitor project (Irwin et al., 2007). In a first stage, all images from the WFCam are transformed into multi-extension FITS files, which contain the data from the detectors of each pawprint. Catalogues and light curves produced at later stages are also collected in binary tables. The pipeline includes the following correction steps: De-biasing and trimming, non-linearity correction, bad pixel replacement, flat-fielding, defringing and sky subtraction. The last step eliminates spatial variations in the sky background while keeping its mean level. The background level is estimated by carrying out a robust σ clipped median for each bin in a grid of 64×64 pixels. The sky background map is filtered by 2D bilinear and median filters to prevent a shift in the sky level in regions dominated by bright stars. Finally, the

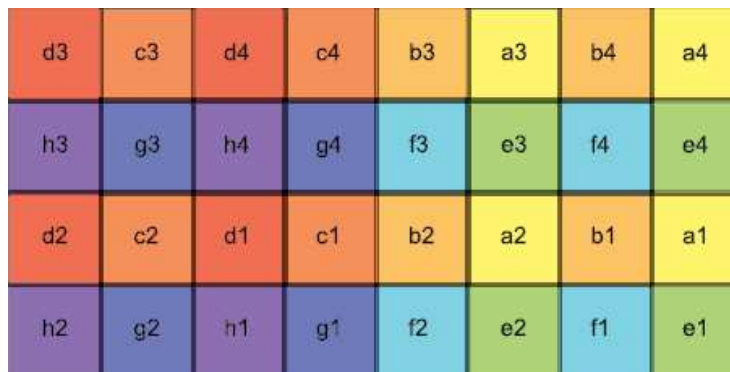


Figure 2.2: Configuration of 8 tailed pawprints (a-h) obtained with WFCam. This uniform observation pattern covers an area in the sky of 1.6 square degrees. Source: Kovács et al. (2013)

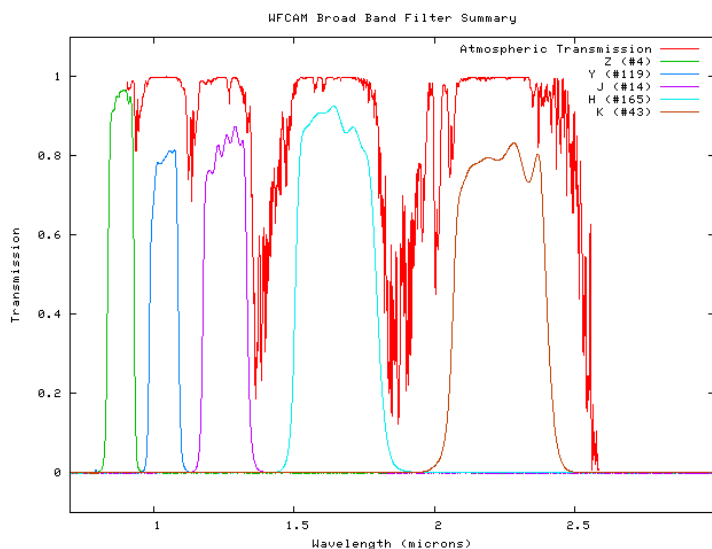


Figure 2.3: Profile of the transmission curves of the *ZYJHK* broad-band filters. Source: http://www.jach.hawaii.edu/UKIRT/instruments/wfcam/user_guide/description.html

9 individual exposure (see §2.1) are stacked to construct the final 90s exposure.

2.3 Astrometry and Photometry

Astrometry and photometry are performed for each detector in the 8 *pawprints* of the WTS and calibrated using bright stars in the field-of-view from the 2-Micron All-Sky Survey (2MASS) catalog (Kleinmann et al., 1994). An entire description of the photometric calibration can be found in Hodgkin et al. (2009). Particularly, the astrometric calibration plays an important role in the DI technique, since a precise alignment of data frames is crucial to success with this method. The astrometry is described by a cubic radial distortion factor (zenithal polynomial transformation) and a six coefficient linear transfor-

mation, which allow for scale, rotation, shear and coordinate offset corrections. On the other hand, photometry and detections of sources are based on the procedure described in Irwin (1985), where fluxes of background-subtracted objects are measured within a series of soft-edged apertures that account for the fractional area of a pixel included in the aperture, with the addition of a simultaneous redistribution of flux from nearby stars. In the sequence of apertures, the area is doubled in each step. The scale size for these apertures is selected by defining a scale radius fixed at 1.0 arcsec for WFCam (2.5 pixels). At 1 arcsec seeing, this aperture contains approximately 2/3 of the total flux of stellar images. Morphological object classification and aperture corrections are based on analysis of the curve of growth of the object flux in the series of apertures (Irwin et al., 2004). The information obtained during the astrometry and photometry process are also stored in FITS files, where header keywords follow the system shown in Calabretta & Greisen (2002) and Greisen & Calabretta (2002). Recording the reduction process in these files, allows us to conserve the data as counts in original pixels and apertures.

2.4 Master catalogues

Besides the data reduction pipeline, the WTS has its own light-curve production pipeline, which is based on Irwin et al. (2007). As a first step, master images are created for each pawprint by stacking the 20 best-seeing photometric frames. The master images define the catalogue of objects of the survey for each pawprint with fixed coordinates and identification numbers (IDs). Thus, the source IDs will never change for the WTS; though, coordinates may change, since the description of the source's proper motion is not included in the pipeline.

In addition, source detection and flux measurement is performed for each master image to create a set of master catalogues by following the same procedure as described in the previous section. Then, astrometric and photometric calibration are recomputed with respect to 2MASS catalogues, which fix the object positions in the survey. Each source has significantly better S/N on the master image, so better astrometry (from reduced centroiding errors) can be achieved compared to a single exposure. The centroiding errors in the placement of apertures can be a source of error in aperture photometry, particularly for faint sources.

The master catalogues are then used to carry out list-driven photometry; this is, the master catalogues are used as input lists to measure the flux of all individual epochs by following the same soft-edged apertures process described in Section §2.3. However, a World Coordinate System² (WCS) transformation is computed between the master catalogues and each individual image using the WCS solutions stored in the FITS headers, so that the position of the stars are not longer free parameter. Any residual errors in placing the apertures will typically be small systematic mapping errors that affect all stars in the same way, affecting the photometry precision of the light curves. These systematics errors

²The FITS World Coordinate System standard defines keywords and usage that provide the description of astronomical coordinate systems in a FITS image header

can be solved by an iterative normalization that corrects for median magnitude differences present in all frames (see below). Following this procedure, we are able to determine the flux for every source of each observational epoch.

2.5 Aperture photometry light-curve construction

Although the photometry of each frame is calibrated individually to 2MASS sources, these values can be refined for better photometric accuracy. Light curves constructed from the default calibrations typically have an Root Mean Square (RMS) of a few per cent (for bright unsaturated stars). To improve upon this, an iterative normalization algorithm is used to correct for median magnitude offsets between frames, but also allowing for a smooth spatial variation in those offsets. In each iteration, light curves are constructed for all stellar objects and a set of selected bright stars ($13 < J < 17$), excluding the most variable objects of the group based on their light-curve RMS. Then for each frame, a polynomial fit is performed on the magnitude differences between the given frame magnitudes and the corresponding median (light curve) magnitude for the selected objects. The polynomial order is kept at 0 (constant) until the last iteration. In the last iteration, a second order, 2D polynomial is fitted as a function of image coordinates. For each frame, the best-fitting polynomial magnitude correction is applied for all objects and the loop starts again until there is no further improvement. Multiple iterations of the constant correction step help to separate inherently variable objects from non-variable ones initially hidden by light-curve scatter caused by outlier frames. The smooth spatial component during the last iteration accounts for the effects of differential extinction, as well as possible residuals from variation in the point spread function across the field of view. It is also found that light-curve variations correlate with seeing. In an additional post-processing step, for each object, a second order polynomial is fitted to differences from median magnitude as a function of measured seeing. Magnitude values are then corrected by this function on a per star basis.

2.6 Bad epoch filtering

Data are taken in a wide range of observing conditions, sometimes with bad seeing (~ 2 arcsec or worse) or significant cloud cover. Additionally, some frames are affected by loss and recovery of guiding or tip-tilt correction during the exposure. We identify and remove bad observational epochs that add outlier data points for a significant number of objects in any chip of a pawprint. Where a single (corrected) epoch has in excess of 30 % of objects deviating by more than 3σ from the median flux, we flag and remove this epoch from all light curves. High ellipticities arise from frames with tracking/slewing problems, while high-magnitude corrections are suggestive of thick (and probably patchy) clouds. Our rejection threshold is a compromise between the number of affected frames and frame quality. At the outlier ratio threshold of 0.3, 4 % of the frames are removed in the 19h

field.

2.7 Transit detection

A variation of the box-fitting (Kovács et al. 2002; see Section §4.1) algorithm developed by Aigrain & Irwin (2004) is included in the pipeline of the WTS to detect transit signals. The algorithm fits box-shaped periodic step function to the phase-folded light curve. The transit-fitting significance is measured by the S_{red} statistics (Pont et al., 2006), which refers to the noise that includes both, white noise (noise only produced by a transiting object) and red or correlated noise³. The red component is produced by systematics in observations from ground-based telescopes. Such systematics can be caused by changes in the airmass, atmospheric conditions, telescopes tracking and flat-fields errors. According to the notation presented in Pont et al. (2006), the S_{red} statistics is expressed as:

$$S_{red} = \frac{d}{\sqrt{\frac{\sigma_0}{n} + \frac{1}{n^2} \sum_{i \neq j} C_{ij}}}, \quad (2.1)$$

where n is the number of transiting points of the light curve, σ_0 is the measured error of each data point, d is the transit depth provided by the algorithm and C_{ij} is the covariance of two transit points. (Pont et al., 2006) suggest a detection threshold of $S_{red} = 6$, i.e., objects that pass this threshold are considered planet candidates. The WTS pipeline uses the same detection threshold to recognize planetary transiting systems.

³The S_{red} also can be found as pink noise in the literature.

Chapter 3

The WTS Difference Imaging light curves

The following chapters (§4, §5, and §6) are largely based on the work of Zendejas et al. (2013). Traditionally, aperture photometry (AP) has been the standard technique to produce light curves in transit surveys. In 1996, a new method to study crowded fields by optimal image subtraction was presented by Tomaney & Crotts (1996) and subsequently improved by Alard & Lupton (1998). This method (usually called "difference imaging", DI) was initially developed to study microlensing events. However, since the majority of transit survey targets are crowded fields (e.g. the disk-plane of the Milky Way Galaxy), image subtraction photometry has become an important tool to search for planetary transits (Pietrukowicz et al., 2010). In the past, some authors have carried out comparisons between different photometric techniques. For instance, Montalto et al. (2007) used the data from a ten-night observing campaign to develop a quantitative test comparing the photometric precision of 3 different photometry algorithms; AP, Point Spread Function (PSF)-fitting photometry¹ and image subtraction photometry, using observations from 4 different ground-based telescopes. They compare the RMS² as a function of the apparent visual magnitude for all photometric techniques. Due to the many factors involved in the observations that directly influence the measurements (e.g. the size of the telescope, instruments, or atmospheric conditions) the quality of the light curves clearly varies depending on the location of the observations. For all cases presented in Montalto et al. (2007), the best RMS was achieved by image subtraction photometry, in some cases a difference in RMS of up to 4 mmag is observed for bright objects. On the other hand, AP and PSF fitting photometry show significant variations of the photometric precision achieved by different telescopes. This discrepancy suggests that the precision obtained by a certain

¹The point spread function or PSF describes the response of any imaging system to a point source. In astronomy, the PSF describes the two-dimensional distribution of light in the focal plane of the telescope for an astronomical point source. In a telescope, the process of image formation is linear in power. Therefore, the images of a point source can be described by expressing the object plane as a sum over two-dimensional light distribution functions. The PSF is determined by the imaging system, which includes efficiency of the detector, tracking errors in the telescope and a dominant term due to atmospheric effects.

²The RMS is a statistical measure that can be used to estimate the error from time series measurements. In observational astronomy, the RMS is commonly used to value the quality of a data set.

photometric technique may depend on the characteristics of the survey, i.e. a particular method might produce different results depending on the observing conditions.

In addition to the standard WTS AP light curves generated by the CASU and WTS pipelines, in this work we alternatively produce a second set of light curves by using DI photometry. We compare the quality of the WTS AP and DI light curves by performing a quantitative comparison between the photometric precision of both sets of light curves. The description and results of this analysis are presented in §3.4.

3.1 Difference Imaging Analysis

In this section, we described in detail the DI technique, since one of the main goals of this study is to show the capability of DI to produce high precision light curves in crowded fields in the search for extra-solar planets. According to the notation presented in Alard & Lupton (1998), the method operates on a reference image $R(x, y)$, which is the combination of the best seeing images from the whole data set. The reference frame is degraded by convolution to match the seeing of each single image. The convolved reference image $C(x, y)$ is the result of convolving the original reference frame $R(x, y)$ with the Kernel $K(u, v)$ and adding a polynomial surface function $B(x, y)$ to account for background differences, i.e.

$$C(x, y) \equiv R(x, y) \otimes K(u, v) + B(x, y), \quad (3.1)$$

where x and y represent the pixel coordinates of the observed region and u and v are the pixel indices of the kernel bitmap which has the same pixel size as the images. The polynomial expression that models the background variations is given by

$$B(x, y) = \sum_{l=0}^{q_b} \sum_{m=0}^{q_b-l} a_{lm} x^l y^m, \quad (3.2)$$

where q_b is the degree of the polynomial.

A difference image $D(x, y)$ is obtained by subtracting the convolved reference image from each single image $S(x, y)$,

$$D(x, y) = \frac{S(x, y) - \{R(x, y) \otimes K(u, v) + B(x, y)\}}{|K|}, \quad (3.3)$$

with $|K|$ being the norm of the kernel, which is used to match the different flux level between the difference images and the reference image (important for the normalization of the light curves) by dividing each single difference image by this value.

To find the optimal kernel that matches the seeing of two frames with different PSFs represents a crucial and complex problem during the DI process. Alard & Lupton (1998)

proposed a method, where the optimal kernel is approximated by a superposition of N kernel base functions $k_i(u, v)$,

$$K(u, v) = \sum_{i=1}^N k_i(u, v), \quad (3.4)$$

which are constituted of 2-dimensional Gaussian functions modulated with a polynomial of order p_i , thus we obtain the expression for the optimal kernel:

$$K(u, v) = \sum_{i=1}^N \exp\left[-\frac{u^2 + v^2}{2\sigma_i^2}\right] \sum_{j=0}^{p_i} \sum_{k=0}^{p_i-j} a_{ijk} u^j v^k, \quad (3.5)$$

To calculate the kernel, we use four base functions ($N = 4$) with $\sigma_i = 1, 2, 3$ and 0.1 pixels, while the degrees of the associated polynomials p_i are 6, 4, 2 and 0 respectively. The kernel size is 11×11 pixels, and we consider a 1st order background polynomial $B(x, y)$. All free parameters, such as the a_{ijk} coefficients and the parameters associated to the background polynomial $B(x, y)$ are determined by minimization of the following expression:

$$\chi^2 = \sum_{x,y} \sum_{u,v} \frac{1}{\sigma_{x,y}^2} [\{R(x, y) \otimes K(u, v)\} + B(x, y) - S(x, y)]^2, \quad (3.6)$$

where $\sigma_{x,y}^2$ is the variance of a Gaussian distribution used to approximate the Poisson noise statistics.

Variations of the PSF over the detector are a common problem in the DI technique. In order to reduce this effect during the estimation of the kernel, Alard (2000) presented an algorithm that uses a space-varying kernel with the coefficients a_{ijk} as a function of the position on the detector. Although the algorithm certainly minimizes the effects of PSF variations, the computing time used to calculate the coefficients a_{ijk} increases considerably. An alternative way to account for PSF variations is to divide the images in subfields and calculate the kernel in each subfield. In our case we divide the images in 10×10 subfields with a size of 200×200 pixels. We tested several parameters to achieve an optimized set of difference images. For each set of parameters, we extract the light curves and measure the photometric precision to verify the quality of the sample. During the testing process, we found that the light curve precision is significantly improved if we mask bright or faint stars while the difference images are produced. Two sets of difference images are created to guarantee the best quality of the light curves. In a first set, we mask all sources with $J \leq 16$ mag, which provides an improvement for objects fainter than this threshold. The second set is produced by masking faint objects, i.e., all sources that hold magnitudes $J \geq 16$, which results in an improvement for bright stars. An example of a single, reference and difference image is shown in Figure 3.1. The light curve extraction process and

more detailed information about photometric precision are given in the following sections.

3.2 DI light curve extraction

Using the difference images, we are able to measure the differential flux of each source. Adding the value measured in the reference image, the total flux of each single star can be estimated. Although differential fluxes are relatively easy to measure in the difference images, because all constant sources are removed, estimating the fluxes in the reference frame is more difficult, especially for objects that have close neighbors. We measure the flux in the reference frame using iterative PSF-photometry. This technique is very successful to measure flux accurately in crowded fields. The method uses bright and isolated stars to extract the PSF. In a first step an initial estimation of the flux of each star is measured from the extracted PSF. In subsequent iterations, all nearby stars are removed before measuring the flux of a particular source. This process continues until all fluxes converge, using in each iteration the improved flux measured in the previous step. The fluxes measured in the difference images are also estimated by PSF-photometry. The PSF is obtained from the convolved reference image, using the same stars employed to estimate the flux in the reference frame, which are a representative sample of stars in each field. Although the fluxes in the difference images certainly could be estimated by using a different photometric technique (e.g. aperture photometry), since the stellar crowd in the field is eliminated, we have chosen PSF-photometry to measure the fluxes because this method is not affected by dead pixels and does not require aperture corrections, which might lead to a wrong evaluation of the flux. Finally, the light curves are normalized to one and barycentrically time corrected using the formula of Meeus (1982). The process of extracting the light curves is applied to both sets (one optimized for bright sources and one optimized for faint sources, see previous section). We obtain the optimized set by choosing the light curve with the better photometric precision for each source.

3.3 The *sysrem* algorithm

Light curves from photometric transit surveys are usually affected by systematic effects that can be associated with atmospheric extinction, detector efficiency or simply PSF changes on the detector. An algorithm to remove systematics in large sets of light curves was proposed by Tamuz et al. (2005). The algorithm, named *sysrem*, has been widely tested and shows a significant improvement in the photometric precision of light curves obtained in transit surveys (Snellen et al., 2007; Mazeh et al., 2009; Irwin et al., 2007). The algorithm searches for systematics that consistently appear in many sources of the sample, hence *sysrem* has the ability to remove effects without any prior knowledge of the origin of the effect, as long as it systematically appears in many stars of the sample. The first attempt in developing the algorithm was to correct effects created by differential

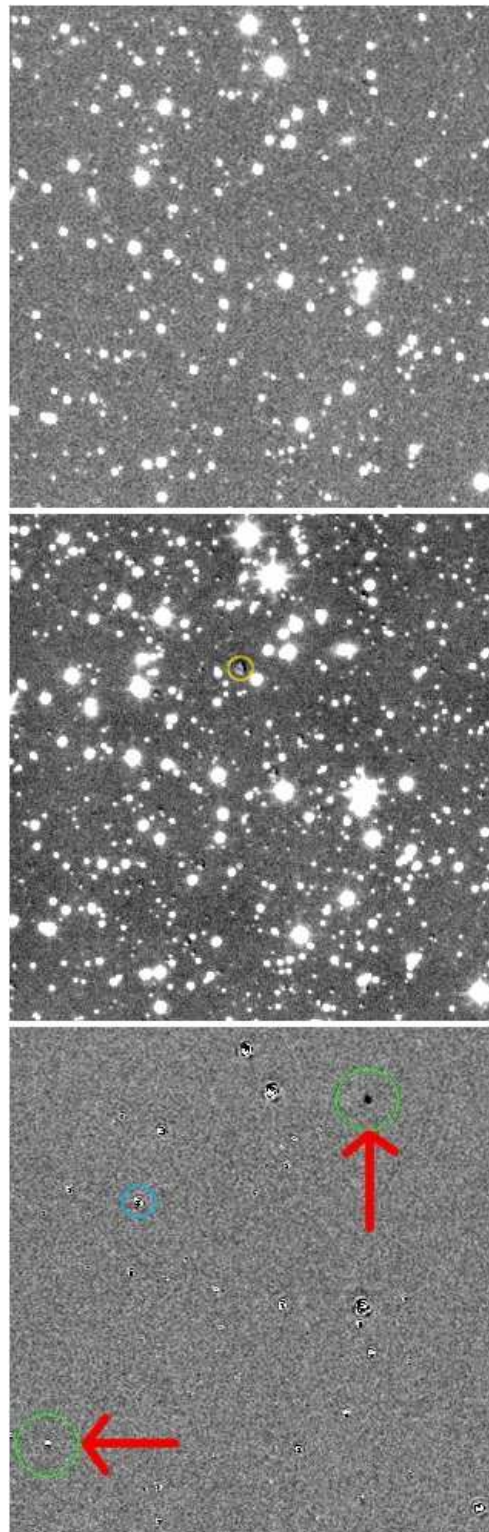


Figure 3.1: The top panel shows a single image of the WTS data set from which the convolved reference frame (middle) panel is subtracted to obtain a difference image (lower panel). In some regions the reference image shows cosmetic patterns (see e.g. yellow circle) that correspond to detector defects. However, they are well below the background noise level and therefore not visible in the single image and difference image (see upper and lower panel). All constant sources have been removed in the difference image and only variable sources remain (arrows mark the position of two variable stars). Residuals (blue circle) at the position of constant bright stars are also visible, which are consistent with the expected Gaussian uncertainties of high photon counts.

atmospheric extinction. Since extinction has a close correlation with the color of stars and airmass, different extinction values are expected to be associated to each object, but the DI technique only takes into account a constant extinction for all sources. In order to correct for this effect, the *sysrem* algorithm considers a set of N light curves with M epochs each. The algorithm removes a residual term $c_i a_j$, where c_i represents the effective extinction coefficient for each source i ($i = 1, \dots, N$), and a_j corresponds to the airmass coefficient for each image j ($j = 1, \dots, M$). The method searches for the best pair c_i and a_j , which minimize the following expression:

$$S_i^2 = \sum_j \frac{(r_{ij} + c_i a_j)^2}{\sigma_{ij}^2}, \quad (3.7)$$

where r_{ij} is the residual flux after subtracting the average flux to each star i in the image j , and σ_{ij} is the uncertainty associated to each measurement. Under the assumption that the airmasses a_j are known, we can estimate the extinction coefficients as:

$$c_i = \frac{\sum_j r_{ij} a_j / \sigma_{ij}^2}{\sum_j a_j^2 / \sigma_{ij}^2} \quad (3.8)$$

At this point, the algorithm removes systematics that are represented as $c_i a_j$, considering a set of initial airmasses a_j , which in principle can be the measured airmass of each image j . Nevertheless, the atmospheric extinction may also depend on other factors (e.g. weather conditions), so it is necessary to define the most appropriated airmass for each image. Thus, the problem can be turned around and we can find the a_j that minimize the equation below,

$$S_j^2 = \sum_i \frac{(r_{ij} + c_i a_j)^2}{\sigma_{ij}^2}, \quad (3.9)$$

using the above calculated effective extinction coefficients c_i (Equation 3.8), the corresponding airmass coefficient of each image is given by

$$a_j = \frac{\sum_i r_{ij} c_i / \sigma_{ij}^2}{\sum_i c_i^2 / \sigma_{ij}^2} \quad (3.10)$$

Once a_j are determined, we can recalculate and find a better fitting estimation of c_i with Equation 3.8, and then search for new a_j coefficients. This process iteratively continues until it converges to the final values c_i and a_j that best account for atmospheric extinction, but which are not necessarily related to the true airmass and colors. The final values c_i and a_j may be instead associated with other effects produced by position on the CCD, seeing, or Moon phase. The *sysrem* algorithm detects systematics as long as a global minimum of the generalized form of S_{ij}^2 is reached. In a first iteration the algorithm acts on the predominant component by subtracting the product $c_i a_j$ to each light curve and removing the most prominent systematic. Subsequent iterations on the corrected light curves result in smaller corrections. This process can be repeated until no significant linear

effects remain in the residual r_{ij}

In this study, we apply the *sysrem* algorithm to both the DI and AP light curves and subsequently include the results in the comparison analysis presented below.

3.4 Quality of the DI light curves and comparison with the AP method

In this section we compare the quality of the WTS light curves produced by AP and DI. We perform a quantitative comparison between the photometric precision of both sets of light curves. In the following, we define explicitly the concept of photometric precision, since it is crucial for this assessment. Calculating the RMS from the photometric measurement for each source allows us to make an accurate comparison between the different photometric analysis. The explicit expression of the RMS is defined as:

$$\text{RMS} = \sqrt{\frac{\sum_{i=1}^{i=N} \left(\frac{I_i - \langle I \rangle}{\langle I \rangle} \right)^2}{N - 1}}, \quad (3.11)$$

where I_i is the brightness measured in a particular star for each i -th image, $\langle I \rangle$ is the mean brightness for the whole data set and N is the number of images. In our case $\langle I \rangle$ has been normalized to one, therefore the above expression is reduced to:

$$\text{RMS} = \sqrt{\frac{\sum_{i=1}^{i=N} (I_i - 1)^2}{N - 1}}, \quad (3.12)$$

we apply this formula to estimate the RMS for each single light curve from the two different sets of light curves. During this process we clip all 4σ -outliers (clipping 3 and 5σ -outliers provides similar results). Note that this step is only for the purpose of calculating the RMS and is not a final operation on the light curves.

In order to improve the quality of the light curves, we consistently apply the *sysrem* algorithm to DI and AP light curves. Note that Irwin et al. (2007) showed that the *sysrem* algorithm does not improve the precision of AP light curves by much and it might additionally produce false variability from the residuals. In our case we find a significant reduction of the scatter of constant light curves for both DI and AP light curves. Any possible false variability created by *sysrem* will not lead to the detection of false-positive candidates because of our conservative criteria applied in the candidate selection process (see below).

To show the capability of the *sysrem* algorithm to improve the photometric precision of light curves, we perform a quantitative analysis on the AP and DI light curves by comparing the RMS of the light curves before and after applying the *sysrem* algorithm. Figure 3.2

shows the RMS difference between the corrected and uncorrected sets of light curves as a function of the J -band magnitude. The results of the comparative analysis indicate a significant improvement in the RMS of bright and faint sources when the *sysrem* algorithm is employed, especially for DI light curves. For bright stars with magnitudes between 12-15 mag, the photometric precision of the DI light curves improves up to 5 mmag. The improvement achieved in the photometric precision of the AP light curves is less significant, where the RMS achieved by sources within the same magnitude range is of ~ 1 -2 mmag. This result agrees with the analysis presented in Irwin et al. (2007).

So far, We have shown the ability of the *sysrem* algorithm of removing systematic effects in photometric time series of transit surveys, which particularly results in the improvement of the RMS of the WTS light curves. We now want to compare the quality of the light curves achieved by the AP and DI techniques and show the set of light curves that provides better photometric precision. We perform an analysis by comparing the RMS of both set of light curves. The results of the comparative analysis are shown in Figure 3.3, which represent the RMS achieved by the DI and AP light curves after applying the *sysrem* algorithm as a function of the J -band magnitude. The DI light curves reach a precision of 3.5 mmag for bright objects in the range of $12 < J < 14$, while the RMS of AP light curves corrected by *sysrem* algorithm reaches a precision ~ 2.5 mmag in the same J -band magnitude interval. The plots show that DI produces better results for faint objects ($J > 16$), however in the bright magnitude range, the quality of AP light curves is slightly better. For magnitudes larger than $J = 16$, the DI light curves show a much higher photometric precision than the AP light curves. The RMS differs up to 5 mmag at $J = 17$ mag and 15-20 mmag at $J = 18$ mag. In Figure 3.4, we show the difference between both RMS as function of the J -band magnitude. A flat part is visible for objects which hold magnitude below $J = 16$, but the RMS of DI light curves does not achieve the same photometric precision reached by AP light curves. As described above, the DI light curves provide clearly the best photometric precision for fainter sources. A complete analysis of the WTS AP light curves is described in Kovács et al. (2013). They reported a series of plots of the RMS as a function of the J -band magnitude with different pipeline optimization. Although, they do not use the *sysrem* algorithm to optimize the photometric precision, those plots are the analogs of Figure 3.3.

These results are in contrast to previous studies, which compare the photometric precision achieved with both methods. For example, Montalto et al. (2007) show that DI photometry achieves an equal or better photometric precision compared to AP and PSF photometry for all magnitudes. However, these studies were carried out at optical wavelengths (V-band) and a direct comparison to a NIR survey (like the WTS) is not possible, since the detector characteristics are different. Imperfect treatment of non-linearity effects at the bright end could be one possible source for the additional systematic noise that we observe in our DI light curves. Another problem might be the non-homogeneous background, which is visible in the WTS images. We can rule out that the effect is caused by a low astrometric accuracy. Any shifts between the reference frame and the single images would produce dipole-shaped residuals in the difference image, contrary to this effect, bright sources show very symmetric noise residuals in our difference images.

Note that although applying the *sysrem* algorithm improves the photometric precision of the WTS light curves, the capability of the algorithm to remove systematic effects is limited. Figure 3.5 shows the number of detected periods around the one-day alias period (see § 1.5.7) before and after using the *sysrem* algorithm. In an ideal case, the algorithm should account for these effects and eliminate the alias peak. In our case, the number of detections around the alias period is reduced by a factor ~ 2 after applying the *sysrem* algorithm.

3.5 Correction of the point-by-point errors derived from the individual images

After removing systematic effects, we carried out a routine visual inspection over a random sample of light curves. We noticed that for many light curves (typically for bright sources) the scatter of the data points was much larger than the error bars. Usually error bars of light curves are estimated by a pipeline taking into account different noise sources, such as the photon noise of the source, background contribution and read-out noise. However, systematic effects caused by PSF-variations or variation in noise level from the background are not included. This seems to be the case of the WTS light curves, which present a wrong estimation of the error bars, which is correlated to the brightness of the object. A simple way to correct the size of the error bars is to compare the RMS of the photometric measurements with the error values, since the RMS is related to the scatter level and it can be associated with the real error for non-variable objects. We perform this test for DI and AP light curves dividing the RMS by the median error calculated in each light curve. The results are shown in Figure 3.6, where this quotient is plotted as a function of the *J*-band magnitude. If the error values were correct, the RMS and median error should be similar and the data points in the plots should be distributed around 1. However, there is an evident discrepancy between both quantities, which is reflected in the shape of the data point distributions.

For our work, it is important to correct the bad estimation on the error bars, since some of our selection criteria (see below) and several parameters that we estimate for our candidates later-on depend on the error bars. In order to correct the error bars, we fit a polynomial (Figure 3.6) to the distribution of data points. The polynomial provides a scale factor as a function of the magnitude, which is used to correct the whole sample. Note that unlike replacing the errors obtained from the images by an estimation of the scatter (RMS), by scaling the error bars with a factor that is a function of the brightness of the objects, we avoid to introduce an overestimation of the errors, principally for variable sources, which can present a significantly scatter (higher RMS) in the light curves. After scaling the error bars, we perform the same test and show the results in Figure 3.7, where we can see that the distribution of data points clearly has been adjusted and they are now located close to 1. The histograms shown in Figure 3.8 also demonstrate that the majority of light curves were re-scaled properly.

Nevertheless, Figure 3.7 shows a second higher RMS sequence for bright stars (14-16 magnitudes), which is reflected in the prominent tails of the histograms. We know from the AP light curves (see Kovács et al. 2013) that the WTS data present a high level of red noise (Pont et al., 2006) also correlated to the magnitude of the objects, being the bright sources the most affected for this effect. Although the *sysrem* algorithm is designed to filter out the red noise, there is a component from the red/pink-noise that remains in the sample of light curves, which can be observed in Figure 3.7, where a significant scatter is visible in the distribution of the data points. The fact that *sysrem* cannot eliminate completely this component of the red/pink noise may produce fake signals and subsequently a large number of false-positives. Figure 3.5 demonstrates that the remaining systematics produce such effects, since a large number of objects fall into the daily alias. Nevertheless, in Section 5.1 we introduce the selection criteria used to detect planet candidate in the WTS -light curves, which have the capability to provide a pure candidate sample, ruling out false positive related to some of these systematics. On the other hand, in this work we do not use the correlated noise to measure the transit fitting significance. Therefore, the polynomial used to correct the error bars does not take into account the dispersion of data points generated by the remaining red/pink-noise component.

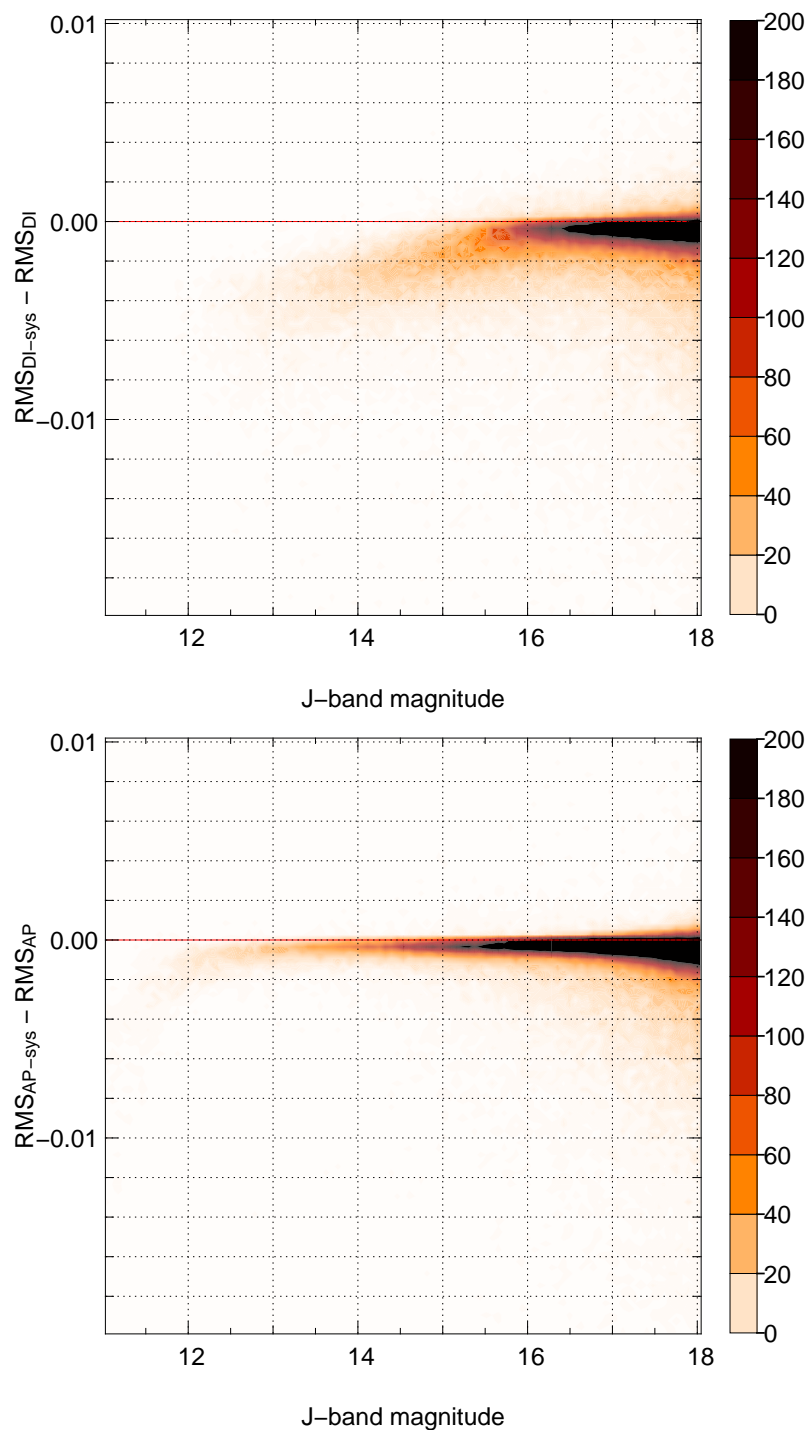


Figure 3.2: RMS difference between the DI and AP light curves before and after applying *sysrem* algorithm (upper and lower panels respectively). The plot shows the improvement achieved in the photometric precision once systematic effects are corrected. The contour color-map shows the density of data points distributed in 100×100 bins.

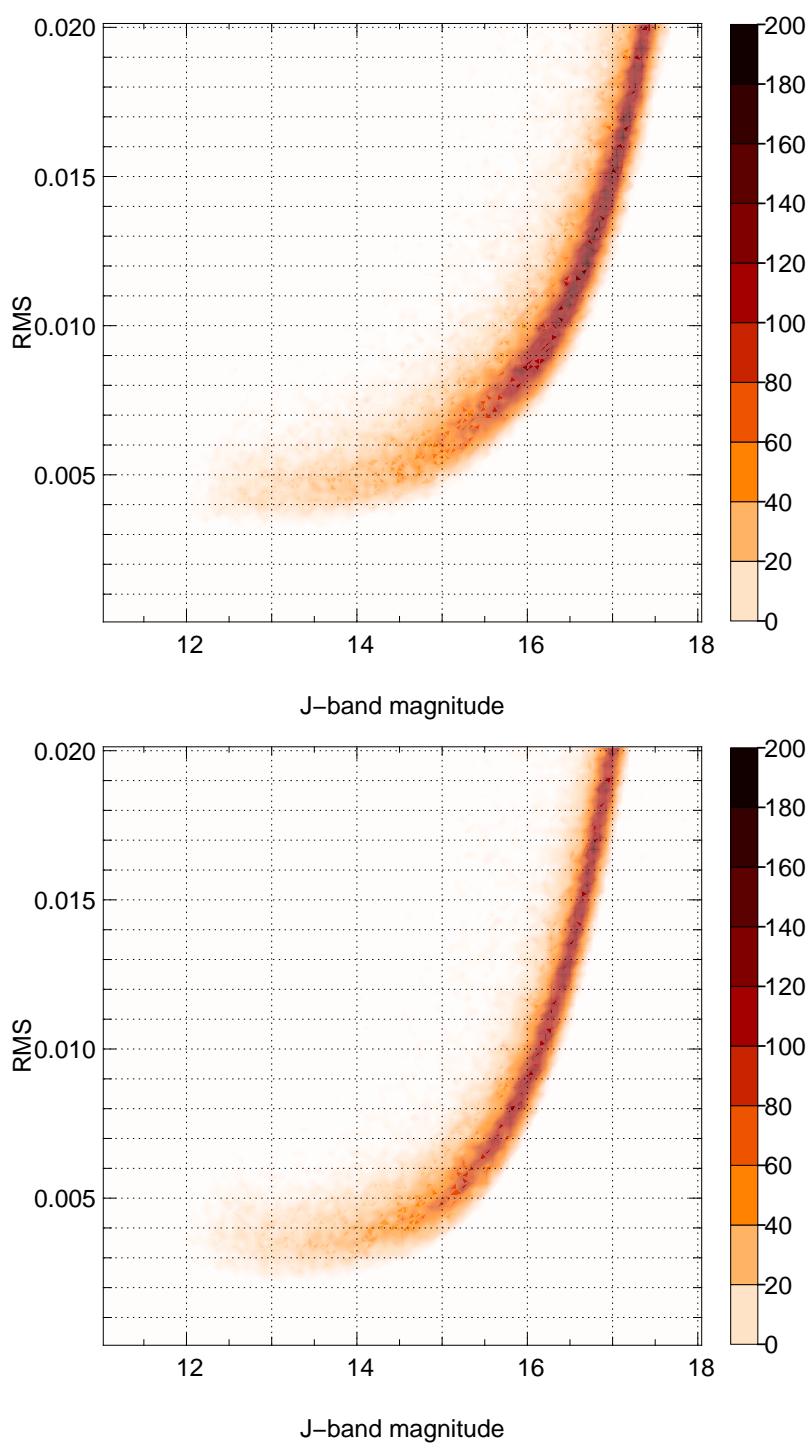


Figure 3.3: RMS of the DI and AP light curves (upper and lower panels, respectively) as a function of the *J*-band magnitude. The RMS corresponds to the measurements obtained after removing systematic effects. The plot is displayed in density of data points in a scale of 100×100 bins.

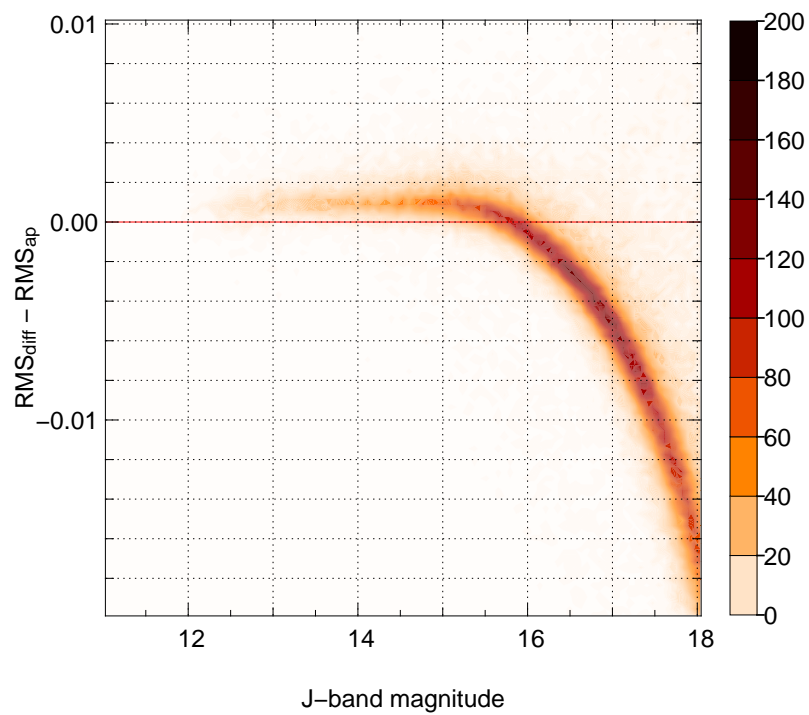


Figure 3.4: Difference between the RMS of DI and AP light curves after removing systematics effects as a function of the J -band magnitude. The plot shows the density of data points in a scale of 100×100 bins.

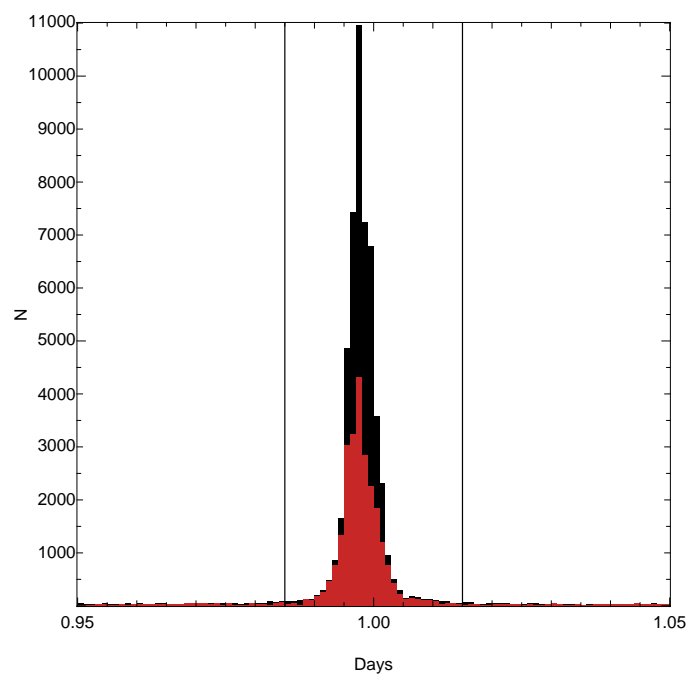


Figure 3.5: Histogram of periods found by our transit detection algorithm, before (black) and after (red) applying the *sysrem* algorithm. The numbers of false detections between 0.985 and 1.015 d periods is reduced by a factor of 2.

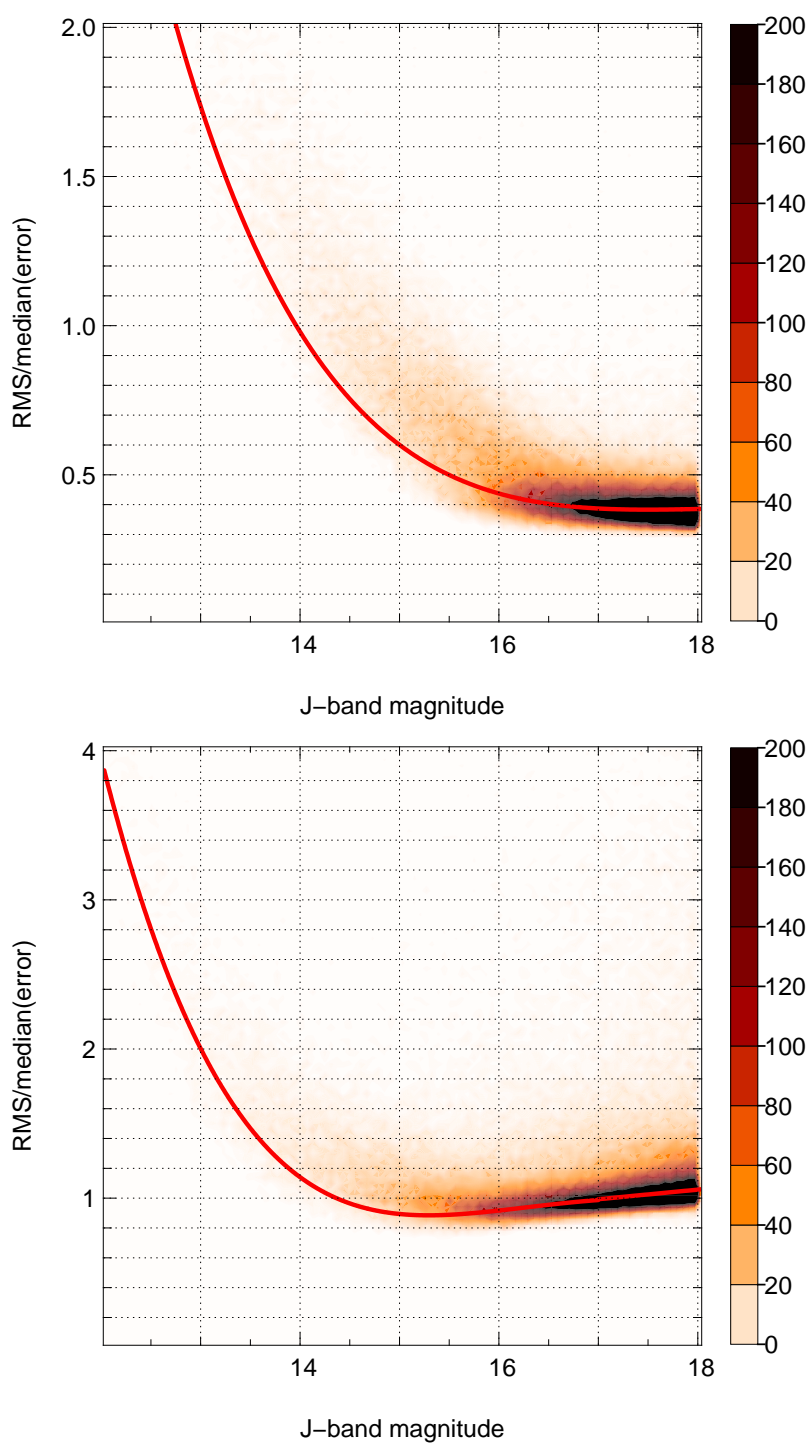


Figure 3.6: Density of data points of the RMS divided by the median error from DI and AP light curves (upper and lower panels, respectively) as a function of J -band magnitude. The solid-red line represents the polynomial used to scale the errors bars. The plots are scaled in 100×100 bins.

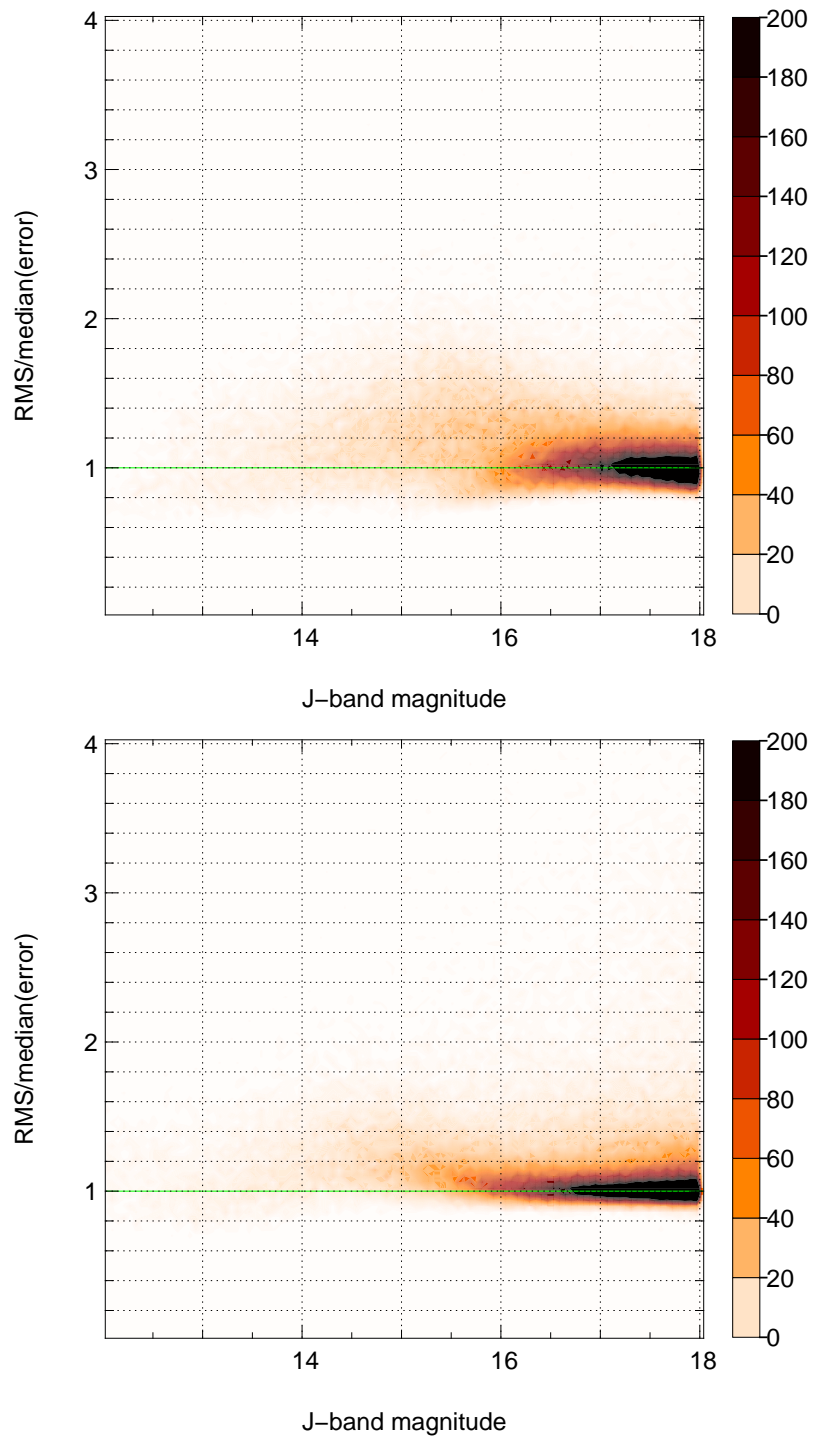


Figure 3.7: Density of data points of the quotient $\text{RMS}/\text{median}(\text{error})$ as a function of the J -band magnitude after re-scaling the error bars on DI and AP light curves (upper and lower panels, respectively). The plots are scaled in 100×100 bins.

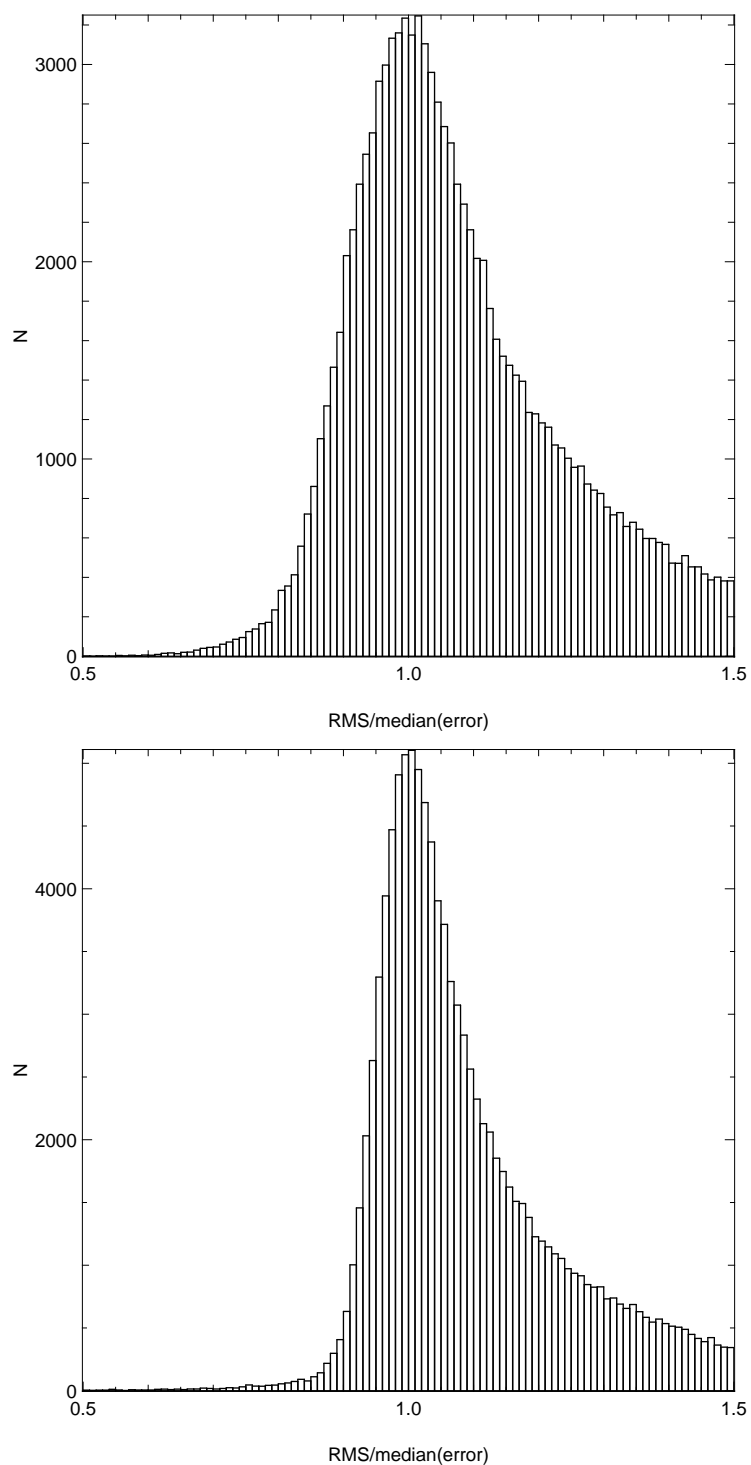


Figure 3.8: Histogram of the RMS scatter divided by the median error value of the DI and AP light curves (upper and lower panels, respectively).

Chapter 4

Transit detection algorithm

Due to the large number of light curves in transit surveys, an efficient detection algorithm is needed to speed up the identification of planet candidates. After the discovery of the first planet transiting its host star, several algorithms have been developed to identify planets that transit their host stars. For instance, Defaÿ et al. (2001) presented an algorithm that uses a multi-frequency Fourier fit to model periodic astronomical time series. Shortly after, Kovács et al. (2002) presented a box-fitting algorithm based on least-squares fit of step functions (BLS) to analyze stellar photometric time series. This algorithm has shown significantly better results than previous works and become a popular tool to search for exo-planets in transit surveys. In following sections, the box-fitting algorithm is described in detail. We also present the implementation to the modified box-fitting algorithm that is used in this work, namely the V -shape parameter.

4.1 The box-fitting algorithm

The box-fitting algorithm was developed by Kovács et al. (2002) to search for periodic signals in stellar light curves produced by a transiting planet. The box-fitting algorithm is based on direct least-square fits of step functions to the folded signal of the photometric time series, which correspond to a certain number of trial periods (Gilliland et al., 2000; Udalski et al., 2002b). The algorithm is designed to analyze low-signals with high-noise levels that are characteristic of large-scale ground-based transit surveys. The algorithm searches for signals that present periodic transitions between two discrete flux levels of the light curve (i.e., the stellar brightness within and outside the transit), with typically much less time spent at the lower level (less than 5 %). The algorithm predicts the detections significance based on various signal parameters, with the S/N being the most relevant parameter. In this context, the S/N is defined as the depth of the transit (Equation 1.19) divided by the uncertainty of the stellar brightness measured inside the transit. The algorithm does not consider other elements involved in a transit, such as ingres/egress phases. Nevertheless, the results are insignificantly affected, since the duration of these

phases are considerable shorter than the length of the transit. Limb-darkening¹ effects are other feature excluded in the fit; however, these effects are small for a first approximation of the real solution of the transit (Deeg et al., 2001). The above assumptions explain the high efficiency of the box-fitting algorithm, which is very effective, as long as it is used for detection purpose. The box-fitting algorithm has shown better efficiency compared to other detection algorithms and become a useful tool in the search for transiting exo-planets, specially for low S/N .

In the following, we describe in detail the box-fitting algorithm:

According to the procedure presented in Kovács et al. (2002), we consider a light curve that shows periodic variations with period P between two different flux levels, H and L . The expected time spent in the lower level L is τP (i.e., the transit duration, see Eqs. 1.20, 1.21, and 1.22), which is considerable short relative to P , where τ typically takes values between 0.01 and 0.1 for Hot Jupiters (Defaÿ et al., 2001). For any distribution of data points in the light curve, the algorithm searches for the best solution and characterize the light curve with 5 parameters, namely P , τ , H , L , and t_0 (epoch of the transit). The number of parameters can be reduced to four by assuming that the average of the signal is zero. Under this assumption, τ can be expressed in terms of H and L :

$$\tau = \frac{1}{1 - \frac{L}{H}}. \quad (4.1)$$

The errors σ_i ($i=1,2..n$) of each data point or photometric measurement x_i are considered to provide the characteristic noise by designating to each x_i a weight w_i defined by

$$w_i = \sigma_i^{-2} \left[\sum_{j=1}^n \sigma_j^{-2} \right]^{-1}, \quad (4.2)$$

and further assuming an arithmetic average of $\{x_i w_i\}$ equal to zero.

In the next step, each photometric time series is folded by using a trial period. The new time series is a permutation of the original light curve, in which the data points and corresponding weights are denoted by $\{\hat{x}_i\}$ and $\{\hat{w}_i\}$, respectively. Similarly, the flux levels take values of $\hat{L}[i_1, i_2]$ for the lower level, and $\hat{H}[1, i_1)-(i_2, n]$ for the upper level. In the following, a step function is fitted to the flux levels of the folded light curve, where the time spent at \hat{L} is characterized by the sum of the weights of each photometric measurement at this level.

¹Limb-darkening is the diminishing intensity effect produced in the disk of a star, where brightness decreases from the center to the edges of the stellar disk. This effect occurs because the density and temperature of a star increase with the depth. At the center of the disk, an observer can see into deeper regions of the atmosphere, where more light is produced. On the other hand, at the edges or limb of the disk, only the upper and cooler layers (i.e, less light is produced) of the atmosphere can be observed, since the line of sight only enters at a very small angles.

Then, the best model is determined by minimizing the expression below for each pair (i_1, i_2) , with respect to \hat{H} and \hat{L} :

$$D = \sum_{i=1}^{i_1-1} \hat{w}_i (\hat{x}_i - \hat{H})^2 + \sum_{i=i_2+1}^n \hat{w}_i (\hat{x}_i - \hat{H})^2 + \sum_{i=i_1}^{i_2} \hat{w}_i (\hat{x}_i - \hat{L})^2, \quad (4.3)$$

which results in the arithmetic average of the two flux levels,

$$H = -\frac{s}{1-r} \quad (4.4)$$

and

$$L = \frac{s}{r} \quad (4.5)$$

where

$$r = \sum_{i=i_1}^{i=i_2} \hat{w}_i, s = \sum_{i=i_1}^{i=i_2} \hat{w}_i \hat{x}_i \quad (4.6)$$

These equations can be combined with Eq.4.3 to obtain the average square deviation of the fit as a function of $\{w_i\}$, $\{x_i\}$, s , and r

$$D = \sum_{i=1}^n \hat{w}_i \hat{x}_i^2 - \frac{s^2}{r(1-r)} \quad (4.7)$$

The last expression is tested and evaluated again for all possible (i_1, i_2) pairs that corresponds to τ values within the selected range; thus, the algorithm recognizes the absolute minimum. From Eq.4.7, we recognize that only the second term of the right side of the equation depends of P , so the goodness of the fit can be characterized by only considering this term, which minimizes the expression with respect to τ and t_0 for any test period P . This leads to introduce the BLS frequency spectrum SR :

$$SR = -MIN \left\{ - \left[\frac{s^2(i_1, i_2)}{r(i_1, i_2)[1 - r(i_1, i_2)]} \right]^{\frac{1}{2}} \right\} = MAX \left\{ \left[\frac{s^2(i_1, i_2)}{r(i_1, i_2)[1 - r(i_1, i_2)]} \right]^{\frac{1}{2}} \right\} \quad (4.8)$$

In the above equation, we have inverted the sign of the expression to get positive values of SR . This implies that high values of SR corresponds to a low χ^2 ; therefore, once we find the maximum value of SR for certain trial period, the best solution of the box-fit is determined, and characterized by the parameters L , H , t_0 , and τ . We can further plot the SR as a function of the inverse of the period $1/P$ to obtain the SR -spectrum, which is normalized to the maximum value of SR . In the SR -spectrum, good detections are represented by high peaks, and fractions or multiples of the true period also appear as high peaks. Figure 4.1 shows the folded light curve of WTS-2b detected by the box-fitting algorithm, and the corresponding SR -spectrum, where a narrow and high peak is visible at the true period.

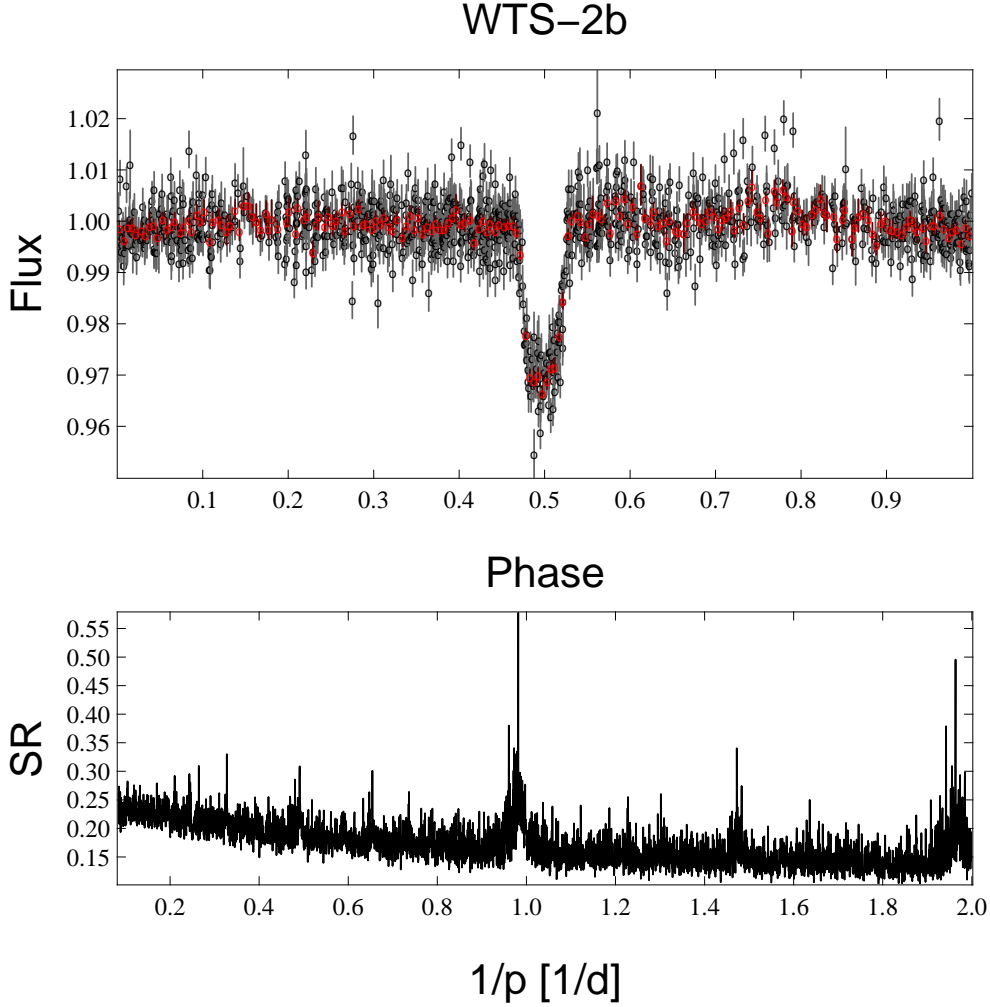


Figure 4.1: Upper panel shows the folded light curve of WTS-2b (black points). The light curve was divided in N bins to speed-up the detections process, which are shown with red points. The SR -spectrum is shown in the lower panel. An evident high peak is located around 1, which corresponds to the true period detected by box-fitting algorithm.

An additional feature that can be used to characterize the detection significance is the signal detection efficiency (SDE), which is expressed by the next equation,

$$SDE = \frac{SR_{high} - \overline{SR}}{SR_{sd}}, \quad (4.9)$$

where SR_{high} corresponds to the SR of the highest peak, and \overline{SR} and SR_{sd} are the average and the standard deviation of all SR values, respectively.

In Kovács et al. (2002), it is shown that the process of finding the absolute minimum of Eq.4.7 can be speeded-up by splitting the folded light in N -bins, and evaluating the SR using the average values of the bins. Carrying out this procedure permits a good solution of the least-squares, while efficiently reducing the computation time. In the next section,

we present the implementation that was carried out in the box-fitting algorithm, as well as the values that are used to run the algorithm in the WTS-light curves to search for transiting planets.

4.2 Implementations to the Box-fitting algorithm: The V -shape parameter

We detect transits in the WTS light curves using an algorithm that is based on the BLS algorithm described in the previous section. Our modifications include a trapezoidal re-fitting of the box-shaped eclipse found by BLS, where the re-fitting is done by symmetrically varying the edges of the box while keeping fixed the duration of the eclipse (“ d ”), which is measured at half the transit depth (see Figure 4.2). We emphasize that the trapezoidal shape is only fitted after the standard parameters provided by the box-fitting algorithm have been found (such as period, transit duration and epoch); however, the eclipse depth may change. We introduce the V -shape parameter:

$$V = \frac{2e}{f + 2e}, \quad (4.10)$$

where e is the duration of the ingress/egress of the eclipse in phase units, and f is the duration of the transit, or flat part of the trapezoid shape (see Figure 4.2). If e is considerably smaller than f , the V -shape parameter is close to 0 and the shape of the fit is box-like. This is the shape of the light curve that we expect for a planet that transits its host star with an orbital inclination of $\sim 90^\circ$. On the other hand, if $f \approx 0$ and $e \gg f$, the V -shape parameter is close to 1 and the fit is V -shaped, which is representative of eclipses produced by grazing eclipsing binaries. In this work, we use the V -shape parameter as selection criterion to reject grazing binary systems that generally have V values larger than transiting planets (see Section §5.1).

In Figure 4.5, one can see the motivation of including the V -shape parameter in our selection criteria. The figure shows the folded light curve of WTS-2b (Birkby et al., 2013b,a), which is characterized by a box-like fit. In the same figure, we present the folded light curve of one eclipsing binary system that was detected in the WTS. In this case the fit is very V -shaped, and presents a V value close to one. Another advantage of our modification is that the V -fit results in a better estimate of the transit depth. This statement is based on a χ_{dof}^2 comparison. In Figure 4.3, we show an example of a folded light curve over-plotted with both the box- and V -shape fits. The transit depths clearly differ from the two models, where the V -fit results in a lower χ_{dof}^2 . Figure 4.4 additionally shows the difference between the reduced χ_{dof}^2 of the trapezoid-fit and the box-fit as a function of the V -shape parameter. The trapezoid-fit shows a significant improvement over the box-fit, especially for high V values.

The DI and AP light curves were split in two different sets, one for F-G-K stars and a second set for M-dwarfs (we refer to Chapter §5). We search for transit periods in the

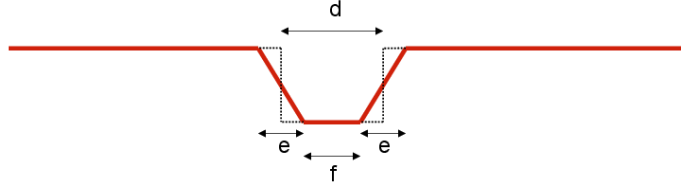


Figure 4.2: Geometry of the symmetrical trapezoid-fit.

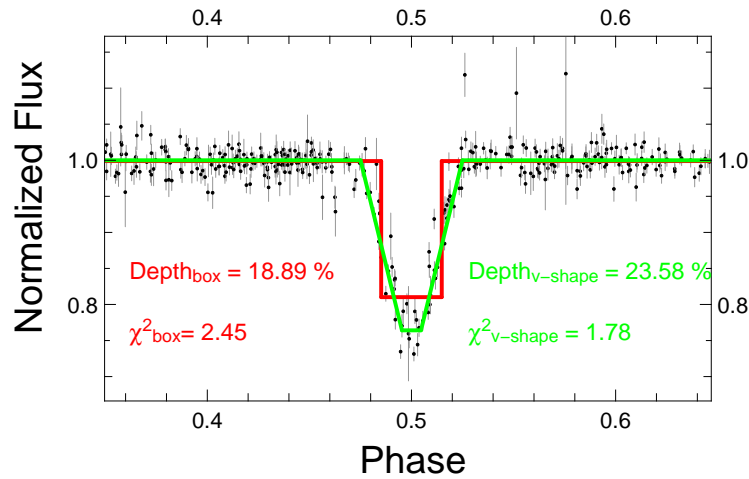


Figure 4.3: Folded light curve of an object from the WTS 19h field and the corresponding box- and trapezoid-shape fits provided by our detection algorithm (red and green solid-lines, respectively). Transit depths vary from both models and the best χ^2_{dof} is reproduced by the V-shape fit.

range between 0.5 and 12 d for the case F-G-K stars, while for M-dwarfs we use a range between 0.8 and 10 d to be consistent with the sensitivity analysis for short-period giant planets around M-dwarfs presented in Kovács et al. (2013). For both sets, we use 100 001 trial periods equally distributed in $1/P$. To speed-up the calculation time, the folded light curves are re-sampled to 200 bins. The fractional transit duration was tested between 0.006 and 0.1 phase units. For each input light curve, we detect the four best-fitting periods with the BLS algorithm and then perform the trapezoidal re-fit for each of them. We then select the period that has the lowest χ^2_{dof} of the improved V-fit.

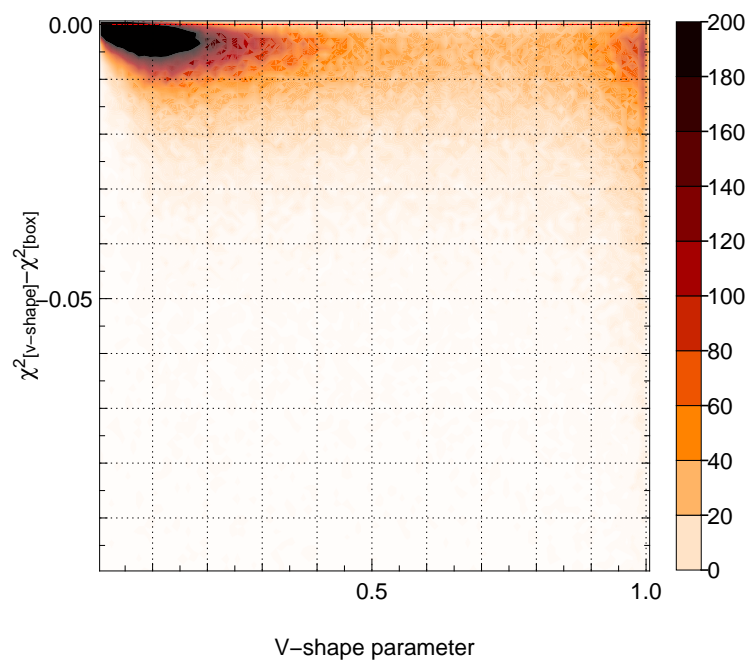


Figure 4.4: χ^2_{dof} comparison between trapezoid-fit and box-fit for transit detections. Since the box-fit is actually included in the trapezoid-fitting (i.e., $V = 0$), positives values are not expected in this plot. On the other hand, a significant improvement in the trapezoid-fit is achieved specially for higher values of V . The plot shows the density of data points and is scaled in 100×100 bins.

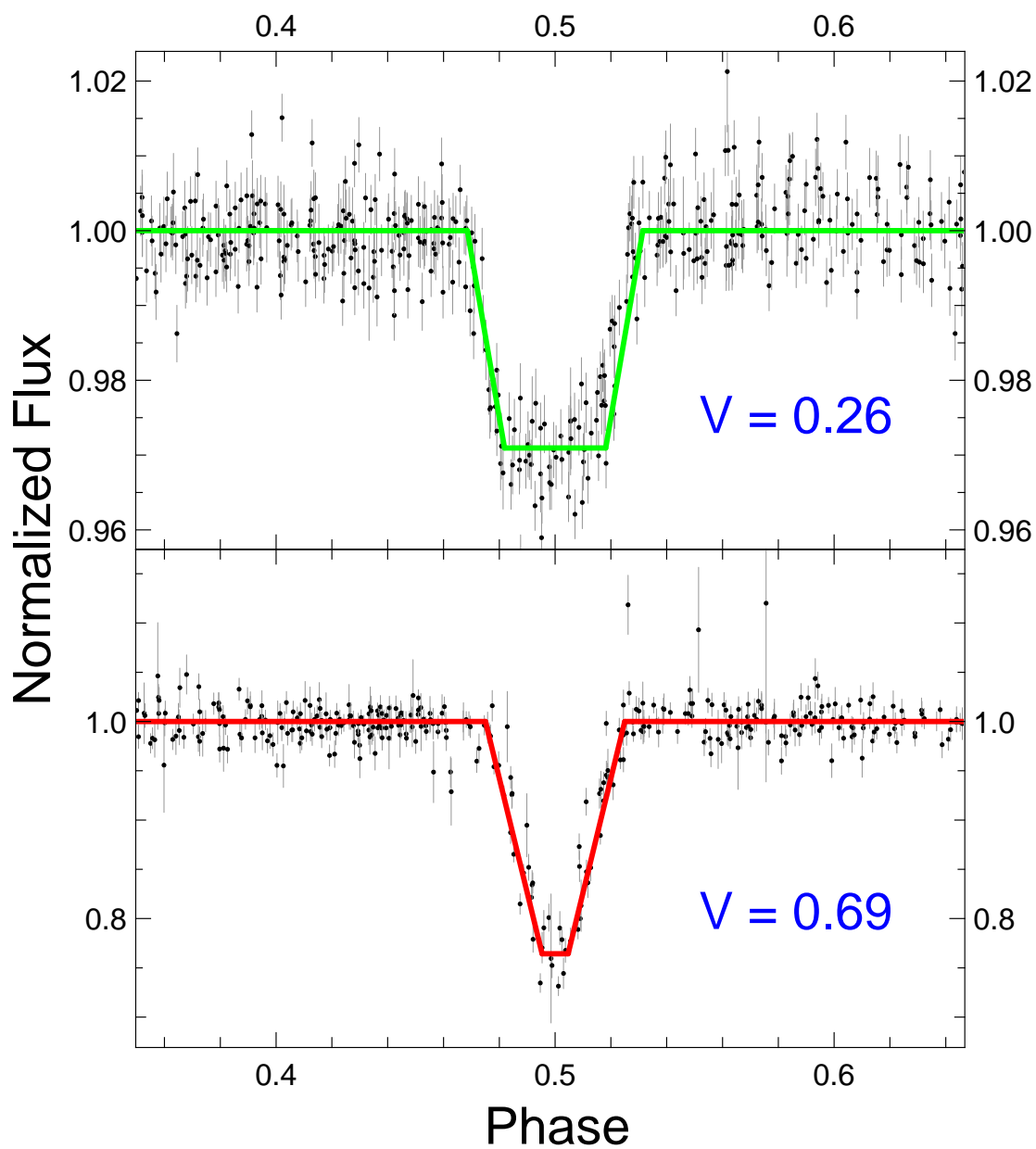


Figure 4.5: Folded light curve of WTS-2b and the corresponding fitting model (green-solid line in upper panel), which shows a box-like shape ($V = 0.26$). The lower panel shows an eclipsing binary detected in the WTS, in which the best-fitting model presents a very V -shaped primary eclipse ($V = 0.69$; red-solid line).

Chapter 5

Selection Criteria

In Section §1.5.7, we describe the different types of false-positives that affect transit surveys. Since false-positives represent an important problem while identifying planet candidates, transit surveys require strategies to efficiently weed up the large number of false-positives in the candidate samples and reduce the number of light curves visually inspected to identify the best candidates. In previous sections, we also mentioned that false-positives can have different origins; for example, a light curve holding a significant number of systematic outliers, or real variability of the flux from the host star (e.g. eclipsing binary systems or variable stars). To deal with these problems, several methods have been suggested to reduce the number of false-positives and facilitate the selection of the best candidates. For instance, Burke et al. (2006) proposed a series of selection criteria based on a χ^2 -minimization equivalent to the analytic solutions provided by BLS method. Later on, Hartman et al. (2009) presented selection criteria divided in different steps, which include the signal-to-pink noise ratio¹ (Pont et al., 2006), the number of data points in the light curves, a magnitude limit, and exclusion of sources with alias periods between 0.99 and 1.02 d or less than 0.4 d. Nevertheless, the majority of selection criteria only remove false-positives not related to real astrophysical variability. Here we propose a selection criterion with the ability to exclude false-positives by taking into account elements from the transit detection algorithm, as well as a new criterion named *V*-shape parameter (see 4.2) that is designed to recognize automatically eclipsing binary systems.

5.1 Description of the Selection Criteria

Due to the large number of light curves in the WTS, it is necessary to set up a number of selection criteria to automatize the selection of candidates and efficiently reduce the number of false-positives in the survey. The selection criteria presented in this work include 8 steps, of which 6 are based on the experience of previous works (Burke et al., 2006; Hartman et al., 2009). The two remaining steps are defined from the results of our transit

¹In the transit statistic detection the white or uncorrelated noise is referred to the signal purely produced in a stellar light curve by a planetary transit. On the other hand, the red or correlated noise is caused by systematics related to changes in the airmass, atmospheric conditions, flat-field errors or detector effects. The signal-to-pink noise contains both components, the white and red noise.

detection algorithm that account for real stellar variability, namely the V -shape parameter and the $S/N - S/N_{rem}$. Particularly, these two criteria consider variability of the stellar flux originated by eclipsing binary systems, which are very common type of false-positives in large sets of light curves. The majority of the selection criteria reported in the literature only remove false-positives caused by systematic errors accumulated during the signal measurement process; so that, the V -shape parameter and the $S/N - S/N_{rem}$ represent two new methods to automatically reject eclipsing binaries from transit surveys (see below).

As an initial cut of the selection criteria, we removed all objects with magnitudes $J > 18$. Objects below J -band = 16 are already difficult to follow-up; nevertheless, we decided to extend the magnitude cut (J -band = 17) used in Kovács et al. (2013) to make use of the improvement achieved by DI light curves for faint objects. In addition, we reject objects for which the detection algorithm found a period that is close to alias periods introduced by the window function of the observing strategy. In particular, we exclude objects with periods in the ranges 0.485-0.515, 0.985-1.015, 1.985-2.015 and 2.985-3.015 d. As an example, Figure 3.5 shows the high number of detections found around the one day alias period. For the sub-field 19g1, we additionally exclude a narrow period range 1.350-1.352 d due to a very high number of false positives in this range. We below introduce six more selection criteria:

- i) **S/N :** One of the most important criteria is the S/N of the eclipse measured from the light curves. In the past, many authors have used different ways to calculate the S/N and many different ways of utilizing it as a selection criterion. For instance, Burke et al. (2006) include the signal-to-white-noise in their selection criteria to set the threshold to $S/N \geq 10$. Hartman et al. (2009) propose the same limit of $S/N \geq 10$, but the threshold corresponds to the pink noise (Pont et al., 2006) in their case. Kovács et al. (2013) use the red noise to fix the detection limit; they suggest a signal-to-red noise of $S_{red} \geq 6$. Our S/N selection criterion accounts only for white noise.
- ii) **$S/N - S/N_{rem}$:** A large fraction of false positive detections are variable stars. To eliminate them, we use a new detection criterion, labeled $S/N - S/N_{rem}$, which is the difference of the S/N found in the BLS analysis and the S/N_{rem} found in a second pass of the algorithm after masking all points during the eclipse that has been detected in the first interaction. For a planet candidate, $S/N - S/N_{rem}$ is very high since the variability is confined to the transit phase. For variable stars, such as eclipsing binaries or sinusoidal variables, there is still variability left, which results in a low value of $S/N - S/N_{rem}$. Note that this criterion eliminates the detection of systems with more than one transiting planet. However, we decided to only search for systems with a single transiting planet, since the WTS survey is only sensitive to periods smaller than ten days.
- iii) **Number of transit points:** Many light curves result in a high S/N detection but only very few points belong to the transit. We therefore require a minimum number of transit points in our candidate selection process. Due to the scheduling of the

WTS, we do not require a minimum number of individual transits as an additional criterion, since a reduce number of transit points guarantees implicitly two transits or more.

- iv) **V_{shape}** : One selection criterion that has not been used in previous studies is the V -shape parameter, which was defined in the previous section. The criterion acts as a filter to eliminate false-positives generated by eclipsing binary systems. An eclipsing binary would be characterized by a very V-shaped eclipse, which has a high V value.
- v) **Depth**: Some detections show a very deep transit signal. A typical brightness dimming that corresponds to a Sun-like star and a Jupiter-like planet is about 1 %. Transit signals that are much deeper are more likely to be eclipsing binary stars. Using a cut on the maximum allowed transit depth we reduce the number of false positive detections. For Jupiter-sized planets around M-dwarfs, the transit depth can be even higher than 10 %. We therefore optimize the detection criteria for M-stars independently (see below).
- vi) **Transit duration**: We impose a limit on the fractional transit duration to exclude candidates that show long eclipses, which are not physically realistic.

5.2 Optimization of Selection Criteria

We optimize our selection criteria with Monte-Carlo simulations by injecting artificial transits in the WTS light curves and recovering the signal with the selection criteria described above (see details in Section §5.3). We split the light curves in two data sets, one for F-G-K stars and one for M-stars. The optimization of the selection criteria was done separately, since we expect some parameters to differ between both data sets. For instance, the transit depth is generally larger for planets that orbit M-dwarfs, and the fractional transit duration is smaller. The optimization of the selection criteria allows us to set a detection efficiency for both sets of light curves and the expected number of planets than can be found in the survey. In addition, the particular analysis of the M-dwarf sample enables the derivation of an upper limit on the occurrence rate of Jupiter-sized planets around low-mass stars (see Section §6.2). In the following sections, we describe the simulation used to optimize the selection criteria and the optimization strategy, and report the optimized selection criteria and corresponding detection efficiency for both data sets. The best candidates that pass the optimized selection criteria are also presented and discuss in detail in the following sections.

5.3 Simulations and optimization strategy

The optimization of the selection criteria is largely based on the simulations described in Koppenhoefer (2009). A final set of optimized selection criteria is obtained by using

such simulations and following the strategy described below. Figure 5.1 summarizes the process of the selection criteria optimization. In a first stage, Monte Carlo simulations are performed by injecting transiting signals in the original WTS DI and AP light curves. The artificial signal is produced using stellar parameter distributions (radius and mass) from the Besançon model of the galaxy (Robin et al., 2003). The chosen stellar parameters are a representative sample of spectral type and magnitude distributions of 1 square degree of the WTS-19h field centered at RA = 19^h34^m48^s and Dec = +36^d01^m45.6^s). Besides stellar radius and masses, spectral classes and J -band magnitudes are also obtained from the Besançon model. The simulations also require limb-darkening coefficients to model the transits, which are deduced from T_{eff} and $\log g$ according to Claret & Bloemen (2011).

The simulations test a 1 R_{Jup} planet population with periods homogeneously distributed in the range from 0.5 to 12 d for F-G-K stars and 0.8 to 10 d for M-dwarfs. The prediction of transits also needs the frequency of stars (f_{\star}) of a specific spectral type that actually have a transiting planet. We use the frequency of planet reported in Gould et al. (2006) that provides an occurrence rate for short-period Jupiter-sized planets of 0.5 %. This frequency was estimated by comparing the number of planets detected in the OGLE-III survey with the number of stars that are sensitive in the survey. For each light curve of the WTS, we pick a random star from the Besançon model that has a similar magnitude ($\Delta_{\text{mag}} \leq 0.05$). Subsequently, a planet with a random oriented inclination vector and period (within the range described above) is assigned to each selected star according to the fraction of stars with this planet population. For each pair star-planet, a transit signal is injected into the light curve using the stellar and planet parameters, inclination, and epoch of the transit. The transit is modeled according to the analytic formula presented in Mandel & Agol (2002), which accounts for ingres/egress and limb-darkening effects. In a computer cluster, we ran 100 simulations for F-G-K stars and 300 for M-dwarfs. We increase the number of simulations for M-dwarfs by a factor of three to statistically compensate the lower number of these stars (about 10 % of the F-G-K star sample). In each run, each light curve is considered once for a transit injection. In order to save computation time, we simulate only those cases, in which the randomly drawn inclination vector allows transit signal to be detected, depending on the geometric probability (P_{tr}) of having a transit in a randomly oriented planetary system (see Section §1.5.6). This constrain results in about 1 200 000 simulated light curves for F-G-K stars and 190 000 for M-dwarfs, which represent an average geometrical transit probability of ~ 11.9 % and ~ 6.1 % for F-G-K stars and M-dwarfs, respectively. Once the simulation are finished, we run our detection algorithm on the modified light curves. In order to consider a true detection, we require the detected period (P_{det}) to be within 1 % of the simulated period (P_{sim}), also allowing values of half, double, and three times of this period. In Figure 5.2, we present a histogram that shows the distribution of the quotient $P_{\text{sim}}/P_{\text{det}}$, where a high number of detections have periods of about 0.5, 1, 2, and 3 times the simulated period.

Once the period match is completed and true detections of the modified light curves are identified, the next step in the optimization of the selection criteria is to remove objects with periods that are close to the alias periods as described in the previous section. This process is carried out in both the simulated and unmodified light curves. In the following,

we simultaneously apply the remaining criteria on both sets of light curves, providing a certain number of recovered detections. These detections are designated as positives and negatives, which correspond to objects that pass the criteria on the modified and original light curves, respectively. Objects from the unmodified set of light curves that pass the criteria (negatives) are considered as false-positives, i.e, we assume that there are no true detections in the original light curves. During this process, we test a wide range of values for each criterion, resulting in a different number of positives and negatives for each set of trial parameters. The final set of selection criteria is determined by fixing the number of negatives while maximizing the number of positives. That is, we select the set of parameters that provide the selected number of negatives, and at the same time minimize the number of true detections (positives) that do not pass the criteria. The number of negatives is strategically selected to be small enough to allow a visual inspection of each detected object and significantly larger than the expected number of planet detections. In the next sections, we report the optimized selection criteria for F-G-K stars, and present the best transiting candidates that pass the optimized selection criteria from the two different samples (DI and AP sets). The optimized selection criteria for M-dwarfs and transiting candidates are presented in Chapter §6.

5.4 Candidates detected around F-G-K stars

After running the simulations, we optimized the selection criteria presented in Section §5.1 for the DI and AP light curves of F-G-K stars. We allowed up to 100 detections on the unmodified light curves on each data set. This number was selected by comparing the total efficiency as a function of detections, while finding a reasonable compromise between number of detections and efficiency (see Figure 5.3) as described in previous section.

Tables 5.1 and 5.2 list the optimized selection criteria for the DI and AP light curves for F-G-K stars and provide the number of objects that remain after each of the selection criteria is applied. In this case, the fractional transit duration turned out to be a useless criterion to detect candidates around these stars. As shown in Figure 5.4, these selection criteria allow us to recover 27/12 % of the signals injected into the DI/AP light curves with $S/N \sim 18/11$ (our minimum required S/N) and up to 80/80 % with $S/N \geq 40/30$, respectively. The resulting total efficiencies are discussed in Section 5.4.4. Note that before applying the magnitude limit, the number of light curves in the DI and AP data sets differ at the 10 % level. This is because the object detection in the DI analysis was going slightly deeper than in the AP analysis. In order to test whether the selection criteria differ from one to another detector, we initially optimize them for each of the sub-fields independently but found almost identical values. We therefore decided to use one single set of selection criteria for F-G-K stars in the the whole 19hrs field.

We visually inspect the 200 detections that pass the optimized selection criteria in the AP and DI data sets to remove candidates that are clear eclipsing binaries with two eclipses of different depth. We also reject objects that show significant out of eclipse variations,

Criterion	Remaining objects	Removed objects	%
$J \leq 18$	102428	362445	76.26
Removed alias period	72012	30416	29.69
$S/N > 18$	7080	64932	90.17
$S/N - S/N_{rem} > 8$	3391	3689	52.10
Transit points > 24	506	2285	85.08
$V_{shape} < 0.6$	288	218	43.08
Depth $\leq 4\%$	100	188	65.27
Transit duration ≤ 0.5	100	0	0.00

Table 5.1: Objects removed by the selection criteria from an original sample of 464873 DI light curves. The number of DI candidates after applying all criteria is 100.

Criterion	Remaining objects	Removed objects	%
$J \leq 18$	102428	326500	74.32
Removed alias period	73201	29227	28.53
$S/N > 11$	5778	67423	92.11
$S/N - S/N_{rem} > 6$	1760	4018	69.54
Transit points > 18	563	1197	68.01
$V_{shape} < 0.7$	360	203	36.06
Depth $\leq 3\%$	100	260	72.22
Transit duration ≤ 0.5	100	0	0.00

Table 5.2: Objects removed by the selection criteria from an original sample of 428928 AP light curves. The number of AP candidates after applying all selection criteria is 100.

very asymmetric eclipse shapes, and candidates which are too noisy to be further analyzed. Figure 5.5 shows an example of an object that was rejected by visual inspection from the candidate list. Our final list of candidates includes eleven objects, of which seven were detected in the AP-light curves and six are from the DI light curves. Two objects were detected in both the DI and AP light curves. One of this detections is WTS-2b that has recently been confirmed as a planet by the Rocky Planets Around Cool Stars² (RoPACS) community (Birkby et al., 2013a,b). The other planet that has been found in the WTS is

²RoPACS is a Marie Curie initial training network. The research of the RoPACS community is based on the data obtained of the WTS.

WTS-1b (Cappetta et al., 2012), which was not detected by our selection criteria due to a very low S/N value.

In the following, we present a detailed analysis of the ten remaining candidates that includes a characterization of the host stars, a light curve fit with an analytic transit model, and a test for double-eclipse binary scenarios. This analysis provides important physical parameters of the host stars and companions, which are used to assess the quality of the candidates. Figure 5.6 shows the folded light curves of our candidates.

5.4.1 Characterization of the host star

The broadband photometric measurements of the host stars of the candidates are listed in Table 5.3. The WFCam provides photometry in five bands (Z, Y, J, H, K). Additional measurements in five optical bands (u, g, r, i, z) were obtained from the database of the Sloan Digital Sky Survey Data Release 7 (SDSS DR7, Adelman-McCarthy & et al. 2009). The table also shows the data set, in which the candidates were detected (DI or AP). The candidate 19b1-02162 was found in both AP and DI data sets. For this case, we use the AP light curve to carry out the analysis, since it presents a lower scatter than the DI light curve. The characterization of the host star is essential for inferring physical properties of the candidates, such as planetary radius and orbit inclination. The Virtual Observatory SED Analyzer³(VOSA, Bayo et al. 2008) is an on-line tool designed to automatically perform several tasks, such as the determination of stellar parameters by analyzing the SED. This analysis was carried out in our candidates using the photometry reported in Table 5.3. The VOSA works with input parameters that can be submitted as ASCII files. They must include a reference name of the source, coordinates, visual extinction A_v , filter names, observed fluxes, and the corresponding errors. Although the VOSA enables us to select among six different fitting models, only two are appropriate for our purpose. For the F-G-K stars, we adopt the Kurucz ATLAS9 templates described in Castelli et al. (1997), which provide better results for a wider temperature range than the NextGen model (Baraffe et al., 1998). The program offers the option of restricting free parameters (T_{eff} , $\log g$ and $[\text{Fe}/\text{H}]$) to speed up the fitting process. We confine the limits to $T_{\text{eff}} = 3\,500\text{--}10\,000\text{K}$, $[\text{Fe}/\text{H}] = 0.0$ and $\log g = 3.5\text{--}5.0$. Note that the selected values of T_{eff} and $\log g$ are compatible with main-sequence stars with spectral types between A and M. The program compares the broadband photometric measurements to theoretical synthetic spectra to find the best-fitting SED. The VOSA tests a large range of stellar models within the given parameter limits. The SED-fit is also sensitive to the extinction A_v , which is used as an additional free parameter. The extinction and the corresponding SED model are obtained by testing 100 different A_v values, which are distributed in a range from 0.01 to 1 magnitudes. We select the values that result in the lowest χ^2 within the valid extinction range from 0.01 up to the maximum allowed extinction that is set by the total Galactic extinction. This upper limit is obtained from the Galactic extinction

³<http://svo2.cab.inta-csic.es/theory/vosa/>

calculator of the NASA/IPAC extragalactic database⁴ (see Figure 5.7). In some cases, the absolute minimum corresponds to an extinction that is higher than the upper limit. For these cases, we select the best solution that are within the allowed range. In Tables 5.4 and 6.4, we mark these particular cases with an asterisk. The resulting best-fitting model provides an estimate of the T_{eff} of the host stars, which are also summarized in Table 5.4 and 6.4. The results show that the T_{eff} of the parent stars are in the range of 4750-6500 K, which corresponds to spectral types between K3 and F5. According to the T_{eff} found in the fit, we derive stellar radii and masses and calculate the surface gravity $\log g$ using 1-5 Gyr isochrones for solar metallicity obtained from the Dartmouth stellar evolution database (Dotter et al., 2008). These values are reported in Tables 5.4 and 6.4 as $R_{1\star}$, M_{\star} , and $\log g_1$. The error ranges of the stellar radii is determined by assuming a precision of 250 K, which is the step size of the grid used in the VOSA fit. Figure 5.8 shows an example of the VOSA fit of our best candidate 19b1-02162.

⁴<http://ned.ipac.caltech.edu/forms/calculator.html>

Optimization of Selection Criteria

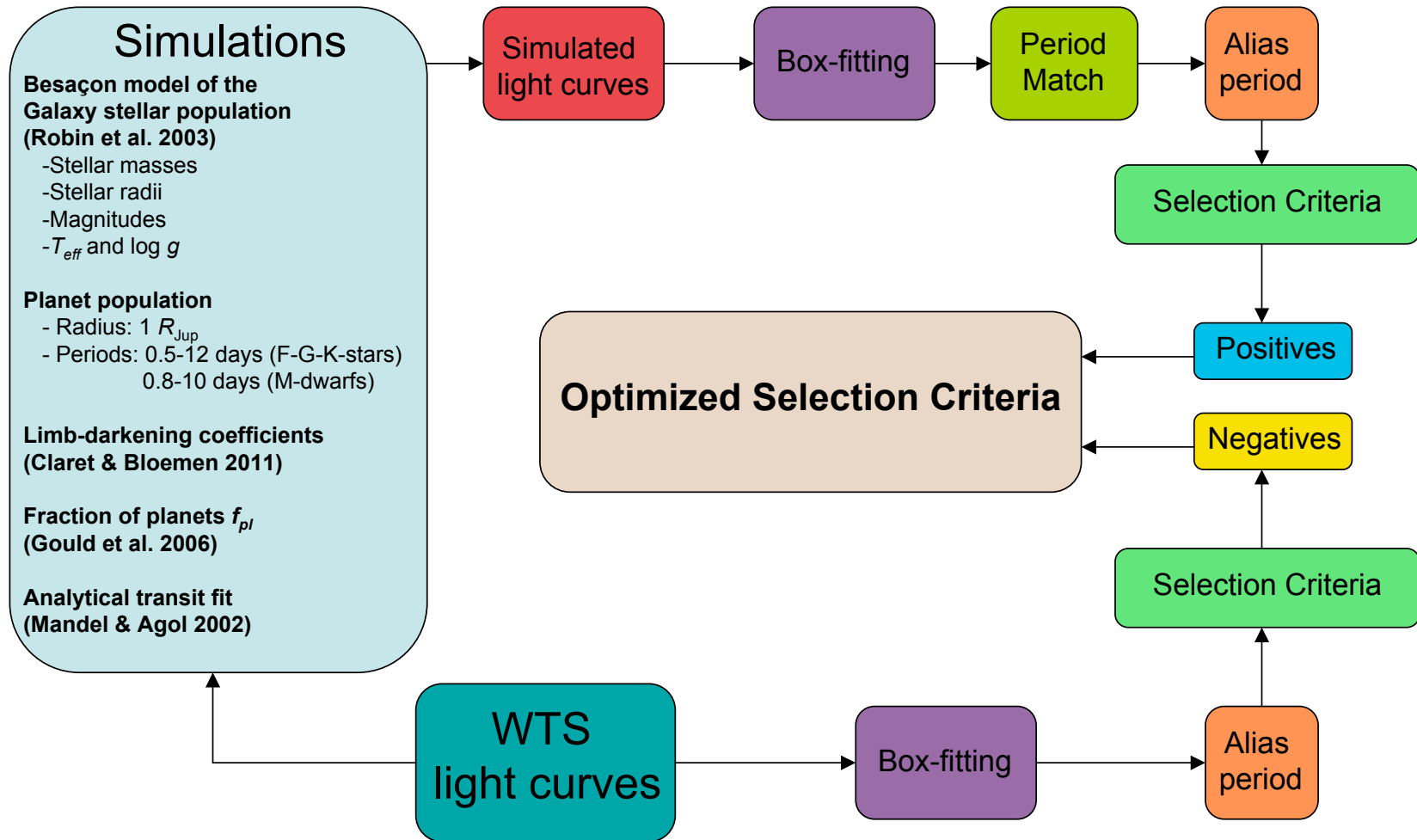


Figure 5.1: Optimization of selection criteria process based on Monte Carlo simulations that includes an analytic transit model.

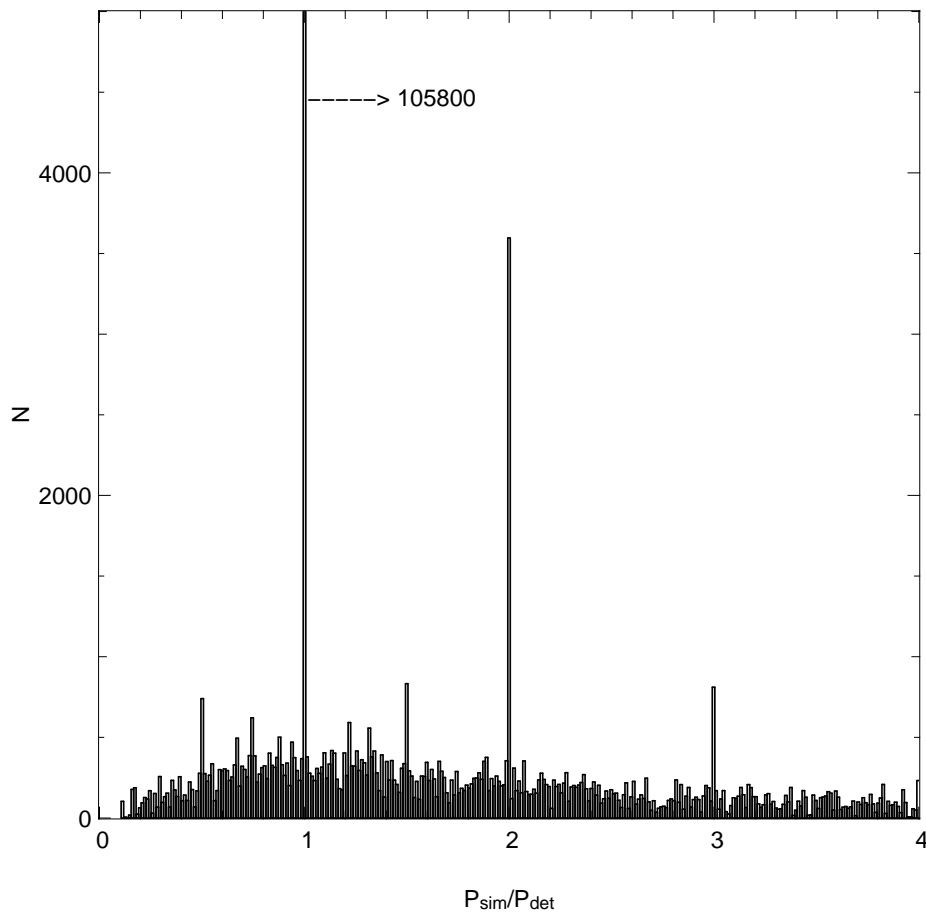


Figure 5.2: Comparison between the P_{sim} and P_{det} . The histogram shows the distribution of the quantity $P_{\text{sim}}/P_{\text{det}}$, where a true detection is considered if such objects have periods that differ 1 % of 0.5, 1, 2, and 3 times the simulated period.

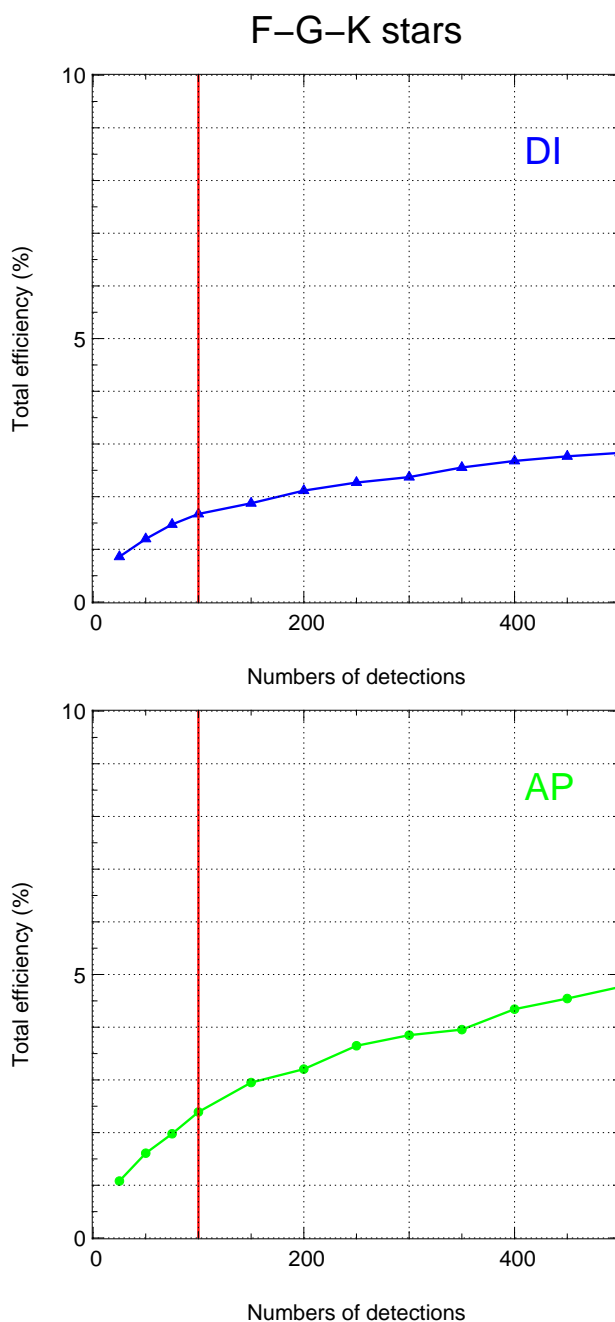


Figure 5.3: Detection efficiency for F-G-K stars derived from the optimized selection parameters as a function of the detections in the unmodified light curves (negatives). The upper panel shows the detection efficiency reached by the DI-light curves, while the lower panel shows the efficiency of AP light curves. We fix the number of detections on the unmodified WTS light curves to 100, since this number enables us to easily inspect by eye the object that pass the selection criteria, while providing a number of detections higher than the expected number of planets. The red line shows our limit of 100 detections.

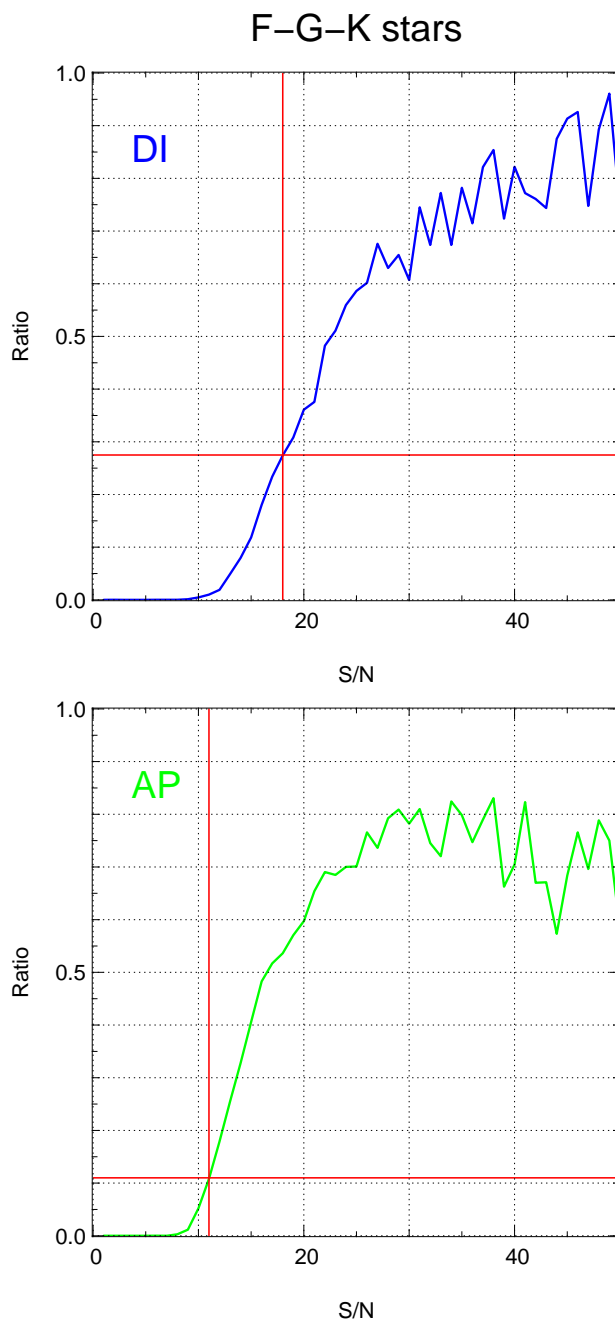


Figure 5.4: Detection efficiency for F-G-K stars as a function of S/N . Upper and lower panel show the cases for DI and AP light curves respectively. Vertical red-lines indicate the optimized S/N values (~ 18 and 11), which allow us to recover 27 and 12 % of the signal injected into the WTS light curves.

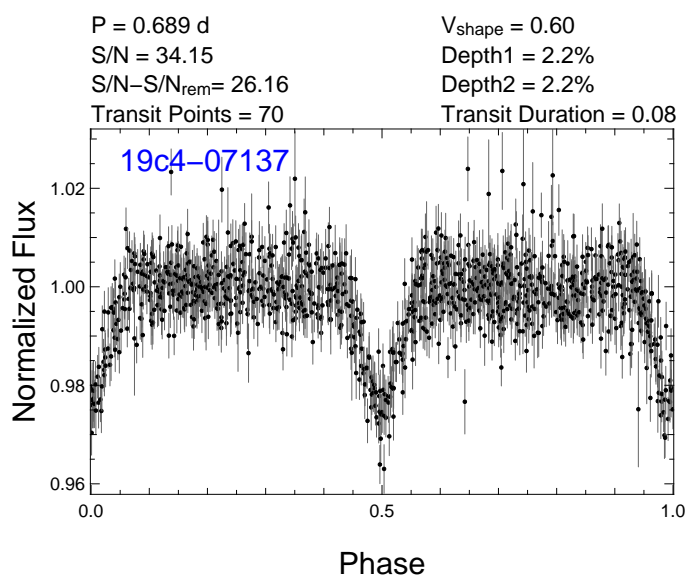


Figure 5.5: Example of an object that passes the optimized selection criteria and is rejected by visual inspection. The object 19c4-07137 was detected in the AP light curves because all values satisfy the cuts of the selection criteria. However, the phase folded light curve corresponds to double the right period ($P=0.689 \text{ d}$), so the real period is $P \approx 0.344 \text{ d}$, which is lower than the period of any known planet around F-G-K stars. The transits depths observed in the plot are the same, which is one hint to know that the light curve is folded with double the right period. On the other hand, the value of the $S/N - S/N_{rem}$ is very high; in a binary scenario, this value should be considerably lower, so the object would be automatically rejected by the selection criteria. Several detections with similar characteristics are excluded from the sample of objects that pass the optimized selection criteria.

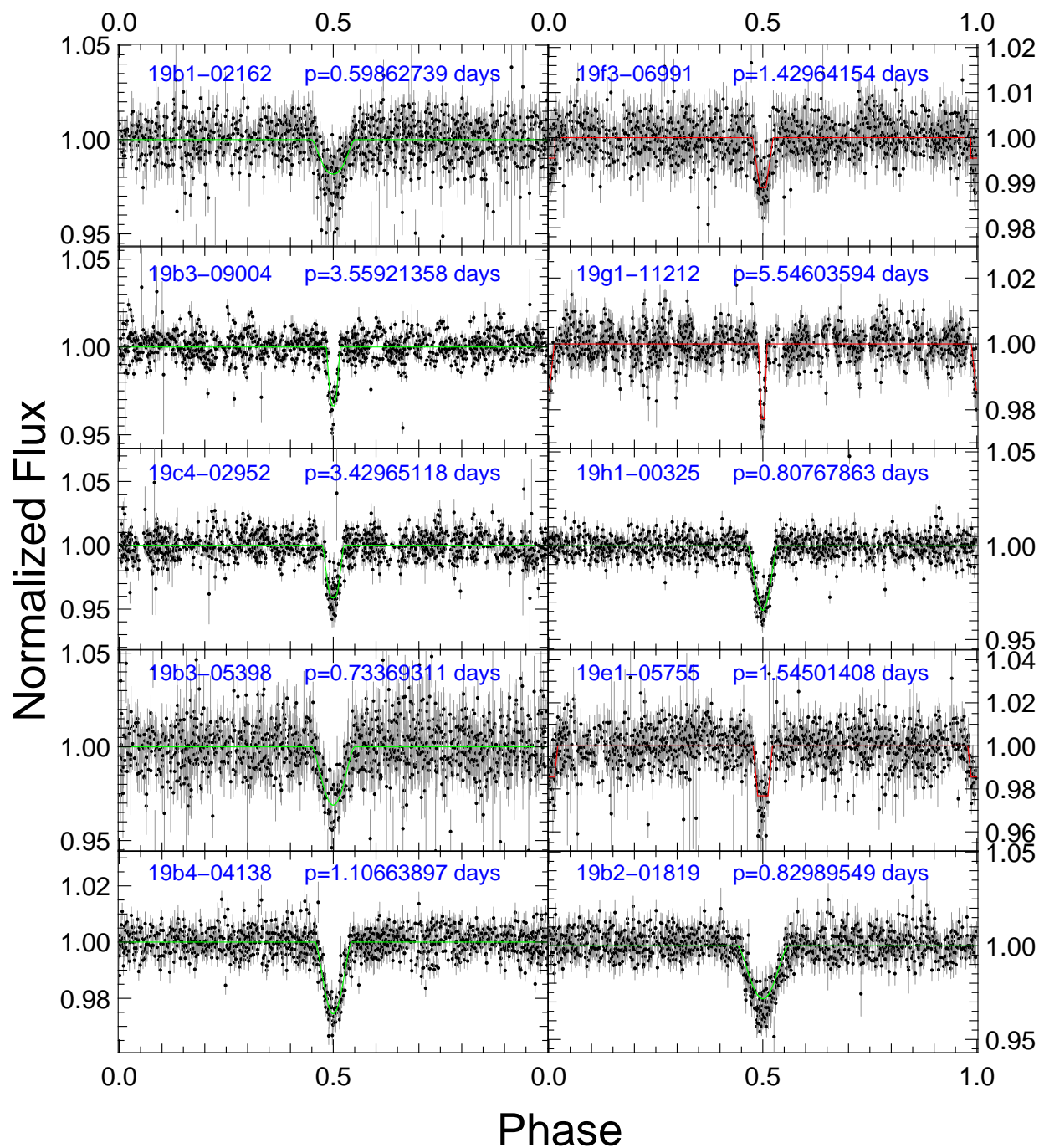


Figure 5.6: Phase-folded light curves of the ten candidates around F-G-K stars found in the WTS 19h field. We overplot the best-fitting single eclipse transit models (green lines) for all objects for which the binary fit does not show an improvement over the single eclipse. The light curves with two eclipses are shown together with the best-fitting trapezoid model (red lines).

Object	Data-set	α	δ	u	g	r	i	z	Z	Y	J	H	K
19b1-02162	AP/DI	293.0112	36.4848	19.00	17.73	17.13	16.89	16.76	16.37	16.22	15.93	15.49	15.37
19f3-06991	AP	293.4682	36.4995	15.97	14.66	14.26	14.13	14.07	13.62	13.56	13.34	13.07	13.02
19b3-09004	DI	293.5208	36.8839	17.97	16.60	16.03	15.80	15.67	15.25	15.17	14.85	14.45	14.39
19g1-11212	AP	293.6753	36.1420	16.57	15.40	14.93	14.81	14.74	14.32	14.25	14.01	13.73	13.65
19c4-02952	DI	293.8666	36.7571	18.53	17.38	16.97	16.79	16.70	16.23	16.11	15.83	15.51	15.46
19h1-00325	AP	294.1531	36.0794	19.55	17.18	16.19	15.84	15.60	15.28	15.03	14.60	14.09	13.91
19b3-05398	AP	293.4401	36.7404	20.51	18.67	18.08	17.81	17.65	17.24	17.12	16.78	16.40	16.33
19e1-05755	DI	292.6870	36.2186	18.04	17.09	16.54	16.29	16.20	15.84	15.73	15.42	15.08	15.01
19b4-04138	AP	292.9365	36.7902	17.04	15.70	15.18	14.95	14.86	14.38	14.28	13.96	13.54	13.47
19b2-01819	DI	293.5220	36.4675	18.27	16.95	16.48	16.32	16.25	15.86	15.75	15.46	15.13	15.07

Table 5.3: List of new candidates around F-G-K stars detected in this work. The second column shows the light curve data set in which the candidates have been detected. The coordinates (J2000.0) are listed in columns 3 and 4. The remaining columns provide broadband photometric measurements of our candidates in ten different filters. The u, g, r, i, z AB-magnitudes were obtained from the Sloan Digital Sky Survey (SDSS) and the Z, Y, J, H, K magnitudes are WFCam measurements in the Vega-system.

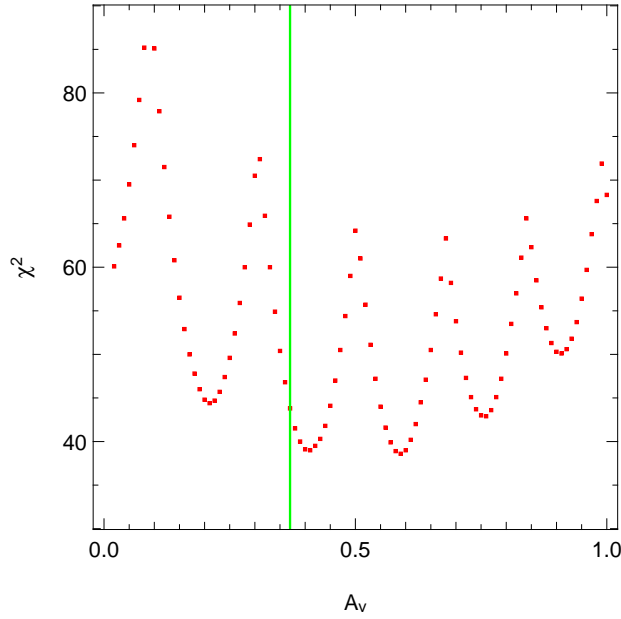


Figure 5.7: χ^2 as a function of the input visual extinction values that are used in the SED fit of our planet candidate 19b1-02162. Although the value of $A_v \sim 0.6$ mag results in the lowest χ^2 , we use the value of $A_v = 0.21$ mag, which is based on the upper limit extinction adopted from the NASA/IPAC Extragalactic Database, since an extinction of $A_v = 0.6$ mag would be physically non-realistic. The upper limit mentioned above is shown with the green solid line. The periodic distribution of the χ^2 is due to the variation of six different stellar spectral-types.

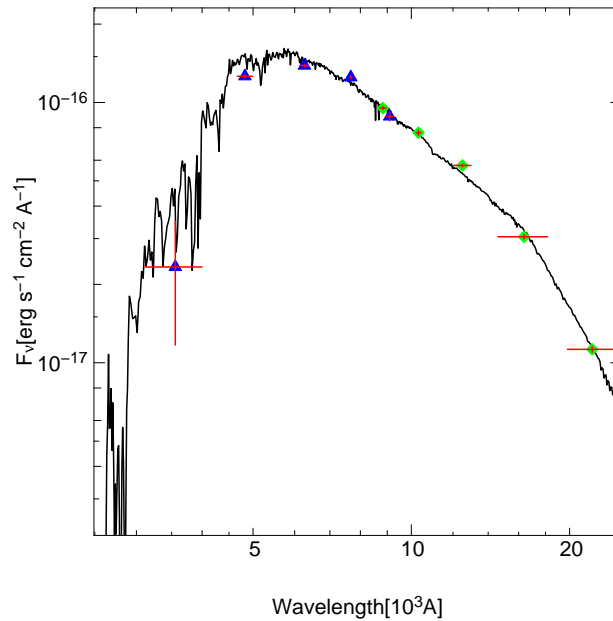


Figure 5.8: Best Kurucz ATLAS9 model derived with the VOSA (black line) for the SED of 19b1-02162. The effective temperature of the best-fitting model is $T_{\text{eff}} = 5500$ K for an extinction of $A_v = 0.21$. Blue triangles represent the SDSS photometry, while the green diamonds correspond to the WFCam photometry. Vertical and horizontal errors bars are the flux uncertainties and the equivalent width of each pass band.

Object	T_{eff} (K)	Spectral Type	$\log g_1$	$\log g_2$	A_v	Distance(pc)	$R1_{\star}(R_{\odot})$	$R2_{\star}(R_{\odot})$	$M_{\star}(M_{\odot})$
19b1-02162	5500	G8	4.56	4.32	0.21*	2188	$0.85^{+0.07}_{-0.05}$	$1.12^{+0.07}_{-0.12}$	$0.95^{+0.07}_{-0.06}$
19f3-06991	6500	F5	4.31	4.05	0.35	1127	$1.23^{+0.20}_{-0.10}$	$1.74^{+0.38}_{-0.16}$	$1.25^{+0.13}_{-0.08}$
19b3-09004	5750	G5	4.52	4.27	0.28	1472	$0.92^{+0.08}_{-0.07}$	$1.22^{+0.03}_{-0.04}$	$1.02^{+0.07}_{-0.07}$
19g1-11212	6250	F7	4.41	4.00	0.22*	1330	$1.13^{+0.20}_{-0.12}$	$1.78^{+0.27}_{-0.18}$	$1.17^{+0.09}_{-0.08}$
19c4-02952	6250	F7	4.41	4.01	0.44*	3119	$1.13^{+0.20}_{-0.12}$	$1.77^{+0.11}_{-0.07}$	$1.17^{+0.09}_{-0.08}$
19h1-00325	4750	K3	4.57	4.43	0.16	773	$0.71^{+0.03}_{-0.04}$	$0.89^{+0.08}_{-0.05}$	$0.78^{+0.04}_{-0.05}$
19b3-05398	6000	G0	4.47	4.19	0.45	4345	$1.00^{+0.13}_{-0.08}$	$1.39^{+0.08}_{-0.07}$	$1.09^{+0.17}_{-0.07}$
19e1-05755	6000	G0	4.47	4.12	0.38	2208	$1.00^{+0.13}_{-0.08}$	$1.51^{+0.06}_{-0.14}$	$1.09^{+0.17}_{-0.07}$
19b4-04138	5750	G5	4.52	3.96	0.45	506	$0.92^{+0.08}_{-0.07}$	$1.74^{+0.03}_{-0.05}$	$1.02^{+0.07}_{-0.07}$
19b2-01819	6250	F7	4.41	3.93	0.38	2559	$1.13^{+0.20}_{-0.12}$	$1.94^{+0.04}_{-0.05}$	$1.17^{+0.09}_{-0.08}$

Table 5.4: Characterization of host F-G-K stars. The T_{eff} is derived from SED-fit. We use 1-5 Gyr isochrones obtained from the Dartmouth stellar evolution database (Dotter et al., 2008) to estimate $R1_{\star}$, $\log g_1$ and M_{\star} . The extinction values (A_v) found in the SED-fit are reported in column 6. In the three cases marked with an asterisk, the best-fitting extinction is higher than the total extragalactic extinction and we report the extinction that corresponds to the minimum χ^2 within the allowed extinction range. The stellar radii $R2_{\star}$ correspond to the best-fitting analytic transit model (see Section 5.4.3). The values of $\log g_2$ reported in column 5 are estimated from the stellar radii $R2_{\star}$, which tend to be higher than $R1_{\star}$, resulting in lower $\log g_2$. The distances reported in column 7 are estimated utilizing the extinction values found in the VOSA analysis, the i -band magnitudes reported in Table 5.3, and the absolute magnitudes M_i , which are obtained from the isochrones.

5.4.2 Secondary eclipse fit

For each candidate, we tested the possibility that we actually detected an eclipsing binary system with similar eclipse depths, where the primary and secondary eclipse have been folded together at half the binary period. To carry out this test, we fold the light curve of each candidate with double the detected period, and fit a primary and secondary eclipse which are offset by 0.5 phase units assuming a circular orbit. Under this assumption, our candidate sample may be contaminated with eclipsing binaries in high eccentric orbits. However, Devor (2005) shows that only $\sim 10\%$ of the binaries studied there with periods shorter than 12 d have eccentricities higher than 0.1. Therefore, the possible contamination is low to start with. Moreover, any candidate with a clear deeper secondary eclipse would be rejected during our visual inspection. Both the primary and secondary eclipses are first fitted with a box and subsequently re-fitted with a symmetrical trapezoid, as described in Section 4.2. A significant difference between the depths of the primary and secondary eclipse indicates that the candidate could be an eclipsing binary rather than a star with a planet. Also a comparison of the χ_{dof}^2 of the binary fit to the χ_{dof}^2 of the fit with the planet period can indicate that the candidate is actually a binary with similar eclipse depths. We would like to point out that the decision of presenting either the planet or binary periods includes a visual examination of the folded light curves (Figures 5.6 and 6.4). This inspection showed that χ_{dof}^2 and eclipse depth differences cannot be used blindly for the discrimination, since they closely depend on the number of points during the eclipses and box-fitting parameters. Note that the trapezium fit is only a crude model of a transit light curve, and we found that the depth estimated by our algorithm did not reflect the true depth as one sees in the folded light curves in some cases. In summary, the discrimination between both scenarios based on the χ_{dof}^2 and eclipse depth values is only used as a hint for selecting either the planet or binary period rather than a decisive proof of the nature of the candidate. The final decision to classify our candidates was done case-by-case and primarily based on the best-fitting radius as found in the analytic transit fit (see Section 5.4.3). Table 5.5 summarizes the results of the secondary eclipse fit analysis.

Object	V	dp(%)	χ_{dof}^2	χ'_{dof}^2	dp $'_1$ (%)	dp $'_2$ (%)	V'_1	V'_2
19b1-02162	0.25	2.05	1.3792	1.3438	2.54	1.37	0.25	0.00
19f3-06991	0.56	0.81	1.0087	0.9545	1.08	0.47	0.58	0.33
19b3-09004	0.31	3.07	4.3247	4.2817	3.44	2.87	0.54	0.01
19g1-11212	0.37	1.49	1.4751	1.4301	2.29	1.34	0.45	0.81
19c4-02952	0.57	4.13	3.3622	3.3617	3.73	3.86	0.00	0.53
19h1-00325	0.43	3.11	4.0514	4.0172	2.92	3.05	0.16	0.38
19b3-05398	0.29	2.66	0.9802	0.9739	2.91	2.55	0.48	0.36
19e1-05755	0.29	1.76	1.7486	1.7211	2.54	1.66	0.80	0.54
19b4-04138	0.64	2.53	1.7270	1.7041	2.51	2.36	0.66	0.62
19b2-01819	0.45	2.80	2.7123	2.6819	2.74	3.07	0.61	0.65

Table 5.5: Comparison of the eclipse shapes, eclipse depths, and χ_{dof}^2 values of the planet scenario (left side of the table) and binary scenario (right side of the table) for F-G-K stars.

5.4.3 Transit fit

We carried out an improved fit to the J -band light curves of the candidates using analytic transit models proposed by Mandel & Agol (2002). For two candidates (19b1-02162 and 19b2-01819), we additionally used an i' -band light curve, covering one full eclipse, which was obtained in a photometric follow-up campaign at the INT on La Palma. In these cases, we performed a simultaneous fit to both light curves. The transit light curve model depends on quadratic limb-darkening coefficients, which were deduced from the linear interpolations in T_{eff} and $\log g$ of the values listed in Claret & Bloemen (2011). We used the T_{eff} of host stars that were previously obtained by the SED analysis (see Section 5.4.1) and the corresponding $\log g$ values from the 1-5 Gyr isochrones, assuming a solar metallicity $[\text{Fe}/\text{H}]=0.0$ and a micro turbulence of 2 km/s. We utilized the values derived from ATLAS atmospheric models using the flux conservation method (FCM). Alternatively, the values can be derived using the least-squares method (LSM). However, a test of the analytic transit fit was carried out by using the values from the two different models. The results showed the same goodness of the fit for both methods, so we have chosen the FCM over the LSM model without any specific preference. Using the WTS J -band light curve, we fitted the mean stellar density $\rho_{\star} \sim M_{\star} / R_{\star}^3$ in solar units, the radius ratio R_{p} / R_{\star} , the impact parameter β_{impact} in units of R_{\star} , the orbital period P , and epoch of the central transit t_0 . The iterative fitting process required starting values for a series of input parameters, such as period, epoch of transit, planet radius, and parameters related to the stellar companion, such as mass and radius. The period, epoch of transit, and planet radius were obtained directly from the results provided by our transit detection algorithm, while the stellar parameters ($R_{1\star}$ and M_{\star}) were estimated by using the previously fitted T_{eff} from the 1-5 Gyr model isochrones for solar metallicity (Dotter et al., 2008). From the best-fit of the analytic transit model, we were able to calculate the intrinsic physical parameters of the candidates and host stars, such as R_{p} and $R_{2\star}$.

The fitting procedure also enabled us to derive an error estimation of the fitted parameters. The errors were calculated using a multi-dimensional grid in which we searched for extreme points with $\Delta\chi^2 = 1$. This method corresponds to a variation of each single parameter, while minimizing over the others. The results of the transit fit are listed in Table 5.4 and 5.6. Figures 5.9 and 5.10 show the best-fitting model of our best candidate 19b-1-02162 in the J and i' -bands, respectively.

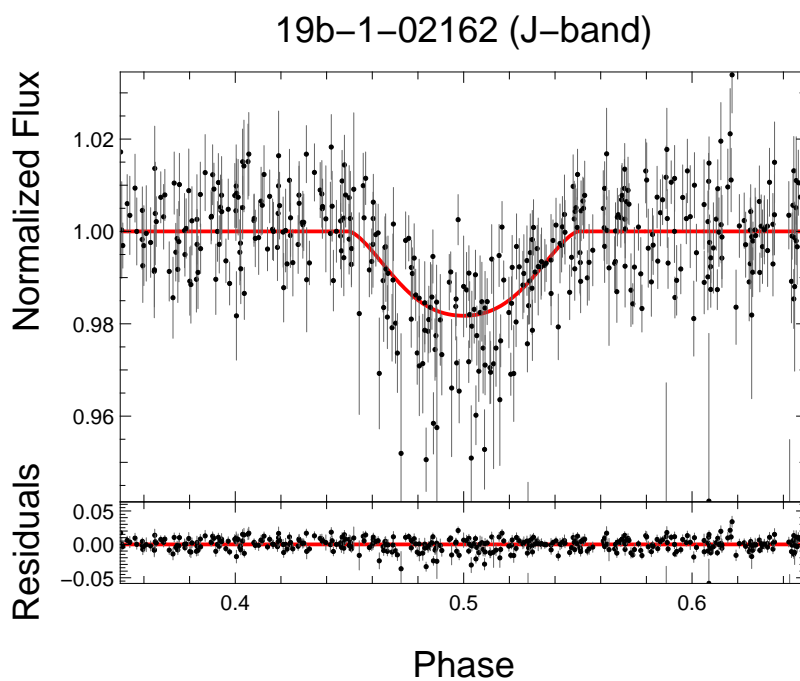


Figure 5.9: Best-fitting model of 19b-1-02162 using the J -band light curve. The top frame shows the best-fit, whereas the bottom frame represents the residuals of the fit.

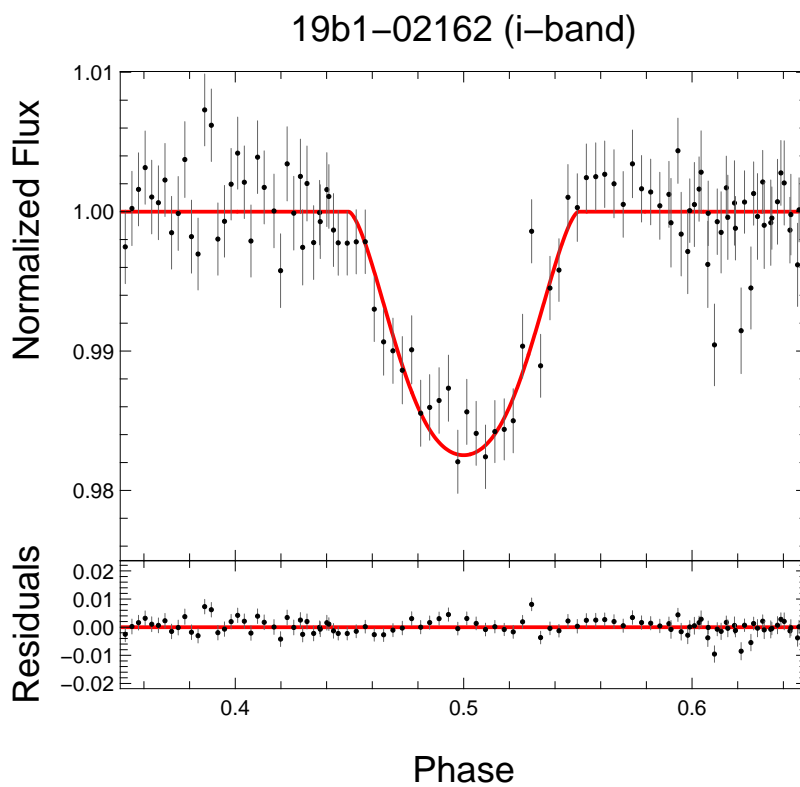


Figure 5.10: Best-fit of 19b-1-02162 using the i' -band light curve.

Candidate	Period(d)	t_0	$i(^{\circ})$	$R_p(R_{\text{Jup}})$	$R_{p,\text{min}}(R_{\text{Jup}})$	$R_{p,\text{max}}(R_{\text{Jup}})$	χ_{dof}^2	Classification
19b1-02162	0.59862739	2454317.7883529	72.01	1.61	1.40	1.97	1.31	P
19f3-06991	0.71482077	2454318.3894489	66.54	1.65	1.43	3.26	1.00	B
19b3-09004	3.55921358	2454320.9406801	84.31	2.22	2.10	2.32	2.07	B
19g1-11212	2.77301797	2454318.9644598	80.23	2.29	3.44	1.94	1.21	B
19c4-02952	3.42965118	2454319.6314035	82.25	3.54	3.36	3.81	1.84	B
19h1-00325	0.80767863	2454318.2698431	72.23	3.97	2.10	4.20	2.01	B
19b3-05398	0.73369311	2454317.9513207	67.12	4.20	3.53	4.99	1.18	B
19e1-05755	0.77250704	2454318.1282676	64.34	5.30	3.00	13.37	1.21	B
19b4-04138	1.10663897	2454318.0883407	67.34	6.14	4.17	8.32	1.30	B
19b2-01819	0.82989549	2454318.2785263	53.23	15.59	15.43	15.98	1.27	B

Table 5.6: Results of the transit fit. Orbital and planetary parameters derived from the analytic transit model. Only one candidate, 19b-1-02162, is considered to be a planet candidate. All other candidates are too large and most likely transiting brown dwarfs or low-mass stars.

5.4.4 Discussion of the candidates

Table 5.6 provides a list of our candidates sorted, according to their best-fitting radius. All candidates except for the first two have very large best-fitting radii, larger than all transiting planets published so far. We therefore conclude that they are systems with a transiting brown dwarf or a low-mass stellar companion.

The first two candidates have best-fitting radii of $1.61 R_{\text{Jup}}$ and $1.65 R_{\text{Jup}}$; however, the secondary eclipse fit results in a slightly better χ^2_{dof} for the binary scenario, and the primary and secondary eclipses show different depths, which are hints to select the binary period instead of the planet scenario. By looking at the folded light curves (Figure 5.6), the second candidate (19f3-06991) is a clear case where the fit with the binary period reveals two well sampled eclipses with different depths. The first candidate (19b1-02162) is not as clear. Although the binary period fit shows two different eclipses with depths of 2.5 and 1.4 %, the single eclipse observed in the i' -band coincides with the deeper eclipse, but has a depth of 1.8 % (see Figure 5.10), which is closer to the shallower eclipse. We therefore conclude that the correct period is unclear for this candidate, and we propose it as a target for high precision photometric follow-up. Figure 5.11 shows a J -band image of 19b1-02162.

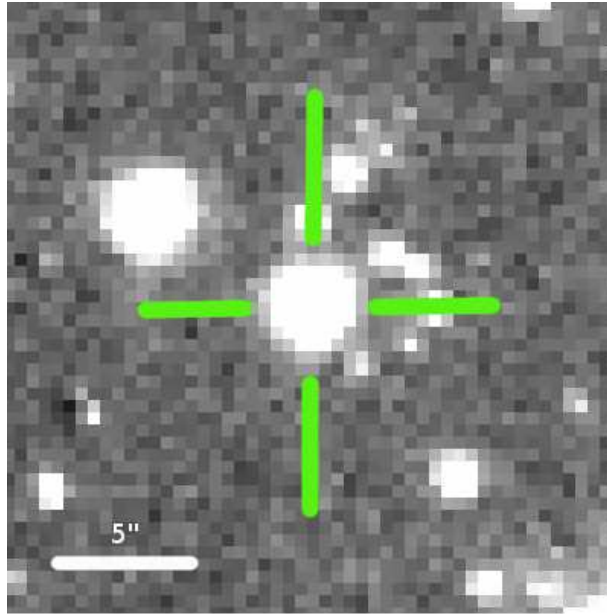


Figure 5.11: Zoom-in showing the crowded neighborhood of the candidate 19b1-02162 on the sky. Our DI pipeline is optimized to deal with such cases.

In order to estimate the number of planets that we expect to find around F-G-K stars in the WTS, we calculate the overall detection efficiency in our simulations by dividing the number of detections (objects that pass the optimized selection criteria on the modified light curves set) by the total number of simulated objects that have a transiting planet, which are $\sim 1.7\%$ and $\sim 2.4\%$ for DI and AP light curves, respectively. Accounting for an average geometrical probability of 11.9% to see transits (as derived from our Monte-Carlo

simulations) and using an occurrence rate for short-period Jupiter-sized planets of 0.5 % (Gould et al., 2006; Howard et al., 2012), we estimate the number of planets that we expect to find around F-G-K stars in the whole sample of 102 428 light curves to be 1.0 (DI) and 1.5 (AP). These values are calculated according to the expression from Burke et al. (2006), which predicts the number of detected planets in a transit survey that has N_* number of stars, with a fraction of them hosting a planetary system f_* , and a probability P_{det} of finding a transiting system in the survey (see details in §6.3). This result is in agreement with the two planets that have been detected in the WTS so far (Cappetta et al., 2012; Birkby et al., 2013a,b).

Chapter 6

M-dwarfs in the WTS

The selection of M-dwarfs in the WTS is based on color cuts in seven SDSS and WFCam bands: $g - r \geq 1.6$, $r - i \geq 0.9$, $i - z \geq 0.5$, $J - H \geq 0.45$ and $H - K \geq 0.17$. These cuts have been derived to include the majority of M-dwarfs selected by Kovács et al. (2013). They identified and classified an M-dwarf sample by using optical photometry from the SDSS DR7, Adelman-McCarthy & et al. 2009) and NIR photometry from the WFCam to carry out an SED-fitting analysis, which provides T_{eff} for objects from the WTS 19h field. The effective temperatures are measured by using NextGen stellar evolutions models (Baraffe et al., 1998) to fit *griz* and *ZYJHK* photometry, from SDSS and WFCam respectively. Based on these cuts, we find 10 375 M-stars brighter than 18 mag in *J*-band. The number of objects with magnitudes brighter than $J = 17$ is 4 073, which is slightly less but still in reasonable agreement with the number of M-dwarfs selected in Kovács et al. (2013), who found 4 600 objects using the SED-fitting approach. Figure 6.1 shows the color cuts on the WTS light curves and the corresponding M-dwarf sample. In the following, we summarize the optimized selection criteria for M-dwarfs and the corresponding detections efficiency.

6.1 Selection criteria for M-dwarfs

We optimized the selection criteria for M-stars by injecting artificial transit signal into the DI and AP light curves of our WTS M-star sample and following the process described in Section §5.3. In the simulations, we always consider planetary radii of $1 R_{\text{Jup}}$ and use an uniform period distribution between 0.8 and 10 d to be consistent¹ with the simulations presented in Kovács et al. (2013), which were used to set upper limits in the occurrence of short-period giant planets around M-dwarfs with *J*-band ≤ 17 mag in the WTS (see Section §6.3). The stellar parameters were taken from the Besançon model of the galaxy as explained above, but restricting the sample to M-dwarfs. We independently optimized the set of selection parameters described in Section §5.1 to identify M-dwarf planet candidates for the DI and AP light curves. Following the process of selection criteria optimization

¹In this work, we have extended the sensitivity analysis of the WTS presented in Kovács et al. (2013) to M-dwarfs brighter than *J*-band = 18 mag, which explains the requirement on the period distribution in our simulations.

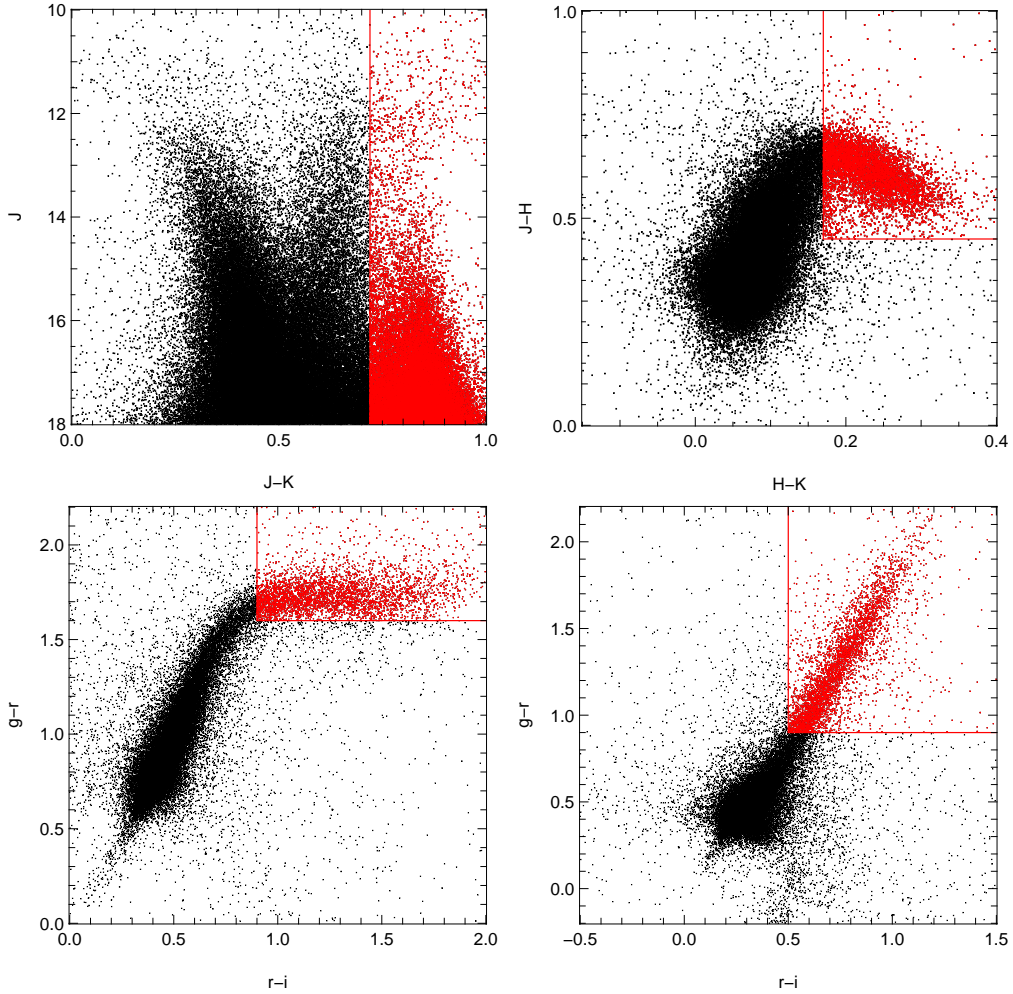


Figure 6.1: Color cuts in seven SDSS and WFCam bands used to identify M-dwarfs in the WTS. The color cuts are based on the color-color and magnitude-color plots of the M-dwarf sample presented in Kovács et al. (2013). The four panels of this figure are the analogous of those plots, where objects that pass the color cuts are pointed out in red, representing our M-dwarf sample of 10 375 objects with $J \leq 18$ mag.

for F-G-K stars, in Figure 6.2, we show the efficiency of the DI and AP light curves as a function of the number of detections on the unmodified light curves. We allow up to 100 detections on each set, since this number provides a reasonable compromise between efficiency and number of objects that are visually inspected. We also permit the detected period to differ up to 1 % from the simulated period, allowing also half, two and three times of this value.

Tables 6.1 and 6.2 list the optimized criteria for the DI and AP light curves. Unlike the case of F-G-K stars, the fractional transit duration turned out to be a useful selection criterion. The V_{shape} parameter turned out not to be important since transits of Jupiter-sized planets orbiting M-dwarfs can be very V-shaped.

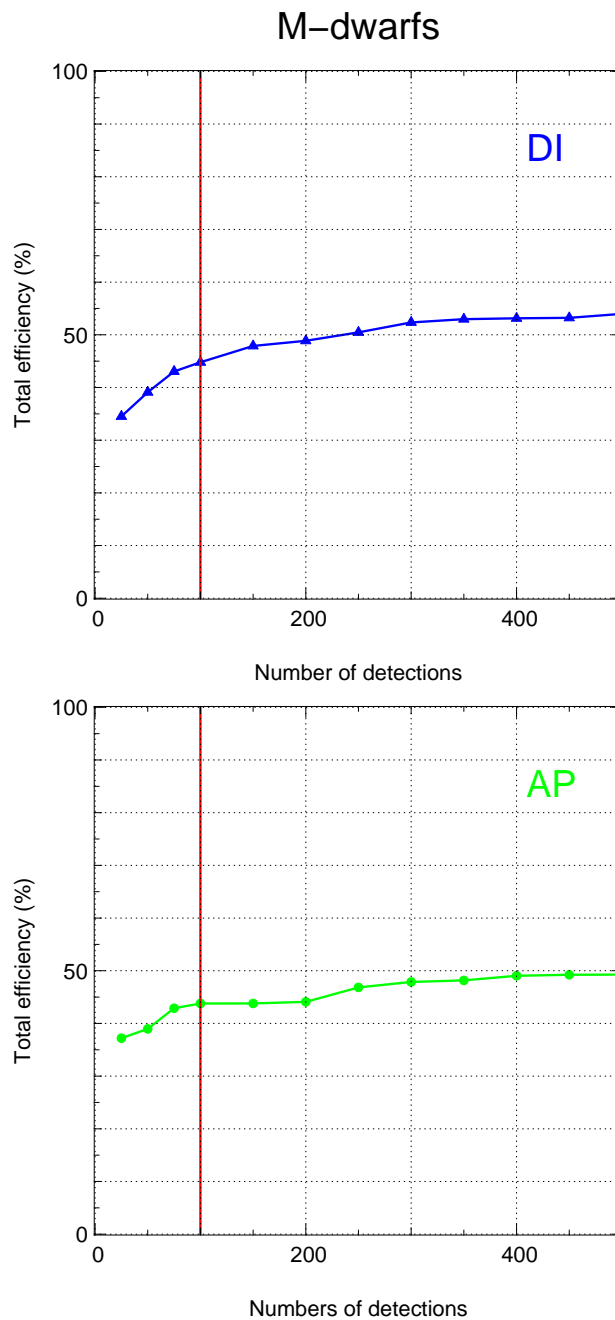


Figure 6.2: Detection efficiency for M-dwarfs derived from the optimized selection parameters as a function of the detections on the unmodified light curves (negatives). The upper panel shows the detection efficiency reached by the DI-light curves, while the lower panel shows the efficiency of AP light curves. We fix the number of detections on the unmodified WTS light curves to 100, since this number enables us to easily inspect by eye the object that pass the selection criteria, while providing a number of detections higher than the expected number of planets. The red line shows our limit of 100 detections.

Figure 6.3 shows the detection efficiency as a function of the apparent host star magnitude. Since the total number of M-stars is dominated by the faint end of the magnitude distribution, the overall efficiency of the DI light curves is slightly higher with 44.8 % with respect to 43.8 % for AP light curves.

Criterion	Remaining objects	Removed objects	%
$J \leq 18$	10375
Removed alias period	7913	2462	23.73
$S/N > 12$	1450	6463	81.68
$S/N - S/N_{rem} > 5$	536	914	63.03
Transit points > 8	164	372	69.40
$V_{shape} < 1.0$	164	0	0.00
Depth ≤ 30 %	138	26	15.85
Transit duration ≤ 0.06	98	40	28.98

Table 6.1: Optimized selection criteria for the DI light curves M-dwarf sample.

Criterion	Remaining objects	Removed objects	%
$J \leq 18$	10375
Removed alias period	8510	1865	17.98
$S/N > 6$	4411	4099	48.17
$S/N - S/N_{rem} > 2$	278	4133	93.70
Transit points > 12	168	110	39.57
$V_{shape} < 1.0$	168	0	0.00
Depth ≤ 30 %	161	7	4.17
Transit duration ≤ 0.08	98	63	39.13

Table 6.2: Optimized selection criteria for the AP light curves M-dwarf sample.

6.2 Candidates detected around M-stars

After a visual examination of the 200 automatically selected objects from the AP and DI light curves, we identified eight possible candidates. All of them were found in both

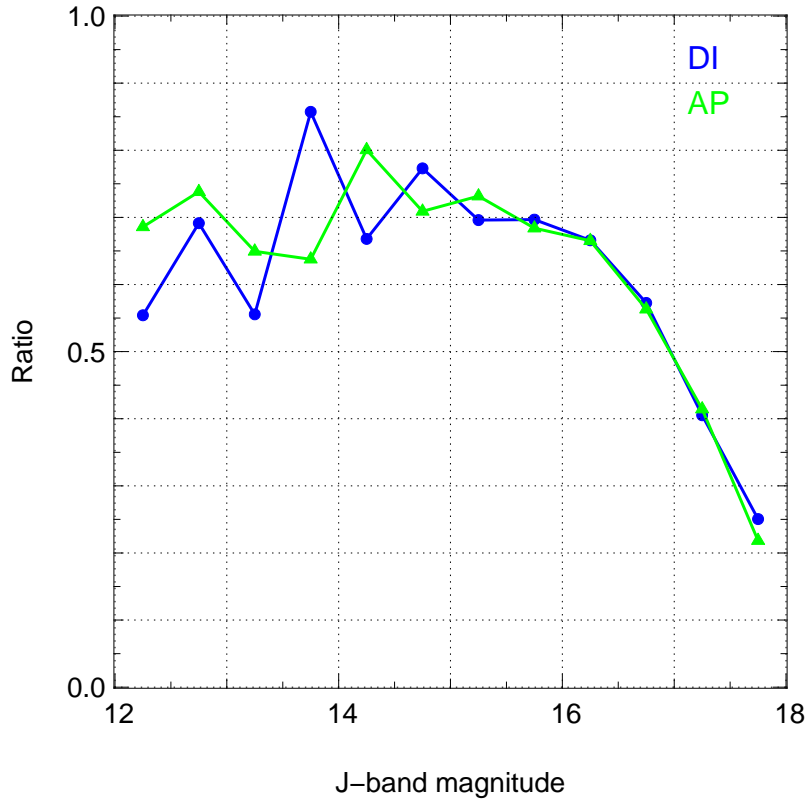


Figure 6.3: Detection efficiency derived from the optimized selection parameters as a function of the host star magnitude.

the AP and DI light curves. Table 6.3 lists the coordinates and broadband photometric data. As for the candidates found in the F-G-K star sample, we performed three different analyses to further assess the possibility of them being transiting planets. The result from the characterization of the host stars is shown in Table 6.4. For the M-dwarf analysis, we used the NextGen model atmosphere grid, which provides a wider range for low T_{eff} , which are more appropriated for M-dwarfs. In this case, we restrict the limits to $T_{\text{eff}} = 1\,800\text{--}4\,500\text{K}$, $[\text{Fe}/\text{H}] = 0.0$, and $\log g = 4.5\text{--}5.5$. All eight stars are in the range of $3300\text{ K} \leq T_{\text{eff}} \leq 3900\text{ K}$, corresponding to spectral types M5 to M0.

In the next step, we carried out a comparative analysis between the planet and binary scenarios, as described in Section §5.4.2. The results are shown in Table 6.5, which reveal different eclipse depths and a significantly better χ_{dof}^2 for two candidates, i.e. 19a1-02980 and 19a1-10878.

Finally, we fit the J -band light curves of the eight candidates with an analytic transit model (see Section §5.4.3). For all faint candidates with $J \geq 17$ mag, we used the DI light curve since the photometric precision is higher compared to the AP light curves. For the brighter candidates 19a1-02980 and 19a1-10878, we used the AP light curves. We determined the best-fitting period, epoch of transit, orbital inclination, and transiting companion radius. The resulting values are listed in Table 6.6, where the smallest of our candidates has a

radius of $2.53 R_{\text{Jup}}$, which exceeds the radius of any planet previously reported. We show the folded light curves of our candidates around M-dwarfs in Figure 6.4.

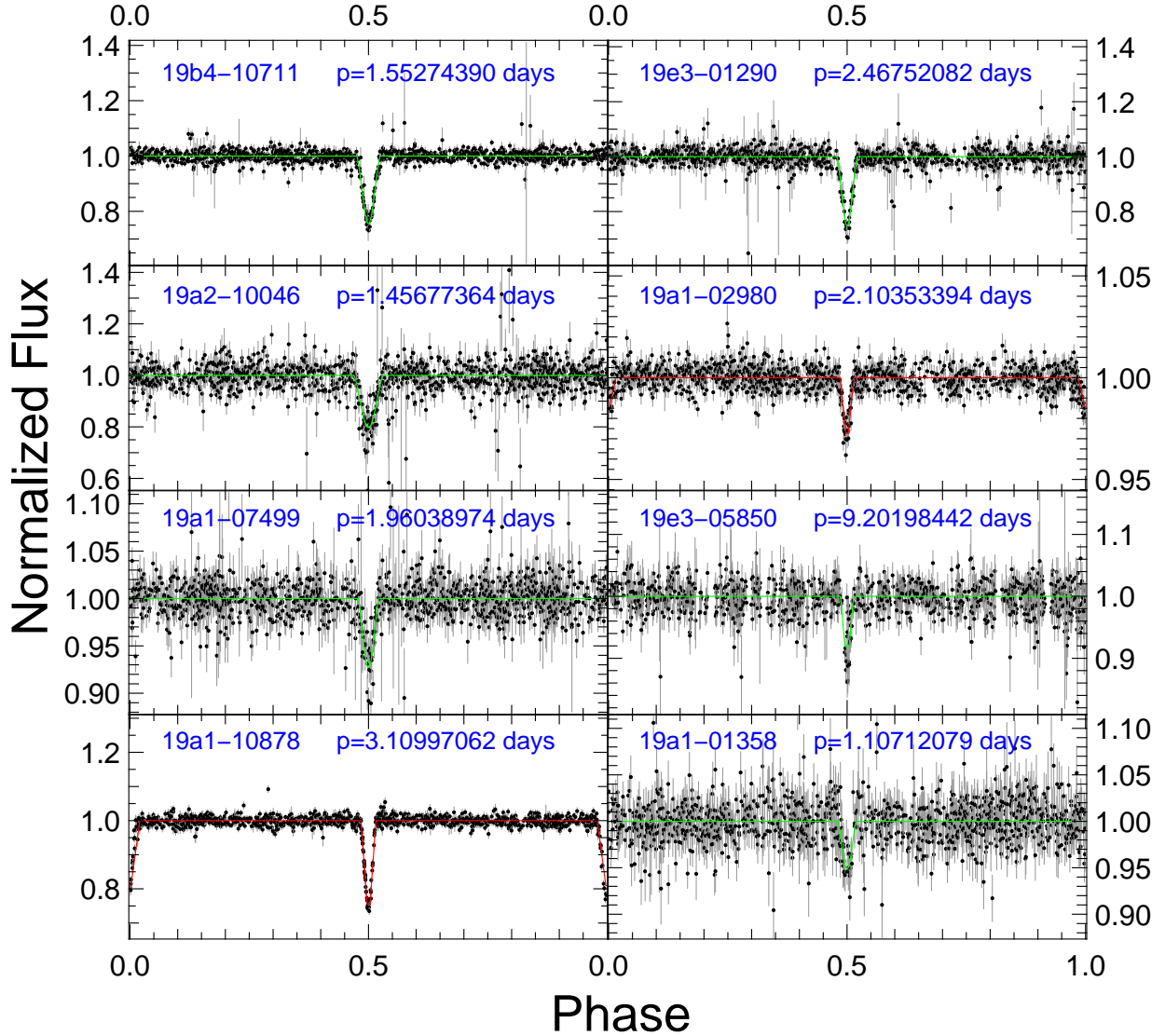


Figure 6.4: Phase-folded light curves of eight candidates that orbit M-dwarfs from the WTS 19h field. As it was done for the candidates around F-G-K stars, we overplot the best-fitting single eclipse with green solid lines, whereas the light curves with two eclipses are shown with the best-fitting trapezoid model, using red-solid lines. In Section §7.2, we present the objects with two eclipses as M-dwarf/M-dwarf eclipsing binary candidates.

Object	Data-set	α	δ	u	g	r	i	z	Z	Y	J	H	K
19b4-10711	AP/DI	293.0253	36.9168	24.10	21.85	20.35	19.07	18.51	17.99	17.63	17.17	16.53	16.25
19e3-01290	AP/DI	293.0688	36.5510	26.66	22.68	21.33	19.94	19.13	18.71	18.32	17.75	17.13	16.87
19a2-10046	AP/DI	293.2753	36.3017	26.61	23.24	21.08	20.19	19.34	18.96	18.57	17.97	17.35	17.16
19a1-02980	AP/DI	292.7127	36.3127	21.33	18.72	17.26	16.53	16.07	15.73	15.40	14.91	14.29	14.07
19a1-07499	AP/DI	292.5977	36.4613	26.39	21.57	19.97	18.98	18.46	18.08	17.68	17.16	16.54	16.30
19e3-05850	AP/DI	293.1396	36.6950	23.30	21.29	19.93	19.17	18.76	18.31	17.98	17.44	16.84	16.66
19a1-10878	AP/DI	292.5126	36.4273	22.94	20.63	19.14	18.10	17.48	17.20	16.82	16.29	15.67	15.40
19a1-01358	AP/DI	292.7526	36.4241	25.11	21.65	20.05	18.89	18.45	17.92	17.55	17.03	16.38	16.16

Table 6.3: List of new candidates around M-dwarfs detected in this work. The second column shows the light curve data set in which the candidates have been detected. The coordinates (J2000.0) are listed in columns 3 and 4. The remaining columns provide broadband photometric measurements of our candidates in ten different filters. The u, g, r, i, z AB-magnitudes were obtained from the Sloan Digital Sky Survey (SDSS) and the Z, Y, J, H, K magnitudes are WFCam measurements in the Vega-system.

Object	$T_{\text{eff}}(\text{K})$	Spectral Type	$\log g_1$	$\log g_2$	A_v	Distance(pc)	$R1_{\star}(R_{\odot})$	$R2_{\star}(R_{\odot})$	$M_{\star}(M_{\odot})$
19b4-10711	3400	M4	4.94	4.68	0.02	676	$0.33^{+0.07}_{-0.09}$	$0.44^{+0.01}_{-0.01}$	$0.34^{+0.09}_{-0.11}$
19e3-01290	3300	M5	5.02	4.49	0.18	703	$0.24^{+0.11}_{-0.09}$	$0.45^{+0.02}_{-0.02}$	$0.23^{+0.11}_{-0.10}$
19a2-10046	3500	M3	4.88	4.50	0.28*	1554	$0.40^{+0.05}_{-0.07}$	$0.61^{+0.02}_{-0.07}$	$0.43^{+0.05}_{-0.09}$
19a1-02980	3900	M0	4.70	4.21	0.15	522	$0.55^{+0.03}_{-0.03}$	$0.99^{+0.04}_{-0.05}$	$0.58^{+0.04}_{-0.02}$
19a1-07499	3600	M2	4.82	4.42	0.18	1063	$0.45^{+0.03}_{-0.05}$	$0.71^{+0.04}_{-0.06}$	$0.48^{+0.04}_{-0.05}$
19e3-05850	3800	M1	4.77	3.98	0.01	1572	$0.52^{+0.03}_{-0.04}$	$1.26^{+0.15}_{-0.02}$	$0.56^{+0.02}_{-0.04}$
19a1-10878	3600	M2	4.82	4.48	0.12	704	$0.45^{+0.03}_{-0.05}$	$0.66^{+0.01}_{-0.01}$	$0.48^{+0.04}_{-0.05}$
19a1-01358	3500	M3	4.88	4.89	0.11	844	$0.40^{+0.05}_{-0.07}$	$0.39^{+0.09}_{-0.03}$	$0.43^{+0.05}_{-0.09}$

Table 6.4: Characterization of M-dwarf parent companions. The T_{eff} is derived from SED-fit with the VOSA. The stellar radii $R2_{\star}$ correspond to the best-fit of the analytic transit model (see Section 5.4.3). The distances reported in column 7 are estimated utilizing the extinction values found in the SED analysis, the i-band magnitudes reported in Table 5.3, and the absolute magnitudes M_i , which are obtained from the isochrones.

Object	V	dp(%)	χ_{dof}^2	χ'_{dof}^2	dp $'_1$ (%)	dp $'_2$ (%)	V'_1	V'_2
19b4-10711	0.69	23.70	1.7020	1.6952	23.87	25.90	0.86	0.66
19e3-01290	0.66	24.98	1.0759	1.0715	25.52	19.95	0.71	0.52
19a2-10046	0.61	19.63	2.0426	2.0596	19.52	17.54	0.62	0.64
19a1-02980	0.72	2.17	1.7077	1.6537	2.70	1.42	0.71	0.79
19a1-07499	0.68	7.38	1.3803	1.3759	7.10	8.01	0.60	0.90
19e3-05850	0.00	7.85	1.1237	1.1203	7.48	7.42	0.00	0.16
19a1-10878	0.65	22.70	1.9194	1.7947	24.19	19.06	0.65	0.80
19a1-01358	0.91	4.67	1.3165	1.3142	5.28	3.30	0.66	0.21

Table 6.5: Comparison between the planet and binary scenario for candidates around M-dwarfs. Comparison of the eclipse shapes, eclipse depths, and χ_{dof}^2 values of the planet scenario (left side of the table) and binary scenario (right side of the table).

Candidate	Period(d)	t_0	$i(^{\circ})$	$R_p(R_{\text{Jup}})$	$R_{p,\text{min}}(R_{\text{Jup}})$	$R_{p,\text{max}}(R_{\text{Jup}})$	χ_{dof}^2	Classification
19b4-10711	1.55274390	2454318.1664350	85.16	2.53	2.34	2.84	1.28	B
19e3-01290	2.46752082	2454318.6477813	85.86	2.64	2.34	3.20	1.01	B
19a2-10046	1.45677364	2454318.7173035	84.48	2.78	2.46	5.31	1.43	B
19a1-02980	1.05176697	2454318.6516446	72.80	3.25	1.93	6.95	1.31	B
19a1-07499	1.96038974	2454318.5897989	81.29	3.45	2.14	7.28	1.18	B
19e3-05850	9.20198442	2454320.1712614	86.81	3.48	3.30	5.03	1.06	B
19a1-10878	1.55498531	2454317.9578553	83.43	3.71	3.49	3.99	1.32	B
19a1-01358	1.10712079	2454318.6005745	76.76	4.94	1.71	7.12	1.09	B

Table 6.6: Characterization of candidates around M-dwarfs, according to the analytic transit fit. Orbital and planetary parameters derived from the analytic transit model fit. All candidates are too large and are most likely transiting brown dwarfs or low-mass stars.

6.3 Sensitivity analysis of the WTS for short-period giant planets around M-dwarfs with $J \leq 17$ mag

A study of the fraction of planets around M-dwarfs from the WTS with $J < 17$ mag was carried out by Kovács et al. (2013). So far, no planets around M-dwarfs have been found in the WTS; therefore, the null detections enables us to set an upper limit on the occurrence of Hot-Jupiter around M-dwarfs. In the following, we describe the method used to measure the sensitivity of the survey and present the main results. In Section §6.4, we additionally extend the analysis to M-dwarfs with fainter magnitudes ($J < 18$), which allows us to place a new upper limit on the fraction of hot giant planets in short-period orbits around M-dwarfs. More details about this analysis can be found in the original work (Kovács et al., 2013).

The sensitivity analysis of the WTS for short-periods giant planets around M-dwarfs is based on the works presented by Burke et al. (2006) and Hartman et al. (2009). For the case of the sensitivity around M-dwarfs with $J < 17$ mag, the analysis is developed by dividing the sample in different star-planet pair scenarios. Neptune and Jupiter-size (0.054 and $1 R_{\text{Jup}}$) planets are considered orbiting around two different subsamples of M-dwarfs (M0-M2 and M2-M4). The M-dwarf sample was selected and classified by an SED-fitting analysis, as it was described above. Then, the number of planets expected to be found in the survey can be calculated by the expression presented in Burke et al. (2006):

$$N_{\text{exp}} = N_{\star} f_{\star} P_{\text{exp}}, \quad (6.1)$$

where N_{\star} is the number of stars involved in the analysis, f_{\star} is the fraction of stars that host a planetary system, and P_{exp} is the probability of finding a planetary system in one of the targets of the survey, in case such star host a planet (not necessarily transiting). P_{exp} is expressed by the equation presented in Burke et al. (2006):

$$P_{\text{exp}} = \iint P_{\text{tr}} P_{\text{r}} p_{\text{den}}(R_{\text{p}}, P) dR_{\text{p}} dP, \quad (6.2)$$

where P_{tr} is the geometric probability of having a transit in a randomly oriented planetary system, P_{r} is the recovery ratio or average probability of detecting signal from a random transiting system, and $p_{\text{den}}(R_{\text{p}}, P)$ is the joint probability density function of planetary radius R_{p} and period P for planetary systems.

In order to estimate P_{exp} , the three factors on the right side of Eq. 6.2 are independently calculated for each planet-star sub-case. P_{tr} is analytically calculated for a random orbital orientation through Eq. 1.15, where a_p is determined by providing an uniform distribution of periods in the range of 0.8-10 d and assuming circular orbits and stellar masses of 0.6 or $0.4 M_{\odot}$ for M0-M2 and M2-M4, respectively. The joint probability density $p_{\text{den}}(R_{\text{p}}, P)$ can be treated as δ function regarding to the R_{p} dependence, since planetary radii only take discrete values (i.e., 0.054 and $1 R_{\text{Jup}}$). For the case of the period dependence, uniform and power-law functions are considered as prior distributions. The power-law functions for the period distribution are based on a model with exponential cutoff at short-periods

that was fitted to a sample of 1 235 planet candidates detected around G and K star from the *Kepler*'s field of view (Howard et al., 2012). Such model was normalized to the period range of 0.8-10 d and used as prior distribution.

P_r is determined by injecting transit signal into a sample of $\sim 4\,600$ WTS light curves² (M-dwarfs) and carrying out Monte Carlo simulations. For each unmodified light curve, a transiting planetary system is generated according to the stellar and planetary parameters described above. A large number of systems are simulated, and subsequently a transit detection algorithm is applied to the simulated light curves. Thus, P_r is estimated as the ratio between successful transit recoveries and the total number of simulated light curves. Two different cases are considered for the recovery ratio. One is related to the S_{red} statistics detection used to identify planet candidates in the WTS pipeline (see Section §2.7); that is, objects with $S_{red} > 6$ are considered signal successfully recovered. On the other hand, the second case additionally requires that the detected period matches the simulated period. The period-match specifically allows the detected period to be a factor of 1, 5/4, 4/3, 3/2, 5/3, 2, 5/2, 3, 4, and 5 of the simulated period. Figure 6.5 shows the recovery ratio for the different planet-star configurations as a function of the J -band magnitude. In addition, the samples are divided in three different period bins, which are taken from Hartman et al. (2009) for extremely-Hot Jupiter (0.8-3 d), very-Hot Jupiter (3-5 d), and Hot Jupiter (5-10 d).

Once P_{exp} is determined, limits on the planetary fraction of giant planets with short-periods around M-dwarfs in the WTS can be estimated from Eq. 6.1 and assuming null detections (so far, no planets around M-dwarfs have been detected in the WTS). However, Eq. 6.1 only provides the expected number of detections, and the real number of detections has to be considered in this analysis, which follows a Poisson distribution³. Thus, the probability of detecting k planets assuming N_{exp} expected number of detections is given by:

$$P_k = \frac{N_{exp}^k}{k!} e^{-N_{exp}}, \quad (6.3)$$

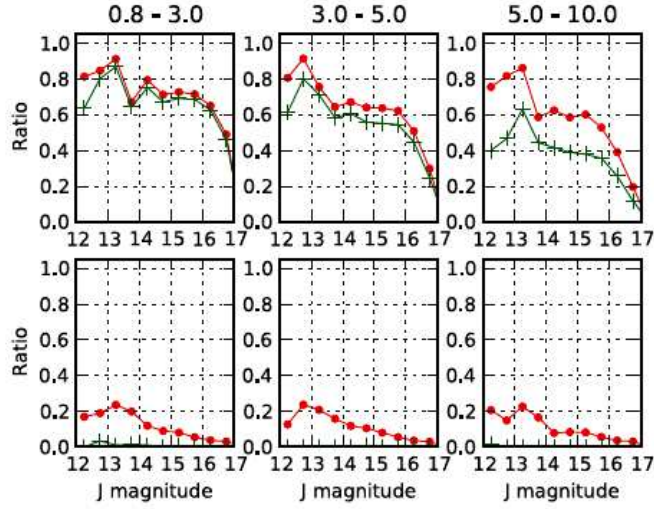
where P_k is evaluated at $k = 0$ as a likelihood function for N_{exp} . Assuming a Bayesian interpretation for the 95 per cent probability credible interval for the Poisson distribution of the number of detections, and the expected number of detections N_{exp} being within the interval $0 \leq N_{exp} < N_{max}$, Eq. 6.3 transforms:

$$P_0(N_{exp} < N_{max}) = \int_0^{N_{max}} e^{-N} dN = 0.95. \quad (6.4)$$

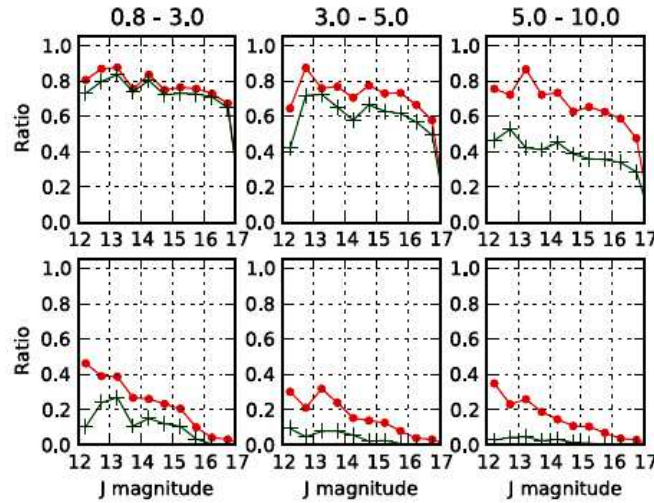
Solving the equation and evaluating the integral limits, $N_{max} \approx 3$, therefore $N_{exp} < 3$. Using this result in Eq. 6.1 allows us to place upper limits on the fraction of stars that

²About 4 600 M-dwarfs in the $11 < J < 17$ mag range were identified in the WTS 19h field through a SED-fit

³A Poisson distribution refers to process where discrete and uncorrelated events occur at some mean rate per unit of time (Press et al., 2002)



(a) M0 + Jupiter, Neptune



(b) M2 + Jupiter, Neptune

Figure 6.5: Recovery ratio as a function of the J -band magnitude and orbital period for different planet-star configurations. Panel a) shows the recovery ratio for the configuration Jupiter and Neptune + M0 stars (upper and lower rows, respectively). Red dots and green crosses are the two recovery ratio cases, i.e., S_{red} threshold and period-match, respectively. Panel b) shows the configuration Jupiter and Neptune + M2 stars. In both cases, the detection efficiency is much higher for Jupiter-size planets, with maximum sensitivity around $J = 13.5$, while dropping towards fainter objects. These plots are the analogous of Figure 6.3 for the detections efficiency of M-dwarfs with $J \leq 18$ presented in this work. (Source Kovács et al. 2013)

have a planetary system at 95 per cent confidence:

$$f_{*95\%} \leq \frac{3.0}{N_* P_{\text{exp}}}. \quad (6.5)$$

The above equation and the null detection result provide upper limits on the fraction of M-dwarfs with $J \leq 17$ mag in the WTS that host short-period giant planets at 95 per cent confidence. Table 6.7 summarizes the results for the different star-planet configurations, period distribution, and recovery ratio cases. For Neptune-size planets the detection probability is very low (in some cases up to two order of magnitude smaller than for Jupiter-size planets), so the resulting upper limits are unrealistic. This is mainly because the noise properties of the WTS are not suitable to detect Neptune-size planets. For Jupiter-size planets, the upper limits on the fraction of stars with planetary systems are very similar for both cases the best-fitting exponential cut power law from *Kepler* and uniform period distributions. Table 6.7 also shows the results for a combined bin that includes both subsamples of stars (M0-M2 and M2-M4), in which an average sensitivity for the whole sample is estimated according to the number of stars in each group. Thus, the WTS can set an upper limit on the occurrence rate of short-period Jupiters around M-dwarfs (M0-4) with $J \leq 17$ mag of $f_{*95\%} = 1.7/2.0$ and $1.8/2.1$ (S_{red} -threshold/period-match) for power law and uniform period distribution, respectively. Figure 6.6 shows the WTS upper limits, which are compared with the results of other planet search projects, such as *Kepler* and the High Accuracy Radial velocity Planet Searcher (HARPS). Note that in Section §1.6.2, we mention that *Kepler* has discovered the first Hot Jupiter orbiting an M-dwarf (Johnson et al., 2012). Nevertheless, the sensitivity analysis for short-period giant planets around low-mass stars presented in this work omits this detection, since the T_{eff} of the host companion of *Kepler* 45 b is marginally out from the T_{eff} range used in our study.

6.4 Extended analysis for M-dwarfs with $J \leq 18$ mag

In this work, we extend the sensitivity analysis of the WTS for short-period (0.8-10 d) Jupiter-size planets around M-dwarfs with $J \leq 18$ mag and $2\,960 < T_{\text{eff}} < 3\,800$. The motivation of this analysis is to make use of the improvement of the photometric precision of the WTS DI light curves for faint objects. Following the approach described in Section §6.3, we derived a new 95 % confidence upper limit on the giant planet occurrence rate for M-dwarfs. The analysis presented in Section §6.2 shows that none of our candidates has a best-fitting radius in the planetary regime. Therefore, we conclude that all candidates that pass the optimized selection criteria and visual inspection filter are transiting brown dwarfs or low-mass stars. This result also confirms the hypothesis presented in Kovács et al. (2013) about the null detection of Jupiter-sized planets around M-dwarfs used to set the upper limits in fraction of stars with planetary systems in the WTS. Unlike the analysis presented in Kovács et al. (2013), we extend the search to all M-type stars with $J \leq 18$ mag, and use a stricter selection criteria that automatically select the best 100 candidates, reducing

System configuration	Period distribution	N_{\star}	P_{exp}	$f_{\star 95\%}$ (%)	P_{exp}	$f_{\star 95\%}$ (%)
			S_{red} -threshold		Period-match	
M0+Jupiter	power low	2844	0.0363	2.9	0.0311	3.4
M2+Jupiter	power low	1679	0.0414	4.3	0.0346	5.2
M0-4+Jupiter	power low	4523	0.0382	1.7	0.0324	2.0
M0+Jupiter	uniform	2844	0.0360	2.9	0.0305	3.5
M2+Jupiter	uniform	1679	0.0405	4.4	0.0332	5.4
M0-4+Jupiter	uniform	4523	0.0377	1.8	0.0315	2.1
M0+Neptune	power low	2844	0.0027	39	0.0001	100
M2+Neptune	power low	1679	0.0025	71	0.0003	100

Table 6.7: Planet detection probability and upper limits on the fraction of planets around M-dwarfs with $J \leq 17$ mag in the WTS. The results correspond to four different star-planets configurations, uniform and power low (*Kepler*) period distributions, and two recovery ratio cases. The values are estimated by assuming an average recovery ratio for the range period of 0.8-10 d. (Data taken from Kovács et al. 2013)

the number of light curves to be visually inspected. In addition, the extra magnitude bin increased the number of sources by a factor of 2.8. An upper limit on the giant planet occurrence rate can be then placed by using Eq. 6.5 and assuming the null detection hypothesis. In our case, we only consider a uniform period distribution in the range of 0.8-10 d. Furthermore, the overall detection efficiency of 44.8 % for DI light curves and the average geometrical probability to see eclipses of ~ 6.1 % (as derived from the Monte Carlo simulations) enable us to estimate a probability of detecting a system in the survey P_{exp} of ~ 0.0273 . Using this value and the total number of sources (10 375) in Eq. 6.5, the resulting upper limit on the occurrence rate of short-period Jupiters around M-dwarfs with $T_{\text{eff}} = 2\,960\text{--}3\,800$ K is ~ 1.1 %. This upper limit is significantly lower than any other reported in the literature (see Figure 6.6). However, it is still higher than the detection rates of Hot Jupiters around hotter stars ($T_{\text{eff}} = 4\,600\text{--}7\,100$ K; see Figure 6.6). Therefore, we cannot conclude from this result that short-period giant planets are unusual around low-mass stars, as it is predicted by the CAGC model of the planet formation theory. Studying larger number of M-dwarfs may statistically push this upper limit to lower levels. One possibility is to analyze the M-dwarf samples from the three remaining fields in the WTS (03, 07, and 17h). Current and future surveys aimed to search planets around M-dwarfs (e.g. Pan-Planets) may also contribute to place stricter upper limits, or finally detect Hot Jupiters that lead to set an occurrence fraction of short-period giant planets around low-mass stars.

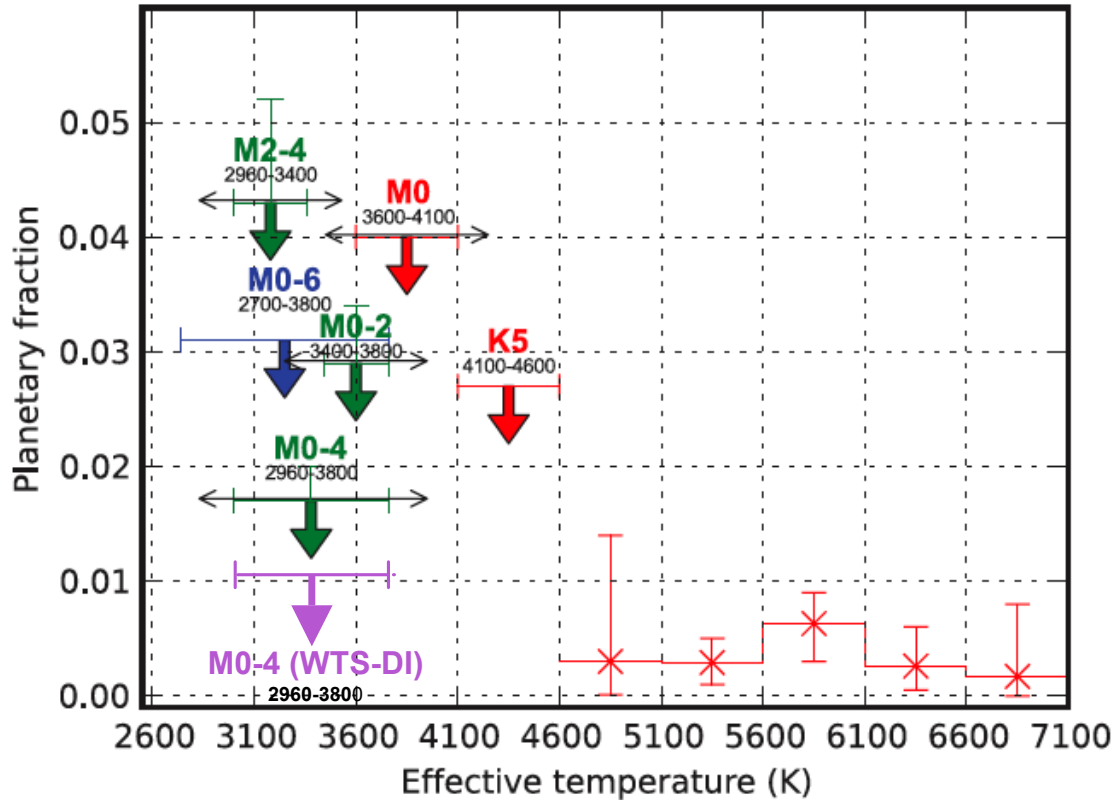


Figure 6.6: Upper limits on the occurrence fraction of planets around M-dwarfs with $J < 17$ mag in the WTS (green arrows; $\sim 4\,600$ objects), *Kepler* (red arrows, based on the work of Howard et al. 2012). In addition, results obtained with radial velocity measurements from the HARPS are shown in blue arrows (Bonfils et al., 2013a). We also present the upper limit of 1.1 % obtained in this work with the DI light curves for M-dwarfs from the WTS 19h field with $J < 18$ mag (purple arrow; 10 375 sources). In the lower right corner of the plot, we show the occurrence fraction of Hot Jupiter around hotter stars ($T_{\text{eff}} = 4\,600 - 7\,100$ K) placed with detections from *Kepler* (Howard et al., 2012). The vertical error bars of the WTS upper limit markers correspond to the uncertainty of the S_{red} -threshold and period-match recovery ratios. The horizontal bars represent widths of temperature bins. Horizontal arrows show estimated uncertainty of bin edges, when they are available. Upper limits and error bars of non-zero fractions correspond to 95 per cent confidence. (Source Kovács et al. 2013. The plot was modified according to the results obtained in this study.)

Chapter 7

Other applications of WTS DI light curves

In the previous sections, we discussed the benefits of using the WTS DI light curves to detect transiting planet candidates, particularly when searching for objects with faint magnitudes ($J > 16$). The DI light curves can be used for additional analyses, such as detection and characterization of faint variable stars. In the next sections, we describe two examples of the results presented by Nefs et al. (2012) and Birkby et al. (2012), which describe the discovery of extremely-short-period M-dwarf eclipsing binaries and M-dwarf eclipsing binaries (MEBs) in the WTS. We show these cases to demonstrate that DI light curves are able to improve the results reported in the literature and to provide new eclipsing binaries candidates when extending the search to fainter magnitudes.

7.1 Extremely-short-period eclipsing binaries

Eclipsing binary stars with extremely-short-periods that are below ~ 0.22 d are very rare systems (Rucinski, 1992; Norton et al., 2011). So far, only few objects with such characteristics have been discovered (e.g. Dimitrov & Kjurkchieva 2010; Maceroni & Montalbán 2004). The parameters of these systems can put strong constraints on formation and evolution theories of low-mass stars (Devor, 2005; Derekas et al., 2007). Recently, Nefs et al. (2012) reported a sample of 31 eclipsing binaries with periods smaller than 0.3 d that were found in the WTS 03, 07, 17 and 19h fields. Four of them are M-dwarf binaries with orbital periods that are considerably shorter than the sharp cut-off period of ~ 0.22 d. We ran our detection algorithm on the 19h field DI light curves with $J < 18$ mag, to make use of the improvement on the photometric precision achieved by the DI light curves of faint objects ($J > 16$). In order to search for extremely-short-period eclipsing binaries, we use the same input parameters reported in Nefs et al. (2012). We reproduce periods and t_0 values of the objects reported previously. In addition, we detected five new eclipsing binaries with periods shorter than 0.23 d. All systems satisfy the color cuts and fit with the red sample (i.e M-dwarfs) presented in Nefs et al. (2012). We additionally use the SDSS color criteria from Ivezić et al. (2005) to eliminate the possibility of being in presence of RR Lyrae.

Other cases of false positives are caused by contamination effects of neighbor stars and stellar variability produced by star spots. However, we eliminate both scenarios, since DI method is designed to reduce the effects caused by very near stellar neighbors. The phase folded light curves also do not present a large scatter in their amplitude, which is generally an indication of variability generated by star spots. Table 7.1 lists the parameters of these systems. Note that the periodic signal of 19c-2-10801 could not be found in the AP light curve at all. We checked for a mismatch in the cross-identification procedure but could not find any object in the vicinity with a comparable variability. We show the folded light curves of all five objects in Figure 7.2.

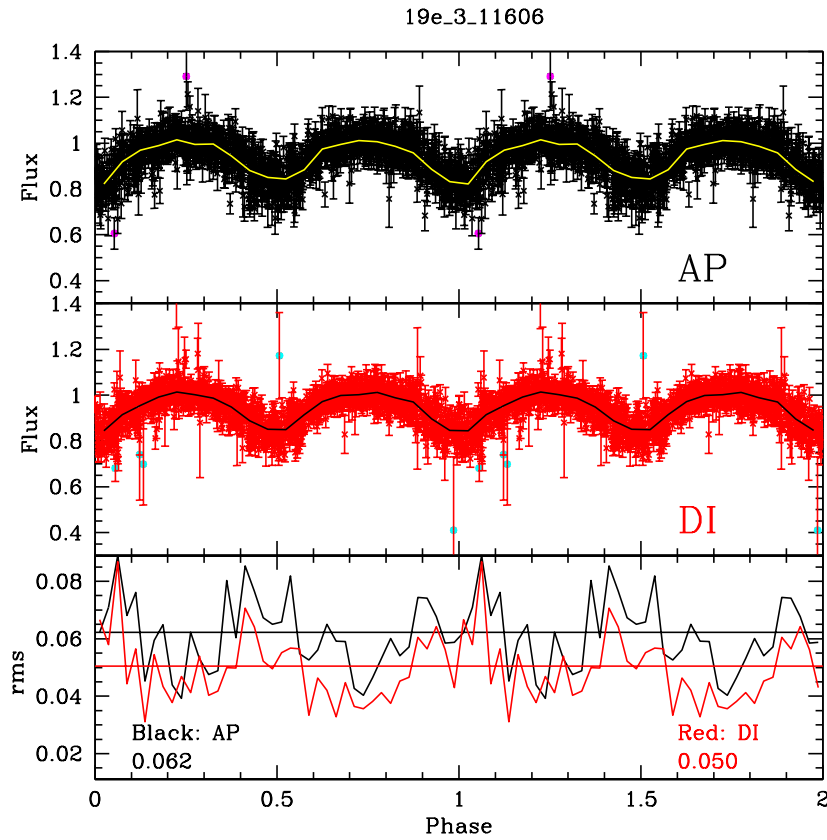


Figure 7.1: Comparison between the AP and DI light curves of an extremely-short-period M-dwarf eclipsing binary system (19e-3-11606) found in the DI light curves. Black and red points in the upper two panels correspond to the AP and DI light curves, respectively. The yellow and black solid lines connect the median values in 40 bins with a size of 0.025 phase units. The lower panel shows the 4σ clipped RMS of the residuals in each bin after subtracting the median. The horizontal lines represent the average RMS of the residuals, which are 0.062 and 0.050 for the AP and DI light curves, respectively.

To show the improvement in the precision of the DI light curves at faint magnitudes, we carry out a statistical comparison of the AP and DI light curves for the system 19e-3-11606, which has a brightness of $J = 17.97$ mag. Figure 7.1 shows the phase-folded DI

and AP light curves and the RMS with respect to the mean in 40 equally spaced bins. The horizontal lines show the 4σ clipped RMS for both light curves, which are 0.050 and 0.062, respectively. The DI light curve, therefore, has an RMS that is about 12 mmag lower, which is a little bit less than what we expected for an object with $J=18.0$ mag. Looking at the other four detected objects, we find that this is a general trend. The lower difference in RMS can be explained by the fact that we are looking at variable objects for which the *system* algorithm cannot reduce systematic effects in an efficient way. It seems that the AP light curves are less affected by this than the DI light curves.

Object	α	δ	Period(d)	t_0	dp'_2/dp'_1	J	u	g	r	i	z	$(r-i)$	$(i-z)$	RMS(AP)	RMS(DI)
19c3-12753	294.3839	36.9062	0.1859752355	2454317.8449795	1.56	17.87	24.93	22.80	21.09	20.08	19.17	1.01	0.91	0.041	0.028
19b2-04235	293.3342	36.4255	0.1974392134	2454317.9485581	1.52	17.32	22.68	22.07	20.16	19.43	18.77	0.74	0.66	0.027	0.023
19c2-10801	294.2404	36.3471	0.1977343597	2454317.9436689	0.88	17.78	25.86	21.37	20.24	19.66	19.36	0.59	0.29	...	0.049
19e3-11606	293.2310	36.6396	0.2106563732	2454317.7894282	1.45	17.97	25.01	21.71	20.31	19.67	19.40	0.65	0.26	0.062	0.050
19c1-00478	293.8732	36.4661	0.2261831592	2454317.8755733	1.57	17.18	23.53	20.44	19.40	18.70	18.35	0.69	0.36	0.028	0.022

Table 7.1: Extremely-short-period M-dwarf eclipsing binary systems with periods below 0.23 d found in this work. We list the period, epoch, eclipse depth ratio, the WFCam J -band, and SDSS $ugriz$ photometry for each candidate. The last two columns provide information on the 4σ clipped RMS of the light curves after removing the periodic signal. In general, the precision of the DI light curves is significantly better than the precision of the AP light curves. This is due to the fact that all objects are fainter than 17 mag in the J -band, which is in the regime where DI light curves present an improvement over AP light curves (see Section 3.4).

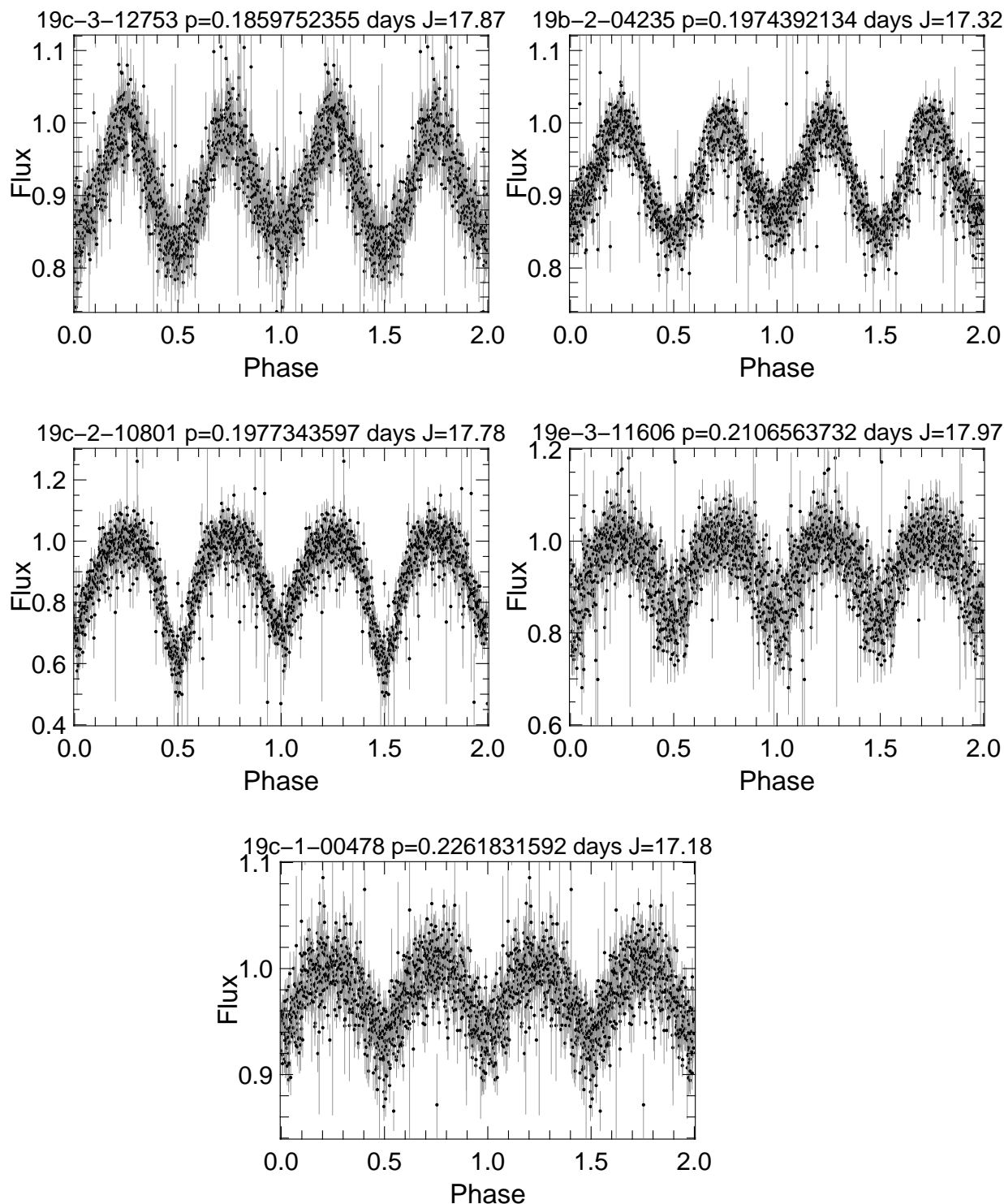


Figure 7.2: Phase-folded light curves of the five extremely-short-period M-dwarf eclipsing binaries found in this work.

7.2 M-dwarf/M-dwarf eclipsing binaries

Recently, Birkby et al. (2012) reported the detection of 16 M-dwarf eclipsing binary systems (MEBs) with $J < 16$ mag found in the WTS AP light curves. These systems are particularly interesting because they provide important information about the fundamental properties of the most abundant stars in our Galaxy (Henry et al., 1997). Nevertheless, the existing theoretical models that describe the evolution of low-mass stars differ from the observed properties of M-dwarfs (López-Morales & Ribas, 2005). More observations and characterization of MEBs can provide new evidence to develop better and more accurate low-mass stellar evolution models (Birkby et al., 2012). We investigate the potential of extending the search for MEBs to fainter systems with magnitudes $J \leq 18$ mag, making use of the improvement in the photometric precision of the DI light curves. In Table 6.6, we report eight candidates classified as eclipsing binary systems, where the objects 19a1-02980 and 19a1-10878 show strong evidence of being MEBs. Furthermore, we detected a third system (19c4-06354) with similar characteristics as the two candidates mentioned above. This object was detected during the optimization process of the selection criteria. All analyses described in Section §6.2 were also carried out on this object, which allow 19c4-06354 to be also classified as a MEB candidate. The system 19a1-02980 was actually reported and confirmed as MEB in Birkby et al. (2012), which supports the remaining fainter detections, since they were identified through the same process. The parameters associated with the main stellar companion of 19a1-02980 and 19a1-10878 are listed in Table 6.4. For the candidate 19c4-06354, we report a primary stellar companion with J -band = 17.97 in a short-period system of $P \sim 0.76$ d and low T_{eff} of 3 500 K. Due to the faint magnitude of the primary stellar companion, this MEB candidate was found only in the DI light curves. A more extensive and meticulous search for MEB systems in the DI light curves (which is out of the scope of this work) could potentially reveal many more detections in the future. Figures 6.4 and 7.3 show the folded light curves of the two candidates and confirmed MEB found in this work.

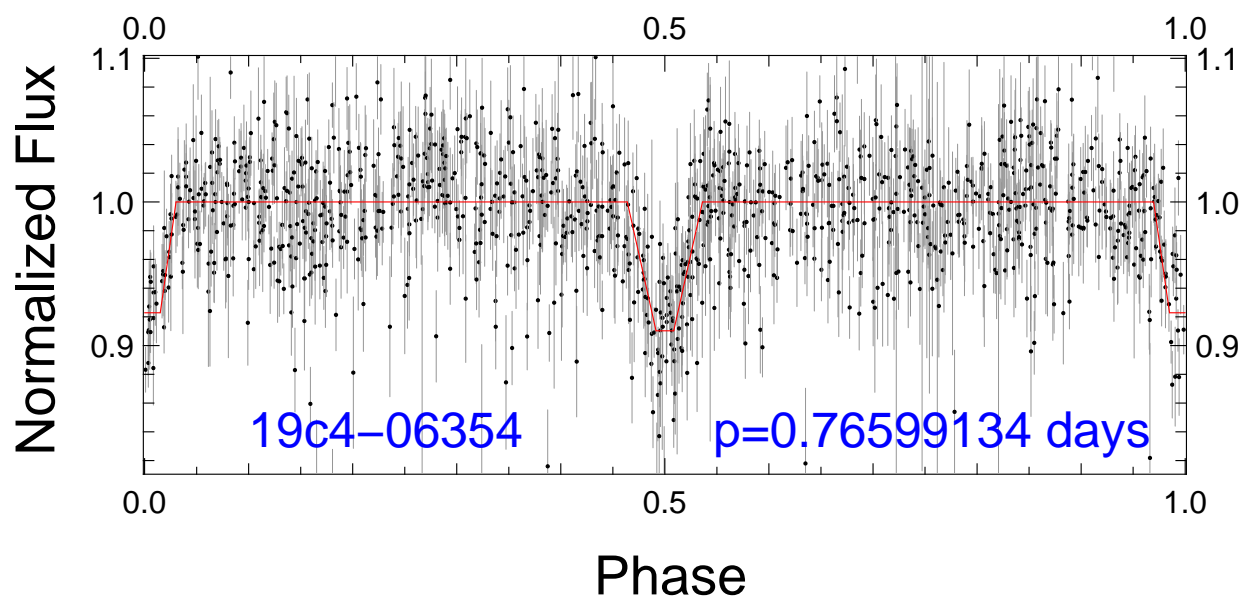


Figure 7.3: Phase-folded light curves of the MEB candidate 19c4-06354 from the WTS 19h field. We overplot on the folded light curves the best-fitting trapezoid model with a red-solid line. The folded light curves of 19a1-02980 and 19a1-10878 are shown in Figure 6.4, since they were detected by our optimized selection criteria during the search of transiting planets. The system 19c4-06354 was separately detected during the optimization process of the selection criteria.

Chapter 8

Conclusions and outlook

We carried out a quantitative comparison between the photometric precision of two different sets of light curves from the 19h field, which represents the most complete field of the Wide-Field Camera Transit Survey (WTS). The light curves were obtained using two different photometric techniques, aperture photometry (AP) and difference imaging (DI). The *sysrem* algorithm was used to remove systematic effects in both data sets and corrected the light curves by scaling the error bars. The WTS AP light curves reach a slightly better photometric precision (by ~ 1 mmag) than the DI light curves for objects brighter than $J \approx 15.5$ mag. On the other hand, the DI light curves show a significant improvement of ~ 2 -20 mmag for sources with magnitudes larger than $J = 16$ mag.

A modified version of the box-fitting algorithm was employed to search for transiting planets in the survey. Our algorithm uses the standard BLS to search for the best trial period and subsequently makes a trapezoid re-fit to the folded light curve, providing a new estimation of the transit depth. A χ^2 comparison shows that the new trapezoid fit provides better results than the traditional box-fitting model. The algorithm also calculates a new parameter based on the geometry of the new trapezoid fit, the V -shape parameter. This parameter has shown the ability to automatically identify and remove eclipsing binary systems from F-G-K star samples.

To select our candidates, we proposed a set of selection criteria; six of them are based on the experience of previous works. Additionally, two new criteria were incorporated, which take advantage of the results obtained with our transit detection algorithm, such as the V -shape parameter. The set of parameters of our selection criteria was optimized using Monte Carlo simulations by injecting transit signals to both the AP and DI light curves. The light curves were split in two different sets, one for F-G-K stars, and a second for M-dwarfs. The optimization of the criteria was performed in both sets separately. The selection criteria have shown the capability of detecting 200 candidates in the DI and AP light curves from an original sample of $\sim 475\,000$ F-G-K stars, while 196 candidates were detected in both sets of light curves from the M-dwarfs sample with 10 375 objects. We carried out a visual examination on the detections and identified 18 relevant transit planet candidates.

A detailed analysis of the 18 candidates was conducted to distinguish planetary from binary candidates, which provided physical parameters of the candidates and their host

stars. The analysis includes a characterization of the parent star and a transit fit of the light curve using a realistic model proposed by Mandel & Agol (2002). Furthermore, we performed a secondary eclipse fit to the phase folded light curve using the double period to detect potential differences in the χ_{dof}^2 and/or the depths of the primary and secondary eclipses that could be an indication of an eclipsing binary system. In our analysis, only one object is classified as a planet candidate, which is proposed for photometric follow-up. The remaining 17 candidates have large best-fitting radii and are therefore classified as binary candidates.

Other applications of the WTS DI light curves were reported. We presented the detection of five new ultra-short-period M-dwarf eclipsing binaries with periods below 0.23 d and $17 < J < 18$ mag. In addition, three detached M-dwarf eclipsing binary candidates were reported; two of them were found in both the AP and DI light curves, while the third and faintest candidate was only detected in the DI light curves sample. Additional discoveries of this type may potentially be revealed by extending the analysis to the remaining WTS fields with DI light curves. These results show that the DI light curves are able to reproduce and improve results reported in the literature. The above leads to our first conclusion, that the WTS DI light curves are useful for many purposes, such as the detection of transit planet candidates and rare eclipsing binary systems, especially at fainter magnitudes.

No planet candidates orbiting an M-dwarf was found in our analysis. Therefore, the null detection hypothesis and upper limits on the occurrence rate of giant planets around M-dwarfs presented in Kovács et al. (2013) down to $J \leq 17$ mag are confirmed. We extended the search for transiting planets to stars with $J \leq 18$ mag. Increasing the number of target stars by going one magnitude deeper and making use of the improvement on the photometric precision of the DI light curves for faint objects, we were able to set a 95 % confidence upper limit of 1.1 % on the occurrence rate of giant planets around M-dwarfs with periods below 10 d, which is significantly lower than any limit published so far. The lack of detections of Hot Jupiters around M-dwarfs suggests that short-period giant planets are not common around low-mass stars, which is in agreement with the CAGC model of planet formation theory. However, the upper limit on the fraction of Hot Jupiters around M-dwarfs estimated in this work (the lowest reported in the literature) is still higher than the occurrence fraction of short-period giant planets around hotter stars. Therefore, we cannot yet provide any solid conclusion on planet formation and orbital migration of exoplanets theories, since there is currently not sufficient observational evidence to affirm that Jovian planets with short-period orbits are less common around M-dwarfs than around solar-like stars. Nevertheless, this may change in the future. The WTS has observations in four different fields (03, 07, 17, and 19h), so extending the sensitivity analysis to the remaining fields may push our upper limit to lower levels (dependent on the number of M-dwarfs in the remaining fields). Other projects dedicated to search for planets around M-dwarfs may also provide new constraints on the fraction of giant planets in short-period orbits around these stars, such as the MEarth, Pan-Planets, and PTF/M-dwarfs projects. Radial velocity surveys may also contribute to reduce this limit. Space missions may also help to impose stricter upper limits, or finally detect Hot Jupiters that lead to place an occurrence fraction of short-period giant planets around low-mass stars. In Section §6.3,

we mentioned that the *Kepler* mission discovered the first Hot Jupiter that orbits an M-dwarf. However this detection was not included in the analysis of Howard et al. (2012) to determine the upper limits shown in Figure 6.6, since the T_{eff} of the host companion was marginally out of the range used in the study. If this planet were part of the analysis of Howard et al. (2012), this detection would mean a $1.1_{-1.1}^{+4.1}$ per cent occurrence rate, which is still compatible with our improved upper limit on the detection rate (see Kovács et al. 2013). This implies that further observations and discoveries of Hot Jupiters around cool stars may place detection limits even lower than those for hotter stars (e.g. G-stars), which may provide further constraints on the theories of planet formation and orbital migration.

In general, space missions will play an important role in the exo-planetary science. For instance, *Kepler* has discovered extra-solar planets with an unprecedented rate, and several hundred of candidates are expected to be confirmed as planets in the near future. Although *Kepler* is not designed to discover planets around M-dwarfs, this mission may detected new Earth-like planets and Hot Jupiters orbiting these type of stars. Gaia is another space mission that will start operations in the near future. Gaia will create a three-dimensional map of the Milky-Way by observing about one billion stars, which will provide statistically valuable information to the exo-planetary science, including characterization of planets around M-dwarfs.

Exo-planet science is currently one of the hottest fields in astronomy and a topic of extensive scientific discussions. Discoveries within this context have revolutionized our knowledge and understanding about planets in other solar systems. Earth analog planets may be detected orbiting within the habitable zone of their host companion, and they also could be very common around Sun-like stars. The development of new technology and instruments will help us to characterize and study such planets, which may even lead to the detection of life on other planets within our Galaxy. In the future, we will perhaps be able to answer our original question: We are not alone in the Universe.

Appendix A

Summary of co-author papers

A sensitivity analysis of the WFCam Transit Survey for short-period giant planets around M dwarfs (Kovács et al., 2013)

The WFCam Transit Survey (WTS) is a near-infrared transit survey running on the United Kingdom Infrared Telescope (UKIRT), designed to discover planets around M dwarfs. The WTS acts as a poor-seeing backup programme for the telescope, and represents the first dedicated wide-field near-infrared transit survey. Observations began in 2007 gathering Jband photometric observations in four (seasonal) fields. In this paper, we present an analysis of the first of the WTS fields, covering an area of 1.6 square degrees. We describe the observing strategy of the WTS and the processing of the data to generate light curves. We describe the basic properties of our photometric data, and measure our sensitivity based on 950 observations. We show that the photometry reaches a precision of ~ 4 mmag for the brightest unsaturated stars in light curves spanning almost 3 yr. Optical (SDSS *griz*) and near-infrared (UKIRT *ZYJHK*) photometry is used to classify the target sample of 4 600 M-dwarfs with *J* magnitudes in the range 11-17. Most have spectral types in the range M0-M2. We conduct Monte Carlo transit injection and detection simulations for short-period (< 10 d) Jupiter- and Neptune-sized planets to characterize the sensitivity of the survey. We investigate the recovery rate as a function of period and magnitude for four hypothetical star-planet cases: M0-2+Jupiter, M2-4+Jupiter, M0-2+Neptune and M2-4+Neptune. We find that the WTS light curves are very sensitive to the presence of Jupiter-sized short-period transiting planets around M dwarfs. Hot Neptunes produce a much weaker signal and suffer a correspondingly smaller recovery fraction. Neptunes can only be reliably recovered with the correct period around the rather small sample (~ 100) of the latest M dwarfs (M4-M9) in the WTS. The non-detection of a hot Jupiter around an M dwarf by the WTS allows us to place an upper limit of 1.7-2.0 per cent (at 95 per cent confidence) on the planet occurrence rate.

Four ultra-short-period eclipsing M-dwarf binaries in the WFCam Transit Survey (Nefs et al., 2012)

We report on the discovery of four ultra-short-period ($P \leq 0.18$ d) eclipsing M-dwarf binaries in the Wide Field Camera (WFCam) Transit Survey. Their orbital periods are significantly shorter than that of any other known main-sequence binary system, and are all significantly below the sharp period cut-off at $P \sim 0.22$ d as seen in binaries of earlier-type stars. The shortest-period binary consists of two M4-type stars in a $P = 0.112$ d orbit. The binaries are discovered as part of an extensive search for short-period eclipsing systems in over 260 000 stellar light curves, including over 10 000 M-dwarfs down to $J = 18$ mag, yielding 25 binaries with $P \sim 0.23$ d. In a popular paradigm, the evolution of short-period binaries of cool main-sequence stars is driven by the loss of angular momentum through magnetized winds. In this scheme, the observed $P \sim 0.22$ d period cut-off is explained as being due to time-scales that are too long for lower-mass binaries to decay into tighter orbits. Our discovery of low-mass binaries with significantly shorter orbits implies that either these time-scales have been overestimated for M-dwarfs, e.g. due to a higher effective magnetic activity, or the mechanism for forming these tight M-dwarf binaries is different from that of earlier-type main-sequence stars.

**The first planet detected in the WTS: an inflated hot
Jupiter in a 3.35 d orbit around a late F star
(Cappetta et al., 2012)**

We report the discovery of WTS-1b, the first extra-solar planet found by the WFCam Transit Survey, which began observations at the 3.8-m United Kingdom Infrared Telescope (UKIRT) in 2007 August. Light curves comprising almost 1 200 epochs with a photometric precision of better than 1 per cent to $J \sim 16$ were constructed for $\sim 60\,000$ stars and searched for periodic transit signals. For one of the most promising transiting candidates, high-resolution spectra taken at the Hobby-Eberly Telescope (HET) allowed us to estimate the spectroscopic parameters of the host star, a late-F main-sequence dwarf ($V = 16.13$) with possibly slightly subsolar metallicity, and to measure its radial velocity variations. The combined analysis of the light curves and spectroscopic data resulted in an orbital period of the substellar companion of 3.35 d, a planetary mass of $4.01 \pm 0.35 M_{\text{Jup}}$ and a planetary radius of $1.49^{+0.16}_{-0.18} R_{\text{Jup}}$. WTS-1b has one of the largest radius anomalies among the known hot Jupiters in the mass range 3-5 M_{Jup} . The high irradiation from the host star ranks the planet in the pM class.

WTS-2 b: a hot Jupiter orbiting near its Roche-limit around a K-dwarf (Birkby et al., 2013b)

We report the discovery of WTS-2 b, a typical hot Jupiter ($M_p = 1.12 M_{\text{Jup}}$, $R_p = 1.30 R_{\text{Jup}}$) in an unusually close 1.02 d orbit to a K2V star. This is the second planet to be found in the infrared light curves of the WFCam Transit Survey (WTS), which operates as a poor-weather program on the United Kingdom InfraRed Telescope (UKIRT). The planet is only 1.5 times the separation from its host star at which it would be destroyed by Roche lobe overflow, and has a predicted remaining lifetime of just ~ 38 Myr, making its detection relatively unlikely given the reasonably old age of the host star ($\gtrsim 600$ Myrs). These calculations assumed that the orbital evolution of the planet under the influence of tidal forces depends simply on the planetary mean motion, with a tidal dissipation quality factor of $Q'_{\text{star}} = 10^6$, as found for Solar system gas giants and binary stars. Q'_{star} is a key factor in determining how frictional processes within a host star affect the orbital evolution of its companion giant planets. It is expected that stars with deeper convective envelopes are more efficient at dissipating the orbital energy of the planet, leading to faster migration. The magnitude of Q'_{star} is largely unconstrained by observations, thus direct measurements of orbital decay across a range of stellar masses are highly valuable. We predict a transit arrival time shift of $T_{\text{shift}} \sim 18$ seconds after 15 years for WTS-2 b for $Q'_{\text{star}} = 10^6$, which is detectable with current instrumentation. We also report a correction to the previously published predicted T_{shift} for WASP-18 b. We calculate that $T_{\text{shift}} = 356$ seconds after 10 years for $Q'_{\text{star}} = 10^6$, which is much larger than the estimated 28 seconds quoted in WASP-18 b discovery paper. Our calculations suggest that direct observational constraints on Q'_{star} across a large range of internal stellar structures is therefore achievable within the decade, via transit arrival time measurements. In addition, we have performed a simple statistical analysis of the observed transiting hot Jupiter population and found that, to first order, the distribution of remaining lifetimes is not inconsistent with our simple model of the tidal orbital evolution i.e. there is a parent population of longer period giant planets that can supply the very close orbit region on the correct timescales, with $Q'_{\text{star}} = 10^6$ for all the host stars, regardless of their internal structure. However, this diagnostic for Q'_{star} is hindered by a lack of detailed understanding of the completeness of the surveys used to detect the population

Bibliography

- Adams, F. C. & Bloch, A. M. 2009: *General Analysis of Type I Planetary Migration with Stochastic Perturbations*, ApJ, 701, 1381
- Adelman-McCarthy, J. K. & et al. 2009: *The SDSS Photometric Catalog, Release 7 (Adelman-McCarthy+, 2009)*, VizieR Online Data Catalog, 2294, 0
- Agol, E., Steffen, J., Sari, R., & Clarkson, W. 2005: *On detecting terrestrial planets with timing of giant planet transits*, MNRAS, 359, 567
- Aigrain, S., Barge, P., Deleuil, M., Fressin, F., Moutou, C., Queloz, D., Auvergne, M., & Baglin, A. 2008: *The CoRoT Exoplanet Programme: Exploring the Gas-Giant/Terrestrial Planet Transition*, in Astronomical Society of the Pacific Conference Series, Vol. 384, 14th Cambridge Workshop on Cool Stars, Stellar Systems, and the Sun, ed. G. van Belle, 270
- Aigrain, S. & Irwin, M. 2004: *Practical planet prospecting*, MNRAS, 350, 331
- Alard, C. 2000: *Image subtraction using a space-varying kernel*, A&AS, 144, 363
- Alard, C. & Lupton, R. H. 1998: *A Method for Optimal Image Subtraction*, ApJ, 503, 325
- Andre, P. & Montmerle, T. 1994: *From T Tauri stars to protostars: Circumstellar material and young stellar objects in the rho Ophiuchi cloud*, ApJ, 420, 837
- Andrews, S. M. & Williams, J. P. 2005: *Circumstellar Dust Disks in Taurus-Auriga: The Submillimeter Perspective*, ApJ, 631, 1134
- Anglada-Escudé, G., Tuomi, M., Gerlach, E., Barnes, R., Heller, R., Jenkins, J. S., Wende, S., Vogt, S. S., Butler, R. P., Reiners, A., & Jones, H. R. A. 2013: *A dynamically-packed planetary system around GJ 667C with three super-Earths in its habitable zone*, A&A, 556, A126
- Armitage, P. J. & Rice, W. K. M. 2005: *Planetary migration*, ArXiv Astrophysics e-prints
- Artymowicz, P. 1993: *On the Wave Excitation and a Generalized Torque Formula for Lindblad Resonances Excited by External Potential*, ApJ, 419, 155

- Artymowicz, P. 2004: *Dynamics of Gaseous Disks with Planets*, in Astronomical Society of the Pacific Conference Series, Vol. 324, Debris Disks and the Formation of Planets, ed. L. Caroff, L. J. Moon, D. Backman, & E. Praton, 39
- Bakos, G., Noyes, R. W., Kovács, G., Stanek, K. Z., Sasselov, D. D., & Domsa, I. 2004: *Wide-Field Millimagitude Photometry with the HAT: A Tool for Extrasolar Planet Detection*, PASP, 116, 266
- Bakos, G. Á., Lázár, J., Papp, I., Sári, P., & Green, E. M. 2002: *System Description and First Light Curves of the Hungarian Automated Telescope, an Autonomous Observatory for Variability Search*, PASP, 114, 974
- Ballard, S., Christiansen, J. L., Charbonneau, D., Deming, D., Holman, M. J., Fabrycky, D., A'Hearn, M. F., Wellnitz, D. D., Barry, R. K., Kuchner, M. J., Livengood, T. A., et al. 2010: *A Search for Additional Planets in the NASA EPOXI Observations of the Exoplanet System GJ 436*, ApJ, 716, 1047
- Ballard, S., Fabrycky, D., Fressin, F., Charbonneau, D., Desert, J.-M., Torres, G., Marcy, G., Burke, C. J., Isaacson, H., Henze, C., Steffen, J. H., et al. 2011: *The Kepler-19 System: A Transiting $2.2 R_{\oplus}$ Planet and a Second Planet Detected via Transit Timing Variations*, ApJ, 743, 200
- Baraffe, I. & Chabrier, G. 1996: *Mass–Spectral Class Relationship for M Dwarfs*, ApJ, 461, L51
- Baraffe, I., Chabrier, G., Allard, F., & Hauschildt, P. H. 1998: *Evolutionary models for solar metallicity low-mass stars: mass-magnitude relationships and color-magnitude diagrams*, A&A, 337, 403
- Barge, P., Baglin, A., Auvergne, M., & CoRoT Team. 2008a: *CoRoT: pioneer space mission for exoplanet transit search*, in IAU Symposium, Vol. 249, IAU Symposium, ed. Y.-S. Sun, S. Ferraz-Mello, & J.-L. Zhou, 3–16
- Barge, P., Baglin, A., Auvergne, M., Rauer, H., Léger, A., Schneider, J., Pont, F., Aigrain, S., Almenara, J.-M., Alonso, R., Barbieri, M., et al. 2008b: *Transiting exoplanets from the CoRoT space mission. I. CoRoT-Exo-1b: a low-density short-period planet around a G0V star*, A&A, 482, L17
- Bayo, A., Rodrigo, C., Barrado Y Navascués, D., Solano, E., Gutiérrez, R., Morales-Calderón, M., & Allard, F. 2008: *VOSA: virtual observatory SED analyzer. An application to the Collinder 69 open cluster*, A&A, 492, 277
- Benedict, G. F., McArthur, B. E., Forveille, T., Delfosse, X., Nelan, E., Butler, R. P., Spiesman, W., Marcy, G., Goldman, B., Perrier, C., Jefferys, W. H., et al. 2002: *A Mass for the Extrasolar Planet Gliese 876b Determined from Hubble Space Telescope Fine Guidance Sensor 3 Astrometry and High-Precision Radial Velocities*, ApJ, 581, L115

- Bennett, D. P. & Rhie, S. H. 2002: *Simulation of a Space-based Microlensing Survey for Terrestrial Extrasolar Planets*, ApJ, 574, 985
- Berta, Z. K., Irwin, J., Charbonneau, D., Burke, C. J., & Falco, E. E. 2012: *Transit Detection in the MEarth Survey of Nearby M Dwarfs: Bridging the Clean-first, Search-later Divide*, AJ, 144, 145
- Bertin, E. & Arnouts, S. 1996: *SExtractor: Software for source extraction.*, A&AS, 117, 393
- Birkby, J., Nefs, B., Hodgkin, S., Kovács, G., Sipőcz, B., Pinfield, D., Snellen, I., Mislis, D., Murgas, F., Lodieu, N., de Mooij, E., et al. 2012: *Discovery and characterization of detached M dwarf eclipsing binaries in the WFCAM Transit Survey*, MNRAS, 426, 1507
- Birkby, J. L., Cappetta, M., Cruz, P., Koppenhoefer, J., Ivanyuk, O., Mustill, A., Hodgkin, S. T., Pinfield, D. J., Sipőcz, B., Kovács, G., Saglia, R., et al. 2013a: *WTS-2 b: Too close for comfort?*, in European Physical Journal Web of Conferences, Vol. 47, European Physical Journal Web of Conferences, 1004
- Birkby, J. L., Cappetta, M., Cruz, P., Koppenhoefer, J., Ivanyuk, O., & Mustill, A. J. 2013b: *WTS-2 b: a hot Jupiter orbiting near its tidal destruction radius around a K-dwarf*, MNRAS, submitted
- Bonfils, X., Delfosse, X., Udry, S., Forveille, T., Mayor, M., Perrier, C., Bouchy, F., Gillon, M., Lovis, C., Pepe, F., Queloz, D., et al. 2013a: *The HARPS search for southern extra-solar planets. XXXI. The M-dwarf sample*, A&A, 549, A109
- Bonfils, X., Lo Curto, G., Correia, A. C. M., Laskar, J., Udry, S., Delfosse, X., Forveille, T., Astudillo-Defru, N., Benz, W., Bouchy, F., Gillon, M., et al. 2013b: *The HARPS search for southern extra-solar planets. XXXIV. A planetary system around the nearby M dwarf GJ 163, with a super-Earth possibly in the habitable zone*, A&A, 556, A110
- Borucki, W. J., Koch, D., Basri, G., Batalha, N., Brown, T., Caldwell, D., Caldwell, J., Christensen-Dalsgaard, J., Cochran, W. D., DeVore, E., Dunham, E. W., et al. 2010: *Kepler Planet-Detection Mission: Introduction and First Results*, Science, 327, 977
- Borucki, W. J., Koch, D. G., Batalha, N., Bryson, S. T., Rowe, J., Fressin, F., Torres, G., Caldwell, D. A., Christensen-Dalsgaard, J., Cochran, W. D., DeVore, E., et al. 2012: *Kepler-22b: A 2.4 Earth-radius Planet in the Habitable Zone of a Sun-like Star*, ApJ, 745, 120
- Borucki, W. J. & Summers, A. L. 1984: *The photometric method of detecting other planetary systems*, Icarus, 58, 121
- Boss, A. P. 1997a: *Formation of giant gaseous protoplanets by gravitational instability*, in Lunar and Planetary Institute Science Conference Abstracts, Vol. 28, Lunar and Planetary Institute Science Conference Abstracts, 137

- Boss, A. P. 1997b: *Giant planet formation by gravitational instability.*, Science, 276, 1836
- Boss, A. P. 1998: *Astrometric signatures of giant-planet formation*, Nature, 393, 141
- Boss, A. P. 2002: *Formation of gas and ice giant planets*, Earth and Planetary Science Letters, 202, 513
- Boss, A. P. 2006a: *Rapid Formation of Gas Giant Planets around M Dwarf Stars*, ApJ, 643, 501
- Boss, A. P. 2006b: *Rapid Formation of Super-Earths around M Dwarf Stars*, ApJ, 644, L79
- Broeg, C., Fortier, A., Ehrenreich, D., Alibert, Y., Baumjohann, W., Benz, W., Deleuil, M., Gillon, M., Ivanov, A., Liseau, R., Meyer, M., et al. 2013: *CHEOPS: A transit photometry mission for ESA's small mission programme*, in European Physical Journal Web of Conferences, Vol. 47, European Physical Journal Web of Conferences, 3005
- Bruno, G. 1980, On the Infinite Universe and Worlds (1584), ed. D. Goldsmith, 5
- Burke, C. J., Gaudi, B. S., DePoy, D. L., & Pogge, R. W. 2006: *Survey for Transiting Extrasolar Planets in Stellar Systems. III. A Limit on the Fraction of Stars with Planets in the Open Cluster NGC 1245*, AJ, 132, 210
- Calabretta, M. R. & Greisen, E. W. 2002: *Representations of celestial coordinates in FITS*, A&A, 395, 1077
- Cappetta, M., Saglia, R. P., Birkby, J. L., Koppenhoefer, J., Pinfield, D. J., Hodgkin, S. T., Cruz, P., Kovács, G., Sipőcz, B., Barrado, D., Nefs, B., et al. 2012: *The first planet detected in the WTS: an inflated hot Jupiter in a 3.35 d orbit around a late F star*, MNRAS, 427, 1877
- Carroll, B. W. & Ostlie, D. A. 2006, An introduction to modern astrophysics and cosmology
- Casali, M., Adamson, A., Alves de Oliveira, C., Almaini, O., Burch, K., Chuter, T., Elliot, J., Folger, M., Foucaud, S., Hambly, N., Hastie, M., et al. 2007: *The UKIRT wide-field camera*, A&A, 467, 777
- Castelli, F., Gratton, R. G., & Kurucz, R. L. 1997: *Notes on the convection in the ATLAS9 model atmospheres.*, A&A, 318, 841
- Chakrabarti, S. K., Das, A., Majumdar, L., & Chakrabarti, S. 2012: *Synthesis of prebiotic molecules and origin of life*, in COSPAR Meeting, Vol. 39, 39th COSPAR Scientific Assembly, 289
- Charbonneau, D., Allen, L. E., Megeath, S. T., Torres, G., Alonso, R., Brown, T. M., Gilliland, R. L., Latham, D. W., Mandushev, G., O'Donovan, F. T., & Sozzetti, A. 2005: *Detection of Thermal Emission from an Extrasolar Planet*, ApJ, 626, 523

- Charbonneau, D., Berta, Z. K., Irwin, J., Burke, C. J., Nutzman, P., Buchhave, L. A., Lovis, C., Bonfils, X., Latham, D. W., Udry, S., Murray-Clay, R. A., et al. 2009: *A super-Earth transiting a nearby low-mass star*, *Nature*, 462, 891
- Charbonneau, D., Brown, T. M., Latham, D. W., & Mayor, M. 2000: *Detection of Planetary Transits Across a Sun-like Star*, *ApJ*, 529, L45
- Charbonneau, D., Brown, T. M., Noyes, R. W., & Gilliland, R. L. 2002: *Detection of an Extrasolar Planet Atmosphere*, *ApJ*, 568, 377
- Charpinet, S., Fontaine, G., Brassard, P., Green, E. M., Van Grootel, V., Randall, S. K., Silvotti, R., Baran, A. S., Østensen, R. H., Kawaler, S. D., & Telting, J. H. 2011: *A compact system of small planets around a former red-giant star*, *Nature*, 480, 496
- Chauvin, G., Lagrange, A.-M., Dumas, C., Zuckerman, B., Mouillet, D., Song, I., Beuzit, J.-L., & Lowrance, P. 2004: *A giant planet candidate near a young brown dwarf. Direct VLT/NACO observations using IR wavefront sensing*, *A&A*, 425, L29
- Chick, K. M. & Cassen, P. 1997: *Thermal Processing of Interstellar Dust Grains in the Primitive Solar Environment*, *ApJ*, 477, 398
- Clampin, M. 2011: *The James Webb Space Telescope and its capabilities for exoplanet science*, in *IAU Symposium*, Vol. 276, *IAU Symposium*, ed. A. Sozzetti, M. G. Lattanzi, & A. P. Boss, 335–342
- Claret, A. & Bloemen, S. 2011: *Gravity and limb-darkening coefficients for the Kepler, CoRoT, Spitzer, uvby, UBVRIJHK, and Sloan photometric systems*, *A&A*, 529, A75
- Collier Cameron, A., Bouchy, F., Hébrard, G., Maxted, P., Pollacco, D., Pont, F., Skillen, I., Smalley, B., Street, R. A., West, R. G., Wilson, D. M., et al. 2007: *WASP-1b and WASP-2b: two new transiting exoplanets detected with SuperWASP and SOPHIE*, *MNRAS*, 375, 951
- Collier Cameron, A., Pollacco, D., Street, R. A., Lister, T. A., West, R. G., Wilson, D. M., Pont, F., Christian, D. J., Clarkson, W. I., Enoch, B., Evans, A., et al. 2006: *A fast hybrid algorithm for exoplanetary transit searches*, *MNRAS*, 373, 799
- Crida, A. & Charnoz, S. 2012: *Formation of Regular Satellites from Ancient Massive Rings in the Solar System*, *Science*, 338, 1196
- D’Angelo, G., Kley, W., & Henning, T. 2003: *Orbital Migration and Mass Accretion of Protoplanets in Three-dimensional Global Computations with Nested Grids*, *ApJ*, 586, 540
- de Bruijne, J. H. J. 2012: *Science performance of Gaia, ESA’s space-astrometry mission*, *Ap&SS*, 341, 31

- de Mooij, E. J. W. & Snellen, I. A. G. 2009: *Ground-based K-band detection of thermal emission from the exoplanet TrES-3b*, A&A, 493, L35
- Deeg, H. 1998: *Photometric Detection of Extrasolar Planets by the Transit-Method*, in *Astronomical Society of the Pacific Conference Series*, Vol. 134, *Brown Dwarfs and Extrasolar Planets*, ed. R. Rebolo, E. L. Martin, & M. R. Zapatero Osorio, 216
- Deeg, H. J., Garrido, R., & Claret, A. 2001: *Probing the stellar surface of HD 209458 from multicolor transit observations*, New A, 6, 51
- Defaÿ, C., Deleuil, M., & Barge, P. 2001: *A Bayesian method for the detection of planetary transits*, A&A, 365, 330
- Deming, D., Seager, S., Richardson, L. J., & Harrington, J. 2005: *Infrared radiation from an extrasolar planet*, Nature, 434, 740
- Demory, B.-O., Gillon, M., Barman, T., Bonfils, X., Mayor, M., Mazeh, T., Queloz, D., Udry, S., Bouchy, F., Delfosse, X., Forveille, T., et al. 2007: *Characterization of the hot Neptune GJ 436 b with Spitzer and ground-based observations*, A&A, 475, 1125
- Derekas, A., Kiss, L. L., & Bedding, T. R. 2007: *Eclipsing Binaries in the MACHO Database: New Periods and Classifications for 3031 Systems in the Large Magellanic Cloud*, ApJ, 663, 249
- Devor, J. 2005: *Solutions for 10,000 Eclipsing Binaries in the Bulge Fields of OGLE II Using DEBiL*, ApJ, 628, 411
- Dimitrov, D. P. & Kjurkchieva, D. P. 2010: *GSC2314-0530: the shortest-period eclipsing system with dMe components*, MNRAS, 406, 2559
- Dole, S. H. 1964, *Habitable planets for man*
- Dotter, A., Chaboyer, B., Jevremović, D., Kostov, V., Baron, E., & Ferguson, J. W. 2008: *The Dartmouth Stellar Evolution Database*, ApJS, 178, 89
- Dressing, C. D. & Charbonneau, D. 2013: *The Occurrence Rate of Small Planets around Small Stars*, ApJ, 767, 95
- Durisen, R. H., Boss, A. P., Mayer, L., Nelson, A. F., Quinn, T., & Rice, W. K. M. 2007: *Gravitational Instabilities in Gaseous Protoplanetary Disks and Implications for Giant Planet Formation*, *Protostars and Planets V*, 607
- Ebel, D. S. 2007: *Planet formation: Theory, observations, and experiments*, by Hubert Klahr and Wolfgang Brandner, *Meteoritics and Planetary Science*, 42, 467
- Feinberg, G., Shapiro, R., & Davies, P. 1980: *Book-Review - Life Beyond Earth - the Intelligent Earthling's Guide to Life in the Universe*, Nature, 288, 34

- Forrest, W. J., Sargent, B., Furlan, E., D'Alessio, P., Calvet, N., Hartmann, L., Uchida, K. I., Green, J. D., Watson, D. M., Chen, C. H., Kemper, F., et al. 2004: *Mid-infrared Spectroscopy of Disks around Classical T Tauri Stars*, ApJS, 154, 443
- Franck, S., von Bloh, W., & Bounama, C. 2007: *Maximum number of habitable planets at the time of Earth's origin: new hints for panspermia and the mediocrity principle*, International Journal of Astrobiology, 6, 153
- Gargaud, M., López-García, P., & Martin, H. 2011, *Origins and Evolution of Life*
- Giacobbe, P., Damasso, M., Sozzetti, A., Toso, G., Perdoncin, M., Calcidese, P., Bernagozzi, A., Bertolini, E., Lattanzi, M. G., & Smart, R. L. 2012: *Photometric transit search for planets around cool stars from the western Italian Alps: a pilot study*, MNRAS, 424, 3101
- Gibson, C. H., Wickramasinghe, N. C., & Schild, R. E. 2010: *Primordial planets, comets, and moons foster life in the cosmos*, in Society of Photo-Optical Instrumentation Engineers (SPIE) Conference Series, Vol. 7819, Society of Photo-Optical Instrumentation Engineers (SPIE) Conference Series
- Gilliland, R. L., Brown, T. M., Guhathakurta, P., Sarajedini, A., Milone, E. F., Albrow, M. D., Baliber, N. R., Bruntt, H., Burrows, A., Charbonneau, D., Choi, P., et al. 2000: *A Lack of Planets in 47 Tucanae from a Hubble Space Telescope Search*, ApJ, 545, L47
- Gingerich, O. 1999, *Introduction to Nicolaus Copernicus*
- Gingerich, O. 2011: *Kepler, Galileo and the birth of modern astronomy*, in IAU Symposium, Vol. 260, IAU Symposium, ed. D. Valls-Gabaud & A. Boksenberg, 172–181
- Goldreich, P. & Tremaine, S. 1979: *The excitation of density waves at the Lindblad and corotation resonances by an external potential*, ApJ, 233, 857
- Goldreich, P. & Tremaine, S. 1980: *Disk-satellite interactions*, ApJ, 241, 425
- Gould, A., Dorsher, S., Gaudi, B. S., & Udalski, A. 2006: *Frequency of Hot Jupiters and Very Hot Jupiters from the OGLE-III Transit Surveys toward the Galactic Bulge and Carina*, Acta Astron., 56, 1
- Goulding, N. T., Barnes, J. R., Pinfield, D. J., del Burgo, C., Kovács, G., Birkby, J., Hodgkin, S., Catalán, S., Sipócz, B., Jones, H. R. A., Jeffers, S. V., et al. 2013: *Periodic variability of spotted M dwarfs in WTS*, in European Physical Journal Web of Conferences, Vol. 47, European Physical Journal Web of Conferences, 1006
- Goulding, N. T., Barnes, J. R., Pinfield, D. J., Kovács, G., Birkby, J., Hodgkin, S., Catalán, S., Sipócz, B., Jones, H. R. A., Del Burgo, C., Jeffers, S. V., et al. 2012: *J-band variability of M dwarfs in the WFCAM Transit Survey*, MNRAS, 427, 3358

- Greisen, E. W. & Calabretta, M. R. 2002: *Representations of world coordinates in FITS*, A&A, 395, 1061
- Haberle, R. M., McKay, C. P., Tyler, D., & Reynolds, R. T. 1996: *Can Synchronously Rotating Planets Support An Atmosphere?*, in *Circumstellar Habitable Zones*, ed. L. R. Doyle, 29
- Haisch, Jr., K. E., Lada, E. A., & Lada, C. J. 2001: *Disk Frequencies and Lifetimes in Young Clusters*, ApJ, 553, L153
- Harrington, J., Luszcz, S., Seager, S., Deming, D., & Richardson, L. J. 2007: *The hottest planet*, Nature, 447, 691
- Hartman, J. D., Gaudi, B. S., Holman, M. J., McLeod, B. A., Stanek, K. Z., Barranco, J. A., Pinsonneault, M. H., Meibom, S., & Kalirai, J. S. 2009: *Deep MMT Transit Survey of the Open Cluster M37 IV: Limit on the Fraction of Stars with Planets as Small as $0.3R_J$* , ApJ, 695, 336
- Heath, M. J., Doyle, L. R., Joshi, M. M., & Haberle, R. M. 1999: *Habitability of Planets Around Red Dwarf Stars*, *Origins of Life and Evolution of the Biosphere*, 29, 405
- Henry, G. W., Marcy, G. W., Butler, R. P., & Vogt, S. S. 2000: *A Transiting "51 Peg-like" Planet*, ApJ, 529, L41
- Henry, T. J., Ianna, P. A., Kirkpatrick, J. D., & Jahreiss, H. 1997: *The solar neighborhood IV: discovery of the twentieth nearest star*, AJ, 114, 388
- Hewett, P. C., Warren, S. J., Leggett, S. K., & Hodgkin, S. T. 2006: *The UKIRT Infrared Deep Sky Survey ZY JHK photometric system: passbands and synthetic colours*, MNRAS, 367, 454
- Hodgkin, S. T., Irwin, M. J., Hewett, P. C., & Warren, S. J. 2009: *The UKIRT wide field camera ZYJHK photometric system: calibration from 2MASS*, MNRAS, 394, 675
- Holman, M. J. & Murray, N. W. 2005: *The Use of Transit Timing to Detect Terrestrial-Mass Extrasolar Planets*, Science, 307, 1288
- Howard, A. W., Marcy, G. W., Bryson, S. T., Jenkins, J. M., Rowe, J. F., Batalha, N. M., Borucki, W. J., Koch, D. G., Dunham, E. W., Gautier, III, T. N., Van Cleve, J., et al. 2012: *Planet Occurrence within 0.25 AU of Solar-type Stars from Kepler*, ApJS, 201, 15
- Irwin, J., Berta, Z. K., Burke, C. J., Charbonneau, D., Nutzman, P., West, A. A., & Falco, E. E. 2011a: *On the Angular Momentum Evolution of Fully Convective Stars: Rotation Periods for Field M-dwarfs from the MEarth Transit Survey*, ApJ, 727, 56

- Irwin, J., Buchhave, L., Berta, Z. K., Charbonneau, D., Latham, D. W., Burke, C. J., Esquerdo, G. A., Everett, M. E., Holman, M. J., Nutzman, P., Berlind, P., et al. 2010: *NLTT 41135: A Field M Dwarf + Brown Dwarf Eclipsing Binary in a Triple System, Discovered by the MEarth Observatory*, ApJ, 718, 1353
- Irwin, J., Charbonneau, D., Nutzman, P., & Falco, E. 2009: *The MEarth project: searching for transiting habitable super-Earth planets around nearby M-dwarfs*, in American Institute of Physics Conference Series, Vol. 1094, 15th Cambridge Workshop on Cool Stars, Stellar Systems, and the Sun, ed. E. Stempels, 445–448
- Irwin, J., Irwin, M., Aigrain, S., Hodgkin, S., Hebb, L., & Moraux, E. 2007: *The Monitor project: data processing and light curve production*, MNRAS, 375, 1449
- Irwin, J. M., Quinn, S. N., Berta, Z. K., Latham, D. W., Torres, G., Burke, C. J., Charbonneau, D., Dittmann, J., Esquerdo, G. A., Stefanik, R. P., Oksanen, A., et al. 2011b: *LSPM J1112+7626: Detection of a 41 Day M-dwarf Eclipsing Binary from the MEarth Transit Survey*, ApJ, 742, 123
- Irwin, M. & Lewis, J. 2001: *INT WFS pipeline processing*, New A Rev., 45, 105
- Irwin, M. J. 1985: *Automatic analysis of crowded fields*, MNRAS, 214, 575
- Irwin, M. J., Lewis, J., Hodgkin, S., Bunclark, P., Evans, D., McMahon, R., Emerson, J. P., Stewart, M., & Beard, S. 2004: *VISTA data flow system: pipeline processing for WFCAM and VISTA*, in Society of Photo-Optical Instrumentation Engineers (SPIE) Conference Series, Vol. 5493, Society of Photo-Optical Instrumentation Engineers (SPIE) Conference Series, ed. P. J. Quinn & A. Bridger, 411–422
- Ivezić, Ž., Vivas, A. K., Lupton, R. H., & Zinn, R. 2005: *The Selection of RR Lyrae Stars Using Single-Epoch Data*, AJ, 129, 1096
- Jehin, E., Gillon, M., Queloz, D., Magain, P., Manfroid, J., Chantry, V., Lendl, M., Hutsemékers, D., & Udry, S. 2011: *TRAPPIST: TRAnsiting Planets and Planetesimals Small Telescope*, The Messenger, 145, 2
- Jenkins, J. M., Caldwell, D. A., Chandrasekaran, H., Twicken, J. D., Bryson, S. T., Quintana, E. V., Clarke, B. D., Li, J., Allen, C., Tenenbaum, P., Wu, H., et al. 2010a: *Overview of the Kepler Science Processing Pipeline*, ApJ, 713, L87
- Jenkins, J. M., Chandrasekaran, H., McCauliff, S. D., Caldwell, D. A., Tenenbaum, P., Li, J., Klaus, T. C., Cote, M. T., & Middour, C. 2010b: *Transiting planet search in the Kepler pipeline*, in Society of Photo-Optical Instrumentation Engineers (SPIE) Conference Series, Vol. 7740, Society of Photo-Optical Instrumentation Engineers (SPIE) Conference Series

- Johnson, J. A., Gazak, J. Z., Apps, K., Muirhead, P. S., Crepp, J. R., Crossfield, I. J. M., Boyajian, T., von Braun, K., Rojas-Ayala, B., Howard, A. W., Covey, K. R., et al. 2012: *Characterizing the Cool KOIs. II. The M Dwarf KOI-254 and Its Hot Jupiter*, AJ, 143, 111
- Kaltenegger, L. 2010: *Characterizing Habitable Exomoons*, ApJ, 712, L125
- Kaltenegger, L. & Traub, W. A. 2009: *Transits of Earth-like Planets*, ApJ, 698, 519
- Karttunen, H., Kröger, P., Oja, H., Poutanen, M., & Donner, K. J. 1987, *Fundamental Astronomy*, 205–207
- Kasting, J. F., Whitmire, D. P., & Reynolds, R. T. 1993: *Habitable Zones around Main Sequence Stars*, Icarus, 101, 108
- Kessler-Silacci, J., Augereau, J.-C., Dullemond, C. P., Geers, V., Lahuis, F., Evans, II, N. J., van Dishoeck, E. F., Blake, G. A., Boogert, A. C. A., Brown, J., Jørgensen, J. K., et al. 2006: *c2d Spitzer IRS Spectra of Disks around T Tauri Stars. I. Silicate Emission and Grain Growth*, ApJ, 639, 275
- Kilic, M., Agol, E., Loeb, A., Maoz, D., Munn, J. A., Gianninas, A., Canton, P., & Barber, S. D. 2013: *Habitable Planets Around White Dwarfs: an Alternate Mission for the Kepler Spacecraft*, ArXiv e-prints
- Kipping, D. M. 2009: *Transit timing effects due to an exomoon*, MNRAS, 392, 181
- Kipping, D. M., Fossey, S. J., & Campanella, G. 2009: *On the detectability of habitable exomoons with Kepler-class photometry*, MNRAS, 400, 398
- Kleinmann, S. G., Lysaght, M. G., Pughe, W. L., Schneider, S. E., Skrutskie, M. F., Weinberg, M. D., Price, S. D., Matthews, K., Soifer, B. T., & Huchra, J. P. 1994: *The Two Micron All Sky Survey*, Ap&SS, 217, 11
- Knutson, H. A., Charbonneau, D., Allen, L. E., Fortney, J. J., Agol, E., Cowan, N. B., Showman, A. P., Cooper, C. S., & Megeath, S. T. 2007: *A map of the day-night contrast of the extrasolar planet HD 189733b*, Nature, 447, 183
- Kokubo, E. & Ida, S. 2002: *Formation of Protoplanet Systems and Diversity of Planetary Systems*, ApJ, 581, 666
- Koppenhoefer, J. 2009: *Searching For Extra-Solar Planets With The Transit Method*, PhD thesis, Max Planck Institute for Extraterrestrial Physics |EMAIL|koppenh@mpe.mpg.de|EMAIL|
- Koppenhoefer, J., Afonso, C., Saglia, R. P., & Henning, T. 2009: *Investigating the potential of the Pan-Planets project using Monte Carlo simulations*, A&A, 494, 707

- Koppenhoefer, J., Saglia, R. P., Fossati, L., Lyubchik, Y., Mugrauer, M., Bender, R., Lee, C.-H., Riffeser, A., Afonso, P., Greiner, J., Henning, T., et al. 2013: *A hot Jupiter transiting a mid-K dwarf found in the pre-OmegaCam Transit Survey*, MNRAS, 435, 3133
- Korpikiewicz, H. 1978: *Astronomy of Anaxagoras.*, Urania (Krakow), 49, 354
- Korycansky, D. G. & Pollack, J. B. 1993: *Numerical calculations of the linear response of a gaseous disk to a protoplanet*, Icarus, 102, 150
- Kovács, G., Hodgkin, S., Sipőcz, B., Pinfield, D., Barrado, D., Birkby, J., Cappetta, M., Cruz, P., Koppenhoefer, J., Martín, E. L., Murgas, F., et al. 2013: *A sensitivity analysis of the WFCAM Transit Survey for short-period giant planets around M dwarfs*, MNRAS, 433, 889
- Kovács, G., Zucker, S., & Mazeh, T. 2002: *A box-fitting algorithm in the search for periodic transits*, A&A, 391, 369
- Lada, C. J., Muench, A. A., Luhman, K. L., Allen, L., Hartmann, L., Megeath, T., Myers, P., Fazio, G., Wood, K., Muzerolle, J., Rieke, G., et al. 2006: *Spitzer Observations of IC 348: The Disk Population at 2-3 Million Years*, AJ, 131, 1574
- Laughlin, G., Bodenheimer, P., & Adams, F. C. 2004: *The Core Accretion Model Predicts Few Jovian-Mass Planets Orbiting Red Dwarfs*, ApJ, 612, L73
- Law, N. M., Kraus, A. L., Street, R., Fulton, B. J., Hillenbrand, L. A., Shporer, A., Lister, T., Baranec, C., Bloom, J. S., Bui, K., Burse, M. P., et al. 2012: *Three New Eclipsing White-dwarf-M-dwarf Binaries Discovered in a Search for Transiting Planets around M-dwarfs*, ApJ, 757, 133
- Lin, D. N. C., Bodenheimer, P., & Richardson, D. C. 1996: *Orbital migration of the planetary companion of 51 Pegasi to its present location*, Nature, 380, 606
- Lin, D. N. C. & Papaloizou, J. 1979: *Tidal torques on accretion discs in binary systems with extreme mass ratios*, MNRAS, 186, 799
- Lin, D. N. C. & Papaloizou, J. 1986: *On the tidal interaction between protoplanets and the protoplanetary disk. III - Orbital migration of protoplanets*, ApJ, 309, 846
- López-Morales, M. & Ribas, I. 2005: *GU Bootis: A New 0.6 M_{solar} Detached Eclipsing Binary*, ApJ, 631, 1120
- Maceroni, C. & Montalbán, J. 2004: *The shortest period M dwarf eclipsing system BW3 V38. II. Determination of absolute elements*, A&A, 426, 577
- Malhotra, R. 1993: *The origin of Pluto's peculiar orbit*, Nature, 365, 819

- Mandel, K. & Agol, E. 2002: *Analytic Light Curves for Planetary Transit Searches*, ApJ, 580, L171
- Mao, S. & Paczynski, B. 1991: *Gravitational microlensing by double stars and planetary systems*, ApJ, 374, L37
- Masset, F. S. 2008: *Planetary migration in gaseous protoplanetary disks*, in IAU Symposium, Vol. 249, IAU Symposium, ed. Y.-S. Sun, S. Ferraz-Mello, & J.-L. Zhou, 331–346
- Masset, F. S. & Papaloizou, J. C. B. 2003: *Runaway Migration and the Formation of Hot Jupiters*, ApJ, 588, 494
- Mayor, M. & Queloz, D. 1995: *A Jupiter-mass companion to a solar-type star*, Nature, 378, 355
- Mazeh, T., Guterman, P., Aigrain, S., Zucker, S., Grinberg, N., Alapini, A., Alonso, R., Auvergne, M., Barbieri, M., Barge, P., Bordé, P., et al. 2009: *Removing systematics from the CoRoT light curves. I. Magnitude-dependent zero point*, A&A, 506, 431
- Mazeh, T., Naef, D., Torres, G., Latham, D. W., Mayor, M., Beuzit, J.-L., Brown, T. M., Buchhave, L., Burnet, M., Carney, B. W., Charbonneau, D., et al. 2000: *The Spectroscopic Orbit of the Planetary Companion Transiting HD 209458*, ApJ, 532, L55
- Meeus, J. 1982, *Astronomical formulae for calculators*, 43
- Montalto, M., Piotto, G., Desidera, S., de Marchi, F., Bruntt, H., Stetson, P. B., Arellano Ferro, A., Momany, Y., Gratton, R. G., Poretti, E., Aparicio, A., et al. 2007: *A new search for planet transits in μ ASTROBJ/NGC 6791/ASTROBJ*, A&A, 470, 1137
- Montgomery, R. & Laughlin, G. 2009: *Formation and detection of Earth mass planets around low mass stars*, Icarus, 202, 1
- Montmerle, T., Augereau, J.-C., Chaussidon, M., Gounelle, M., Marty, B., & Morbidelli, A. 2006: *From Suns to Life: A Chronological Approach to the History of Life on Earth 3. Solar System Formation and Early Evolution: the First 100 Million Years*, Earth Moon and Planets, 98, 39
- Morbidelli, A., Tsiganis, K., Crida, A., Levison, H. F., & Gomes, R. 2007: *Dynamics of the Giant Planets of the Solar System in the Gaseous Protoplanetary Disk and Their Relationship to the Current Orbital Architecture*, AJ, 134, 1790
- Moutou, C., Mayor, M., Lo Curto, G., Ségransan, D., Udry, S., Bouchy, F., Benz, W., Lovis, C., Naef, D., Pepe, F., Queloz, D., et al. 2011: *The HARPS search for southern extra-solar planets. XXVII. Seven new planetary systems*, A&A, 527, A63

- Nefs, S. V., Birkby, J. L., Snellen, I. A. G., Hodgkin, S. T., Pinfield, D. J., Sipőcz, B., Kovács, G., Mislis, D., Saglia, R. P., Koppenhoefer, J., Cruz, P., et al. 2012: *Four ultra-short-period eclipsing M-dwarf binaries in the WFCAM Transit Survey*, MNRAS, 425, 950
- Nelson, A. F., Benz, W., & Ruzmaikina, T. V. 2000: *Dynamics of Circumstellar Disks. II. Heating and Cooling*, ApJ, 529, 357
- Neuhäuser, R., Guenther, E. W., Wuchterl, G., Mugrauer, M., Bedalov, A., & Hauschildt, P. H. 2005: *Evidence for a co-moving sub-stellar companion of GQ Lup*, A&A, 435, L13
- Norton, A. J., Payne, S. G., Evans, T., West, R. G., Wheatley, P. J., Anderson, D. R., Barros, S. C. C., Butters, O. W., Collier Cameron, A., Christian, D. J., Enoch, B., et al. 2011: *Short period eclipsing binary candidates identified using SuperWASP*, A&A, 528, A90
- Osten, R. A., Hawley, S. L., Allred, J. C., Johns-Krull, C. M., & Roark, C. 2005: *From Radio to X-Ray: Flares on the dMe Flare Star EV Lacertae*, ApJ, 621, 398
- Paczynski, B. 2003: *Gravitational Microlensing: Black Holes, Planets; OGLE, VLTI, HST and Space Probes*, ArXiv Astrophysics e-prints
- Papaloizou, J. C. & Savonije, G. J. 1991: *Instabilities in self-gravitating gaseous discs*, MNRAS, 248, 353
- Papaloizou, J. C. B. & Terquem, C. 2006: *Planet formation and migration*, Reports on Progress in Physics, 69, 119
- Pascucci, I., Laughlin, G., Gaudi, B. S., Kennedy, G., Luhman, K., Mohanty, S., Birkby, J., Ercolano, B., Plavchan, P., & Skemer, A. 2011: *Planet Formation Around M-dwarf Stars: From Young Disks to Planets*, in Astronomical Society of the Pacific Conference Series, Vol. 448, 16th Cambridge Workshop on Cool Stars, Stellar Systems, and the Sun, ed. C. Johns-Krull, M. K. Browning, & A. A. West, 469
- Pepliński, A., Artymowicz, P., & Mellema, G. 2008a: *Numerical simulations of type III planetary migration - I. Disc model and convergence tests*, MNRAS, 386, 164
- Pepliński, A., Artymowicz, P., & Mellema, G. 2008b: *Numerical simulations of type III planetary migration - II. Inward migration of massive planets*, MNRAS, 386, 179
- Perryman, M. A. C. 2000: *Extra-solar planets*, Reports on Progress in Physics, 63, 1209
- Pesic, P. 2001: *Book Review: Ptolemy's almagest / Princeton University Press, 1998*, Archaeoastronomy, 16, 102

- Pietrukowicz, P., Minniti, D., Díaz, R. F., Fernández, J. M., Zoccali, M., Gieren, W., Pietrzyński, G., Ruíz, M. T., Udalski, A., Szeifert, T., & Hempel, M. 2010: *Millimag-nitude photometry for transiting extrasolar planetary candidates . V. Follow-up of 30 OGLE transits. New candidates*, A&A, 509, A4
- Pollacco, D. L., Skillen, I., Collier Cameron, A., Christian, D. J., Hellier, C., Irwin, J., Lister, T. A., Street, R. A., West, R. G., Anderson, D. R., Clarkson, W. I., et al. 2006: *The WASP Project and the SuperWASP Cameras*, PASP, 118, 1407
- Pollack, J. B., Hubickyj, O., Bodenheimer, P., Lissauer, J. J., Podolak, M., & Greenzweig, Y. 1996: *Formation of the Giant Planets by Concurrent Accretion of Solids and Gas*, Icarus, 124, 62
- Pont, F., Zucker, S., & Queloz, D. 2006: *The effect of red noise on planetary transit detection*, MNRAS, 373, 231
- Press, W. H., Teukolsky, S. A., Vetterling, W. T., & Flannery, B. P. 2002, Numerical recipes in C++ : the art of scientific computing
- Pudritz, R. E. 2002: *Clustered Star Formation and the Origin of Stellar Masses*, Science, 295, 68
- Rauer, H. & Catala, C. 2011: *The PLATO mission*, in IAU Symposium, Vol. 276, IAU Symposium, ed. A. Sozzetti, M. G. Lattanzi, & A. P. Boss, 354–358
- Raymond, S. N., Quinn, T., & Lunine, J. I. 2006: *High-resolution simulations of the final assembly of Earth-like planets I. Terrestrial accretion and dynamics*, Icarus, 183, 265
- Raymond, S. N., Scalo, J., & Meadows, V. S. 2007: *A Decreased Probability of Habitable Planet Formation around Low-Mass Stars*, ApJ, 669, 606
- Ricker, G. R., Latham, D. W., Vanderspek, R. K., Ennico, K. A., Bakos, G., Brown, T. M., Burgasser, A. J., Charbonneau, D., Clampin, M., Deming, L. D., Doty, J. P., et al. 2010: *Transiting Exoplanet Survey Satellite (TESS)*, in Bulletin of the American Astronomical Society, Vol. 42, American Astronomical Society Meeting Abstracts #215, #450.06
- Rivera, E. J., Lissauer, J. J., Butler, R. P., Marcy, G. W., Vogt, S. S., Fischer, D. A., Brown, T. M., Laughlin, G., & Henry, G. W. 2005: *A $\sim 7.5 M_{\oplus}$ Planet Orbiting the Nearby Star, GJ 876*, ApJ, 634, 625
- Robin, A. C., Reylé, C., Derrière, S., & Picaud, S. 2003: *A synthetic view on structure and evolution of the Milky Way*, A&A, 409, 523
- Rodgers, J., Ruff, W., & Hughes, D. W. 1980: *Book-Review - the Harmony of the World - a Realization for the Ear of Kepler-Johannes Astronomical Data from Harmonices Mundi 1619*, Nature, 283, 607

- Rosenblatt, F. 1971: *A Two-Color Photometric Method for Detection of Extra solar Planetary Systems*, *Icarus*, 14, 71
- Rucinski, S. M. 1992: *Can full convection explain the observed short-period limit of the W UMa-type binaries?*, *AJ*, 103, 960
- Ruden, S. P. 1999: *The Formation of Planets*, in NATO ASIC Proc. 540: The Origin of Stars and Planetary Systems, ed. C. J. Lada & N. D. Kylafis, 643
- Safronov, V. S. 1972, Evolution of the protoplanetary cloud and formation of the earth and planets.
- Santerne, A., Díaz, R. F., Moutou, C., Bouchy, F., Hébrard, G., Almenara, J.-M., Bonomo, A. S., Deleuil, M., & Santos, N. C. 2012: *SOPHIE velocimetry of Kepler transit candidates. VII. A false-positive rate of 35% for Kepler close-in giant candidates*, *A&A*, 545, A76
- Sartoretti, P. & Schneider, J. 1999: *On the detection of satellites of extrasolar planets with the method of transits*, *A&AS*, 134, 553
- Scalo, J., Kaltenegger, L., Segura, A. G., Fridlund, M., Ribas, I., Kulikov, Y. N., Grenfell, J. L., Rauer, H., Odert, P., Leitzinger, M., Selsis, F., et al. 2007: *M Stars as Targets for Terrestrial Exoplanet Searches And Biosignature Detection*, *Astrobiology*, 7, 85
- Selsis, F., Kasting, J. F., Levrard, B., Paillet, J., Ribas, I., & Delfosse, X. 2007: *Habitable planets around the star Gliese 581?*, *A&A*, 476, 1373
- Sing, D. K. & López-Morales, M. 2009: *Ground-based secondary eclipse detection of the very-hot Jupiter OGLE-TR-56b*, *A&A*, 493, L31
- Skumanich, A. 1972: *Time Scales for CA II Emission Decay, Rotational Braking, and Lithium Depletion*, *ApJ*, 171, 565
- Smith, M. W., Seager, S., Pong, C. M., Villaseñor, J. S., Ricker, G. R., Miller, D. W., Knapp, M. E., Farmer, G. T., & Jensen-Clem, R. 2010: *ExoplanetSat: detecting transiting exoplanets using a low-cost CubeSat platform*, in Society of Photo-Optical Instrumentation Engineers (SPIE) Conference Series, Vol. 7731, Society of Photo-Optical Instrumentation Engineers (SPIE) Conference Series
- Snellen, I. A. G., van der Burg, R. F. J., de Hoon, M. D. J., & Vuisjsje, F. N. 2007: *A search for transiting extrasolar planet candidates in the OGLE-II microlens database of the galactic plane*, *A&A*, 476, 1357
- Sozzetti, A., Bernagozzi, A., Bertolini, E., Calcidese, P., Carbognani, A., Cenadelli, D., Christille, J.-M., Damasso, M., Giacobbe, P., Lanteri, L., Lattanzi, M. G., et al. 2013: *The APACHE Project*, in European Physical Journal Web of Conferences, Vol. 47, European Physical Journal Web of Conferences, 3006

- Stamenkovic, V. & Breuer, D. 2012: *Thermal Evolution and Habitability of Super-Earths*, in European Planetary Science Congress 2012, 758
- Steel, D. & Hennessy, R. A. S. 2001: *Book Review: Worlds Without End: The Historic Search for Extraterrestrial Life (R.A.S. Hennessy)*, Journal of Astronomical History and Heritage, 4, 96
- Steele, P. R., Saglia, R. P., Koppenhoefer, J., Burleigh, M. R., & Cappetta, M. 2013: *White dwarfs in the WTS: Eclipsing binaries*, in European Physical Journal Web of Conferences, Vol. 47, European Physical Journal Web of Conferences, 4001
- Steffen, J. H. & Agol, E. 2005: *Development and Application of the Transit Timing Planet Detection Technique*, in Bulletin of the American Astronomical Society, Vol. 37, American Astronomical Society Meeting Abstracts, #166.03
- Struve, O. 1952: *Proposal for a project of high-precision stellar radial velocity work*, The Observatory, 72, 199
- Tamuz, O., Mazeh, T., & Zucker, S. 2005: *Correcting systematic effects in a large set of photometric light curves*, MNRAS, 356, 1466
- Tanaka, H., Takeuchi, T., & Ward, W. R. 2002: *Three-Dimensional Interaction between a Planet and an Isothermal Gaseous Disk. I. Corotation and Lindblad Torques and Planet Migration*, ApJ, 565, 1257
- Tarter, J. C., Backus, P. R., Mancinelli, R. L., Aurnou, J. M., Backman, D. E., Basri, G. S., Boss, A. P., Clarke, A., Deming, D., Doyle, L. R., Feigelson, E. D., et al. 2007: *A Reappraisal of The Habitability of Planets around M Dwarf Stars*, Astrobiology, 7, 30
- Terquem, C. E. J. M. L. J. 2003: *Stopping inward planetary migration by a toroidal magnetic field*, MNRAS, 341, 1157
- Tinetti, G., Vidal-Madjar, A., Liang, M.-C., Beaulieu, J.-P., Yung, Y., Carey, S., Barber, R. J., Tennyson, J., Ribas, I., Allard, N., Ballester, G. E., et al. 2007: *Water vapour in the atmosphere of a transiting extrasolar planet*, Nature, 448, 169
- Tomaney, A. B. & Crofts, A. P. S. 1996: *Expanding the Realm of Microlensing Surveys with Difference Image Photometry*, AJ, 112, 2872
- Toomre, A. 1964: *On the gravitational stability of a disk of stars*, ApJ, 139, 1217
- Trilling, D. E., Benz, W., Guillot, T., Lunine, J. I., Hubbard, W. B., & Burrows, A. 1998: *Orbital Evolution and Migration of Giant Planets: Modeling Extrasolar Planets*, ApJ, 500, 428

- Udalski, A., Paczynski, B., Zebrun, K., Szymanski, M., Kubiak, M., Soszynski, I., Szewczyk, O., Wyrzykowski, L., & Pietrzynski, G. 2002a: *The Optical Gravitational Lensing Experiment. Search for Planetary and Low-Luminosity Object Transits in the Galactic Disk. Results of 2001 Campaign*, Acta Astron., 52, 1
- Udalski, A., Szymanski, M., Kaluzny, J., Kubiak, M., & Mateo, M. 1992: *The Optical Gravitational Lensing Experiment*, Acta Astron., 42, 253
- Udalski, A., Zebrun, K., Szymanski, M., Kubiak, M., Soszynski, I., Szewczyk, O., Wyrzykowski, L., & Pietrzynski, G. 2002b: *The Optical Gravitational Lensing Experiment. Search for Planetary and Low-Luminosity Object Transits in the Galactic Disk. Results of 2001 Campaign – Supplement*, Acta Astron., 52, 115
- Udry, S., Bonfils, X., Delfosse, X., Forveille, T., Mayor, M., Perrier, C., Bouchy, F., Lovis, C., Pepe, F., Queloz, D., & Bertaux, J.-L. 2007: *The HARPS search for southern extra-solar planets. XI. Super-Earths (5 and 8 M_{\oplus}) in a 3-planet system*, A&A, 469, L43
- Vidal-Madjar, A., Désert, J.-M., Lecavelier des Etangs, A., Hébrard, G., Ballester, G. E., Ehrenreich, D., Ferlet, R., McConnell, J. C., Mayor, M., & Parkinson, C. D. 2004: *Detection of Oxygen and Carbon in the Hydrodynamically Escaping Atmosphere of the Extrasolar Planet HD 209458b*, ApJ, 604, L69
- Vidal-Madjar, A., Lecavelier des Etangs, A., Désert, J.-M., Ballester, G. E., Ferlet, R., Hébrard, G., & Mayor, M. 2003: *An extended upper atmosphere around the extrasolar planet HD209458b*, Nature, 422, 143
- Ward, W. R. 1997: *Protoplanet Migration by Nebula Tides*, Icarus, 126, 261
- Ward, W. R. & Hourigan, K. 1989: *Orbital migration of protoplanets - The inertial limit*, ApJ, 347, 490
- Warren, S. & Hewett, P. 2002: *WFCAM, UKIDSS, and $z = 7$ Quasars*, in Astronomical Society of the Pacific Conference Series, Vol. 283, A New Era in Cosmology, ed. N. Metcalfe & T. Shanks, 369
- Weidenschilling, S. J. & Marzari, F. 1996: *Gravitational scattering as a possible origin for giant planets at small stellar distances*, Nature, 384, 619
- Werner, M. W., Roellig, T. L., Low, F. J., Rieke, G. H., Rieke, M., Hoffmann, W. F., Young, E., Houck, J. R., Brandl, B., Fazio, G. G., Hora, J. L., et al. 2004: *The Spitzer Space Telescope Mission*, ApJS, 154, 1
- Wetherill, G. W. 1980: *Formation of the terrestrial planets*, ARA&A, 18, 77
- Winn, J. N. 2010: *Transits and Occultations*, ArXiv e-prints

- Wolszczan, A. & Frail, D. A. 1992: *A planetary system around the millisecond pulsar PSR1257 + 12*, Nature, 355, 145
- Wright, J. T. & Gaudi, B. S. 2013, Exoplanet Detection Methods, ed. T. D. Oswalt, L. M. French, & P. Kalas, 489
- Wuchterl, G. 1996: *Formation of Giant Planets Close to Stars*, in Bulletin of the American Astronomical Society, Vol. 28, AAS/Division for Planetary Sciences Meeting Abstracts #28, 1108
- Zendejas, J., Koppenhoefer, J., Saglia, R. P., Birkby, J. L., Hodgkin, S. T., Koács, G., Pinfield, D. J., Sipőcz, B., Barrado, D., Bender, R., del Burgo, C., et al. 2013: *Searching for transits in the WTS with difference imaging light curves*, A&A
- Zendejas, J., Segura, A., & Raga, A. C. 2010: *Atmospheric mass loss by stellar wind from planets around main sequence M stars*, Icarus, 210, 539

Acknowledgments

On top of these acknowledgments, I am profoundly thankful to Johannes Koppenhöfer. This thesis would not have been successfully completed without your support from beginning to end. But I specially want to thank him for his sincere friendship. I am heartily grateful to Roberto Saglia for the scientific contribution to this thesis. His valuable and useful comments were fundamental for the development of this work. I also would like to thank Roberto for patiently reading the innumerable versions of the thesis. I would like to express my gratitude to Ralf Bender for giving me the opportunity of being part of these honorable institutions.

I would like to make an special distinction to David Pinfield for the great idea of RoPACS. I am totally thankful to David and Roberto for letting me be part of RoPACS. In this point, I also would like to thank all the RoPACS community; I have wonderful memories of our meetings. I am also grateful to Jayne Birkby for the suitable suggestions and ideas that considerably improved the results of my work.

I would like to thank sincerely Jon Sundqvist for spending time reading and correcting my manuscript. The English and spelling of the final version could have been much worse without him. I learned a lot with his comments. Many thanks to Christian and Ben for their German and English contribution to this thesis. I also appreciated very much the technical help of Tadziu Hoffmann. All my gratitude to my office-mates for the amazing and friendly atmosphere that they brought to our office. My time at the USM would not have been definitely the same without them.

I specially would like to thank Teresa Avila for generously spending time filling down kilograms and kilograms of bureaucracy sheets. The hours of tedium coupled with some bottles of tequila resulted in my economic support of the last year.

I am deeply grateful to Ute for being with me during my health problems. “Freunde sind wie Sterne, du kannst sie nicht immer sehen, aber du weisst, dass sie da sind”

Special thanks and all my love to mi Jefe, mi Jefa, Lety, Claus, Artur and Santiago, my lovely family that always are close to me despite the distance. Finally, I want to thank those people that are unconditionally part of my life. I am immensely grateful to all of you for helping me to make possible the culmination of this story. Your courage, friendship and optimism guided my way when there was no more reason to continue. You always will be in my heart.

I acknowledge the support of RoPACS network during this research, a Marie Curie Initial Training Network funded by the European Commissions Seventh Framework Programme. This publication makes use of the VOSA, developed under the Spanish Virtual Observatory project supported from the Spanish MICINN through grant AyA2008-02156.

This work has made use of the NASA/IPAC Extragalactic Database (NED) which is operated by the Jet Propulsion Laboratory, California Institute of Technology, under contract with the National Aeronautics and Space Administration.

Furthermore, I have made use of NASA’s Astrophysics Data System, and the SIMBAD database operated at CDS, Strasbourg, France.

Curriculum Vitae

Name: Jesús Zendejas Domínguez
Citizenship: Mexican
Date of birth: 16th August 1982
Place of birth: Morelia-Michoacan, Mexico

Education

- **2009-2013, PhD in Astrophysics**
University Observatory Munich, Faculty of Physics
Ludwig-Maximilians-Universität (USM-LMU)
Munich, Germany
- **2007-2009, Masters in Astrophysics**
Institute of Astronomy
Universidad Nacional Autónoma de México IA-UNAM)
Mexico, D.F.
- **2001-2006, Bachelor in Physics**
Faculty of Science
Universidad Nacional Autónoma de México
Mexico D.F.
- **1997-2000, High School**
National High School No.5
Universidad Nacional Autónoma de México
Mexico D.F.